

Master-Thesis

Investigation on the Aeroacoustics and Flow Pattern of a NACA65(12)-10 Aerofoil with Serrated Leading Edges

Submitted by: Oliver Koster

Matriculation number: 667192

Duesseldorf

May 2017

Supervisor (First examiner)

Prof. Dr.-Ing. Jörg Becker-Schweitzer
Institute of Sound and Vibration Engineering
Fachbereich Maschinenbau und Verfahrenstechnik
Münsterstraße 156, 40476 Düsseldorf
joerg.becker-schweitzer@hs-duesseldorf.de

Second examiner

Dr. Tze Pei Chong
College of Engineering, Design and Physical
Sciences
Brunel University London
Uxbridge UB8 3PH, United Kingdom
t.p.chong@brunel.ac.uk

Abstract

This thesis describes a study on the application of leading edge undulations as a passive flow-control device for enhancing aerofoil performance and reducing AGI noise. This noise generation mechanism is fundamental in the field of aeroacoustics.

The aim of this thesis is the investigation on the aerodynamic performance, flow pattern and aeroacoustics of a NACA65(12)-10 aerofoil with different sinusoidal leading edges.

The first part comprises an aerodynamic study using ten different leading edge undulations with the influencing factors amplitude (A) and wavelength (λ) in order to characterise the aerofoil performance. Lift and drag forces are measured using a force balance equipped to an open circuit type wind tunnel at Brunel University London.

The second part investigates the boundary layer characteristics of the NACA65(12)-10 aerofoil equipped with two different leading edges. The study focuses on serrated leading edge designs with superior aerodynamic or aeroacoustic performance. The investigation is performed in an open-jet wind tunnel at the Brunel University London where a grid is used to create high turbulent incoming flow. Measurements at different streamwise and spanwise locations are made to describe the flow characteristics. Hot-wire anemometry is used in this experiment.

The third part presents a study on surface oil flow visualisation which is used to validate the results of the boundary layer measurements and to visualise near wall vortices as well as separation zones on the aerofoil.

In the fourth part, investigations in the two-dimensional plane of the near wake of the aerofoil are made to provide further information on the flow physics. A cross-wire configuration is used to measure single boundary profiles and 2D planes.

Acknowledgement

I would like to thank my first examiner Prof. Dr.-Ing. Jörg Becker-Schweitzer for the supervision of this project.

I would like to thank my supervisor Prof. Dr.-Ing. Frank Kameier for making this project and this great experience possible. I am grateful for the support, the helpful suggestions and the opportunity to be part of this research.

I would like to express my gratitude to Dr. Tze Pei Chong, my second examiner and supervisor at Brunel University London. Thank you for the tremendous support, your guidance and your advice whenever it was needed.

I would like to thank Till Biedermann for supporting me with this project and helping me with the planning of my work. Thank you for the supervision during the whole time and the help with all the arrangements.

I would like to thank the Institute of Sound And Vibration Engineering at the Hochschule Düsseldorf for funding this research during my time at the Brunel University London.

I would also like to thank the PhD students and friends Laith Al-Sadawi, Philip Woodhead, Auris Juknevicus, Jonne Jeyalingam and Chioma Muhammad for their amazing support and company during my time at Brunel University.

I would like to thank Kevin Robinson for his technical support and advice in the laboratories.

Finally, I would like to thank my parents for their support and help.

Nomenclature

Latin

a	Mean-line loading designation	[-]
a_0	Lift force aft zero reading	[N]
A	Amplitude of serrations	[mm]
A_u	Lift force aft (uncorrected)	[N]
c	Chord length	[m]
C_D	Drag coefficient	[-]
C_{Du}	Uncorrected drag coefficient	[-]
C_{fL}	Lift coefficient in frictionless flow	[-]
C_L	Lift coefficient	[-]
C_{Lu}	Uncorrected lift coefficient	[-]
C_p	Static pressure coefficient	[-]
d	Distance between hot wire probe an aerofoil surface	[mm]
d_{GRID}	Mesh bar diameter	[mm]
d_0	Drag force fore zero reading	[N]
D	Drag force	[N]
D_u	Drag force fore (uncorrected)	[N]
f	Frequency	[Hz]
F_u	Lift force fore (uncorrected)	[N]
f_0	Lift force fore zero reading	[N]
h	Test section height	[m]

h_{GRID}	Grid height	[mm]
k^2	Yaw-coefficient	[-]
K_χ	Normalised streamwise wavenumber	[-]
K_η	Constant factor	[m ⁻¹]
L	Lift force	[N]
m_{GRID}	Mesh size of grid	[mm]
p_i	Static pressure measured at location i	[Pa]
p_∞	Atmospheric pressure	[Pa]
p_s	Static pressure	[Pa]
p_t	Total pressure	[Pa]
p	Atmospheric pressure	[Pa]
p	Sound pressure	[Pa]
Re_c	Chord based Reynolds number	[-]
R_{specific}	Universal gas constant	[J kg ⁻¹ K ⁻¹]
R_0	Sensor resistance at ambient temperature	[Ω]
R_w	Sensor resistance at operating temperature	[Ω]
S	Surface area baseline leading edge	[m ²]
S_m	Surface area serrated leading edge (measured)	[m ²]
t	Aerofoil thickness	[m]
T	Temperature	[K]
u	Free stream velocity	[m s ⁻¹]
w_{GRID}	Grid width	[mm]

Greek

α	Angle of attack (geometric)	[°]
α_0	Temperature coefficient of resistance	[%/C]
$\Gamma(x)$	Gama function	[-]
Δ	Absolut difference	[various]
κ_e	Wavenumber	[m ⁻¹]
ϵ_{sb}	Solid blockage correction factor	[-]
ϵ_{wb}	Wake blockage correction factor	[-]
η	Dynamic fluid viscosity	[kg m ⁻¹ s ⁻¹]
λ	Wavelength of serrations (also W)	[mm]
λ_2	Body shape factor	[-]
Λ_{uu}	Spanwise integral length scale	[mm]
ρ	Fluid density	[kg m ⁻³]
$\phi_{uu}^{VK}(\omega)$	Longitudinal power-density spectrum Von Karman	[dB/ Hz]
$\phi_{uu}^L(\omega)$	Longitudinal power-density spectrum Liepmann	[dB/ Hz]
ω	Angular frequency	[rad/s]

List of Abbreviations

ACARE	Advisory C ouncil for A eronautical R esearch
A/D	Analog to D igital converter
AoA	A ngle of A ttack
AGI	A irfoil- G ust- I nteraction
BNC	B ritish N avy C onnector
BSLN	B aseline (straight leading edge)
CTA	C onstant T emperature A nomometer
HWA	H ot- W ire A nomometry
ISAVE	Institute of S ound A nd V ibration E ngineering
ISVR	Institute of S ound and V ibration R esearch
LE	L eading E dge
LES	L arge E ddy S imulation
N	N umber of samples
NACA	N ational A dvisory C ommittee for A eronautics
Re	R eynolds number
Re _c	C hord based R eynolds number
RMS	R oot M ean S quare
RPM	R ounds P er M inute [min ⁻¹]
SLS	S elective L aser S intering
SPL	S ound P ressure L evel [dB]
SR	S ampling R ate
T	S ampling T ime
TCR	S ensor T emperature C oefficient
TE	T railing E dge
Tu	T urbulence I ntensity

Table of Contents

Abstract.....	III
Acknowledgement.....	IV
Nomenclature.....	V
List of Abbreviations.....	VIII
1 Introduction	1
1.1 Aims and objectives.....	3
1.2 Thesis structure	4
2 Literature Review	5
3 NACA65(12)-10.....	9
3.1 Aerofoil design.....	9
3.2 Static pressure distribution	10
3.3 Leading edge design	12
4 Aerodynamic measurements.....	15
4.1 Experimental setup & measurement facilities	15
4.2 Experimental procedures.....	16
4.3 Results & discussion	19
5 Boundary layer measurements.....	24
5.1 Experimental setup & measurement facilities	24
5.1.1 Anechoic chamber & wind tunnel.....	24
5.1.2 Aerofoil setup.....	25
5.2 Hot-Wire setup	26
5.2.1 System configuration	27
5.2.2 Anemometer setup	28
5.2.3 Traversing system	30
	IX

5.2.4 Velocity calibration & data conversion.....	30
5.3 Experimental methodology	31
5.3.1 Generation of turbulence	31
5.3.2 Measurement procedure.....	34
6 Data analysis boundary layer measurements	38
6.1 Suction side.....	38
6.1.1 Boundary layer profiles	38
6.1.2 Turbulence intensity.....	43
6.1.3 Spectral analysis.....	47
6.2 Pressure side	51
6.2.1 Boundary layer profiles	51
6.2.2 Turbulence intensity.....	53
6.2.3 Spectral analysis.....	54
7 Comparison of experimental measurements to the numerical simulations.....	57
8 Surface oil flow visualisation.....	62
8.1 Setup.....	62
8.2 Suction side A45W26	62
8.3 Pressure side A45W26	64
9 Wake measurements	67
9.1 Hot-Wire setup	67
9.1.1 Velocity calibration.....	67
9.1.2 Yaw calibration	69
9.2 Experimental setup.....	72
10 Data analysis wake measurements	74
10.1 Velocity profiles	74
10.2 Turbulence intensity	77
10.3 Spectral analysis	81
11 Conclusion	83

References.....	84
Appendix A – Aerodynamic measurements.....	88
Appendix B – Boundary layer measurements.....	91
Appendix C – Wake measurements	121
Appendix D – A12W26 LE.....	135
Eidesstattliche Erklärung.....	137

1 Introduction

Millions of people in Europe are affected by noise pollution every day. A high level of industrialisation and a strong demand on transportation lead to an increase of noise emission. With the growing aircraft industry and the use of new sources of energy like wind turbines, regulations on environmental pollution, especially in terms of fuel emissions and noise, arise continuously. Aerodynamic sound generation from surfaces that rotate as propulsive devices, e.g. rotor or fan blades, are recognized as one of the dominant noise sources for aircrafts. One of the targets in the 7th Environment Action Programme by the EU is the reduction in noise pollution by 2020 (European Commission, 2012). The Advisory Council for Aeronautical Research (ACARE) published a report to reduce noise levels by 50% until 2020 compared to the year 2000 (ACARE, 2015). The European Commission sets targets in the *Flight Path 2050* programme to reduce aircraft noise emissions by 65% until the year 2050 (European Commission, 2011). In addition, renewable sources of energy, such as wind power, are an important topic of recent politics. Unfortunately, wind turbine noise is one of the major issues for the use of wind energy. Aerodynamic noise from the blades is generally considered to be the dominant noise source (Figure 1).



Figure 1: Wind turbine with projection of the noise source distribution in the rotor plane (averaged over many revolutions) (Oerlemans, 2011)

New technologies and approaches are needed to reduce the emitted aerofoil sound and achieve the future goals set by the European Commission. Since nature has always inspired human achievements and has led to effective systems, materials, structures and other benefits, scientists are trying to adopt mechanisms from nature to the fields of

aerodynamic and aeroacoustics. The study of this bio-inspired technologies is known as biomimetics and was first examined extensively by Schmitt (1969). He defines biomimetics as the study of the function of biological systems as models for the design and engineering of materials and machines. Many recent studies which are related to aerodynamic and aeroacoustics of wing sections investigate the silent flight of the owl and try to transfer the mechanism to the aerofoil geometry. The wings of an owl are equipped with wavy comb-type leading edges and fringe type trailing edges which can reduce the flow induced noise (Figure 2). Geyer, et al. (2014) conclude that the sound pressure level difference, compared to non-silently flying birds, is significant at medium and high frequencies. Both the geometrical modification of the aerofoil leading edge and trailing edge are of high interest in ongoing research. However, the application of leading edge undulations is also due to another inspiration by nature.

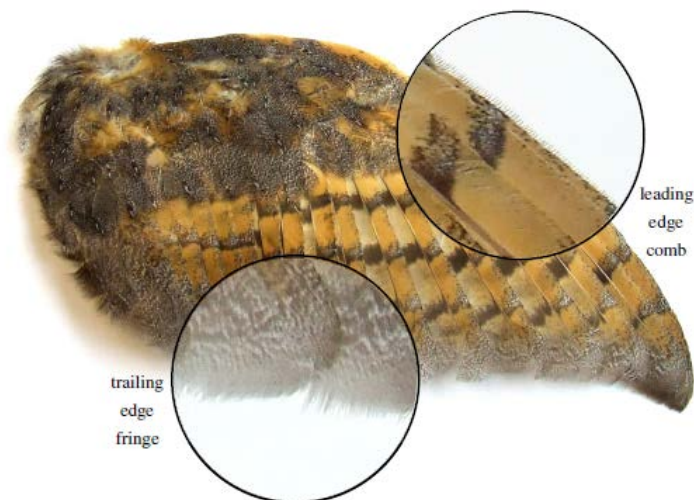


Figure 2: Separated barn owl wings (Geyer, et al., 2014)

The stall-delaying properties of the humpback whale flipper have been observed and quantified in recent studies, both experimental and numerically. Fish et al. (1995) undertook a detailed study to understand the mode of operation of the tubercles and suggested that they may act as a passive flow-control device, delaying the stall angle. The tubercles on the leading edge of the flipper can be described as rounded protuberances that alter the flow-field. Figure 3 shows humpback whales' flippers with undulations on the leading edge. The mechanism behind these undulations can be compared to that of a vortex generator whereby the boundary layer is reenergized. As a result, the application of leading-edge tubercles for passive flow-control has potential in the design of wind turbines and may be particularly appropriate for wings at high angle of attack. The maintenance of lift at high angles of attack leads to enhanced performance and manoeuvrability. However, leading edge undulations can also be applied to reduce

aerofoil-gust-interaction noise (AGI) where the free stream turbulence interacts with the aerofoil leading edge what leads to broadband noise radiation. In the context of this work the focus is on the aerodynamic mechanism and the aeracoustics of different leading edge configurations subjected to turbulent flow.



Figure 3: Photographs of humpback whales' flippers showing the leading edge with tubercles (Fish, et al., 2011)

1.1 Aims and objectives

This thesis describes a study of the application of leading edge undulations as a passive flow-control device for enhancing aerofoil performance and reducing AGI noise.

The aim of this thesis is the development of an efficient method to investigate and describe the influence of serrated leading edges on aerofoil performance and on the streamwise flow pattern downstream of the serrated edges. The research is focused on serrated leading edge designs with superior aerodynamic or aeroacoustic performance based on a NACA65(12)-10 aerofoil. Detailed measurements at different streamwise and spanwise locations are necessary to describe the flow characteristics. Additionally, examinations on the boundary layers at both the suction and pressure sides are of interest and can be compared to each other. Further investigations in the two-dimensional plane of the near wake of the aerofoil can provide further flow physics and complement the overall results. Several experimental techniques are to be used in this study, which comprise aerodynamic measurements of the lift and drag force, hot-wire anemometry (single and cross hot-wires) and surface oil flow visualisation. Boundary layer and wake measurements are conducted in the open-jet wind tunnel at Brunel University. The aerodynamic forces measurements are conducted in an open circuit type wind tunnel. These experiment results obtained from the Brunel University will be

compared with numerical results provided by ISAVE. The effects of the serrations on the flow pattern are discussed and an interpretation of the results given.

1.2 Thesis structure

This thesis describes the results of an experimental study performed at the Brunel University London aimed to investigate the aeroacoustics and flow pattern of a NACA65(12)-10 aerofoil with serrated leading edges. The organisation of this thesis is as follows.

Chapter 2 presents the fundamentals of leading edge noise and an overview of recent publications.

Chapter 3 describes the NACA65(12)-10 aerofoil used in this experimental investigation and examines the leading edge design.

Chapter 4 presents the aerodynamic measurements conducted in the open circuit suction type wind tunnel of ten different leading edges. Lift and drag coefficients are calculated and presented.

Chapter 5 deals with boundary layer measurements conducted in the open-jet aeroacoustic wind tunnel using hot-wire anemometry. The experimental setup, the measurement facilities and the methodology are described.

Chapter 6 presents the results of the boundary layer measurements. Single boundary layer profiles are presented as well as contour plots of the turbulence intensity. Spectral analysis gives an insight of the energy distribution.

Chapter 7 compares the velocity profiles measured in the boundary layer to numerical results provided by ISAVE.

Chapter 8 presents an oil flow visualisation which is performed on the suction and pressure side of the serrated leading edge.

Chapter 9 deals with hot-wire measurements using a cross-wire in the near wake of the aerofoil and explains the yaw-calibration procedure.

Chapter 10 presents the results of the near wake measurements. Boundary layer profiles, contour plots and the spectral analysis are presented.

2 Literature Review

The literature review focuses on leading edges subjected to high turbulent flow and on the theory of leading edge serrations. Experimental and numerical studies, recent publications and fundamental literature are considered to provide an introduction and give an overview of the topic.

Aerodynamic sound is generated when a solid surface, e.g. an aerofoil is situated in an unsteady and non-uniform flow. This noise generation mechanism is known as aerofoil-gust-interaction (AGI) noise and fundamental in the field of aeroacoustics. AGI noise is a significant noise source in many different applications since wind turbine blades, fans, propellers, aero-engines, etc. are constantly subjected to gust or turbulent wakes. Goldstein (1978) describes the AGI noise to be generated by surface pressure fluctuations close to the aerofoil leading edge. It arises due to the rapid distortion of the vorticity field impinging on the LE (Amiet, 1975). The pressure fluctuations are supposed to balance the momentum fluctuations that occur due to the distortion of the velocity disturbance. Already 1934, Graham related the leading edge comb of an owl to the interaction with fluctuations in the incoming air flow. He noted that these structures effect the local pressure gradient and result in a reduction of noise. Sonderman (1974) was one of the first who actively used leading edge serrations to control aerofoil noise from two different size rotors. His experiment used various rotor speeds, different serration geometry, different positions of the serrations and a variation in blade angle. It was noticed that the overall noise reductions vary between 4 and 8 dB. However, the aerodynamic characteristics were highly sensitive to the position of the serrations. Many studies have been performed regarding the aerodynamic characteristics of serrated leading edges. Therefore, the geometry of the LE was altered from a sawtooth shape to a wavy leading edge. Whereas Ito (2009) found out that the post-stall aerodynamic benefit of serrated LE was only observed at low Reynolds number (2.1×10^4), several other authors showed that LE undulations may lead to a more beneficial stall behaviour and post-stall performance in a wide range of flow speeds (Johari, et al., 2007; Hansen, et al., 2011; Skillen, et al., 2014). However, a weak pre-stall performance was observed but can be reduced by optimising the LE design (Hansen, et al., 2011). The aerodynamic performance of leading edge undulations is also part of the present work. Ten different leading edges are tested to obtain information about the influence of the amplitude and wavelength on the characteristic values. Nevertheless, further understanding of the aeroacoustic effects of the undulated LEs is necessary. Narrow band vortex shedding noise can effectively be reduced from stationary and rotating aerofoils using leading edge serrations by 4 to 8 dB (Hersh, et al., 1974). They point out

that the tones, generated by the periodic fluctuating forces near the trailing edge by forming vortices which alter the wake such that the velocity fluctuations change from periodic to random, are reduced by the LE serrations. Migliore & Oerlemanns (2004) also observed that AGI noise can be the dominant noise when the level of turbulence impinging on the aerofoil is sufficiently high. Similar observations have also been made by Hansen, et al. (2012). The application of undulated LEs to a NACA0021 aerofoil at Reynolds number of 1.2×10^5 resulted in a reduction in aerofoil tonal noise. Streamwise vortices behind the root tend to break up the coherence of vortex generation at the trailing edge and can be identified as being the reason for the reduction in tonal self-noise. These observations can be confirmed by Longhouse (1977) and Arndt & Nagel (1972). Lau, et al. (2013) performed numerical simulations to investigate the effects of wavy leading edges on aerofoil-gust-interaction (AGI) noise. They found out that the main factor that determines the noise reduction performance is the ratio of the LE amplitude (A) to the wavelength of the gust. Significant noise reductions were achieved when the ratio of A to the gust wavelength exceeds 0.3. Far field noise reductions can be achieved, since the wavy leading edge causes a more rapid phase variation of pressure fluctuations along the LE as compared to the baseline LE (Lau, et al., 2013). A numerical and experimental investigation by Clair, et al. (2013) into the effect of sinusoidal leading edges on AGI noise showed a reduction in sound power level of about 3 – 4 dB without affecting the aerodynamic performance. Further studies were conducted describing the dependence of noise reduction on the geometric parameters of the leading edge. Haeri, et al. (2014) and Narayanan, et al. (2015) showed that the serration amplitude is mainly the factor that determines noise control performance. Chong, et al. (2015) conducted a study on turbulence-leading edge interaction noise with 12 sinusoidal leading edges. It was shown that the largest reduction in aerofoil noise can be associated with the LE of the largest amplitude (A) and smallest wavelength (λ), whereas a small amplitude and large wavelength is preferred to maintain the aerodynamic performance. Much more recently, Biedermann, et al. (2016) performed an experimental aeroacoustic study in order to quantify the effects of five influencing parameters on the broadband noise emission and reduction of serrated leading edges subjected to turbulent flow. It was observed that the Reynolds number (Re) and the free-stream turbulence intensity (Tu) contribute to the broadband noise emission. The main factors for effective broadband noise reduction were the serration amplitude (A/c), the Reynolds number (Re) and the serration wavelength (λ/c). Large serration amplitudes and small to intermediate wavelength reduced the broadband noise in the most effective way. Furthermore, counter-rotating vortices could be visualised at the lower edges of the pressure side and are believed to be the main mechanism in the reduction of broadband noise radiation.

Camara (2013) performed detached eddy simulations using a sinusoidal leading edge for passive stall control. Figure 4 shows the flow topology on the suction side of the leading edge wing section. Instantaneous vortical structures have been visualised. It can be seen that these streamwise structures are formed at the valley(s) of the leading edge and propagate to the trailing edge.

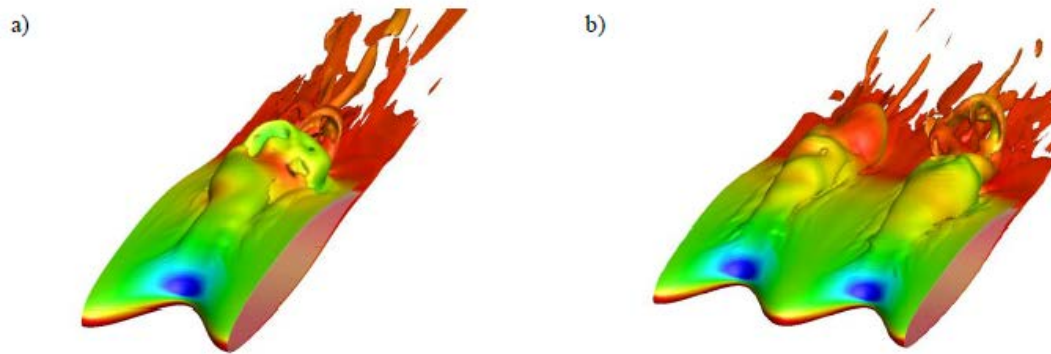


Figure 4: Instantaneous flow fields of a NASA LS(1)-0417 a) S1 (one wavelength) and b) S2 (two wavelengths) at an AoA of 7.5 degrees with $Re = 1.6 \times 10^5$ (Camara, 2013)

Skillen, et al. (2015) performed LES simulations for the flow over a symmetrical NACA0021 aerofoil with leading edge undulations. Figure 5 shows slices of the streamwise vorticity providing an insight of the strong spanwise velocity gradients and the formation of secondary flow. It is believed that low-inertia near-wall fluid is transported away by the secondary flow, whereas high-momentum fluid is drawn from above, re-energising the boundary layer.

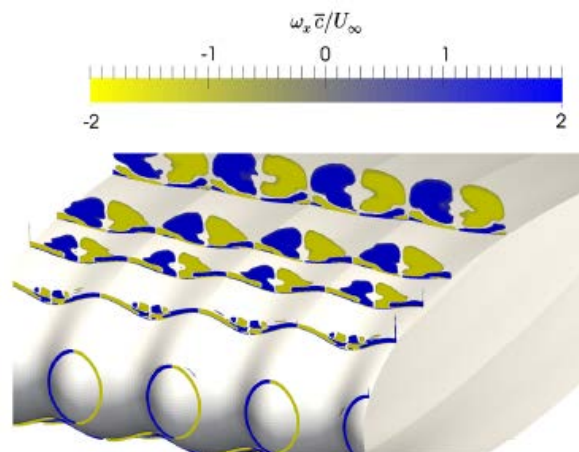


Figure 5: Slices colored by time-averaged streamwise vorticity (Skillen & Revell, 2015).

Skillen, et al. (2015) also provides an overview of the surface flow on the suction side which shows the time-averaged wall shear-stress lines (Figure 6). Additionally, a sketch indicates the flow direction, separation and reattachment of the flow. Strong flow acceleration between the undulation peaks can be identified which is believed to

augment turbulence levels. The main separation line at the mid-chord of the aerofoil shows strong spanwise variation which can be assigned to a complex three-dimensional flowfield in this region. Shear flow along this separation is believed to generate a large vortex system.

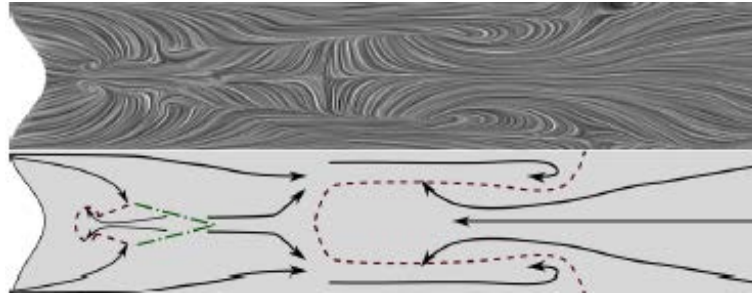


Figure 6: Time-averaged wall shear stress (top) and schematic of flow direction (bottom) with indication of separation (dashed line) and reattachment (dot-dashed line) (Skillen & Revell, 2015)

3 NACA65(12)-10

This chapter deals with the characteristics of a NACA65(12)-10 wing section and gives a brief description about the sinusoidal leading edges which are to be used in this study. The aerodynamic characteristics and the noise reduction capability are strongly affected by the shape of the aerofoil and the attached leading edge.

3.1 Aerofoil design

The NACA65(12)-10 aerofoil is used in this experiment to investigate the aerodynamic characteristics and aeroacoustic performance of serrated leading edges. It was chosen for the EU-funded FLOCON project as a representing aerofoil for high lift devices and was, therefore, also used in the empiric-statistical aeroacoustic study by Biedermann. Furthermore this specific aerofoil has been subjected to various experimental and numerical investigations at Brunel University London and is in the ongoing research of high interest in terms of aerodynamics and acoustics. The aerofoil is characterised by a high-cambered profile and its asymmetric shape. Figure 7 shows the cross section view of the model including dimensionless coordinates and characteristic lines. The chord line is defined as the straight line connecting the leading edge and the trailing edge. An angle of attack of zero is given when the chord line and the incoming flow are aligned. The asymmetric shape of the model leads to the presence of lift forces at zero AoA. The camber of this wing section is defined by the mean line and the thickness distribution.

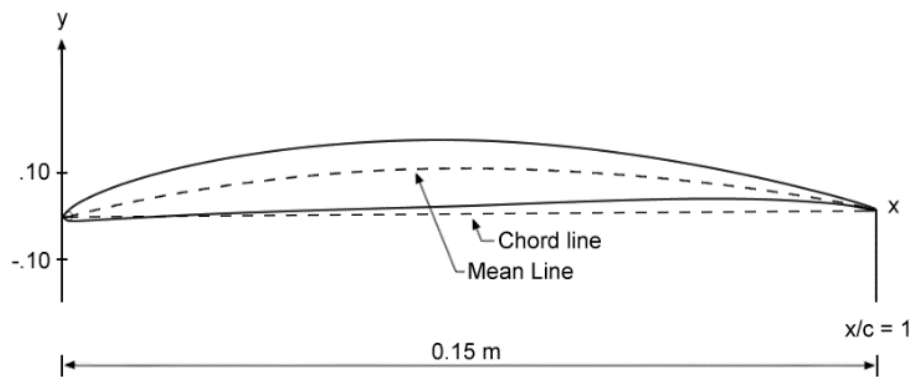


Figure 7: NACA65(12)-10 coordinates

The numbering system for this NACA aerofoil is based on the aerofoil geometry. The 6 is the series designation and denotes a high maximum lift coefficient as well as a very low drag over a range of operating conditions. The aim of the geometrical shape of the 6-series was to maximize the region over which the airflow remains laminar. However, the drag coefficient is designated to be high outside of the optimum range of operating conditions for this aerofoil and in general, the 6-series shows a poor stall behaviour. This

aerofoil is known for high-speed application and suitable for use as fan blades. The second digit 5 denotes the chord wise position of minimum pressure in tenths of the chord behind the leading edge at zero lift. In the designation the lift coefficient in a frictionless flow C_{fL} is given by the numbers in the parentheses. In this case the number of $C_{fL} = 1.2$ is in direct relation to the camber of the aerofoil. The last two digits indicate the aerofoil thickness with a value of 10 percent of the chord. The basic mean line used is described by $a = \frac{x}{c} = 1$ (Abbot, et al., 1945) which defines the uniform chordwise loading. Both the manufacturing of the aerofoil main model (McEwen, 2015) via Selective Laser Sintering (SLS) and the design of the serrated leading edges (Biedermann, 2015) with the CAD software NX9.0 were performed in previous studies.

3.2 Static pressure distribution

The objective of this section is to examine the surface pressure distribution to create a basis for further investigations. A body immersed in a flowing fluid is exposed to both pressure and viscous forces. The forces on a body when air flows around it can be determined via measurement of the pressures on the body's surface. The geometry of this body and the external flow leads to a pressure distribution at the edge of the boundary layer. This distribution is of decisive importance for the development of the boundary layer. For example, the transition from laminar to turbulent and the detachment of the boundary layer from the wall depends on the pressure at position x . A NACA65(12)-10 aerofoil provided by the ISVR is used to measure the static pressure distribution. It is composed of a main steel body and a detachable sharp trailing edge with an overall chord length of 0.15 m. The body is equipped with a set of ten pressure holes along the chord in the mid-span plane both on pressure and suction side of the aerofoil, which allow the measurement of the static and unsteady pressure. The pressure tapings are located at the following positions, where x/c is the chordwise distance of the holes from the leading edge, normalised by the aerofoil chord: 0.017, 0.05, 0.083, 0.13, 0.2, 0.27, 0.33, 0.47, 0.6, 0.73, 0.92, 0.93 (Gruber, 2012).

The static pressure coefficient given by C_p in equation 3.1 is measured using a *Furness Controls Limited FCO510* micromanometer connected to a *Furness Controls* channel switcher and a pitot-static tube.

$$C_p = \frac{p_i - p_\infty}{\frac{1}{2} \rho u^2}, \quad (3.1)$$

where p_i is the static pressure measured at location i along the aerofoil chord, p_∞ the atmospheric pressure, ρ the density of air and u the freestream velocity (equation 4.1)

Figure 8 shows the static pressure coefficient calculated from the experimental data using equation 3.1 for an AoA of 0° and free stream velocity of 24 ms^{-1} . Because the velocity of the flow over the top of the aerofoil is higher than the free stream velocity, the pressure over the top is negative. Similarly the velocity along the lower side of the aerofoil is less than the free stream velocity and the pressure there is positive. Hence, both the negative pressure and the positive pressure contribute to the lift force acting on the aerofoil. For comparison, a contour plot of the simulation performed by Schreiber (2017) is included (Figure 9). The pressure distribution along the chord shows reasonable agreement with the experimental data. The point near the leading edge on the upper surface of the aerofoil with a maximum pressure ($\sim 300 \text{ Pa}$) is known as the stagnation point. From this point the pressure is decreasing in streamwise direction until it reaches the chord wise position of $x/c = 0.5$ with a minimum pressure of -200 Pa . This region is known as a favourable pressure gradient because it is the natural direction of the flow. The stream velocity is noticeable higher in this part. From this point of minimum pressure to the trailing edge, the pressure is increasing, causing an adverse pressure gradient. The flow loses velocity over this region and tends to lift up from the surface of the aerofoil. On the pressure side, the specific aerofoil geometry results in an increase of pressure towards the trailing edge. Here, the dominant effect is the adverse pressure gradient inhibiting the natural flow. The deceleration takes place in accordance with Bernoulli's law. In the boundary layer the viscous forces are dominant and the reduced kinetic energy of the boundary-layer air limits its ability to flow against the adverse pressure gradient. Overall, accelerated flows are considerably more stable than decelerated flows. The strong influence of the pressure gradient on stability and on the amplification of small disturbances was already proved experimentally in the past (Schlichting, et al., 2006). However, for the purpose of this study it should be noted that the pressure gradients in spanwise direction are also of high interest. It is expected that tubercles remarkably alter the surface pressure distribution in spanwise direction in comparison with the baseline foil. These effects are investigated in Chapter 5 Boundary layer measurements.

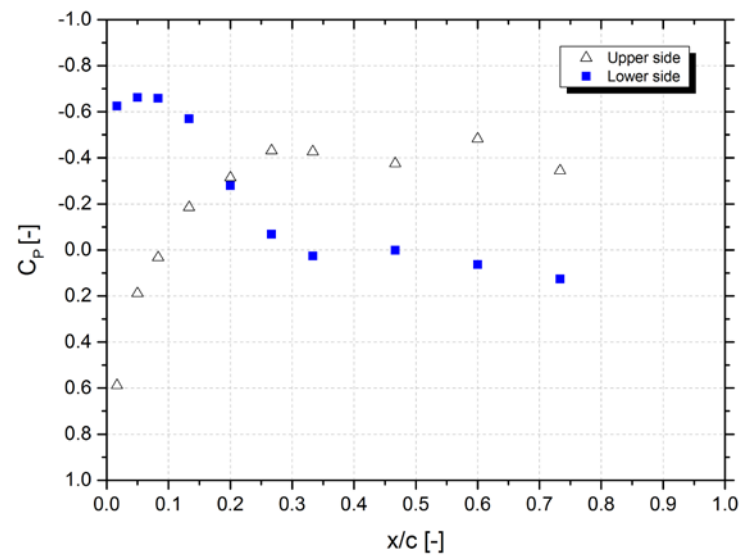


Figure 8: Experimental pressure distribution NACA65(12)-10 with baseline LE measured at AoA = 0° and $U = 24 \text{ ms}^{-1}$

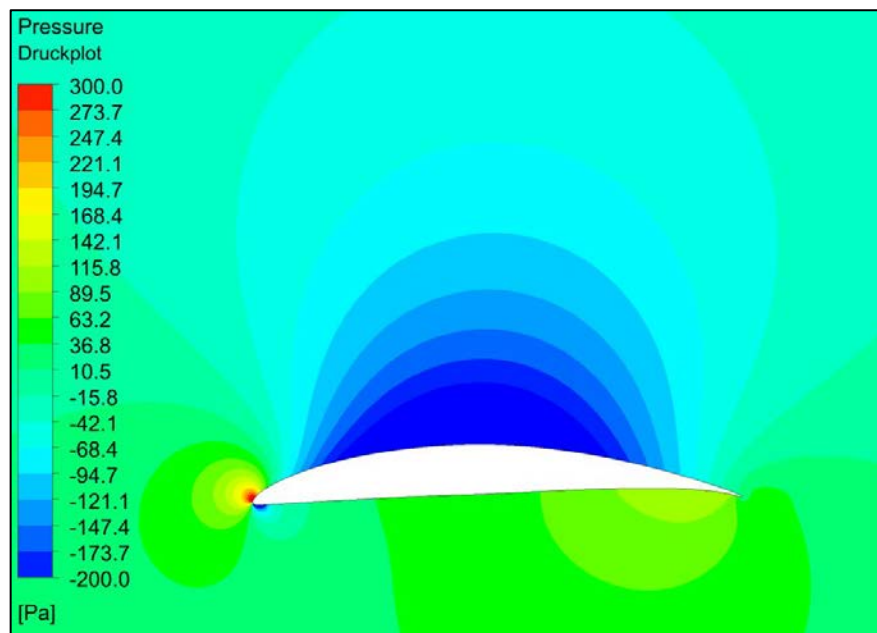


Figure 9: Numerical pressure distribution [Pa] NACA65(12)-10 with baseline LE at AoA = 0° and $U = 25 \text{ ms}^{-1}$ (Schreiber, 2017)

3.3 Leading edge design

The design of the serrations can be described by a sinusoidal curve along the leading edge with the characteristic shape of semi-cyclic serration tips. Two parameters define

the sinusoidal curve: The serration amplitude A includes a range of 12 mm to 45 mm and the observed wavelength λ reaches from 7.5 mm to 45 mm. Figure 10 shows the 3D-model of the aerofoil including the attachable leading edge (A45W26). Additionally the top and side view provides the definition of the characteristic parameters. The aerofoil model is composed of the main body with a chord of 100 mm and an interchangeable leading edge with a chord of 50 mm. The geometry modification only affects the leading edge region while the rest of the aerofoil, including the overall chord length (c), remains unchanged. Nine different types of leading edges and the baseline with a span of 495 mm each are used in the aerodynamic study. The geometrical details are provided in Table 1. Due to the different amplitudes of the leading edges, the surface area of the serrated aerofoil compared to an aerofoil with a straight LE changes and therefore the wing characteristics may be different from the ones predicted. The value S_m presents the measured surface area for each aerofoil configuration.

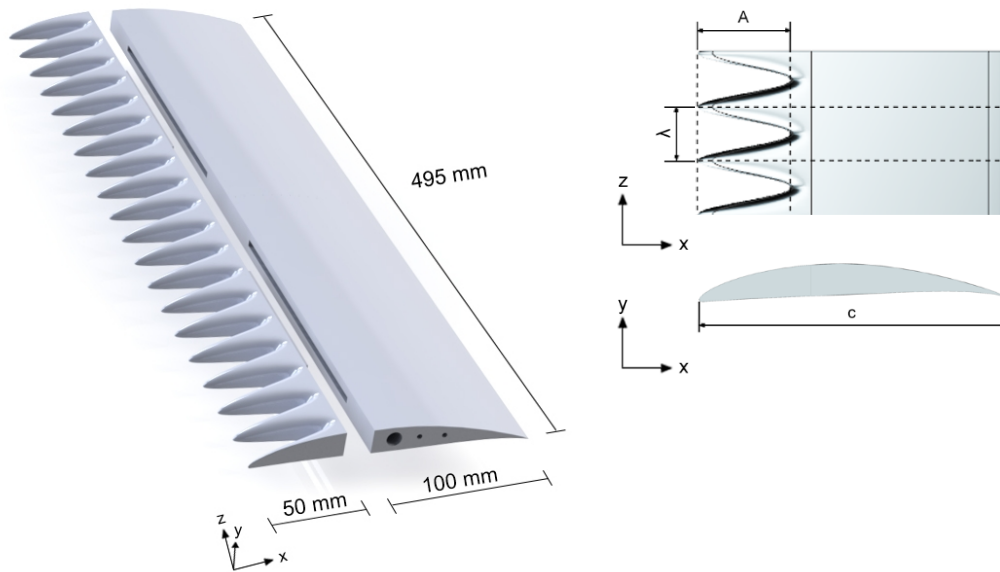


Figure 10: NACA65(12)-10 model. Left: Isometric drawing with attachable leading edge (A45W26) and main body. Right: Top and side view of aerofoil including characteristic parameters.

Table 1: Geometrical parameters of LE serrations					
ID LE	A	λ	A/c	λ/c	S_m
-	[mm]	[mm]	[-]	[-]	[m ²]
Baseline	-	-	-	-	0.07425 (S)
A12W26	12	26	0.08	0.17	0.07128
A22W18	24	18	0.16	0.12	0.06831
A22W34	24	34	0.16	0.23	0.06831
A29W26	32	26	0.21	0.17	0.06633
A29W45	32	45	0.21	0.3	0.06633
A29W7.5	32	7.5	0.21	0.05	0.06633
A35W18	38	18	0.25	0.12	0.06485
A35W34	38	34	0.25	0.23	0.06485
A45W26	45	26	0.3	0.17	0.06311

4 Aerodynamic measurements

Aerodynamic measurements of a two-dimensional NACA65(12)-10 wing section are conducted to characterise the aerodynamic performance of the aerofoil with different leading edges. Lift and drag forces are measured under various angles of attack and the corresponding coefficients are calculated. The results of these measurements provide the background for further aeroacoustics experiments.

4.1 Experimental setup & measurement facilities

The aerodynamic measurements were conducted in the Aerodynamic Laboratory at the Brunel University. The wind tunnel is an open circuit, suction type wind tunnel with a closed test section of 500 (height) x 500 (width) mm. The air enters the wind tunnel through a nozzle with a ratio of 3:1 which is equipped with several mesh and honeycomb screens to reduce the turbulence intensity of the free stream and to create a high-quality flow with a turbulence intensity of about 0.2 to 0.3%. An axial fan (990 mm, 8 blades, 32.5°) which is powered by a 7.5 kW motor produces a maximum free stream velocity of 35 ms⁻¹ and is located at the exit of the diffuser. On each side of the test section, there are three interchangeable acrylic glass windows to allow different configurations.

A three-component balance by Plint & Partners LTD is used to measure the aerodynamic forces produced by the aerofoil inside the wind tunnel. The balance consists of a force plate and an aluminium mounting plate which is secured to the wind tunnel working section. The force plate is able to rotate about the horizontal axis. The aerofoil model is inserted with a Ø12 mm mounting stem in the model support of the force plate. This support is free to rotate for adjustment of the angle of attack, while its position may be locked by means of the incidence clamp. The forces acting on the force plate are transmitted by flexible cables to strain gauge load cells which measure the lift and the drag forces. The drag cable lies horizontally and passes through the centre of the force plate stem, while the two lift cables act vertically and are positioned equidistant from the model support. Pitching moment can be calculated by multiplying the difference of fore and aft by 0.127 (Plint & Partners LTD Engineers, 1986). The accuracy of the readings is found to be ±0.05 N. The three-component balance is calibrated prior to the measurements to ensure accuracy of the readings. Calibration is carried out by removing it from the wind tunnel and installing it to a mounting frame. Zero readings of the load cells are checked before any load is applied. The cells are adjusted by setting the adjusting screw until the display shows a value of zero. The calibration procedure involves the application of known lift and drag forces using dead weights. It is important that the force balance is completely levelled both vertically and horizontally during the

calibration procedure. Any deviations given from the forces are corrected by adjusting the cable tensions until similar readings for both load components, aft and fore, are achieved. Three calibrations are made to check the linearity of the relationship between load and cell output.

4.2 Experimental procedures

A standard pitot-static tube is used to measure the total pressure p_t and the static pressure p_s of the free stream in the test section. To ensure the measurement of the correct free stream velocity, dynamic pressure calibrations are made without the aerofoil model because the model's static pressure field would influence the pressure sensed by the static ports. During acquisition of the data, the pitot-static tube is placed with an acceptable anti-streamwise distance in front of the model (~80 mm). To calculate the velocity, the pressures from the two orifices are connected across a *Furness Controls Limited FCO510* micromanometer. The indicated dynamic pressure is in direct relation to the flow speed. A scheme of the set-up can be found in Figure 11.

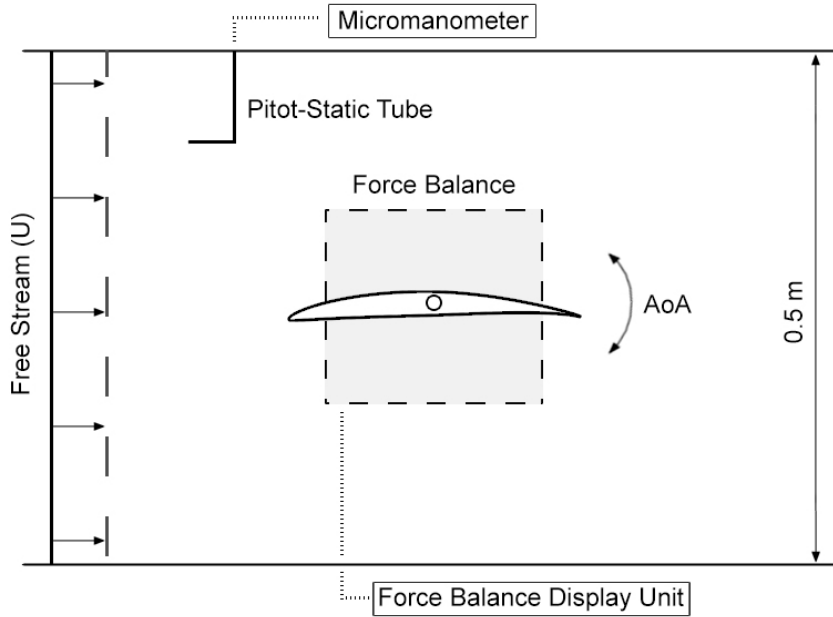


Figure 11: Experimental setup in the working section of the wind tunnel

The free stream velocity u can be calculated from Bernoulli's incompressible equation

$p_t = p_s + \frac{1}{2} \cdot \rho \cdot u^2$ after computing the density ρ from the equation of state.

$$u = \sqrt{\frac{2(p_t - p_s)}{\rho}}, \left\{ \rho = \frac{p}{R_{specific} \cdot T} \right. \quad (4.1)$$

Where p_t is the total pressure, p_s the static pressure and T the absolute temperature in the test section. The universal gas constant for dry air $R_{specific}$ is 287.058 J/(kg K).

The pitot-static tube with hemispherical tip has some inherent error. To achieve the highest accuracy, the yaw should be less than 3°.

Since the free stream velocity represents an influencing parameter on the lift curve, all measurements are taken at 15 ms⁻¹ and 25 ms⁻¹. The velocity is adjusted through a dial by varying the RPM of the motor.

The corresponding chord-based Reynolds numbers are $\sim 1.5 \times 10^5$ and $\sim 2.5 \times 10^5$ according to equation 4.2. Where c is the chord length of the aerofoil (m) and η is the dynamic fluid viscosity (18.24×10^{-6} kg m⁻¹ s⁻¹ at ambient temperature of 20° C).

$$Re_c = \frac{\rho \cdot u \cdot c}{\eta} \quad (4.2)$$

All tests are undertaken at angles of attack (AoA) α ranging from -20° to 20° at 15 ms⁻¹ and reduced AoA of -15° to 15° degrees at 25 ms⁻¹ to prevent damage on the aerofoil due to strong vibrations at higher flow speed. The rotating dial mechanism of the mounting plate is used to adjust the angle over this range with an estimated uncertainty of ± 0.2 degrees. Force readings displayed on the display unit are noted for every leading edge configuration and each angle of attack. In order to verify the results and to check the accuracy of the measurements, three sets are taken for each LE in the AoA range. Prior to every measurement set, readings for ambient room temperature as well as pressure are noted for use in subsequent data processing. Furthermore, the values corresponding to the zero readings of lift and drag at the start of each series of measurement as well as at the end are noted.

Lift and drag forces from the three-component balance are directly obtained in Newtons and have to be corrected to determine the actual lift and drag force using the following equations:

$$L = (A_u - a_0) + (F_u - f_0) \quad (4.3)$$

$$D = (D_u - d_0) \quad (4.4)$$

Where L is the actual lift force, A_u the lift force aft load cell, a_0 the zero reading (wind off) aft load cell, F_u the lift force fore load cell, f_0 the zero reading (wind off) fore load cell, D the actual drag force, D_u the uncorrected (measured) drag force from the drag load cell which includes both parasite and lift-induced drag and d_0 the zero reading (wind off) drag load cell.

The lift coefficient C_L is defined as

$$C_L = \frac{L}{\frac{1}{2} \rho \cdot u^2 \cdot S}, \quad (4.5)$$

where S is the platform area of the aerofoil. Similarly, the drag coefficient is defined as

$$C_D = \frac{D}{\frac{1}{2} \rho \cdot u^2 \cdot S}. \quad (4.6)$$

Since the flow conditions in a wind tunnel are not the same as in an unbounded airstream, the lift and drag coefficients have to be corrected. The wind tunnel test section is finite in size and produces changes in flow patterns. This so called blockage effect leads to lift increments, as well as an increment in drag (Crites R., 1995). The determination of reliable aerodynamic coefficients of an aerofoil needs to be corrected using the solid-blockage correction as well as a correction factor for the wake blockage.

The total blockage error can be estimated by the following equation:

$$C_D = C_{Du} \cdot (1 - 3\varepsilon_{sb} - 2\varepsilon_{wb}) \quad (4.7)$$

$$\varepsilon_{sb} = \frac{\pi^2}{3} \cdot \frac{\lambda_2}{4} \cdot \frac{t^2}{h^2} = 0.822 \cdot \lambda_2 \cdot \frac{t^2}{h^2} \quad (4.8)$$

Where ε_{sb} is the solid-blockage correction factor, t the aerofoil thickness (m) and h the wind tunnel test section height (m). The body shape factor λ_2 is a function of the fineness ratio $\frac{c}{t}$ and thickness ratio $\frac{t}{c}$, respectively. It can be estimated with sufficient accuracy by interpolation (Glauert, 1933). For a NACA65-0xx aerofoil, a value of 4.1 is suggested (with $\lambda_2 \cdot t^2 = \frac{1}{4} \Lambda \cdot c^2$, where Λ is introduced by Allen, et al. (1944)).

$$\varepsilon_{wb} = \frac{\Delta U_h}{u} = \frac{c}{2 \cdot h} \cdot C_{du} \quad (4.9)$$

Where ε_{wb} is the wake blockage correction, ΔU_h the induced horizontal velocity from the wake blockage (ms^{-1}) and u the uncorrected freestream velocity (ms^{-1}). C_{du} is the uncorrected drag coefficient which can be calculated from the force balance measurements.

The presence of ceiling and floor prevents the normal curvature of the flow thus the aerofoil appears to have more camber relative to the straightened flow. According to that, the aerofoil in a closed section has more lift and momentum than it would have in an open freestream and, therefore, has to be corrected.

$$C_L = C_{Lu} \cdot (1 - \sigma - 2\varepsilon) \begin{cases} \sigma = \frac{\pi^2}{48} \cdot \left(\frac{c}{h}\right)^2 \\ \varepsilon = \varepsilon_{sb} + \varepsilon_{wb} \end{cases} \quad (4.10)$$

4.3 Results & discussion

In this section, the results of the aerodynamic measurements including lift and drag coefficients for the NACA65(12)-10 aerofoil are presented and discussed. Preliminary results have shown that despite the noise reduction capability of such passive treatments, they can also significantly change the aerodynamic behaviour of the aerofoil. The objective of this experiment is to identify the effects of sinusoidal leading edges compared to the baseline type. Therefore, the baseline leading edge acts as a reference case in this study.

Figure 12 presents the results of lift coefficients for the aerofoil with leading edge serrations over the AoA range of -20° to 20° and Reynolds number of 1.0×10^5 . Results are presented for serrations with different amplitudes of $A/c = 0.08$, $A/c = 0.21$ and $A/c = 0.3$ with a constant wavelength of $\lambda/c = 0.17$. The aim of this comparison is to provide information on how the serration amplitudes influence the lift coefficient in the designated AoA range. The baseline leading edge acts as a reference for the observation of aerodynamic performance of the different leading edges. The comparison requires a constant surface area S of the aerofoil, even though the reduced surface in case of the undulated LE results in a reduction of the subjected surface to the flow. According to equation 4.5 a smaller wing area (see Table 1) would lead to a higher C_L between 5 and 25% depending on the serration amplitude. In the following passage the lift curve is analysed. The results show individual post-stall characteristics for each LE and indicate a clear tendency in slope characteristics. The maximum C_L coefficients vary with various patterns. It can be seen that larger serration amplitudes decrease the slope up to 40% and lower the maximum C_L (C_{LMAX}) up to 25%. While the large serration amplitude ($A/c = 0.3$) experience a sharp stall and unsteady post-stall behaviour, small serration amplitudes show a significant increase in the maximum stall angle (AoA_{STALL}) and have smoother stall characteristics. The serrated leading edge $A/c = 0.08$, $\lambda/c = 0.17$ (smallest amplitude, intermediate wavelength) impacts the curve progression by delaying the stall angle up to 6° while the lift coefficient remains high ($C_L = 1.24$) compared to the untreated NACA65(12)-10.

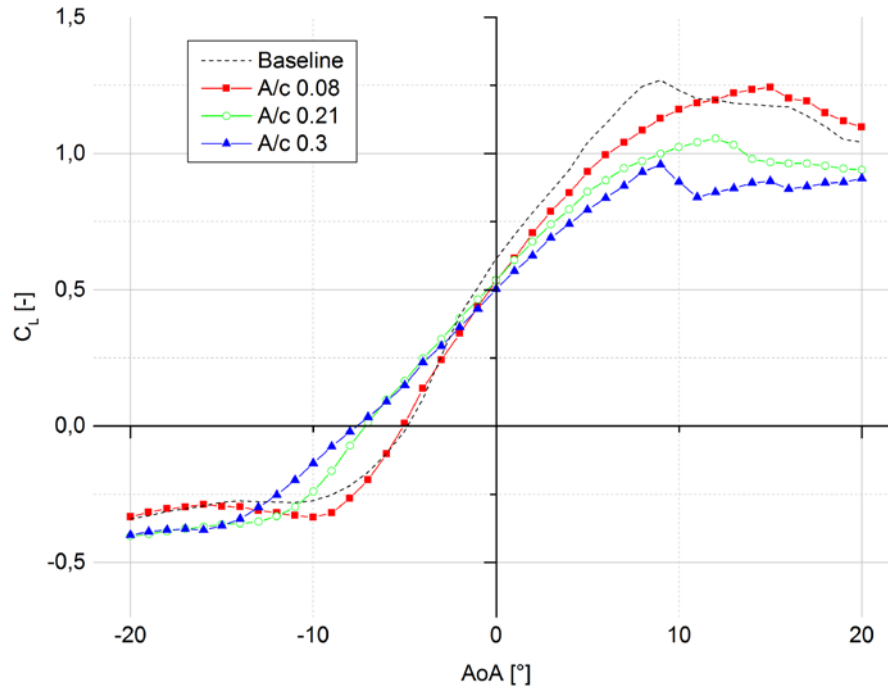


Figure 12: Lift coefficient vs. AoA for $\lambda/c = 0.17$ varying the serration amplitude at $Re = 1.0 \times 10^5$

The conclusion can be drawn that the application of serrated leading edges significantly delays the stall flow field, but on the other hand reduces the lift coefficient. Thus, small serration amplitudes achieve the highest stall delay and show a decent behaviour after C_{LMAX} . Large amplitudes lead to a high loss in lift and cause an unsteady post-stall performance.

The analysis of the C_D characteristics for the wavelength of $\lambda/c = 0.17$ (Figure 13) confirms the constant influence of the serration amplitude. All curves have the same point of interception at zero AoA with a value of $C_D = 0.04$. The single curves are slightly tilted anticlockwise with increasing amplitude. While the smallest serration $A/c = 0.08$ shows nearly the same behaviour as the baseline LE, higher amplitudes cause a higher drag in the positive AoA range and a reduced drag in the negative AoA range up to 60% compared to the baseline LE. Especially the drag increase in the post-stall area is noticeable.

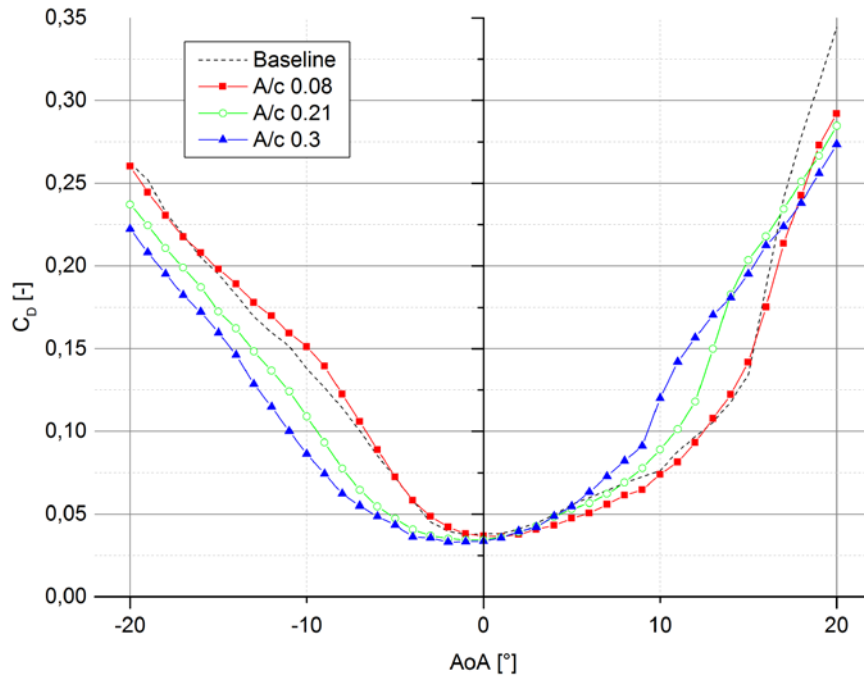


Figure 13: Drag coefficient vs. AoA for $\lambda/c = 0.17$ varying the serration amplitude at $Re = 1.0 \times 10^5$

The following passage deals with the effect of wavelength on the characteristic values C_{LMAX} and AoA at C_{LMAX} as well as the slope characteristics and post stall behaviour. Figure 14 presents the results for $\lambda/c = 0.05$, $\lambda/c = 0.17$ and $\lambda/c = 0.3$ with a constant amplitude of $A/c = 0.21$. It can be clearly seen that the variation of wavelength is an influencing factor for the aerodynamic performance. Higher wavelengths achieve an increase in C_{LMAX} of up to 25% as well as a delay in stall. The slope is increased by 8%. Overall, the performance is significantly lower compared to the baseline leading edge. The lift-to-drag ratio given by C_L/C_D is an indicator providing information about the aerodynamic efficiency (Figure 15). Results are presented for serrations with amplitudes of $A/c = 0.08$ to $A/c = 0.3$ and wavelengths of $\lambda/c = 0.05$ to $\lambda/c = 0.3$. The data confirms the previous observations that small amplitudes ($A/c = 0.08$, $A/c = 0.16$, $A/c = 0.21$) lead to superior aerodynamic performance while wavelengths of intermediate (or larger) dimensions ($\lambda/c = 0.17$, $\lambda/c = 0.23$, $\lambda/c = 0.3$) achieve higher lift coefficients. Furthermore, it can be seen that the serration with the characteristic amplitude of $A/c = 0.08$ (minimum) and wavelength of $\lambda/c = 0.17$ (intermediate) shows nearly the same performance with slightly higher peak values (19.86) than the untreated aerofoil, while all other undulations lead to a strikingly decreased operating range. The aerofoil $A/c = 0.21$ $\lambda/c = 0.05$ shows a reduction in $(C_L/C_D)_{MAX}$ of 25%.

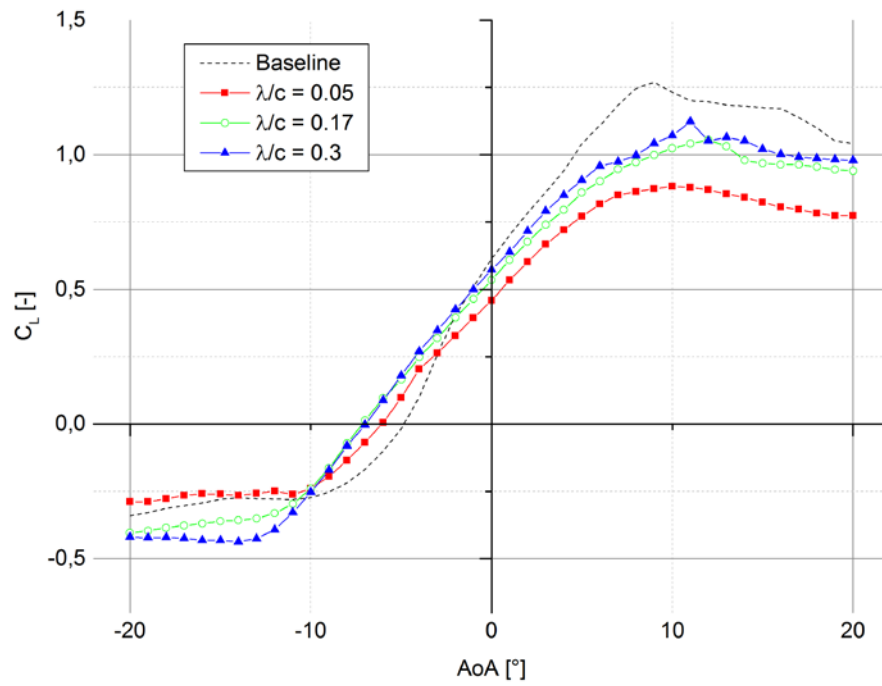


Figure 14: Lift coefficient vs. AoA for $A/c = 0.21$ varying the wavelength at $Re = 1.0 \times 10^5$

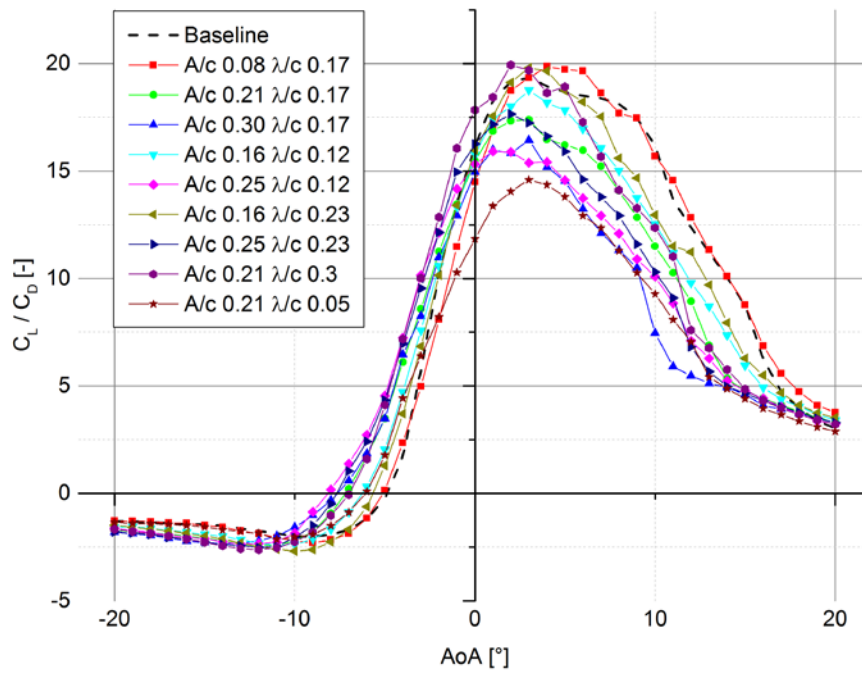


Figure 15: Lift-to-drag ratio vs. AoA for leading edge serrations varying A and λ at $Re = 1.5 \times 10^5$

Overall, the experimental data shows that the aerodynamic performance is mainly a function of amplitude and is less sensitive to the serration wavelength. Small amplitudes can effectively delay the stall and thus considerably improve the aerodynamic performance. Larger serration amplitudes lead to a decrease in lift coefficient and show an unsteady post-stall behaviour. The results determined from the variation of the serration wavelength indicate that the presence of intermediate to large λ can strengthen the performance observed with small amplitude. The results of the experimental drag data indicate that the serrations have only a minimal effect on C_D and rather lead to a shift in the curve progression. The experimental results are summarised in Table 2.

Table 2: Aerodynamic characteristics of the NACA65(12)-10 aerofoil using serrated leading edges

A/c	λ/c	C_{LMAX}	AoA at C_{LMAX}	C_{DMIN}	$(C_L/C_D)_{MAX}$	AoA at $(C_L/C_D)_{MAX}$
0,08	0,17	1,24	15	0,04	19,86	4
0,21	0,17	1,05	12	0,03	17,39	3
0,3	0,17	0,96	9	0,03	16,42	3
0,16	0,12	1,05	12	0,03	18,76	3
0,25	0,12	1,03	11	0,03	15,91	1
0,16	0,23	1,15	14	0,03	19,8	3
0,25	0,23	1,07	11	0,03	17,64	2
0,21	0,3	1,12	11	0,03	19,93	3
0,21	0,05	0,91	10	0,04	14,59	3

5 Boundary layer measurements

This chapter aims to deliver a fundamental understanding on the effects of wavy leading edges on the flow and turbulence pattern of different serrated leading edges at different streamwise locations. Therefore two leading edges with different serration amplitudes are exposed to turbulent flow and compared to the baseline LE. The results of this section should be linked to recent acoustic studies dealing with airfoil-gust-interaction (AGI) noise. Lau, et al. (2013) analysed the AGI-noise-reducing mechanism of wavy leading edges using numerical solutions. They described that the local pressure fluctuations around the LE area disperse over a retarded period of time resulting in smaller amplitudes and time derivatives, compared to those on a straight leading edge. Kim, et al. (2016) point out that the reduction of noise is related to the rapid de-correlation of surface pressure fluctuations along the LE. When the geometry of sinusoidal leading edges is considered experimentally, such spanwise variations result in spanwise components of flow. Comparatively small spanwise variations of pressure tend to produce large crossflows in the boundary layer (Abbott & Von Doenhoff, 1949). Since the air close to the surface has lost most of its momentum, it tends to flow directly towards the region of lowest pressure. These crossflows become particularly marked under conditions approaching separation. The flow of this low-energy air from one section to another tends to delay separation. Boundary layer profiles and the turbulence intensity is measured and analysed to investigate these processes. Additionally, analysis of the spectral components is used to provide information about how the energy of the signal is distributed with respect to frequency.

5.1 Experimental setup & measurement facilities

This chapter presents the experimental setup for the hot-wire anemometry and gives an overview about the facilities which are used during the boundary layer measurements. The experimental arrangement including the anechoic chamber and the wind tunnel is described and an introduction to the hot-wire system is made.

5.1.1 Anechoic chamber & wind tunnel

The boundary layer measurements are conducted in the aeroacoustic wind tunnel facility at Brunel University. The open jet wind tunnel is placed within a hemi-anechoic chamber with the dimensions of 4 m (width) x 5 m (length) x 3.4 m (height) and has a rectangular nozzle exit with dimension of 0.10 m (height) x 0.30 m (width). The jet can achieve a maximum velocity of about 80 ms^{-1} . Figure 16 shows the plan, side and front view of the

aeroacoustic wind tunnel. The free jet contains a turbulence intensity of about 0.15 - 0.25 % at 20 ms^{-1} test speed and is characterised by a very low background noise produced by the bare jet in comparison to the noise radiated from an aerofoil in the air stream (Vathylakis, et al., 2014).

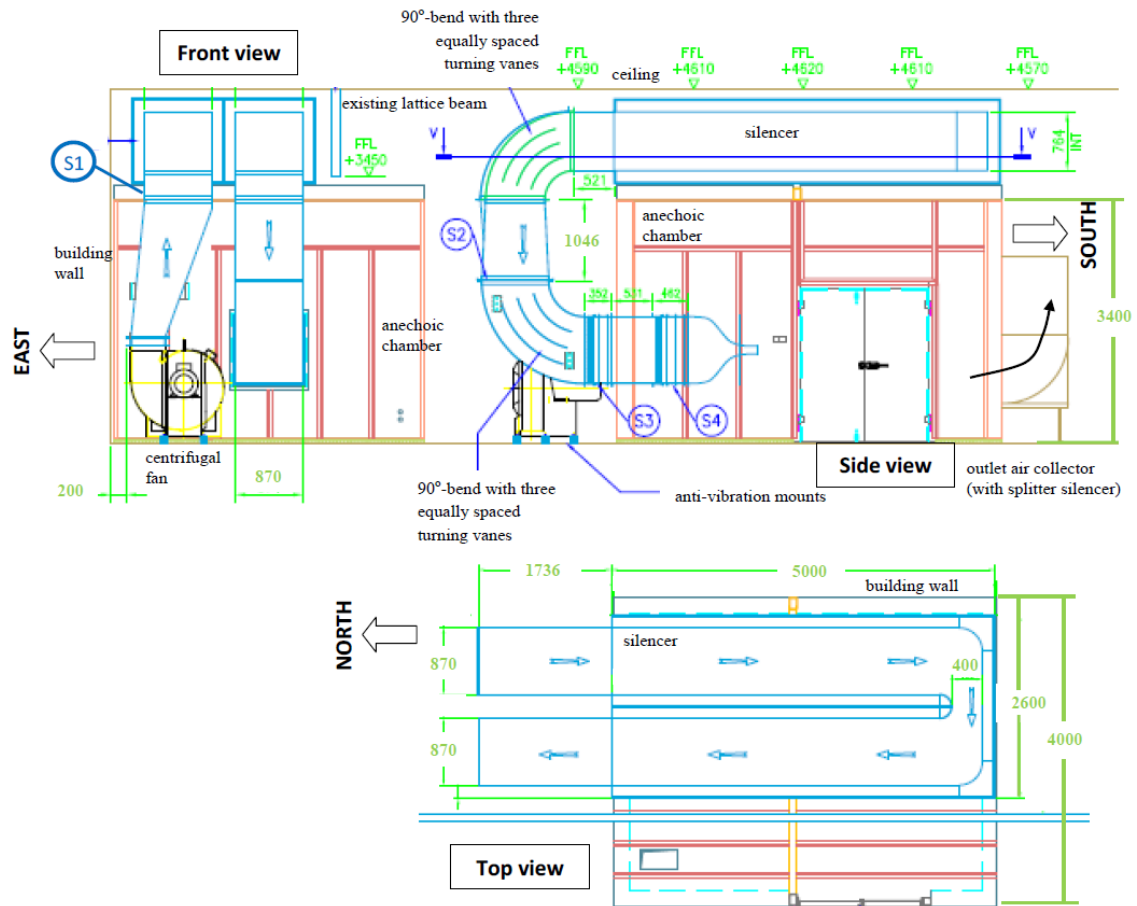


Figure 16: Plan side and front views of the aeroacoustic wind tunnel and the anechoic chamber (Vathylakis, et al., 2014)

5.1.2 Aerofoil setup

The NACA65(12)-10 aerofoil consisting of leading edge and main body is mounted in front of the nozzle exit using clamps which are inserted into the side plates of the nozzle. In total, 300 mm of the span are exposed to the open jet. Invisible smooth tape is applied to the intersection of the leading edge and the main body to ensure that the aerofoil has a continuous surface. Additionally, small gaps at the clamps and sideplates which would influence the flow are taped. The aerofoil position in z-direction is marked to ensure the reproducibility of the setup. The wooden grid is placed inside the nozzle and fixed with four wires. Its position is leveled to make sure that the distance from the grid to the aerofoil is consistent over the whole span. The hot-wire probe is traversed to the exact measurement locations using an angle gauge and a self-made positioning template

which can be stuck to the aerofoil surface. With this procedure the reproducibility of the experiment can be ensured. The experimental arrangement is illustrated in Figure 17.

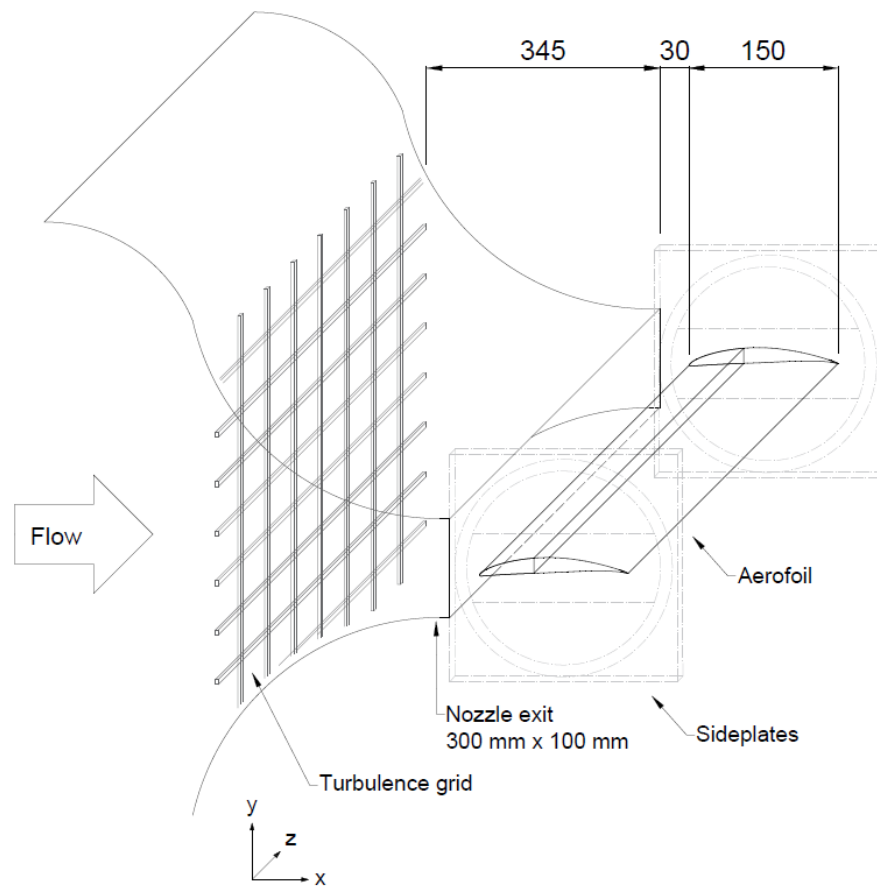


Figure 17: Aerofoil setup for the hot-wire measurements including the nozzle exit with characteristic dimensions and the turbulence grid

5.2 Hot-Wire setup

Hot-wire anemometry (HWA) is a technique primarily to measure velocity and temperature fluctuations. It is based on the convective heat transfer from a heated wire placed in a fluid flow where the temperature is a function of the velocity of the fluid. Consequently, any change in the fluid flow condition which affects the heat transfer from the heated element can be described with hot-wire. HWA is used for experimental fluid mechanics within many different fields. One advantage is the small size of the wire element compared to other velocity measurements so that the disturbance of the measured flow can be kept as small as possible. Very accurate results can be achieved in carefully controlled experiments (0.1 – 0.2%) in which 1% accuracy is realistic for practical applications. Furthermore the technique allows the measurement of velocity fluctuations of fine scale and of high frequencies. The signal-to-noise ratio of HWA is

very good since it can have very low noise levels (Bruun, 2002). In this study a multichannel constant temperature anemometer (CTA) by *Dantec Dynamics Type 54N80* is used. The electrical circuit in this anemometer is part of a Wheatstone bridge configuration.

5.2.1 System configuration

In this project, a boundary layer probe *55P15* by *Dantec Dynamics* is used to measure the flow in the boundary layer of the aerofoil. As seen in Figure 18, the shape of the prongs permit measurements close to the solid wall of the surface without disturbance from the probe body, which is out of the boundary layer. The probe consists of a miniature wire with a very high frequency response and is suitable for applications in air flows with turbulence intensities (Tu) up to 10% (Jørgensen, 2002). The 1.25 mm long platinum-plated tungsten wire is of $5\ \mu m$ diameter and directly welded to the hot-wire prongs. The probe body consists of a ceramic tube with a diameter of 1.9 mm. It is plugged into the probe support, which is equipped with a cable and BNC connector.

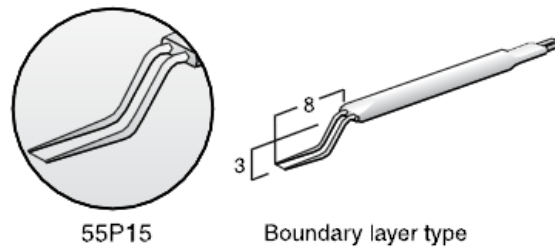


Figure 18: Boundary layer probe (55P15) (Dantec Dynamics)

The CTA has a built-in signal conditioner with a 10 kHz low-pass filter to remove electronic noise and prevent aliasing. A high-pass filter is not needed because it would only remove the low frequency fluctuations (DC-part) prior to spectral analysis (Jørgensen, 2002). Furthermore, the offset and gain of the CTA is carefully adjusted to optimise the input range for the A/D board (0 – 5 V) and to achieve a high resolution. The analogue signal is digitised by a 12-bit A/D card (PD2-MFS-1M/12) after running through an eight channel BNC connector board. The application software *ThermalPro* by *TSI* is used both for probe calibration and data acquisition. Data analysis is carried out with *MathWorks MATLAB* and *Microsoft Excel*. The data acquisition is defined by the sampling rate (SR) of 20 kHz and the number of samples (N) of 256,000 which together determine the sampling time ($T = N/SR$) of 13.1 seconds. For spectral analysis the sampling rate must be at least two times higher than the highest occurring fluctuation frequency in the flow (equation 5.1 & 5.2). The number of samples depends on the required uncertainty.

$$SR \geq 2 \cdot f_{max} \text{ (Nyquist criteria)} \quad (5.1)$$

$$SR \geq 2 \cdot f_{cut-off} \text{ (based on low-pass filter setup)} \quad (5.2)$$

The probe is mounted with the probe axis parallel to the dominant velocity component (u). The coordinate system of the probe (x, y, z) matches the laboratory coordinate system (u, v, w). High accuracy and consistency of the boundary layer measurements can only be guaranteed, if the distance d (0.2 mm) between the sensor element of the hot-wire probe and the aerofoil surface is constant in spanwise direction (Figure 19). In order to ensure that the aerofoil axis is aligned to the movement of the hot-wire probe, a *Pro 360* spirit level (accuracy 0.1°) is used by placing it on top of the probe support and on the aerofoil surface. Furthermore, a metal sheet with a thickness of 0.2 mm is used to check the distance d at different positions.

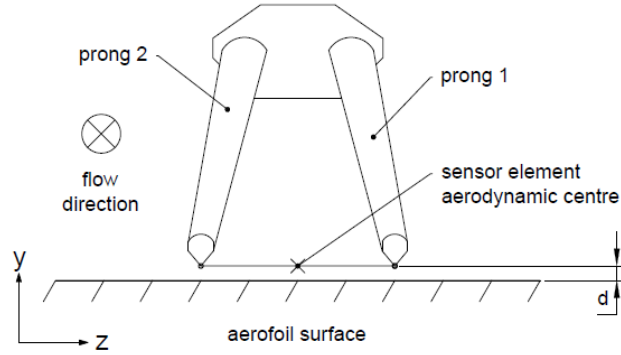


Figure 19: Detail of the hot-wire probe close to the aerofoil surface

5.2.2 Anemometer setup

One important step before starting the experiment is the adjustment of the CTA. A high temperature across the sensor element results in high frequency response, signal to noise ratio and velocity sensitivity. The operating temperature of the sensor is defined by the overheat ratio a according to equation 5.3.

$$a = \frac{R_w - R_0}{R_0} \quad (5.3)$$

Where R_w is the sensor resistance at operating temperature T_w and R_0 is its resistance at ambient (calibration) temperature T_0 . The over temperature can be calculated using equation 5.4:

$$T_w - T_0 = \frac{a}{\alpha_0}, \quad (5.4)$$

where α_0 is the sensor temperature coefficient of resistance at T_0 . The sensor resistance at 20°C R_{20} , the leads resistance R_L , the support resistance R_s , the cable resistance R_c and the sensor temperature coefficient (TCR) α_0 are provided by the manufacturer. The values for the boundary layer probe type 55P15 are provided in Table 3. Jørgensen recommends an overheat ratio of $a = 0.8$ whereas a chosen wire temperature of 250°C leads in this specific case to a ratio of $a = 0.83$.

Table 3: Probe type 55P15

R_{20}	3.50 Ω
R_L	0.5 Ω
α_0	0.36 %/C
R_s	0.05 Ω
R_c	0.20 Ω

The dynamic response of the CTA can be tested by injecting a small electronic square-wave signal into the bridge and observing the response of the anemometer's output. The time it takes for the bridge to get into balance is related to the time constant and the bandwidth of the system. A shorting probe (type 55 H30) is exposed to the maximum expected velocity of 35 ms⁻¹ and the CTA is connected to an oscilloscope. Figure 20 shows the result of the test which can be adjusted by modifying the amplifier filter and the gain. A smooth response with 15% undershoot represents the right settings.

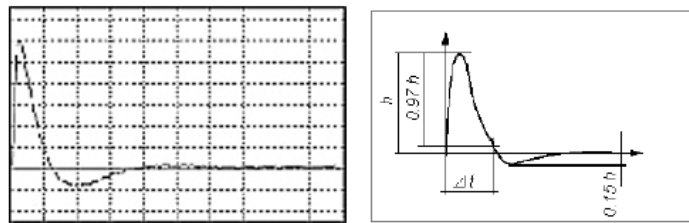


Figure 20: Square wave test. Left: Result of oscilloscope. Right: Correct square wave test with characteristic parameters (Jørgensen, 2002)

5.2.3 Traversing system

Since automatic probe movement is part of the experimental procedure, a two-axes traverse system (*iselgermany*) is used for the hot-wire measurements. The traverse mechanism is connected to the central unit box and can be controlled by the *ThermalPro* software. The accuracy of the movement is within 0.003 mm. It is paid attention that the traverse doesn't disturb the flow at the probe position.

5.2.4 Velocity calibration & data conversion

Calibration of the hot-wire probe system is necessary to establish a relation between the CTA output (E) and the flow velocity (u). The probe is exposed to a set of known velocities in the range of 0 – 35 ms^{-1} and the corresponding values of the voltages are noted. The flow speed is calculated using a pitot-static tube which is placed close to the hot-wire, measuring the dynamic and barometric pressure. Additionally, the flow temperature was measured using a digital thermometer. The first step to convert the data records from voltages into velocities for the scheduled hot-wire experiments is the application of a polynomial curve fit of 4th order (equation 5.5) (Figure 21).

$$u = C_0 + C_1E + C_2E^2 + C_3E^3 + C_4E^4 \quad (5.5)$$

Where C_0 to C_4 are calibration constants and u the flow velocity. Alternatively, a power law curve fitting can be applied by plotting E^2 as a function of u^n (Figure 22). With the help of a linear trend line (King's law), the calibration constants A and B can be obtained. For this calibration a value of 0.52 for the scaling power n results in the best curve fit.

$$E^2 = A + B \cdot u^n \quad (5.6)$$

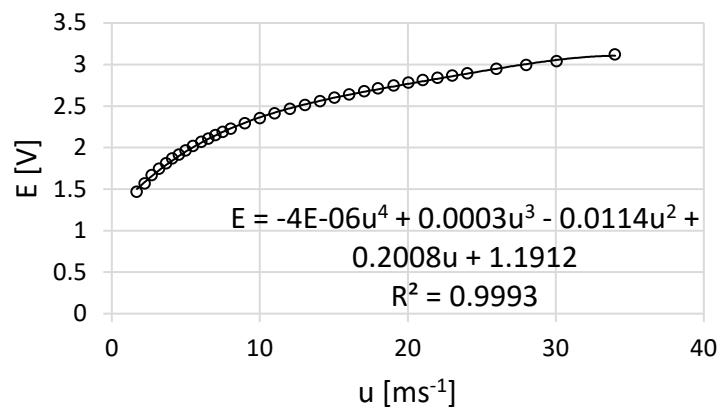


Figure 21: Boundary layer probe calibration polynomial regression of 4th order

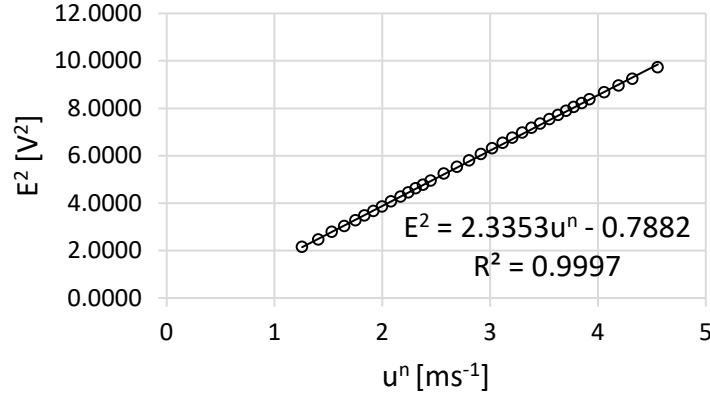


Figure 22: Boundary layer probe calibration fitting with King's law

Since one of the most important sources of error in measuring velocity using hot-wire anemometry is the change in the hot-wire calibration due to changes in the ambient temperature, the temperature is noted at the beginning and the end both for the calibration and the experiment (Perry, 1982). In order to minimize this error an accurate correction method is necessary. Bruun (2002) presents a technique where the output voltage E_w is corrected to a reference temperature T_r :

$$E_{w,r} = E_w \cdot \left[\frac{T_w - T_r}{T_w - T_a} \right]^{\frac{1}{2}}, \quad (5.7)$$

where T_w is the wire temperature, T_a the ambient temperature and T_r the reference temperature which is equal to the calibration temperature. This correction is only valid for small temperature changes (up to two or three degrees) because otherwise the changes in fluid properties would lead to an over-correction.

5.3 Experimental methodology

In this section the generation of turbulence using a bi-planar orthogonal square grid and the measurement plan for the hot-wire boundary layer measurements are discussed.

5.3.1 Generation of turbulence

The noise radiation at the leading edge of an aerofoil is strongly dependent on the turbulence intensity of the incoming flow. Meshes and/or grids are well known for the ability to reduce the turbulence intensity and improve the flow steadiness (Chong, et al., 2015). Some combinations of the mesh length (m_{GRID}) and the wire diameter (d_{GRID}) can produce the opposite effect and increase the turbulence intensity downstream of the

device. In order to choose a suitable grid design for this experiment, it is important to define the characteristic parameters describing the turbulence (Schade & Kunz, 2007):

$$Tu = \frac{1}{\sqrt{3}} \cdot \frac{|\bar{u}'|}{\bar{u}} = \sqrt{\frac{\overline{u'^2} + \overline{v'^2} + \overline{w'^2}}{3(\bar{u}^2 + \bar{v}^2 + \bar{w}^2)}} \quad (5.8)$$

If the velocity fluctuation is equal in all three directions with $\overline{u'^2} = \overline{v'^2} = \overline{w'^2}$, the turbulence can be described as isotropic turbulence and is equal to the standard deviation of the flow velocity (equation 5.10) in relation to the mean flow velocity (equation 5.9).

$$u_{mean} = \frac{1}{N} \sum_{i=1}^N u_i \quad (5.9)$$

$$u_{rms} = \left(\frac{1}{N-1} \sum_{i=1}^N (u_i - u_{mean})^2 \right)^{0.5} \quad (5.10)$$

$$Tu_{isotrop} = \frac{u_{rms}}{u_{mean}} \quad (5.11)$$

To investigate the leading edge broadband noise due to aerofoil-gust-interaction (AGI), a bi-planar orthogonal square grid with square section bars is used in this experiment. The turbulence intensity at the leading edge should be of high turbulence with at least 5%. According to Laws & Livesey (1978) the ideal mesh-to-diameter ratio is $m_{GRID}/d_{GRID} \sim 5$ which is adopted in the current study with $m_{GRID} = 45$ mm and $d_{GRID} = 9$ mm (Figure 23). The grid is placed within the nozzle after the large curvature point to minimise the effect of the accelerated flow to be re-laminarised. The fitting of the grid to the nozzle yields to overall dimensions of w_{GRID} (width) = 361 mm and h_{GRID} (height) = 208 mm.

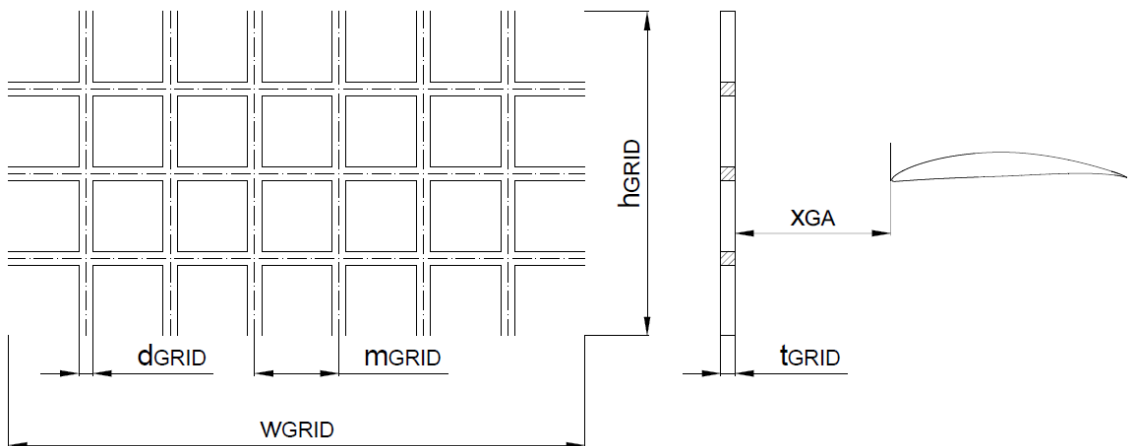


Figure 23: Characteristic parameter of the turbulence grid

Since the turbulence intensity shows a strong dependence on the distance between the measurement location and the mesh position, the flow has to be checked on isotropy. About ten times the mesh length m_{GRID} is required to ensure a fully isotropic turbulence (Laws & Livesey, 1978). Due to the nozzle geometry and the mounting position of the aerofoil model, the criterion is difficult to be fulfilled in the current study.

$$x_{GA} = 375 \text{ mm} < m_{GRID} \cdot 10 = 450 \text{ mm} \quad (5.12)$$

Nevertheless, hot-wire anemometry is used to examine the isotropy of the grid-generated turbulence at the position of the aerofoil leading edge (aerofoil dismounted). The probe is exposed to velocities of $u = 20 \text{ ms}^{-1}$, $u = 25 \text{ ms}^{-1}$ and $u = 30 \text{ ms}^{-1}$ and the velocity power spectral density is compared to the most common theoretical models by Von Karman (eq. 5.13) and Liepmann (eq. 5.14). Despite the application of an exponential function (eq. 5.15), the dilution in the high frequency region caused by the Kolmogorov scale is still visible. However, the overall measured streamwise velocity spectra shows good agreement with a $-5/3$ decay rate (Figure 24). The Van Karman spectrum is fitted to the experimental data. The turbulence intensity measured at this point is amounted to be 5%.

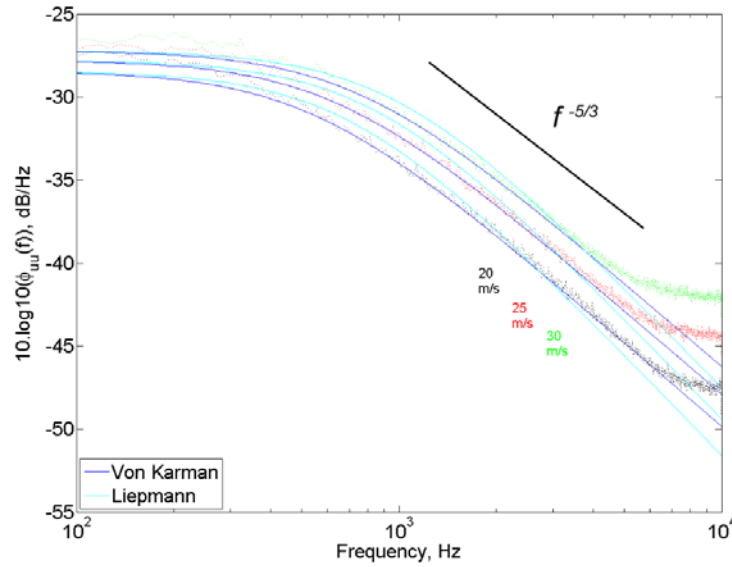


Figure 24: Comparison of power spectrum density to Von Karman model (blue) and Liepmann model (light blue) at $u = 20 \text{ ms}^{-1}$ (black), $u = 25 \text{ ms}^{-1}$ (red) and $u = 30 \text{ ms}^{-1}$ (green).

$$\phi_{uu}^{VK}(\omega) = \frac{\overline{u'^2} \Lambda_{uu}}{\pi \cdot U_0} \cdot \frac{1}{\left[1 + \left(\frac{K_\chi}{\kappa_e}\right)^2\right]^{5/6}}, \begin{cases} K_\chi = \frac{\omega}{U_0}; \omega = 2\pi f \\ \kappa_e = \frac{\sqrt{\pi}}{\Lambda_{uu}} \cdot \frac{\Gamma(5/6)}{\Gamma(1/3)} \end{cases} \quad (5.13)$$

Where $\overline{u'}$ is the velocity fluctuation, Λ_{uu} the integral length scale, U_0 the mean velocity, κ_e the reduced wavenumber, K_x the streamwise wavenumber and ω the angular frequency.

$$\phi_{uu}^L(\omega) = \frac{\overline{u'^2} \Lambda}{\pi \cdot U_0} \cdot \frac{1}{1 + K_x^2 \Lambda^2}, K_x = \frac{\omega}{U_0}; \omega = 2\pi f \quad (5.14)$$

$$G_{Kolmogorov} = \exp\left((-9/4) \cdot (K_x/K_\eta)^2\right), K_\eta \approx 4.8 \cdot 10^4 m^{-1} \quad (5.15)$$

Where K_η is used to scale the spectrum in the high frequency region.

5.3.2 Measurement procedure

This section presents the measurement procedure for the hot-wire boundary layer measurements. The selected measurement positions result from four different influencing factors. First of all, an extensive literature review both in the field of numerical analysis (CFD) and of experimental studies is carried out. The results show that not only the aeroacoustics mechanism in the interstices of the serrations, but also the development of the flow pattern in streamwise direction is of interest. Secondly, preliminary tests are conducted using hot-wire anemometry. The boundary layer is measured at different streamwise positions while alternating the flow speed to estimate the growth of the boundary layer for the final experiment. The measurement of the static pressure distribution of the aerofoil supports this approach. The third influencing factor is the selection of the leading edges to be investigated. Aerodynamic measurements showed that the leading edge A12W26 ($A/c = 0.08$, $\lambda/c = 0.173$) can effectively delay the stall and thus considerably improve the aerodynamic performance and is therefore of significance for the upcoming experiment. As a counterpart, the leading edge with the dimensions A45 ($A/c = 0.3$) and W26 ($\lambda/c = 0.173$) has a weak performance when it comes to aerodynamic efficiency. However, Biedermann (2015) and Chong, et al. (2015) stated the superior characteristics of this leading edge in the reduction of aerofoil-gust-interaction noise where the free stream turbulence interacts with the aerofoil leading edge what leads to broadband noise radiation. The baseline LE acts as a reference for these two leading edge configurations. Last but not least, experiences from prior experiments at the Brunel University related to the boundary layer development linked to leading edge undulations helped in the finalisation of the exact hot-wire measurement plan. Figure 25 and Figure 26 illustrate the selected measurement planes on the suction side for the NACA65(12)-10 aerofoil equipped with the A12W26 LE and A45W26 LE. Measurements for both configurations and the baseline are taken at the exact same

locations to perform a one-to-one comparison of the acquired data. The following positions in streamwise direction (x) are chosen for the suction side (normalised by the chord): $x/c = 0.04, 0.08, 0.3, 0.33, 0.5, 0.66, 0.93$.

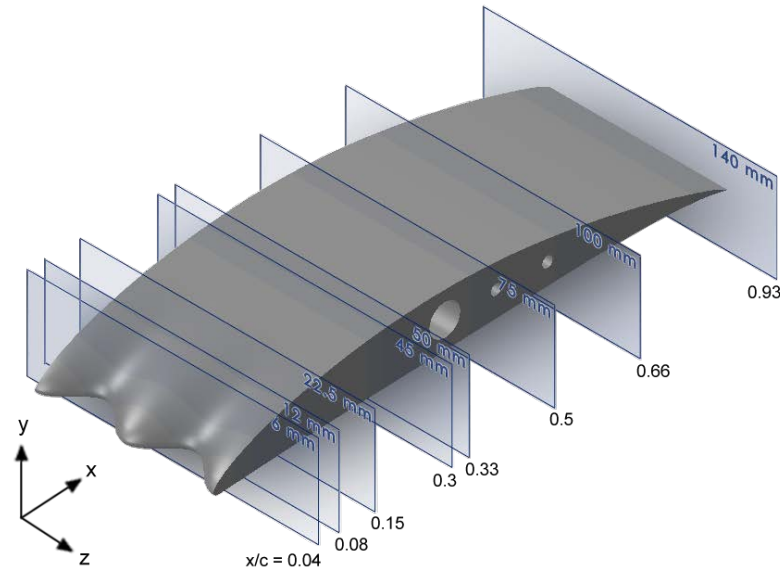


Figure 25: Measurement planes for the NACA65(12)-10 aerofoil with the leading edge A12W26 ($A/c = 0.08$, $\lambda/c = 0.173$)

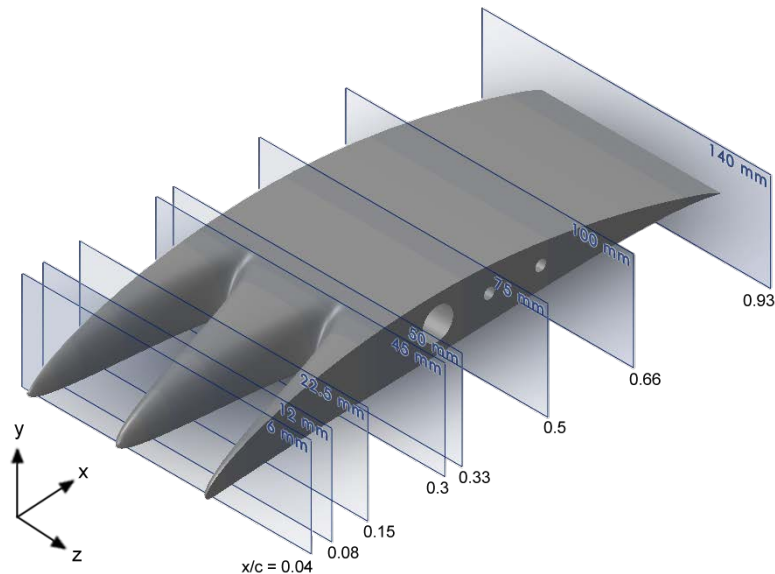


Figure 26: Measurement planes for the NACA65(12)-10 aerofoil with the leading edge A45W26 ($A/c = 0.3$, $\lambda/c = 0.173$)

In order to guarantee a high resolution of the measurements a small Δz of 2.6 mm was used for the traverse file resulting in the following positions in spanwise direction (z): 0, 2.6, 5.2, 7.8, 10.4, 13, 15.6, 18.2, 20.8, 23.4, 26, 28.6, 31.2, 33.8, 36.4, 39, 41.6, 44.2, 46.8, 49.4, 52 (mm). Hence, two wavelengths are measured each time which allows to check the consistency of the data. Figure 27 shows an overlay of the top-view for all three leading edges. Each cross (X) displays the position of the hot-wire probe center. The red crosses indicate additional measurement locations on the pressure side of the aerofoil.

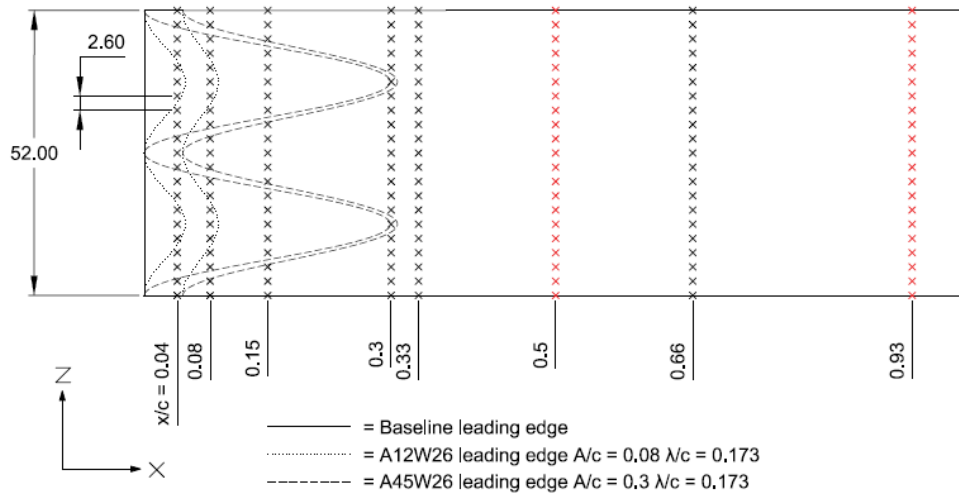


Figure 27: Detail of hot-wire probe locations on the aerofoil surface. Crosses in red mark the additional locations on the pressure side

The vertical traversing in y -direction takes place in the range of $0 \text{ mm} \leq y \leq 30 \text{ mm}$ in very small steps of 0.05 mm near the aerofoil surface since the gradient is expected to be high in this area (Figure 28). In the interstices of the leading edge even more points have been added in $-y$ direction (up to -8 mm) to gain more information about the flow velocity between the tips of the undulations. The dimensions of the probe support and the sideplates, as well as the fact that the probe influences the flow in narrow locations, restricted further measurements in the serrations. Overall, the number of measurement points for each profile sums up to 1197.

All tests are undertaken at a free stream velocity of 25 ms^{-1} . The corresponding chord-based Reynolds numbers is $\sim 2.5 \times 10^5$ according to equation 4.2. The angle of attack (AoA) represents no influence factor for this experiment. Thus, the angle is set to zero degree for all measurements. The turbulence grid is used for all experiments, therefore resulting in a turbulence intensity (Tu) of 5%.

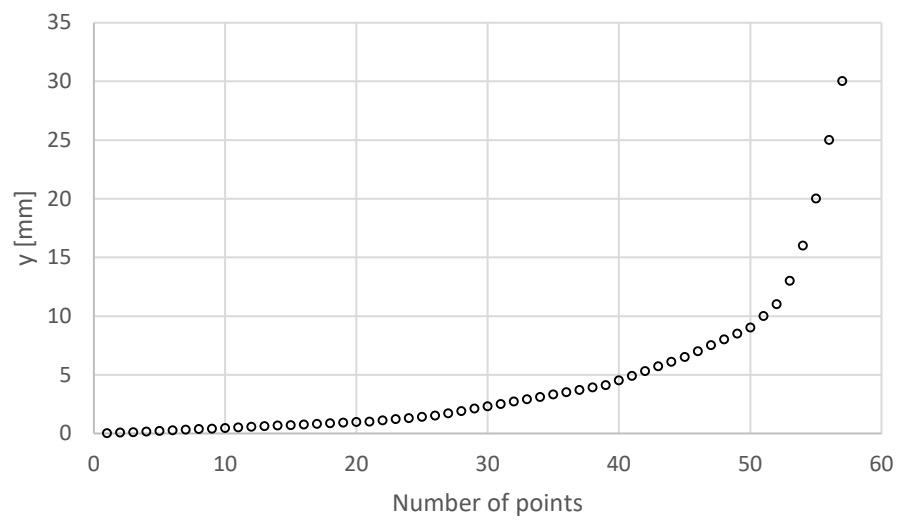


Figure 28: Positions of the hot-wire probe in y-direction

6 Data analysis boundary layer measurements

This chapter presents the data analysis for the boundary layer measurements which have been realised with hot-wire anemometry. The conversion and evaluation of the acquired data for the NACA65(12)-10 aerofoil including the serrated leading edges baseline (straight), A12W26 and A45W26 yields to the decision that this chapter will only compare the baseline LE to the A45W26 LE. Data analysis for the aerofoil equipped with the A12W26 LE can be found in the appendix of this thesis. The decision is caused by the fact that the aerodynamic and aeroacoustic effects which can be demonstrated by the hot-wire analysis are of such small dimension for the LE with an amplitude of 12 mm, that a high-standard comparison wouldn't be possible. However, an even more detailed comparison of the serrated leading edge characterised by an amplitude of 45 ($A/c = 0.3$) and wavelength of 26 ($\lambda/c = 0.173$) to the straight leading edge is performed.

The first section of this chapter presents the suction side of the aerofoil and compares the boundary layer at different streamwise and spanwise positions. In the next step the analysis of turbulence profiles in form of contour plots and the spectral analysis are conducted. The second part deals with the investigations on the pressure side.

As the signal from a turbulent flow is of random nature, a statistical description of the data is necessary. Information about the amplitude distribution in the signal can be found in the amplitude domain analysis where one time series is sampled. After the data from the sensor is converted into velocity components, it is possible to calculate the mean velocity (equation 5.9), the standard deviation (equation 5.10) and the turbulence intensity (equation 5.11).

6.1 Suction side

This section presents the data analysis for the suction side of the NACA65(12)-10 aerofoil. The baseline leading edge is compared to the serrated leading edge (A45W26).

6.1.1 Boundary layer profiles

Figure 29 shows an overview of contour plots of the boundary layer profiles normalised by the free-stream velocity. The left side presents the straight baseline leading edge and the right side displays the A45W26 LE. A three-dimensional leading edge section has been illustrated on the right side to determine characteristic locations like the peak ($z = -26$, $z = 0$, $z = 26$) and the trough ($z = -13$, $z = 13$). The free stream is flowing in positive x-direction. The axes of the system are defined as follows: the x-axis shows the chordbased measurement positions (x/c) in streamwise position, the y-axis describes the

height of the boundary layer (mm), the z-axis is intended to mark the spanwise positions (mm) and the colourbar describes the velocity component u normalised by the free-stream velocity. The observation of the baseline on the left shows a jet on the top of the surface which can be attributed to the pressure gradient. The emergence of a visible boundary layer can only be seen near the trailing edge at the position of $x/c = 0.93$. A reduced velocity can be observed in the first measurement plane at $x/c = 0.04$. This phenomena can be either explained by the stagnation point in this area or is due to the limitations of the hot-wire probe which is not able to perform perpendicular measurements at the leading edge because of the curvature of the aerofoil. During the comparison to the results of A45W26 at $x/c = 0.04$, the reduced velocity can attributed to the former. The serration seems to significantly reduce the influence of the stagnation point in the root region since the flow is accelerated between the peaks. Further downstream ($x/c = 0.5$ and $x/c = 0.66$) the flow behaves contrary, resulting in thicker boundary layer peaks at the troughs. In the next step, detailed countour plots and boundary layer profiles help to quantify these assumptions.

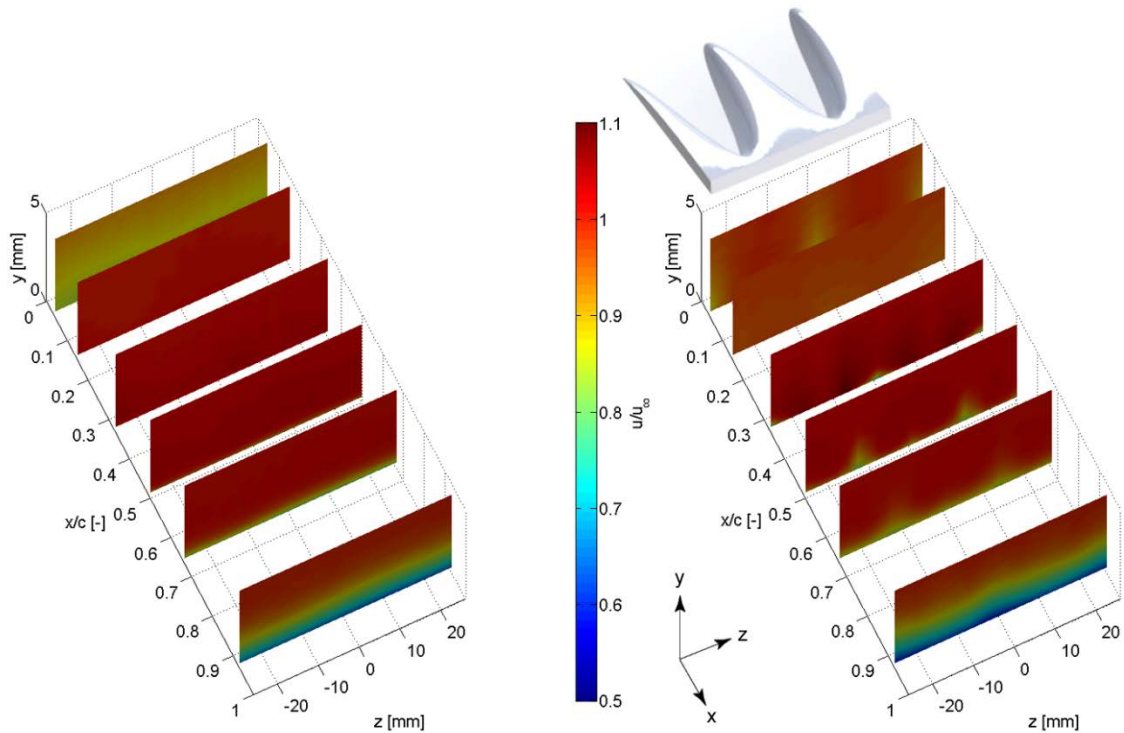


Figure 29: Overview boundary layer profiles normalised by the free-stream, baseline (left) vs. A45W26 (right) suction side, $\text{AoA} = 0^\circ$, $Tu = 5\%$, $U = 25\text{ms}^{-1}$

Figure 30 shows contour plots of the boundary layer normalised by the free-stream velocity at $x/c = 0.04$ comparing the baseline and the serration (A45W26) leading edges. As stated in the introduction, it is believed that the reduced flow velocity of $u/u_\infty = 0.8$ in

the near wall region can be attributed to the stagnation point. The serration case shows the accelerated flow in the interstices ($z = -13$ and $z = 13$) and a development of a boundary layer on the peaks of the undulation.

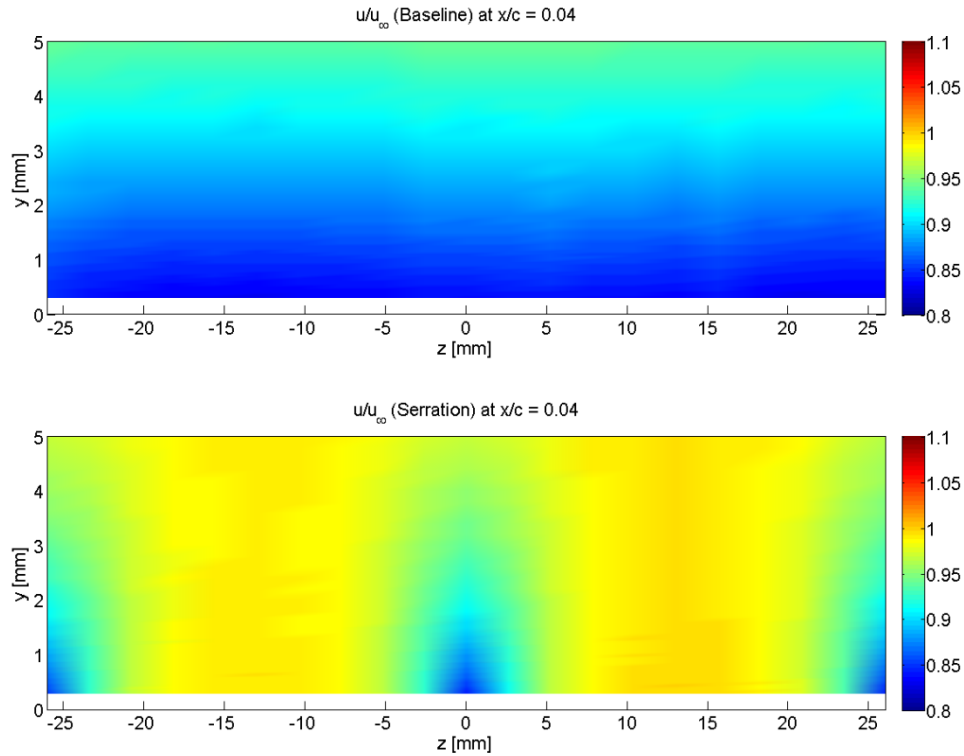


Figure 30: Boundary layer profiles normalised by the free-stream, baseline vs. A45W26 at $x/c = 0.04$ suction side, $AoA = 0^\circ$, $Tu = 5\%$, $U = 25\text{ms}^{-1}$

To gain further information about the flow pattern in the leading edge, boundary layer measurements have been taken in the interstices of the undulations going below the actual aerofoil surface to -5 mm and -8 mm, respectively. Figure 31 shows the boundary layer profiles of baseline (dotted line), serration at $z = 0$ mm (red) and serration at $z = 13$ mm (blue) at the streamwise position of $x/c = 0.04$. A strong difference between the profiles at this point can be observed. While the baseline profile is determined by the stagnation point and high pressure area, the velocity in the root is reduced with its low at $y = 0$ mm. The flow seems to be accelerated in the direction of both suction and pressure side. Figure 32 ($x/c = 0.15$) marks the position at half of the serration amplitude. It can be observed that the flow on the baseline starts to get accelerated due to the pressure gradient on the suction side. The profiles at the peak and root can't be described as typical boundary layer properties. The lower velocities in u direction lead to the conclusion that secondary flow is present at this point which can be characterised with spanwise velocity components.

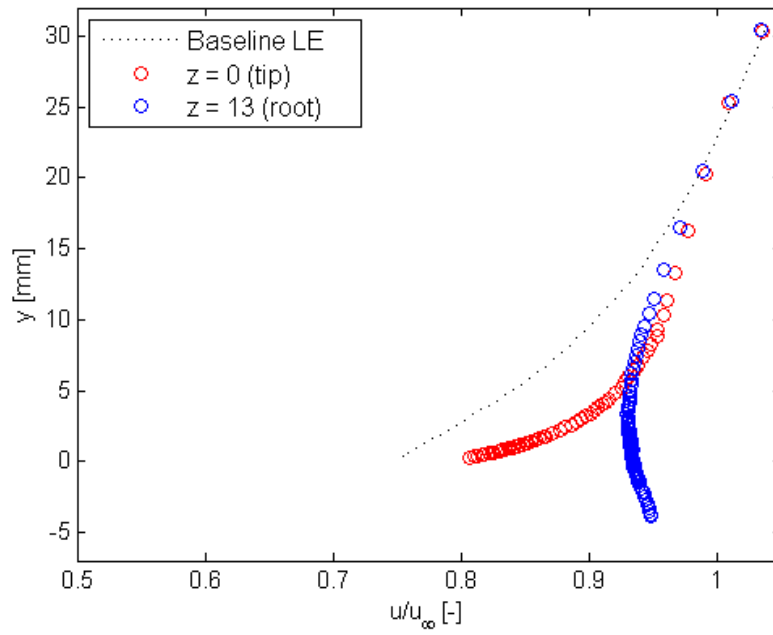


Figure 31: Boundary layer profiles normalised by the free-stream, baseline vs. A45W26 at $x/c = 0.04$ suction side. Comparison between tip and root for $AoA = 0^\circ$, $Tu = 5\%$, $U = 25\text{ms}^{-1}$

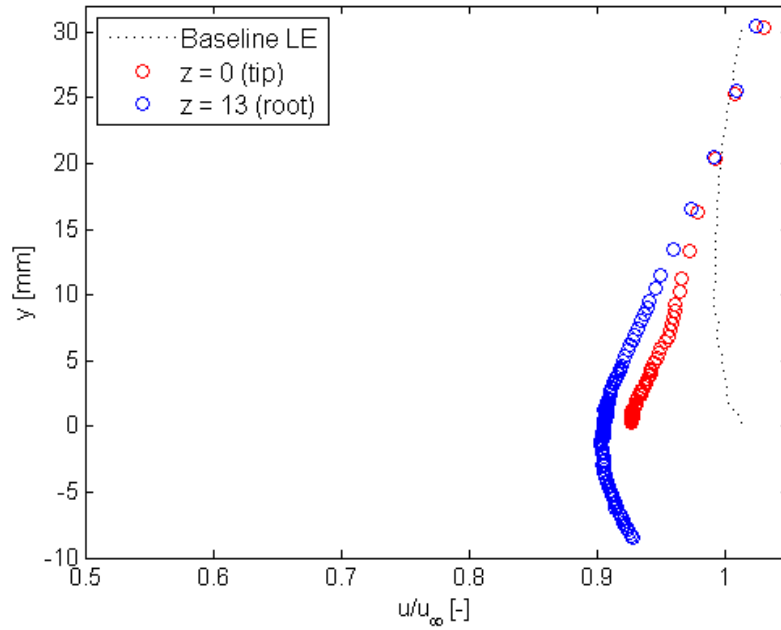


Figure 32: Boundary layer profiles normalised by the free-stream, baseline vs. A45W26 at $x/c = 0.15$ suction side. Comparison between tip and root for $AoA = 0^\circ$, $Tu = 5\%$, $U = 25\text{ms}^{-1}$

Detailed contour plots of the boundary layer normalised by the free-stream velocity comparing the baseline and the serration (A45W26) leading edges are presented in the next section. Figure 33 and Figure 34 are showing the streamwise positions $x/c = 0.5$ and $x/c = 0.67$. It can be observed in both cases that the boundary layer is significantly higher at the root positions and slightly lifted at the peaks. This attribute of lowered

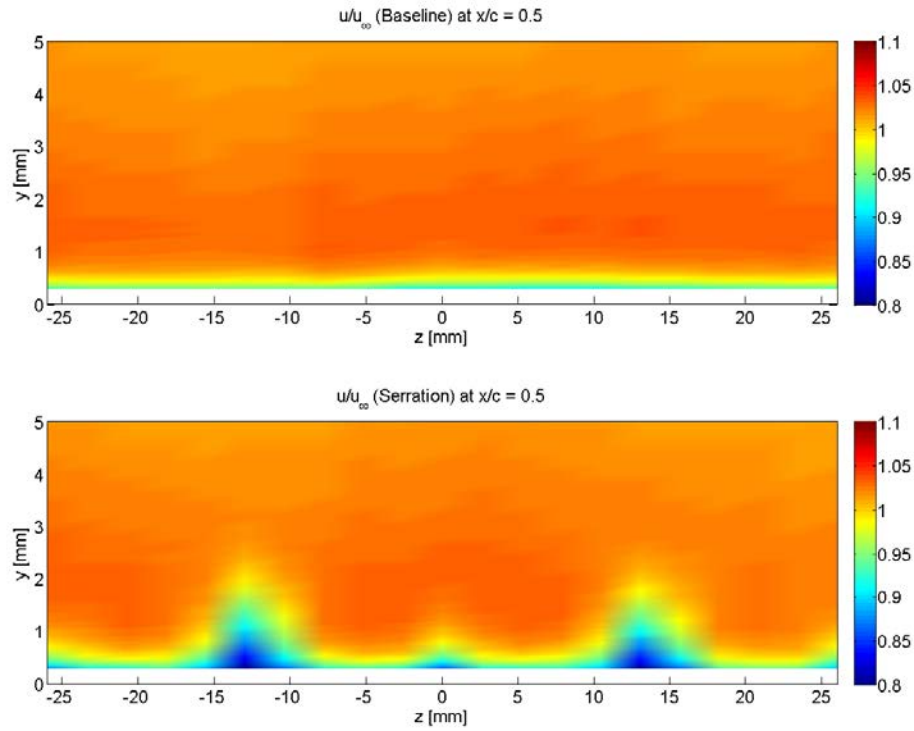


Figure 33: Boundary layer profiles normalised by the free-stream, baseline vs. A45W26 at $x/c = 0.5$ suction side, $AoA = 0^\circ$, $Tu = 5\%$, $U = 25\text{ms}^{-1}$

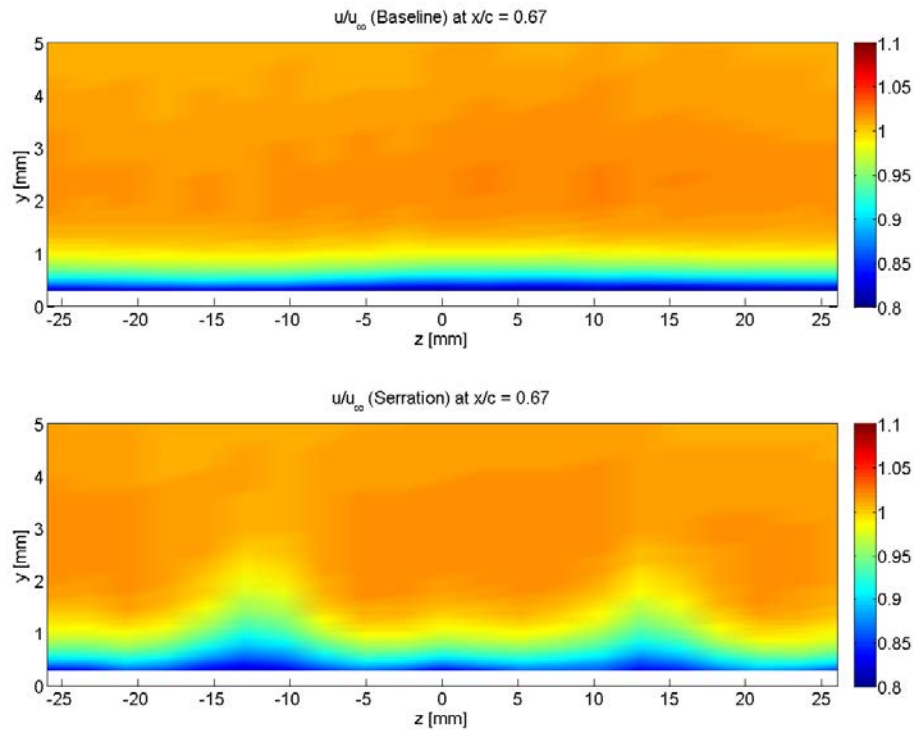


Figure 34: Boundary layer profiles normalised by the free-stream, baseline vs. A45W26 at $x/c = 0.67$ suction side, $AoA = 0^\circ$, $Tu = 5\%$, $U = 25\text{ms}^{-1}$

velocity leads to the assumption of the existence of vortical structures at this spanwise positions. This observed trend is continued in Figure 35 ($x/c = 0.93$). The overall boundary layer thickness for the baseline and serration is nearly identical. At the trailing edge position a thickness of two millimeter can be described.

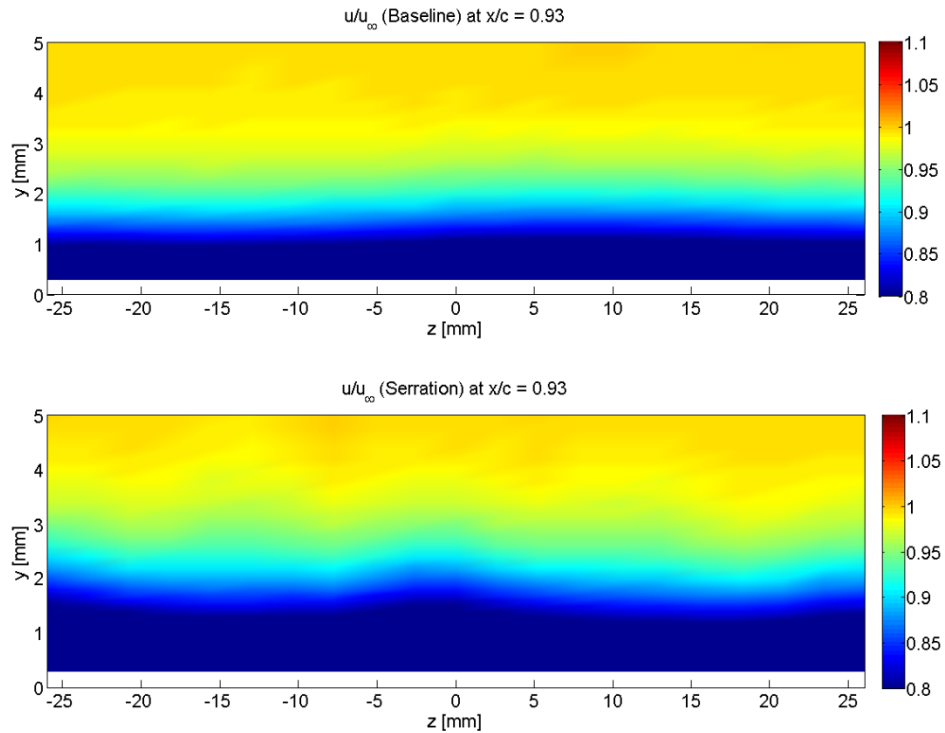


Figure 35: Boundary layer profiles normalised by the free-stream, baseline vs. A45W26 at $x/c = 0.93$ suction side, $AoA = 0^\circ$, $Tu = 5\%$, $U = 25\text{ms}^{-1}$

6.1.2 Turbulence intensity

The primary role of HWA is the use as a research tool for turbulent flow studies. Turbulence is an essential process in fluid flows. It contributes significantly to the transport of momentum, heat and mass. Additionally, turbulence is of importance when it comes to the generation of fluid friction loss and fluid induced noise. Because of the increased interchange of momentum from different parts of the layer, turbulent boundary layers are much more resistant to separation than laminar layers (Abbot, et al., 1945). This section deals with the presentation of the turbulence intensity for the suction side. Figure 36 shows an overview of the contour plots for the Tu at distinct streamwise locations. The left side presents the straight baseline leading edge and the right side displays the A45W26 LE. Again, a three-dimensional leading edge section has been illustrated on the right side to determine characteristic locations. The colourbar shows

the turbulence intensity u_{RMS}/u_{∞} . The baseline LE shows a very homogeneous picture with increased turbulence near the trailing edge. The overall Tu at the leading edge seems to be increased as well of about 1%. This finding can be backed up by single measurements in the interstices where lowered Tu was visible due to the effect of serrations. On closer examination of the A45W26 LE (right), it has to be noted that the high turbulent regions at $x/c = 0.5$ near the roots, seem to dissolve and propagate at $x/c = 0.66$ and $x/c = 0.93$ in the direction of the peaks. These phenomena will be considered in more detailed Tu contour plots.

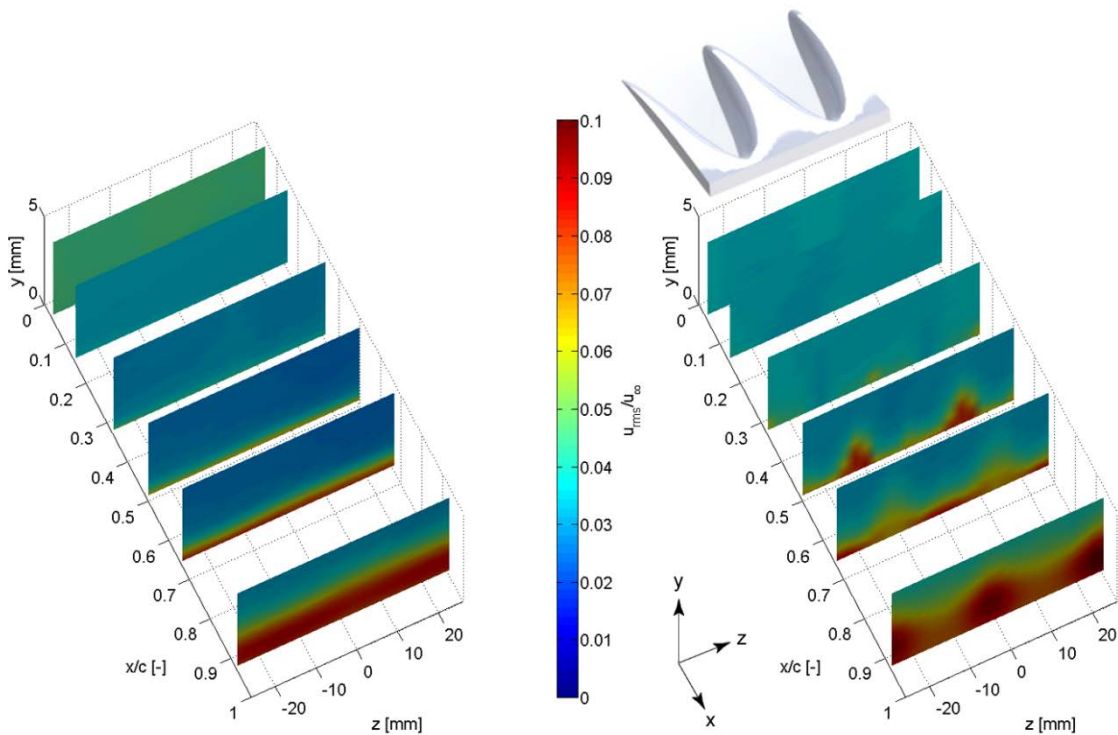


Figure 36: Overview turbulence profiles baseline (left) vs. A45W26 (right) suction side, AoA = 0°, Tu = 5%, U = 25ms⁻¹

Figure 37 shows a contour plot of the turbulence intensity for the baseline (top) and the serration (bottom) where the x-axis presents the spanwise locations. As expected, the overall Tu is lowered in case of the serration by 1%. Detailed consideration reveals, that even a reduction of 2% is existent at the root positions. Figure 38 displays the turbulence intensity at $x/c = 0.5$. Compared to the baseline, a clear pattern becomes apparent for the serrated leading edge. High turbulent regions shaped as peaks with a Tu of 8% can be found at the spanwise location of the roots ($z = -13$ and $z = 13$). These peaks have a height in y-direction of about 2.5 mm. Small elevations of turbulence intensity can also be found at the tip regions. These turbulent flows can be associated with vortex structure emanating from the troughs.

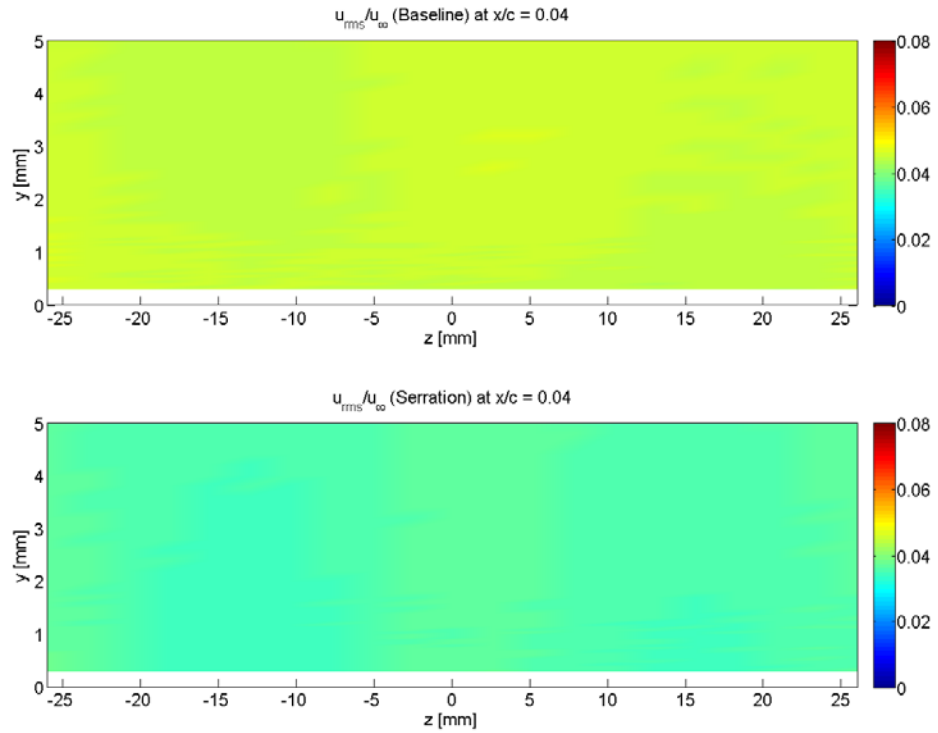


Figure 37: Tu profiles baseline vs. A45W26 at $x/c = 0.04$ suction side, $AoA = 0^\circ$, $Tu = 5\%$, $U = 25\text{ms}^{-1}$

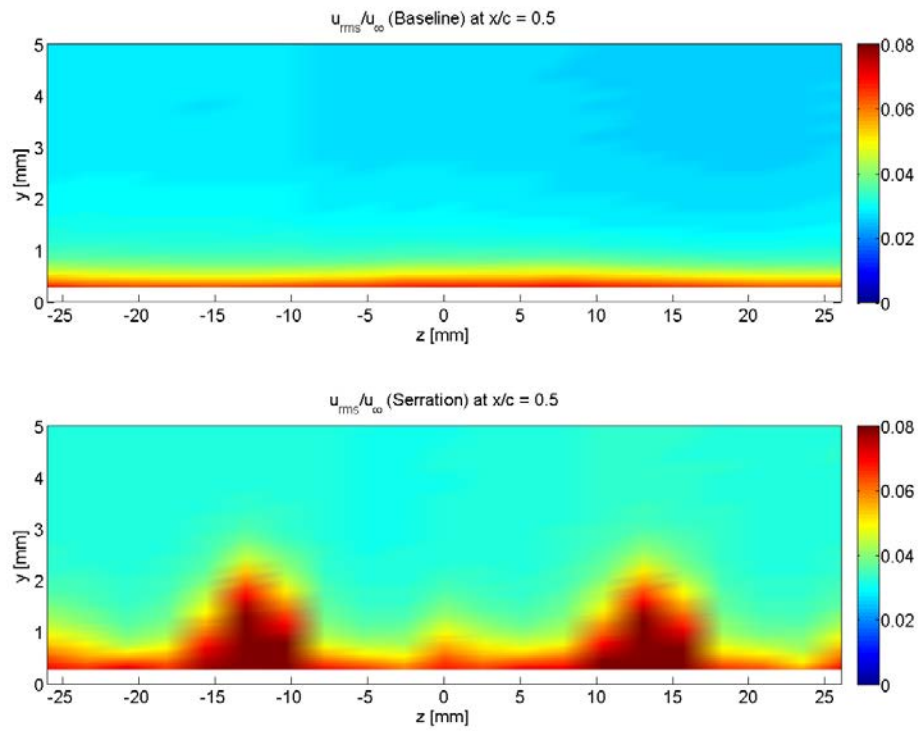


Figure 38: Tu profiles baseline vs. A45W26 at $x/c = 0.5$ suction side, $AoA = 0^\circ$, $Tu = 5\%$, $U = 25\text{ms}^{-1}$

Figure 39 ($x/c = 0.67$) and Figure 40 ($x/c = 0.93$) show the propagation of these vortical structures further downstream. At the streamwise position of $x/c = 0.67$ the prominent high intensity regions at the root positions seem to weaken. High turbulence intensity of 8% is now visible near the tip location. These high turbulences coincide with the baseline profile. The contour plot at $x/c = 0.93$ near the trailing edge confirms the assumption that the vortices and high turbulent regions at the root, respectively, slowly dissolve streamwise. The comparison of the baseline and the serrated case leads to the conclusion that the Tu is even reduced at the spanwise position of the roots of about one to two percent. This phenomenon can be related to the suppression in tonal noise at the trailing edge. As Hansen (2012) describes, streamwise vortices behind the root tend to break up the coherence of vortex generation at the trailing edge.

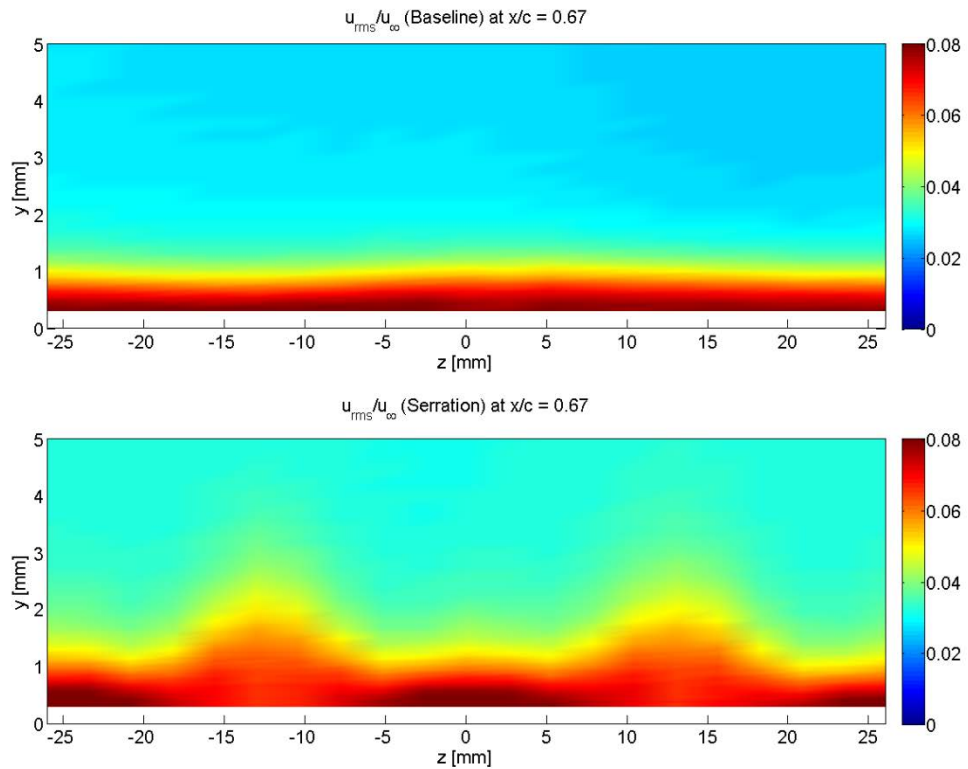


Figure 39: Tu profiles baseline vs. A45W26 at $x/c = 0.67$ suction side, $AoA = 0^\circ$, $Tu = 5\%$, $U = 25\text{ms}^{-1}$

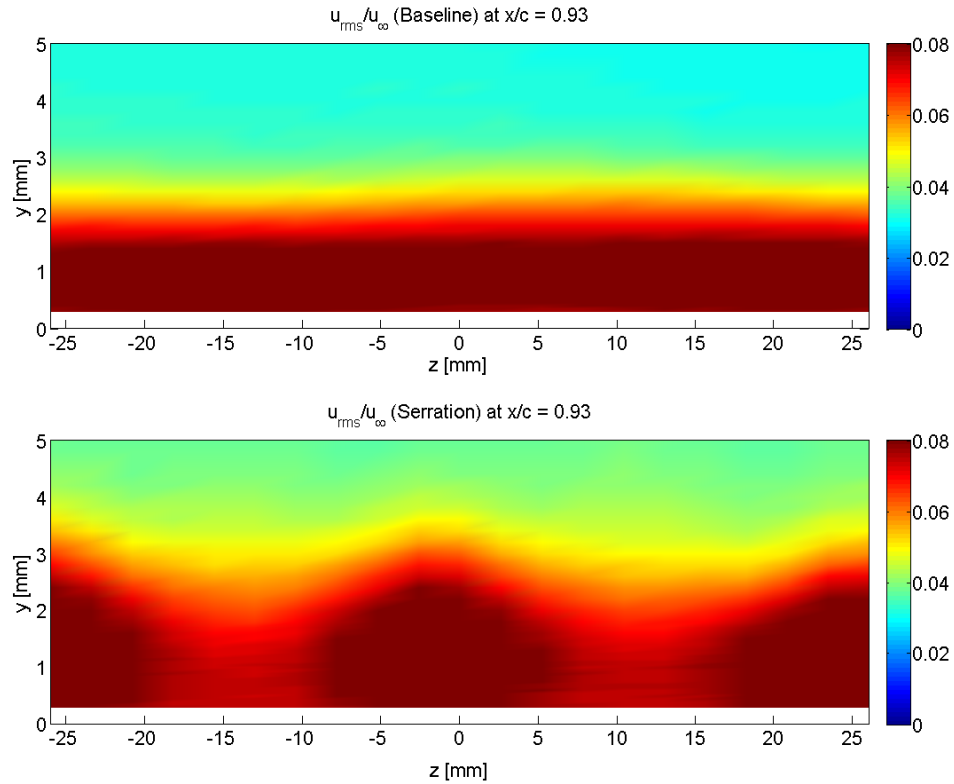


Figure 40: Tu profiles baseline vs. A45W26 at $x/c = 0.93$ suction side, $AoA = 0^\circ$, $Tu = 5\%$, $U = 25\text{ms}^{-1}$

6.1.3 Spectral analysis

Spectral-domain data analysis is used to provide information about how the energy of the signal is distributed with respect to frequency. Three dimensional contour plots have been generated using isosurfaces to illustrate the turbulence fluctuations with respect to the leading edge geometry. Figure 41 shows the turbulence of the baseline leading edge at the streamwise position of $x/c = 0.5$ on the suction side. The x-axis describes the spanwise positions ranging from -26 to 26 mm. The z-axis (*log scale*) presents the frequency and the y-axis (*log scale*) the measurement positions starting from the aerofoil surface. A colourbar helps to identify the magnitude of the fluctuations. The baseline is compared to the serrated leading edge in Figure 42. It can be observed that the A45W26 LE shows velocity fluctuations with high magnitude at the root region with low frequencies. These fluctuations are elevated in y-direction up to two millimeters, whereas the baseline shows a value of about 0.3 mm. The large velocity fluctuation in frequency confirms that the flow from the root is producing high mix turbulence flow. The injection of high momentum fluid from the free stream into the boundary layer could be due to a strong pressure gradient at the surface of the aerofoil. The results of the isosurface plots

correspond very well with the contour plots for the turbulence intensities. Figure 43 and Figure 44 are presenting the turbulence further downstream of the serrations at $x/c = 0.67$. The comparison of both plots reveals, that the serration significantly reduces the high energy fluctuations in the low frequency region compared to the baseline. This performance is passed further downstream which can be seen in Figure 45 and Figure 46. Baseline and serration show the same expansion in y-direction of about two to three millimeters and the same magnitude. The only difference is the ability of the serration to cause a reduction in the low frequency region.

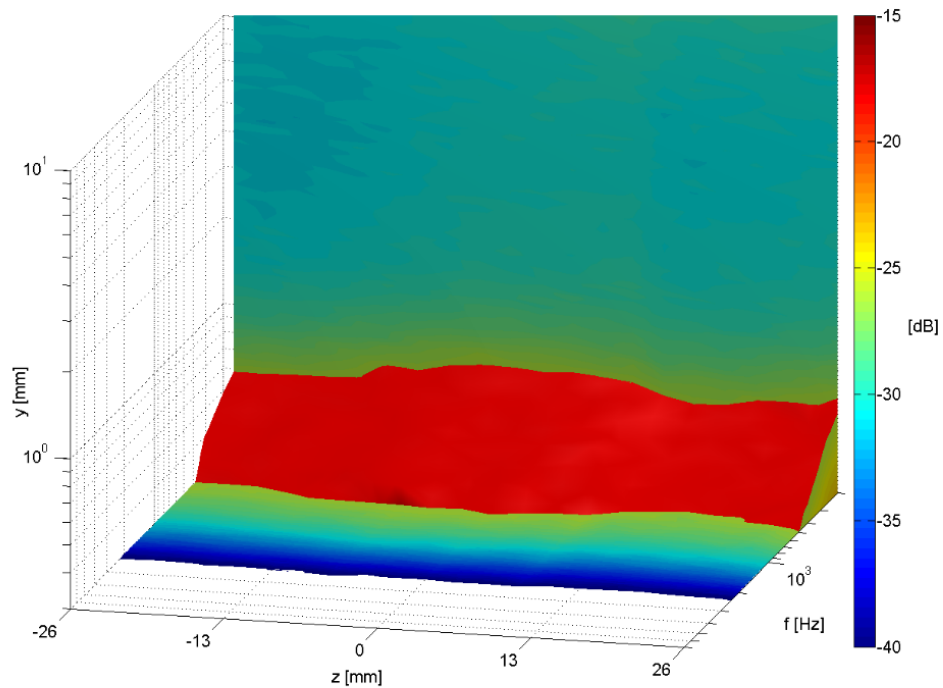


Figure 41: Baseline turbulence at $x/c = 0.5$ suction side, $AoA = 0^\circ$, $Tu = 5\%$, $U = 25\text{ms}^{-1}$

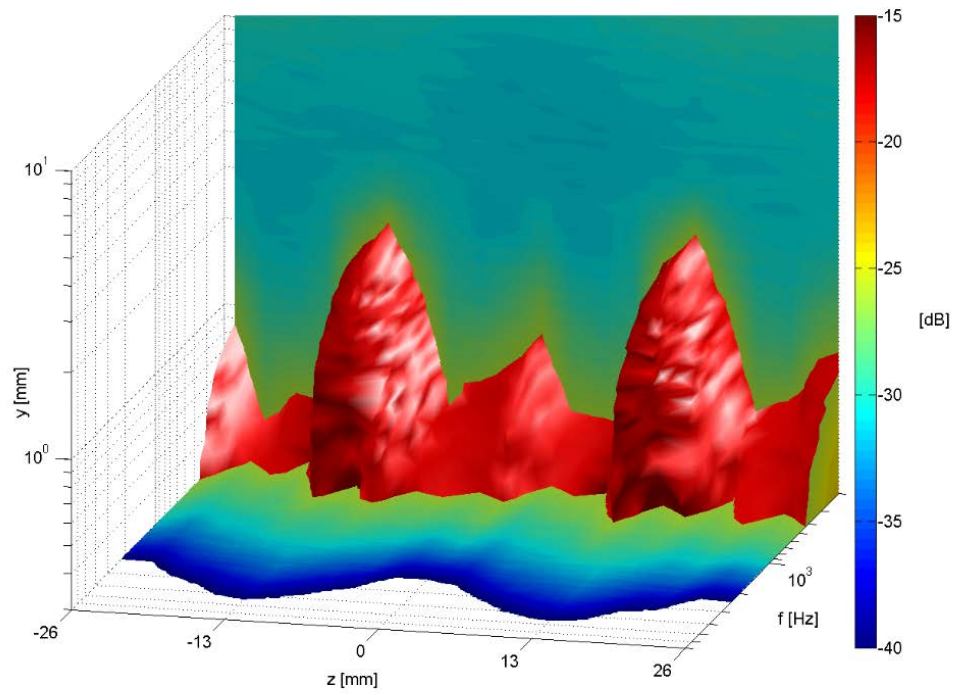


Figure 42: A45W26 turbulence at $x/c = 0.5$ suction side, $AoA = 0^\circ$, $Tu = 5\%$, $U = 25\text{ms}^{-1}$

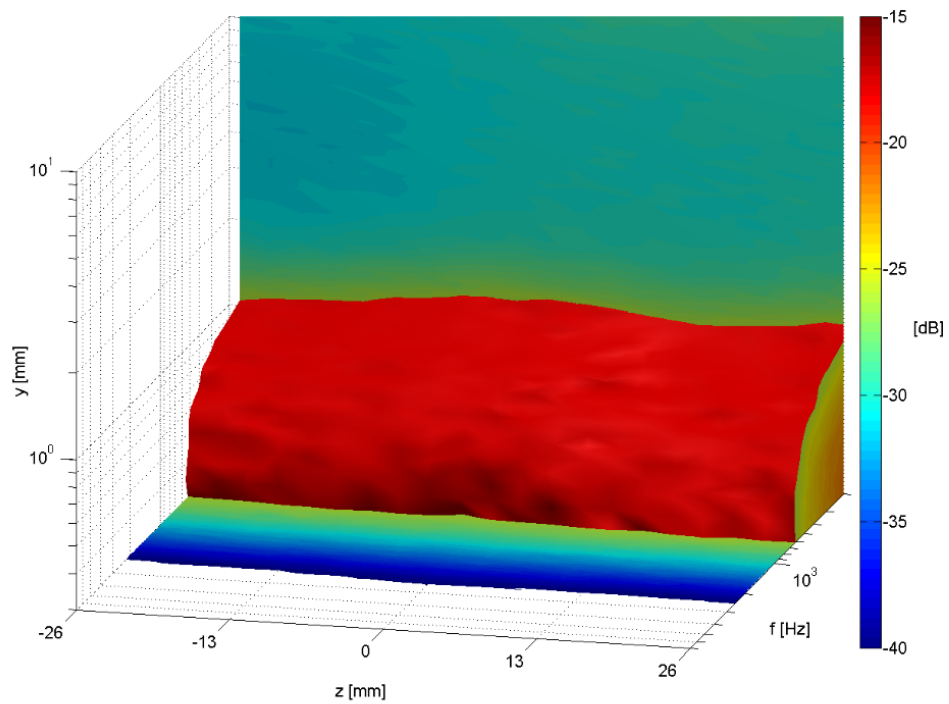


Figure 43: Baseline turbulence at $x/c = 0.67$ suction side, $AoA = 0^\circ$, $Tu = 5\%$, $U = 25\text{ms}^{-1}$

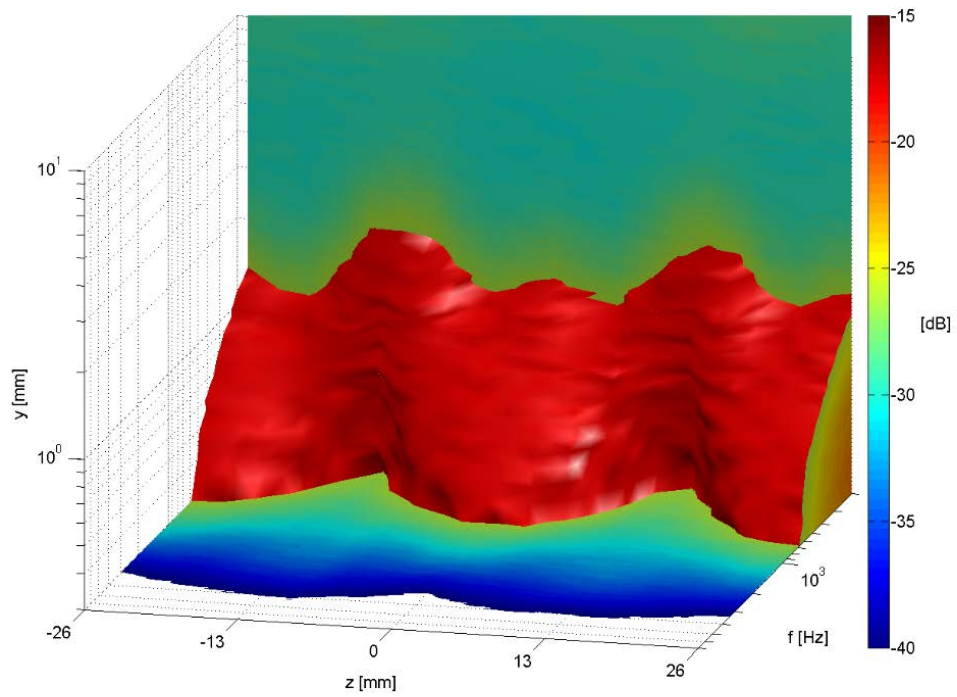


Figure 44: A45W26 turbulence at $x/c = 0.67$ suction side, $AoA = 0^\circ$, $Tu = 5\%$, $U = 25 \text{ ms}^{-1}$

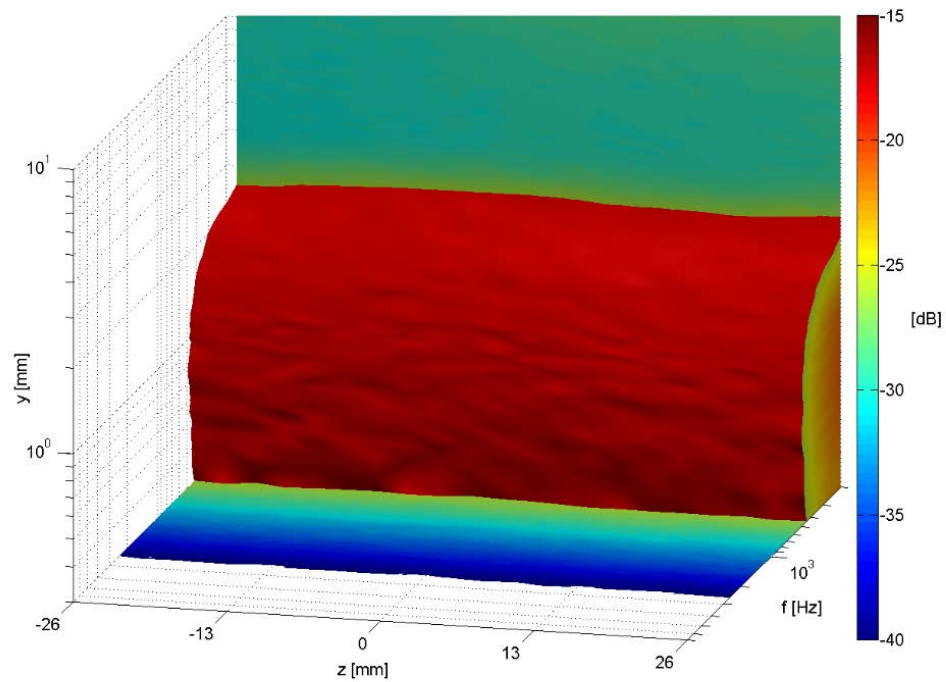


Figure 45: Baseline turbulence at $x/c = 0.93$ suction side, $AoA = 0^\circ$, $Tu = 5\%$, $U = 25 \text{ ms}^{-1}$

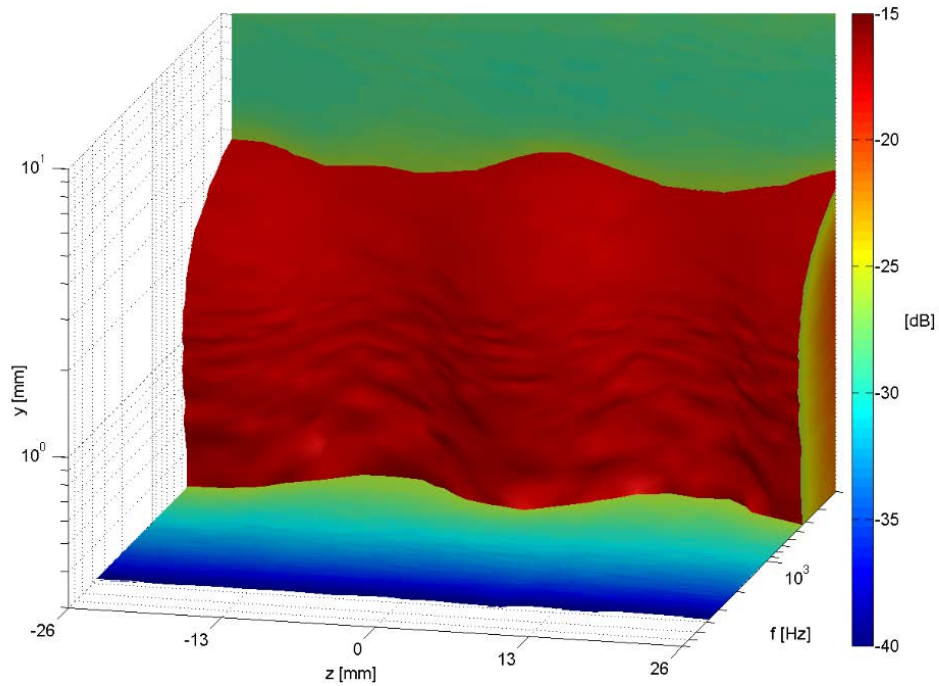


Figure 46: A45W26 turbulence at $x/c = 0.93$ suction side, $AoA = 0^\circ$, $Tu = 5\%$, $U = 25\text{ms}^{-1}$

6.2 Pressure side

This section presents the data analysis for the pressure side of the NACA65(12)-10 aerofoil. The baseline leading edge is compared to the serrated leading edge (A45W26).

6.2.1 Boundary layer profiles

Figure 47 shows contour plots of the boundary layer normalised by the free-stream velocity at $x/c = 0.5$ comparing the baseline and the serration (A45W26) leading edges. It can be observed that there is a strong difference between the straight and the undulated leading edge. While the baseline shows a relatively thick (~ 5 to 10 mm) and consistent boundary layer, the same is almost completely suppressed in the serration case. Only two distinct circular areas of approx. eight millimeters of diameter present a reduction of velocity (u) of 50%. The same measurements at the position of $x/c = 0.93$ (Figure 48) show related pattern, whereas the breakup of the vortice structures is still present. Nevertheless, the boundary layer is again suppressed in a wide range.

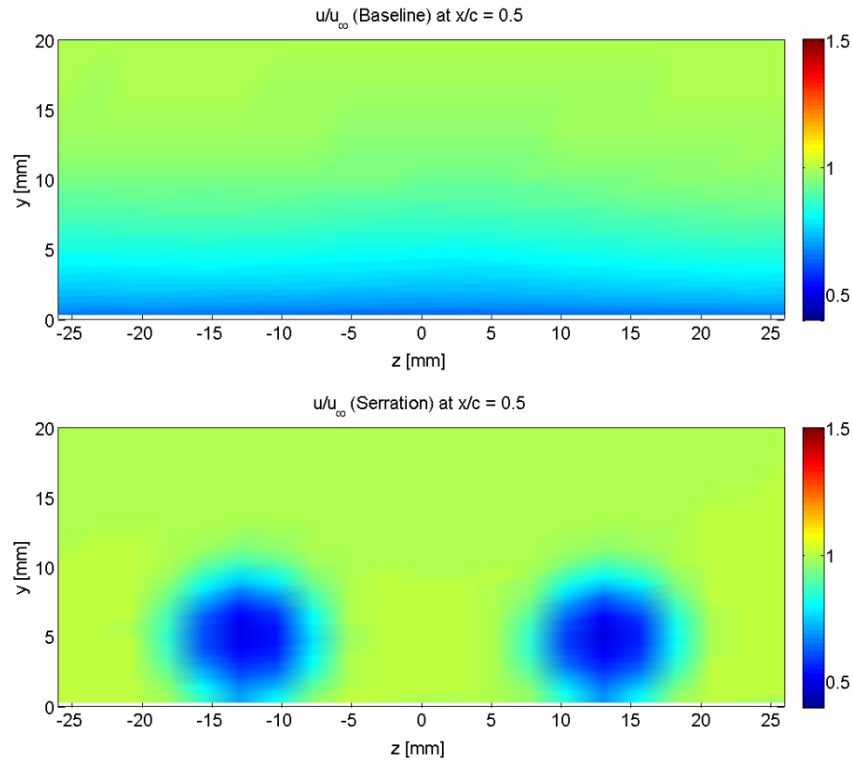


Figure 47: Boundary layer profiles normalised by the free-stream, baseline vs. A45W26 at $x/c = 0.5$ pressure side, $AoA = 0^\circ$, $Tu = 5\%$, $U = 25\text{ms}^{-1}$

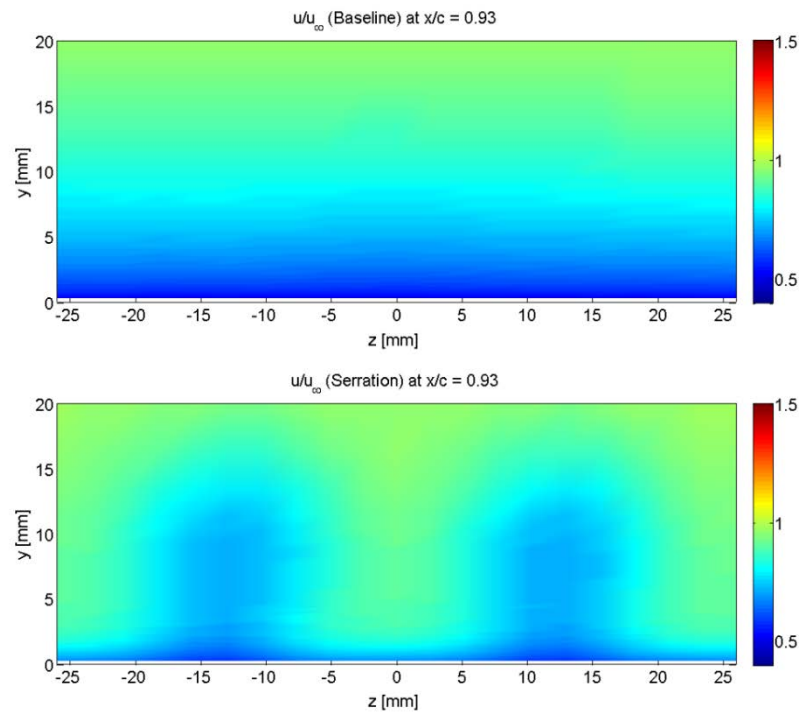


Figure 48: Boundary layer profiles normalised by the free-stream, baseline vs. A45W26 at $x/c = 0.93$ pressure side, $AoA = 0^\circ$, $Tu = 5\%$, $U = 25\text{ms}^{-1}$

6.2.2 Turbulence intensity

Figure 49 shows a contour plot of the turbulence intensity for the baseline and the serration at $x/c = 0.5$ where the x-axis presents the spanwise locations. This plot corresponds very well with the velocity distribution shown in the previous chapter. The baseline shows a turbulence over the whole span of about 11% which is elevated up to 10 millimeters in y-direction. For the serration case, the turbulence is only present in the vortical structures at the roots of the undulations ($z = -13$ and $z = 13$). The rest of the flow is characterised by a Tu of 5%. The circular structures show an interesting pattern with high turbulence (16%) in a semi-circle in the upper region and relatively low turbulence (9%) in the center. This can clearly be associated to rotating vortices. Figure 50 shows the contour plots for the streamwise location at $x/c = 0.93$. It is noticeable that the overall turbulence decreases but the area where it occurs increases. The vortex structure of the serration are now even more lift up from the surface and expand in y-direction to about 20 millimeters.

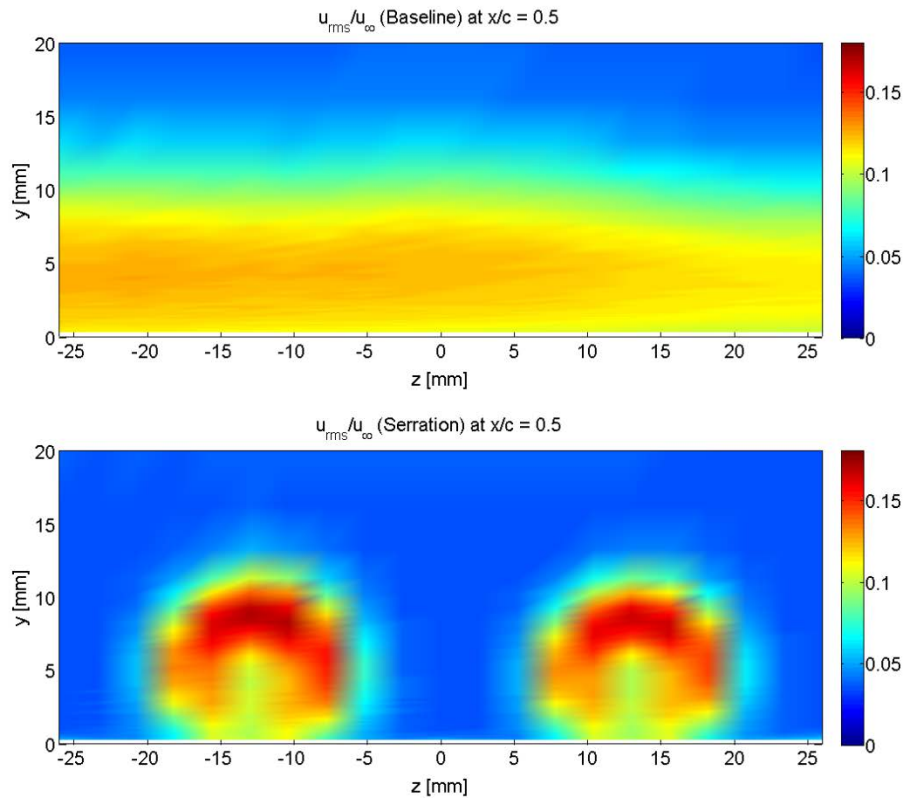


Figure 49: Tu profiles baseline vs. A45W26 at $x/c = 0.5$ pressure side, $AoA = 0^\circ$, $Tu = 5\%$, $U = 25\text{ms}^{-1}$

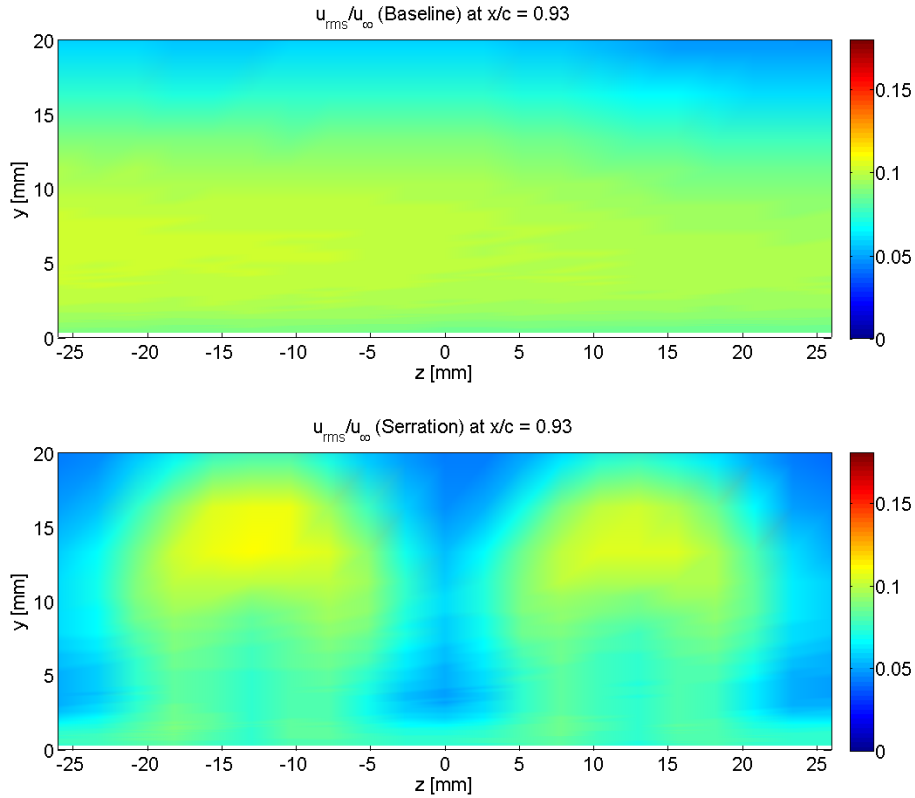


Figure 50: Tu profiles baseline vs. A45W26 at $x/c = 0.93$ pressure side, $AoA = 0^\circ$, $Tu = 5\%$, $U = 25\text{ms}^{-1}$

6.2.3 Spectral analysis

Figure 51 and Figure 52 show the turbulence of the baseline leading edge compared to the serration at the streamwise position of $x/c = 0.5$ on the pressure side. As seen from the Tu contour plots, the turbulence is suppressed in a wide range of spanwise locations. This observation can also be made in Figure 52 where the low frequency turbulence is suppressed. Only the root region shows two vortices with counter-rotating structures. Further downstream this special effect isn't that prominent anymore. Figure 53 and Figure 54 describe the fluctuations at the chordwise position of $x/c = 0.93$. Suppression in turbulence now is only left to the higher elevated structures in y -direction (4 – 20 mm).

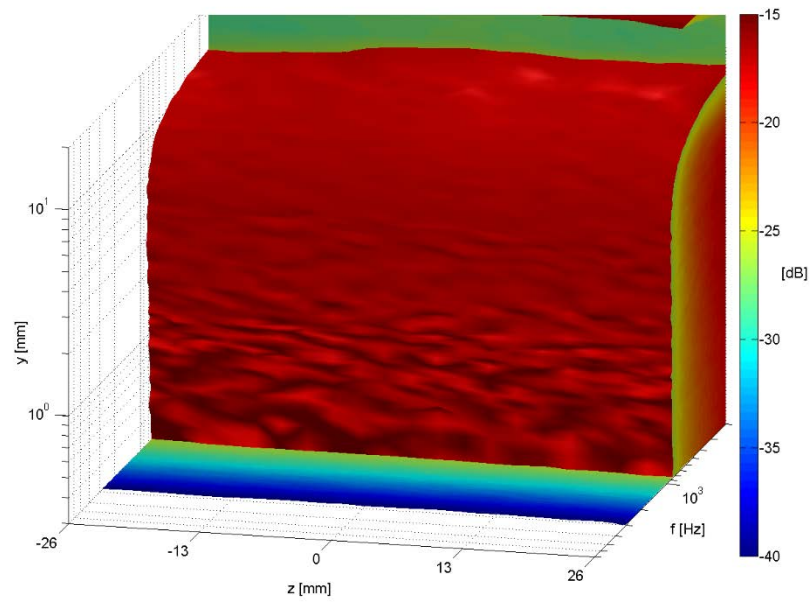


Figure 51: Baseline turbulence at $x/c = 0.5$ pressure side, $AoA = 0^\circ$, $Tu = 5\%$, $U = 25\text{ms}^{-1}$

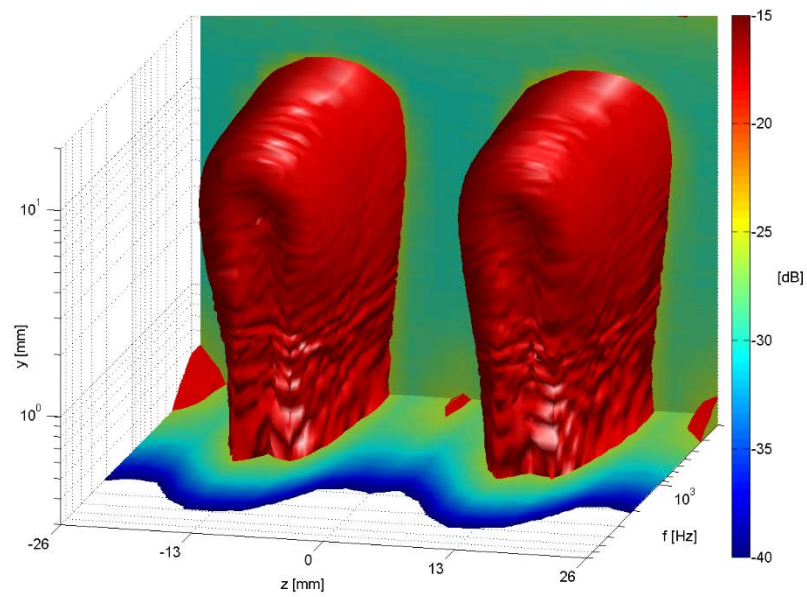


Figure 52: A45W26 turbulence at $x/c = 0.5$ pressure side, $AoA = 0^\circ$, $Tu = 5\%$, $U = 25\text{ms}^{-1}$

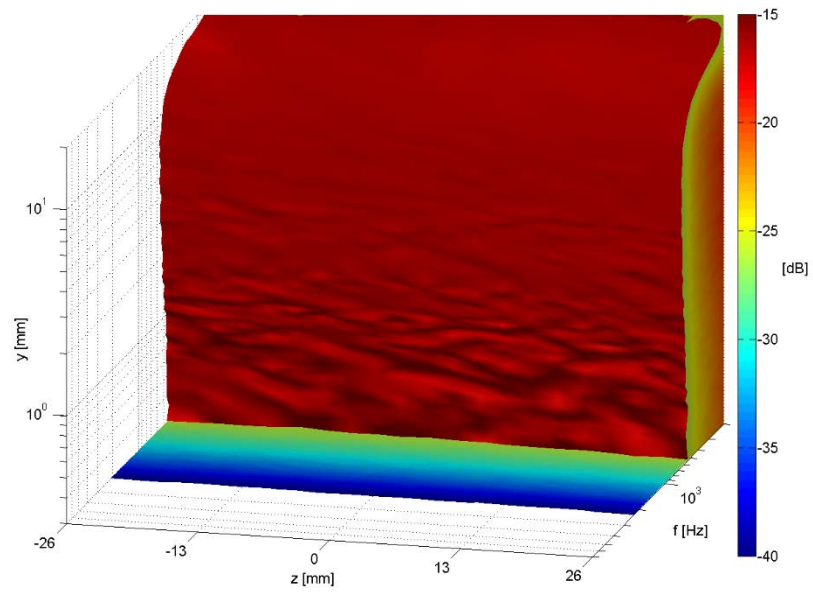


Figure 53: Baseline turbulence at $x/c = 0.93$ pressure side, $AoA = 0^\circ$, $Tu = 5\%$, $U = 25\text{ms}^{-1}$

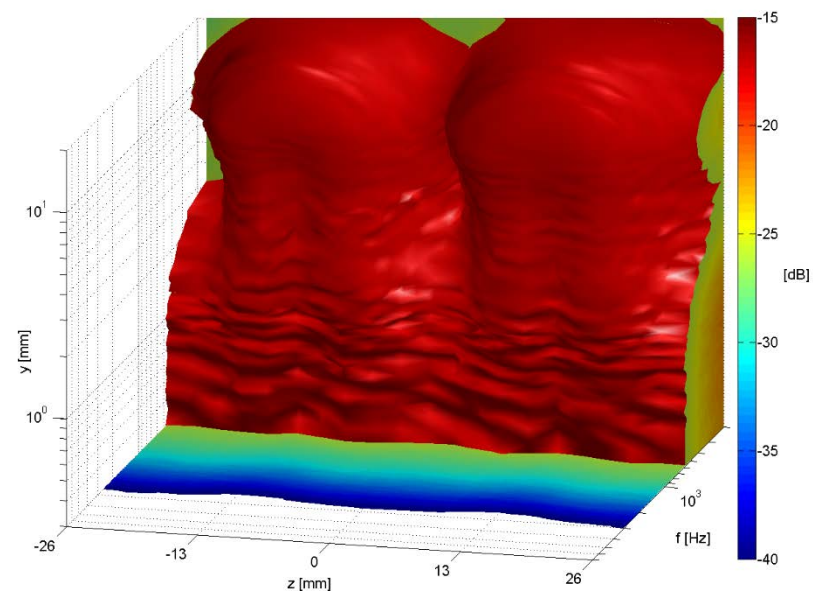


Figure 54: A45W26 turbulence at $x/c = 0.93$ pressure side, $AoA = 0^\circ$, $Tu = 5\%$, $U = 25\text{ms}^{-1}$

7 Comparison of experimental measurements to the numerical simulations

The aim of this chapter is the comparison of boundary layer measurements performed experimentally in the open-jet wind tunnel at the Brunel University London and numerical simulations carried out by Schreiber (2017) provided by ISAVE of the Hochschule Düsseldorf.

Measurements in the boundary layer of a NACA65(12)-10 aerofoil have been conducted using hot-wire anemometry. The aerofoil was equipped with a sinusoidal leading edge which is characterised by an amplitude of 45 mm ($x/c = 0.3$) and a wavelength of 26 mm ($\lambda/c = 0.173$). Measurements have been taken at eight streamwise locations (x) ranging from 6 mm near the leading edge to 140 mm near the trailing edge. The aerofoil is defined by an overall chord length (c) of 150 mm. In spanwise direction, three locations are of interest. The peak of the aerofoil marks the position of $z = 0$ mm, the midpeak is located at $z = 5.2$ mm and the trough of the undulation can be found at $z = 13$ mm. Figure 55 shows a cross-section of the NACA65(12)-10 aerofoil with A45W26 LE at the root position of $z=13$ mm. The profile of this section displays, that velocity profiles in the range of 6 – 45 mm at the leading edge are not expected to produce a good result, since no near wall relationship can be measured. Nevertheless, all boundary layer profiles normalised by the chord are plotted for each spanwise location. The profile in black represents the straight leading edge (baseline) and the red profile can be allocated to the serrations. All hot-wire measurements are conducted with a configuration of an angle of attack (AoA) of zero degree, turbulence intensity (Tu) of 5% and free-stream velocity of 25 ms^{-1} ($Re \sim 2.5 \times 10^5$).

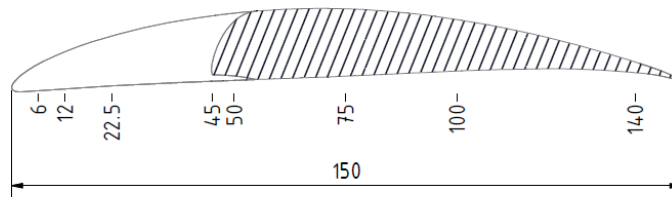


Figure 55: Cross-section A45W26 at $z = 13$ mm (root) (dimensions in mm)

The numerical simulations performed by Schreiber (2017) have the same configuration as the experiment. Solely the velocity of the free stream in the simulation with 15 ms^{-1} ($Re \sim 1.5 \times 10^5$) is lower than in the hot-wire study. Since the Reynolds numbers are relatively small, the influence of their difference on the boundary layer and the transition respectively, is considered negligible. Figure 56 shows the contour plot of the baseline

aerofoil. In this case, the boundary layer thickness is defined as the layer where the flow velocity reaches 99% of the free-stream velocity (δ_{99}). Overall, the boundary layer for the straight LE can be described as very thin and is characterised by laminar properties. Noticable is the stagnation point close to the leading edge forming a separation bubble. Only a slight difference between pressure and suction side can be observed, in which the boundary layer on the lower side seems to be thicker.

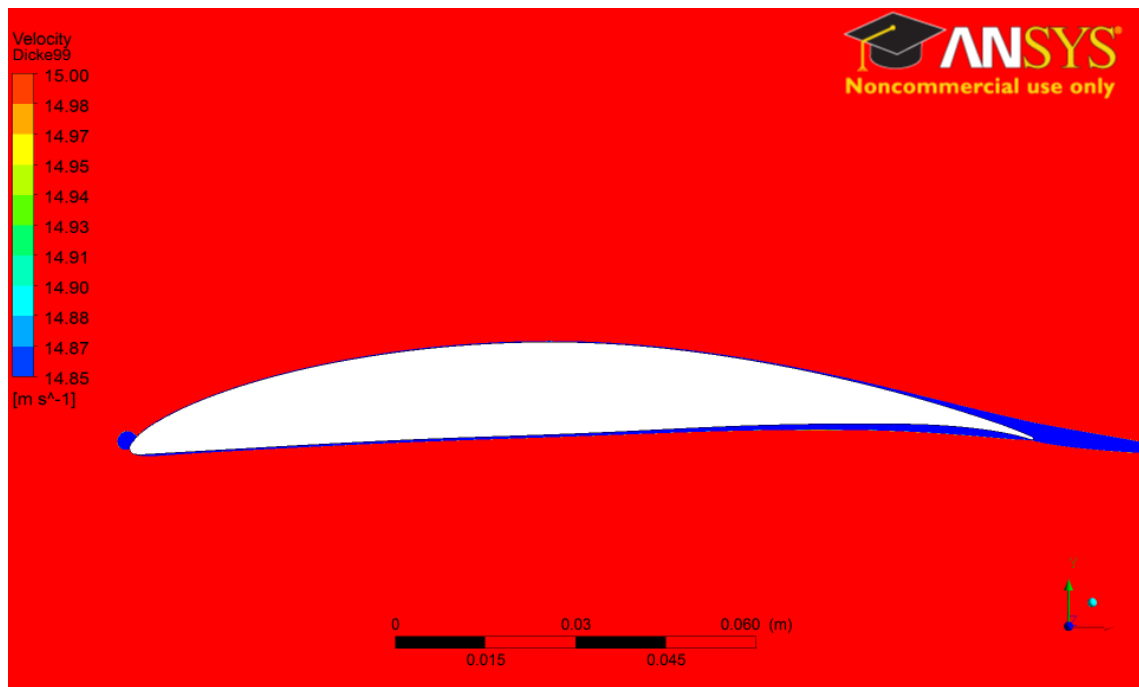


Figure 56: Overview boundary layer thickness numerical results for the baseline aerofoil with an AoA of 0° and $u = 15\text{ms}^{-1}$ (Schreiber, 2017)

Figure 57 shows the boundary layer for the A45W26 LE with a cross-section at the tip ($z = 0$) of the sinusoidal undulations. It can be seen that the boundary layer on the suction side is separated in the leading edge area and attaches approximately at a streamwise position close behind the root. The boundary layer itself is slightly thicker compared to the baseline. On the pressure side no boundary layer is visible with the given criterion of δ_{99} . The single boundary layer profiles obtained by the experiment (Figure 58) show a related behaviour. A first measurable boundary layer appears at the chordwise position of $x/c = 0.3$ at the root of the serration. From there on it grows from approx. one mm to four mm. While the difference between baseline and serration for the experimental data is very obvious at $x/c = 0.3$ and $x/c = 0.33$, it seems that the boundary layer recovers approaching the trailing edge. Figure 59 displays the numerical result for the spanwise position at $z = 6.5\text{ mm}$ also known as the midpeak. The boundary layer shows a similar behaviour as the peak region of the A45W26 LE. No boundary layer is visible on the pressure side and the thickness is increased on the suction side near the trailing edge.

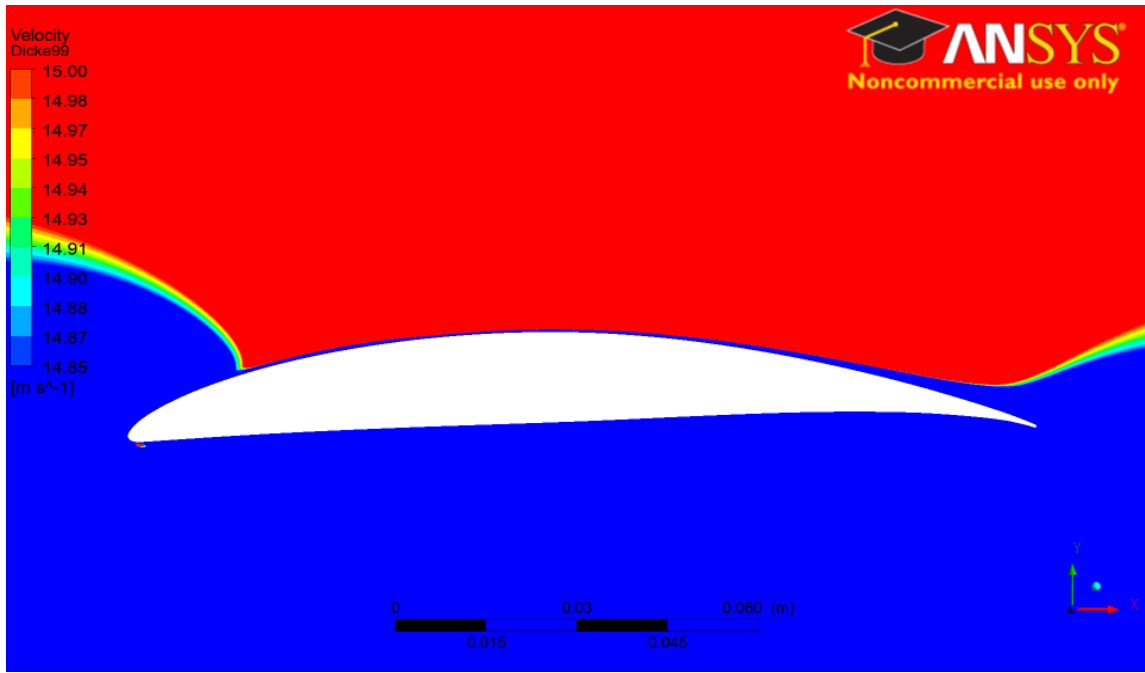


Figure 57: Overview boundary layer thickness numerical results for the A45W26 LE at $z = 0$ (peak) with an AoA of 0° and $u = 15\text{ms}^{-1}$ (Schreiber, 2017)

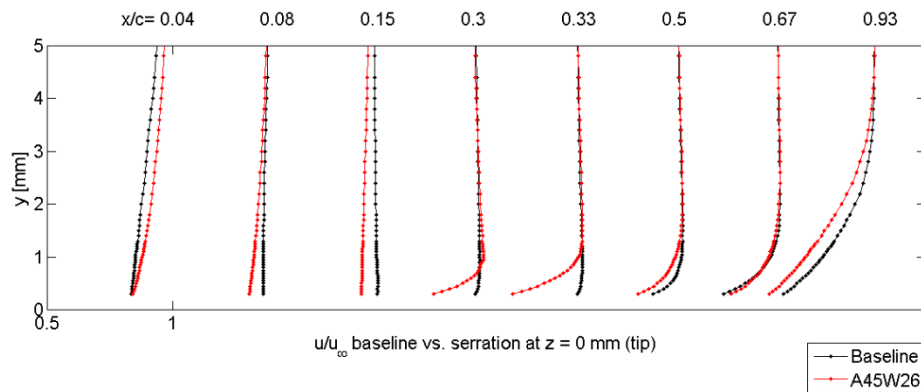


Figure 58: Streamwise boundary layer profiles for the baseline (black) vs. A45W26 (red) at $z = 0$ mm (tip) suction side, AoA = 0° , $Tu = 5\%$, $U = 25\text{ms}^{-1}$

The profiles calculated from the experimental data in Figure 60 show hardly any difference between the serration and baseline. The layer near the trailing edge for the serration seems to be a little bit thicker which can be attributed to the higher turbulent flow. Figure 61 shows the contour plot for the serration at the trough ($z = 13$ mm). It can be seen that the boundary layer is remarkably thicker on the suction side compared to the other slices and the baseline. Additionally, flow of high velocity seems to emerge from the root on the pressure side. This could be an indication for vortical structures. The experimental data for the suction side in Figure 62 shows a similar development. Especially the boundary layer profiles at $x/c = 0.5$ and 0.67 for the serration are comparatively thick.

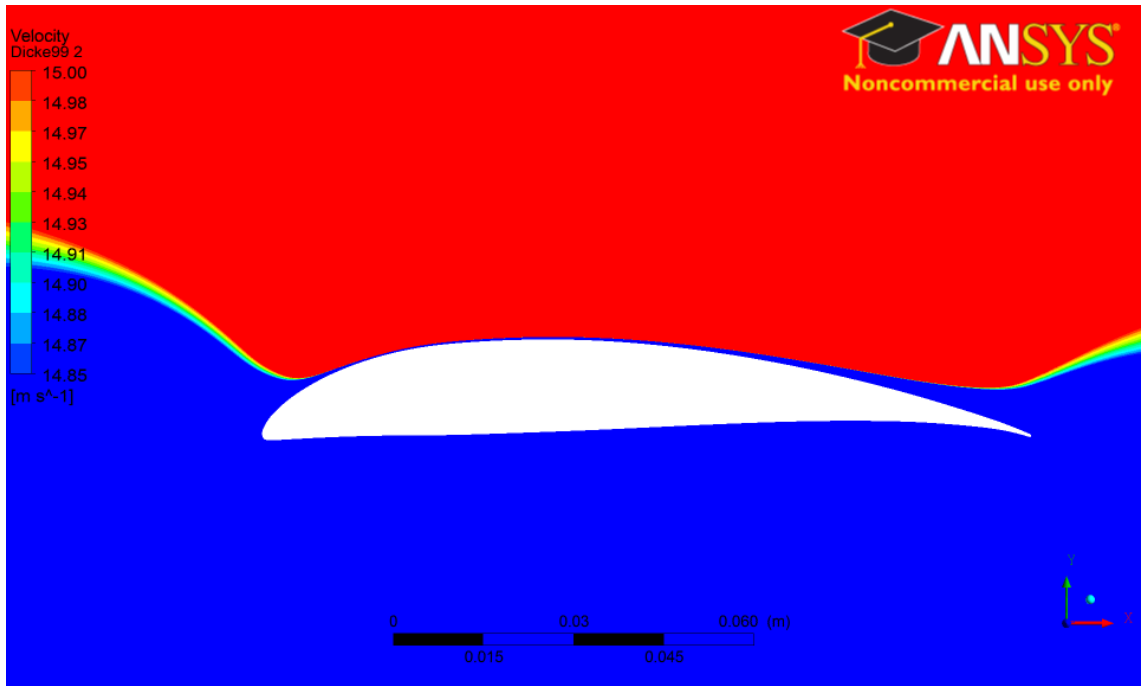


Figure 59: Overview boundary layer thickness numerical results for the A45W26 LE at $z = 6.5$ (midpeak) with an AoA of 0° and $u = 15\text{ms}^{-1}$ (Schreiber, 2017)

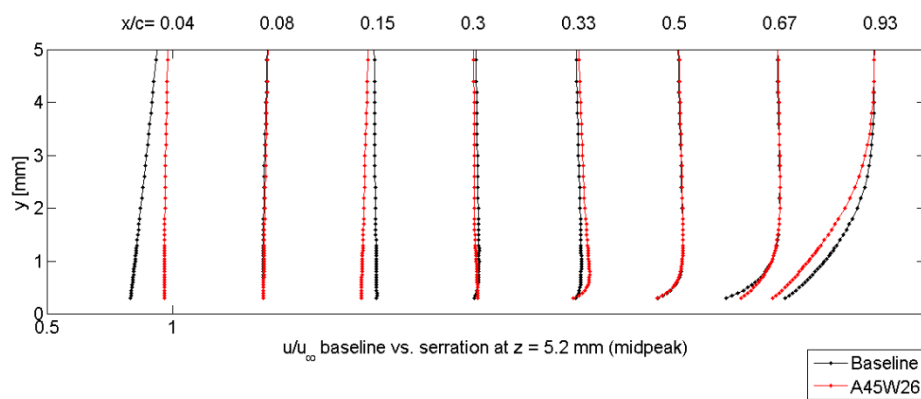


Figure 60: Streamwise boundary layer profiles for the baseline (black) vs. A45W26 (red) at $z = 5.2\text{ mm}$ (midpeak) suction side, AoA = 0° , $Tu = 5\%$, $U = 25\text{ms}^{-1}$

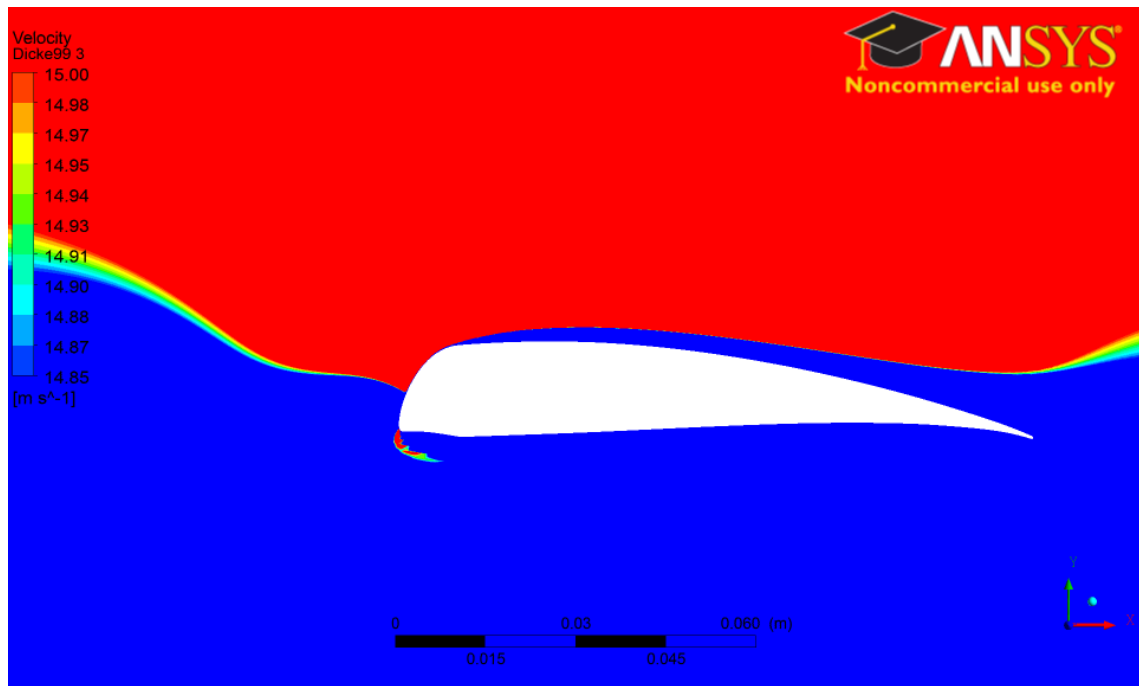


Figure 61: Overview boundary layer thickness numerical results for the A45W26 LE at $z = 13$ (trough) with an AoA of 0° and $u = 15\text{ms}^{-1}$ (Schreiber, 2017)

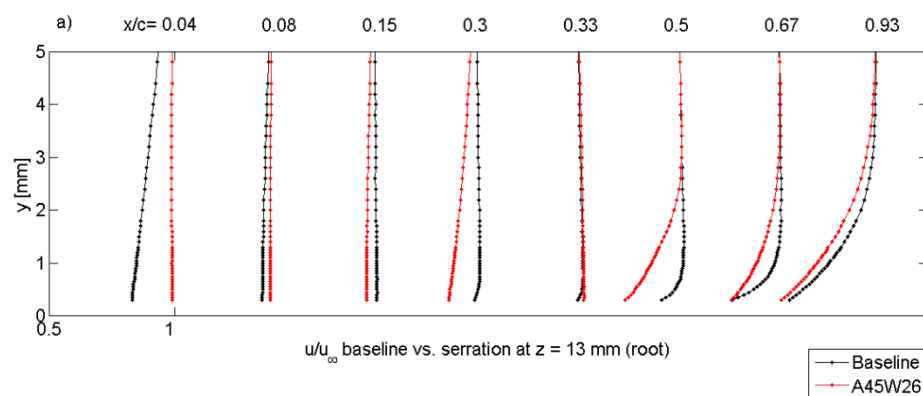


Figure 62: Streamwise boundary layer profiles for the baseline (black) vs. A45W26 (red) at $z = 13$ mm (trough) suction side, AoA = 0° , $Tu = 5\%$, $U = 25\text{ms}^{-1}$

8 Surface oil flow visualisation

Oil flow visualisation is performed in order to validate the boundary layer measurements and to gain more information about the mechanism in the boundary layer in streamwise direction. Not only the flow pattern (reverse flow and separation) is of interest, but also the near wall vortices are to be examined.

8.1 Setup

The oil flow visualisation is performed for the sinusoidal leading edge A45W26 ($A/c = 0.3$, $\lambda/c = 0.17$) on both upper and lower sides of the aerofoil. The oil flow mixture consists of 44% paraffin, 4% linseed oil and 2% titanium dioxide. Linseed oil and paraffin are used to control the viscosity of the fluid whereas titanium dioxide dyes the mixture and provides a good contrast to the black colour of the aerofoil. In order to achieve a smooth and evenly distributed coating, the mixture is applied carefully with a sponge. A camera (video mode) which is set up on a tripod is positioned with sufficient distance to the nozzle exit above and below the aerofoil respectively. All tests are conducted at zero angle of attack and flow speed of 25 ms^{-1} (Reynolds number 2.5×10^5) with a turbulence intensity of 5%.

8.2 Suction side A45W26

Results of the oil flow visualisation are presented via selected images of the corresponding video files. Since the oil mixture spreads slowly in streamwise direction over time, each figure shows a specific phase of the flow. Several snap-shots are used to describe the individual flow pattern at different locations on the aerofoil. Each figure shows the entire chord length of 0.15 m in streamwise direction and four wavelengths (W26, $\lambda/c = 0.17$) in spanwise direction. The free-stream is flowing from the leading edge on the right side in the direction of the trailing edge to the left side. The flow pattern for the baseline leading edge is uniform across the entire span. Boundary layer separation is apparent only near the trailing edge of the aerofoil (Chong, et al., 2015). Figure 63 shows the selection of the surface oil flow for the suction side of the aerofoil at the time step of six seconds after the jet was set to 25 ms^{-1} . Acceleration of the flow between the leading edge tips causes a pressure drop and leads to suction peaks behind the troughs of the undulation. Secondary flow draws the low inertia flow from the peaks which is subsequently replaced by high momentum airflow from the freestream. The air behind the troughs reattaches as high turbulent flow and single streamwise vortices are generated. The development of these vortices in streamwise direction can be seen in Figure 64 and Figure 65. Each vortex seems to expand towards the trailing edge penetrating the boundary layer almost to the end leaving only a small pocket for

separation. Additionally a slight shift of the vortices in spanwise direction from the roots towards the peaks can be identified. This pattern corresponds with the boundary layer measurements and can be attributed to the adverse pressure gradient on top of the aerofoil. A closer look on the vortex shedding also reveals that a pair of streamwise counter-rotating vortices emanate in the region of $x/c = 0.5$ on each trough (Figure 63). Compared to the single vortices, the adjacent vortices seem only able to weakly energise the boundary layer.

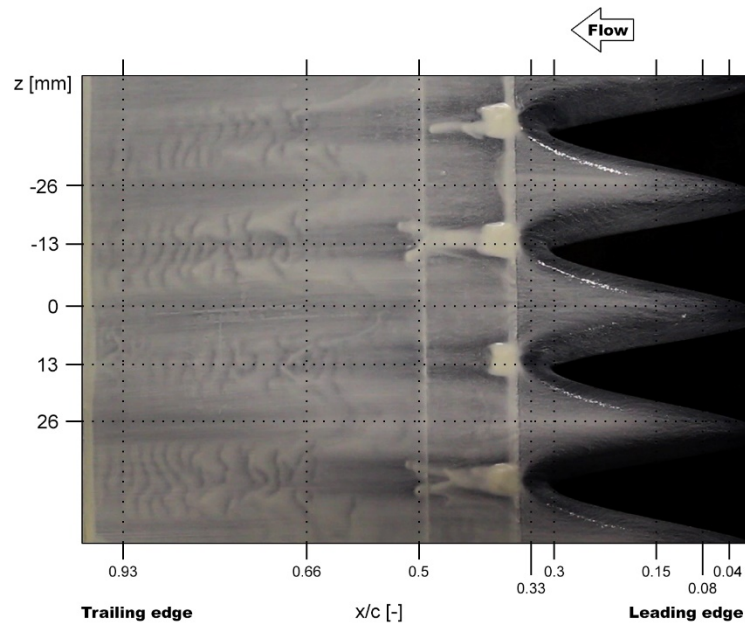


Figure 63: Surface flow visualisation A45W26 suction side with $Tu = 5\%$ at $t = 5s$

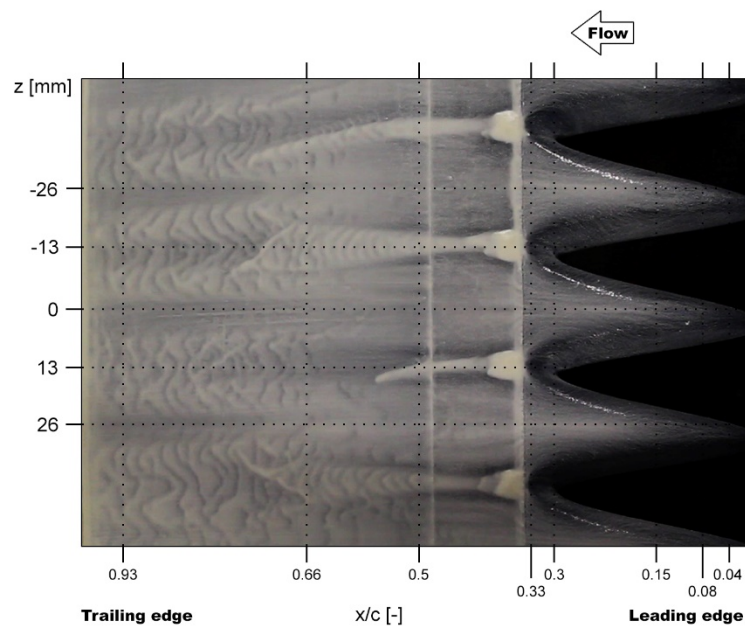


Figure 64: Surface flow visualisation A45W26 suction side with $Tu = 5\%$ at $t = 6s$

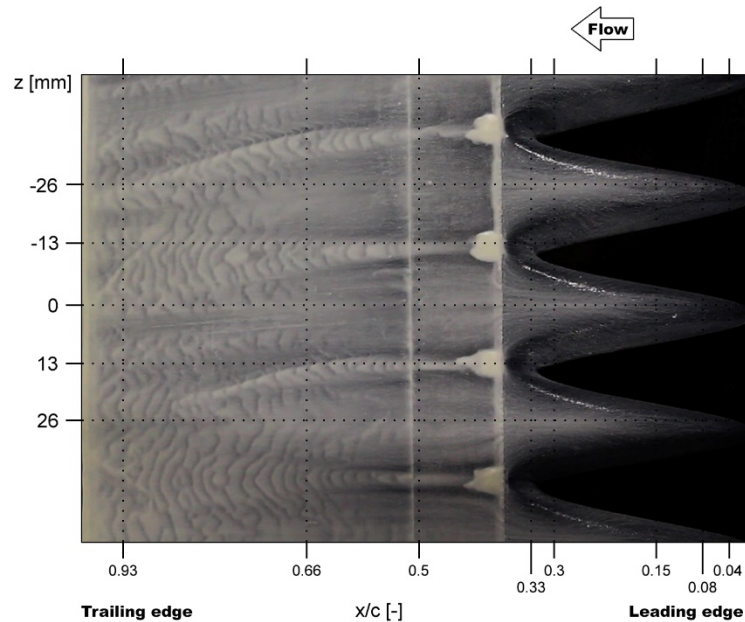


Figure 65: Surface flow visualisation A45W26 suction side with $Tu = 5\%$ at $t = 7s$

8.3 Pressure side A45W26

This section shows a selection of the visualisation for the pressure side of the aerofoil. Similarly to the upper side, suction peaks with separation are visible in the troughs of the leading edge (Figure 66). Again, the air is accelerated between the peaks and reattaches as high turbulent flow forming a pair of streamwise vortices in the root region. These counter-rotating vortices move straight to the trailing edge while growing bigger and lifting up from the surface (Figure 67 and Figure 68). This flow pattern is corresponding very well with the strong vortices which can be seen in the boundary layer measurements. Comparing both the upper and lower side of the aerofoil, the pressure side seems to be energised with way more turbulent flow. The snap-shots show that the expansion of the vortices is present on the whole surface area of the aerofoil. Boundary layer separation in the trailing edge region is completely suppressed. However, from the oil flow visualisation it is difficult to derive any further information regarding the ability of the leading edge to reduce the turbulence-leading edge interaction noise. Secondary flow in the interstices which is fed by the high turbulent incoming flow is still regarded as the main mechanism for the reduction in broadband noise because the main flow is deflected away from the stagnation point. Furthermore, as seen in Chapter 5, the secondary flow tends to reduce the turbulence intensity in the serrations which supports the noise reduction. The findings show reasonable agreement with the numerical results of Skillen & Revell (2015).

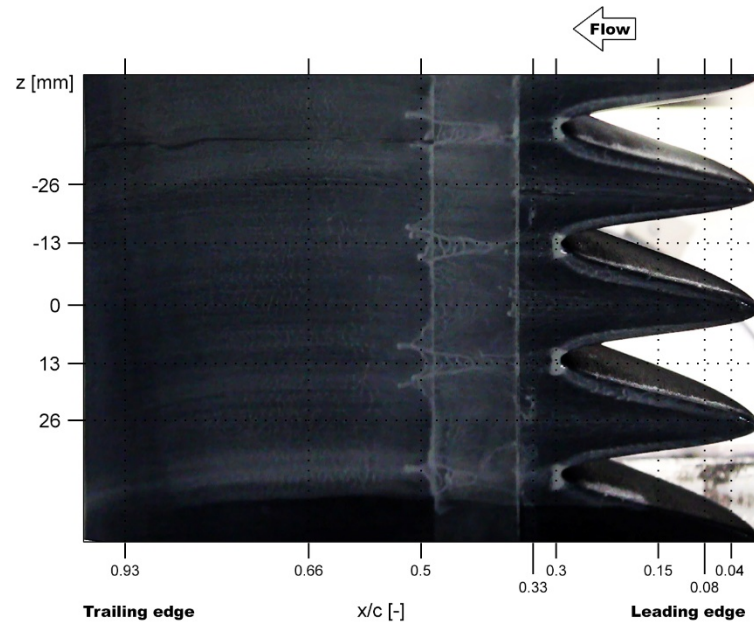


Figure 66: Surface flow visualisation A45W26 pressure side with $Tu = 5\%$ at $t = 6s$

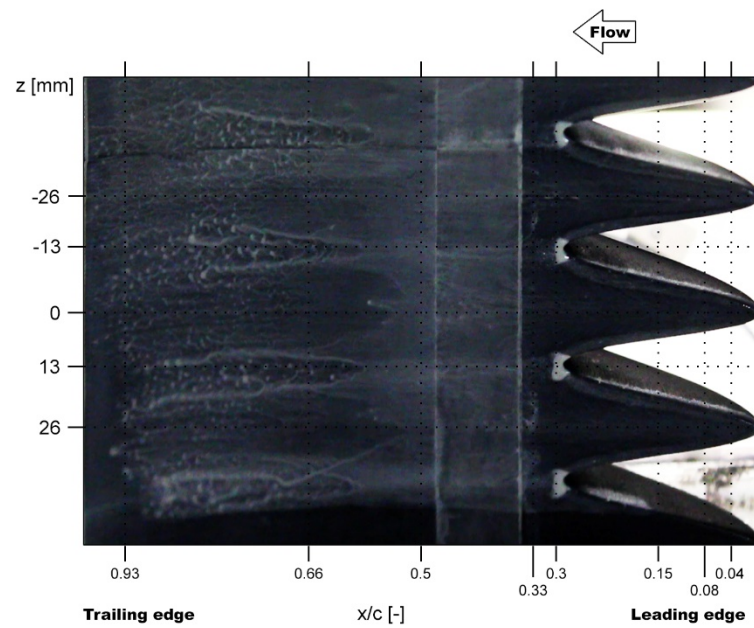


Figure 67: Surface flow visualisation A45W26 pressure side with $Tu = 5\%$ at $t = 17s$

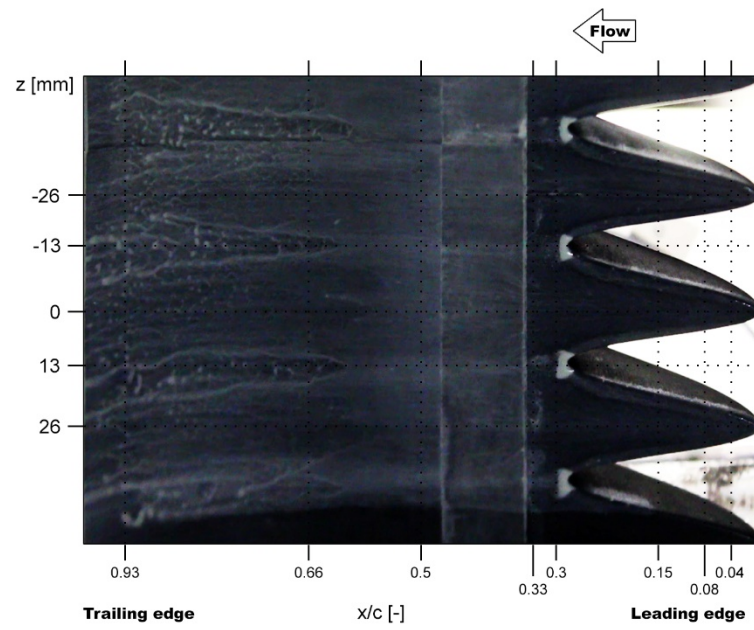


Figure 68: Surface flow visualisation A45W26 pressure side with $Tu = 5\%$ at $t = 22s$

9 Wake measurements

This chapter describes the hot-wire method used for measuring three components of the velocity in the near wake of the aerofoil. The study of velocity fluctuations in the wake of the aerofoil is of interest to gain further information on the vortex structures separated from the aerofoil surface. The wake is expected to contain sufficient turbulent energy and is able to have great influence not only on the aerodynamic characteristics of the wing but also on the aeroacoustics. Wherever possible, an attempt is made to relate the power spectrum of turbulence to the mean properties of the flow. The aim is to provide further information on flow physics and to complement the overall results.

9.1 Hot-Wire setup

In this project, an X-array wire probe 55P61 by *Dantec Dynamics* is used to measure the flow in the wake of the aerofoil. The probe measures two velocity components simultaneously in turbulent, instationary two-dimensional flow fields. As seen in Figure 69 the probe is a miniature wire probe with two 1.25 mm long platinum-plated tungsten wire of $5\ \mu\text{m}$ diameter. The two inclined wires are placed close together with a distance of 1 mm forming an X. For signal analysis purposes it is assumed that the two wires are contained in the same plane. Two sensor identification marks on the ceramic probe body showing either one dot or two dots mark the orientation of the wires. The X-probe with straight prongs is mounted with the probe axis parallel to the direction of the main flow. The coordinate system of the probe (x,y,z) matches the laboratory coordinate system (u,v,w).

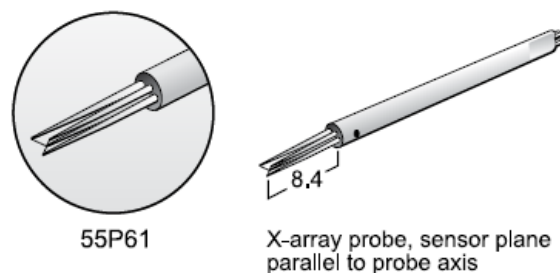


Figure 69: 55P61 X-hot-wire probe (Dantec Dynamics)

9.1.1 Velocity calibration

For calibration, the parallel probe-stem is aligned with the x-axis of the coordinate system selected. The first step of the calibration process is similar to the one performed with the

single-wire probe. A relation between the CTA output (E) and the flow velocity (u) is established by exposing the probe to flow velocities in the range of $0 - 35 \text{ ms}^{-1}$. The flow speed is calculated using a pitot-static tube which is placed next to the hot-wire. Temperature correction according to equation 5.7 is applied and the acquired data is fitted with a polynomial curve fit of 4th order (equation 5.5). Additionally, a power law curve fitting, known as King's law, is performed and the calibration constants A and B are obtained. This calibration procedure is applied for both wires simultaneously. Figure 70 to Figure 73 show the results of the velocity calibration with each having an accurate curve fit and a coefficient of determination (R^2) of at least 0.999.

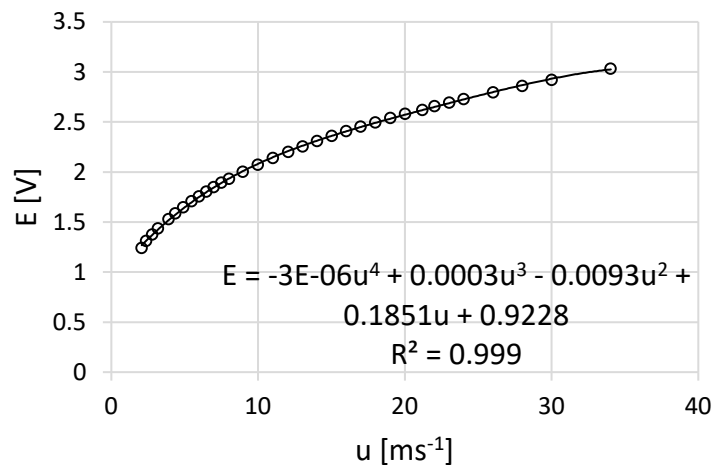


Figure 70: X-Wire probe calibration of wire 1. Polynomial regression of 4th order

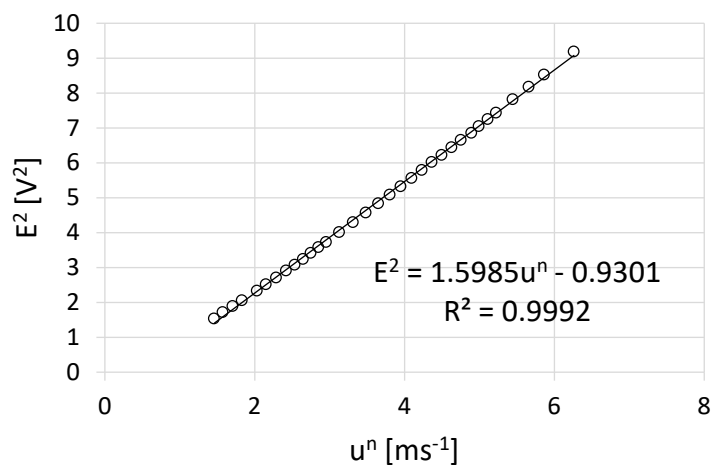


Figure 71: X-Wire probe calibration of wire 1 (King's law)

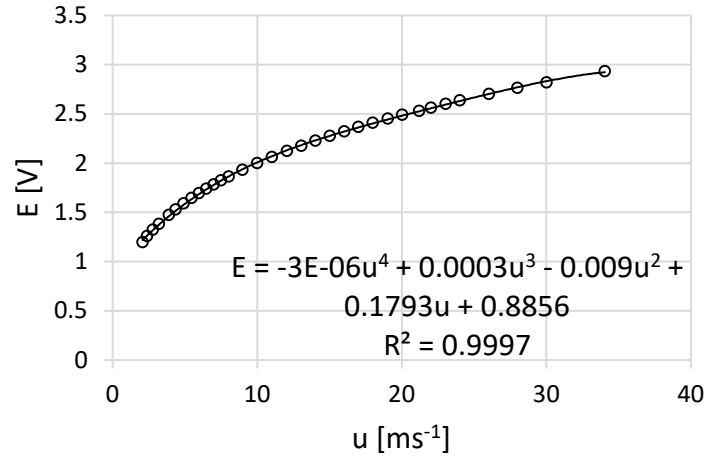


Figure 72: X-Wire probe calibration of wire 2. Polynomial regression of 4th order

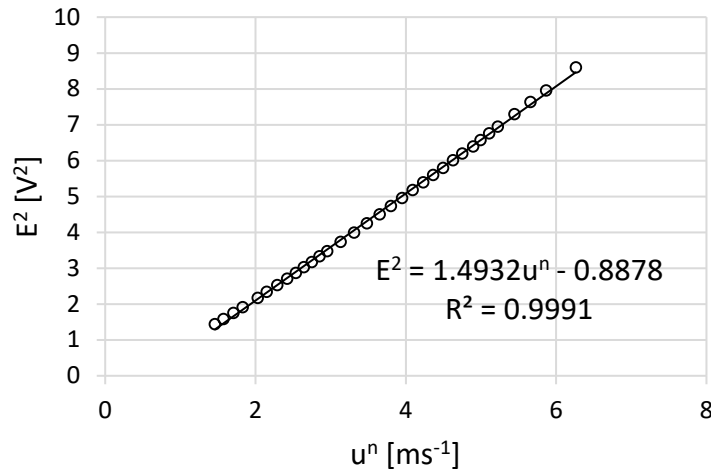


Figure 73: X-Wire probe calibration of wire 2 (King's law)

9.1.2 Yaw calibration

The directional calibration of the X-wire probe is performed to provide the individual directional sensitivity coefficients for the sensors. The yaw coefficients k_1 and k_2 are used to decompose calibration velocities into the velocity components u and v (Jørgensen, 2002). A probe coordinate system (x, y) is defined with respect to wire 1 and wire 2 as shown in Figure 74. The directional calibration requires the ability to rotate the probe on an axis through the crossing point of the wires perpendicular to the wire plane. Since no automatic rotation unit is available, the rotation of the X-probe is performed manually with great care. The maximum angle α_{max} which is expected in the experiment between the velocity vector u_α and the probe axis is estimated to be 48° . A total number

of 17 angular positions with steps of 6° is selected for the calibration. The probe is exposed to half of the free stream velocity defined for the experiment. In this case, the directional calibration velocity $u_{dir,cal} = 1/2 \cdot U_0$ is adjusted to 13 ms^{-1} . The application software ThermalPro is used to acquire the voltages E_1 and E_2 from the two sensors in each angular position, starting with the probe rotated to $-\alpha_{max}$. The velocity data for both wires at each angular position is calculated using King's law (Figure 75). The result of the calibration shows good consistency. In the next step the squared yaw factor k_1^2 and k_2^2 for sensor 1 and sensor 2 is calculated.

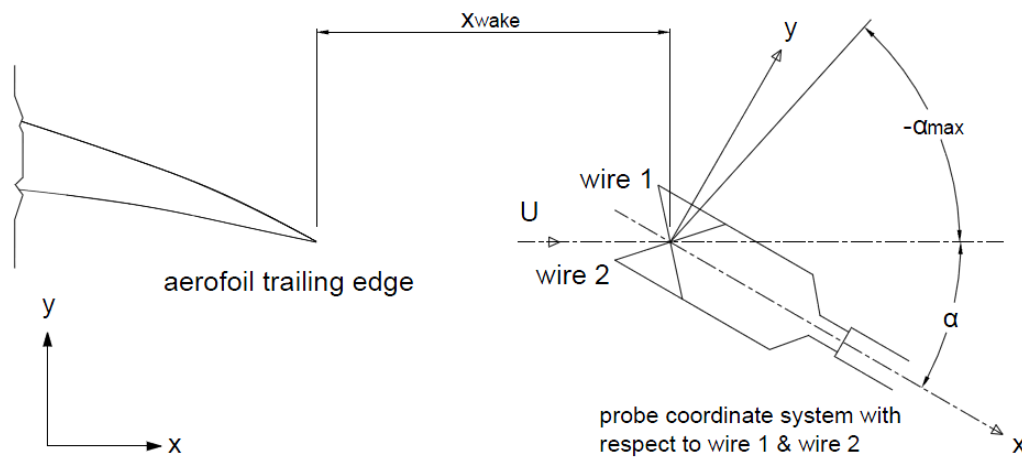


Figure 74: X-hot-wire probe with coordinate system and angle notation. Distance between aerofoil trailing edge and X-probe center is set to 3 mm (according to Bruun, 2002).

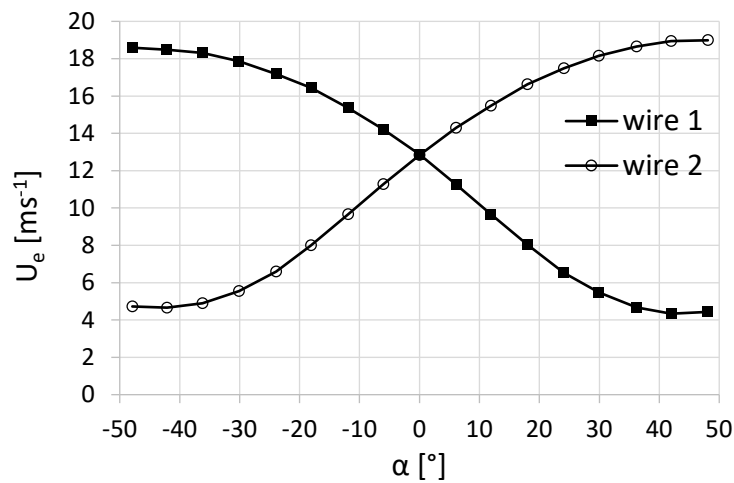


Figure 75: Yaw calibration wire 1 and wire 2 at $u = 13 \text{ ms}^{-1}$

For the decomposition of the X-probe, the calibrated velocities and the yaw coefficient k^2 are used to calculate the velocity components in the probe coordinate system. The calibration velocities u_{cal1} and u_{cal2} have already been calculated by linearisation. The k^2 results from the curve fit to the yaw calibration data. Figure 76 and Figure 77 show that for both wires a yaw-coefficient of $k_1^2 = k_2^2 = 0.04$ can be obtained. This value corresponds with the default value by *Dantec Dynamics* for miniature wire probes. The velocities u_1 and u_2 are then calculated using the following equations:

$$k_1^2 \cdot u_1^2 + u_2^2 = \frac{1}{2} \cdot (1 + k_1^2) \cdot u_{cal1}^2 \quad (9.1)$$

$$k_2^2 \cdot u_2^2 + u_1^2 = \frac{1}{2} \cdot (1 + k_2^2) \cdot u_{cal2}^2 \quad (9.2)$$

$$u_1 = \frac{\sqrt{2}}{2} \cdot \sqrt{(1 + k_2^2) \cdot u_{cal2}^2 - k_2^2 \cdot u_{cal1}^2} \quad (9.3)$$

$$u_2 = \frac{\sqrt{2}}{2} \cdot \sqrt{(1 + k_1^2) \cdot u_{cal1}^2 - k_1^2 \cdot u_{cal2}^2} \quad (9.4)$$

The velocities u and v in the probe coordinate system are then calculated from equation 9.5 and equation 9.6. The same calculation is applied for the rotated probe to calculate the velocities u and w .

$$u = \frac{\sqrt{2}}{2} \cdot u_1 + \frac{\sqrt{2}}{2} \cdot u_2 \quad (9.5)$$

$$v = \frac{\sqrt{2}}{2} \cdot u_1 - \frac{\sqrt{2}}{2} \cdot u_2 \quad (9.6)$$

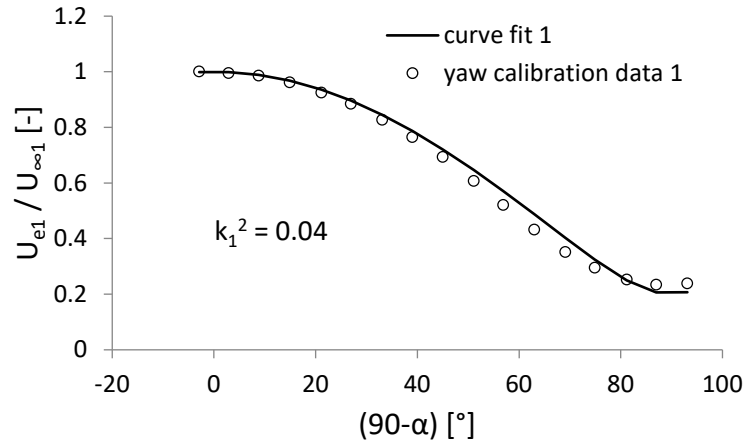


Figure 76: Curve fit of the yaw calibration data wire 1

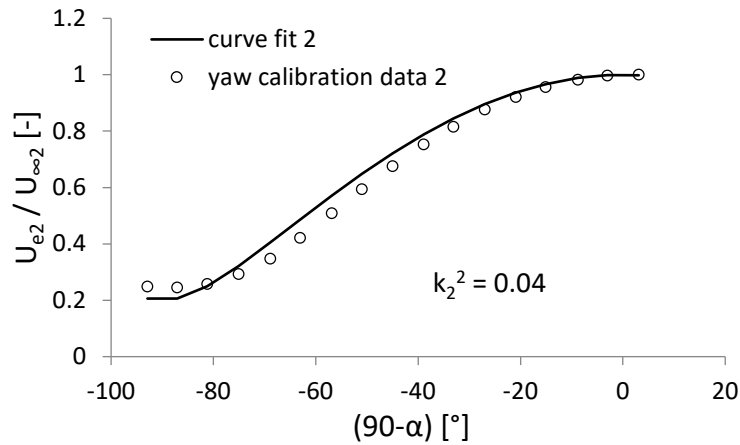


Figure 77: Curve fit of the yaw calibration data wire 2

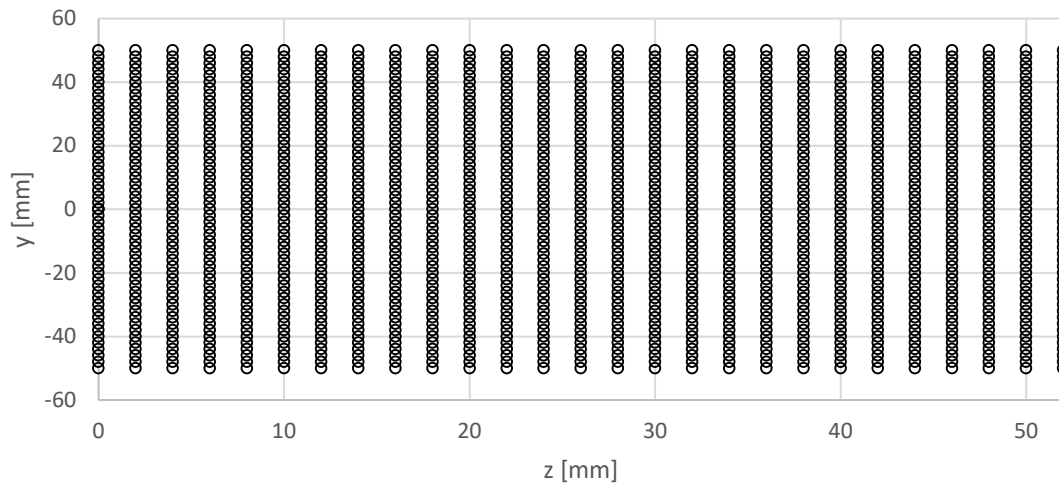
9.2 Experimental setup

Most of the steps during the measurement procedure for the X-Wire probe are similar to those for the boundary layer probe described in Chapter 5. Since an X-probe provides two output signals, a two-channel digital-measurement system is required. The two signals are acquired simultaneously by the A/D-unit and the signal conditioning is adjusted separately in the CTA unit (see Chapter 5 for settings of the gain, offset and resistance). Furthermore, for both two low-pass filter the same settings are selected and the data acquisition parameters are adjusted (see Chapter 5 for adjustment of N, number of samples, SR, sampling rate and T, total sampling time). During the data acquisition two simultaneous digital time-series are recorded. Since the objective of this experiment is the obtainment of all three velocity components (u, v, w) , the measurement plan according to Table 4 is designed.

Table 4: Measurement plan X-probe.

Step	Action	Probe orientation
1	Wake measurement of the u and v velocity component for the baseline	● in positive y -direction
2	Wake measurement of the u and w velocity component for the baseline	●● in positive y -direction
3	Wake measurement of the u and v velocity component for the A45W26	● in positive y -direction
4	Wake measurement of the u and w velocity component for the A45W26	●● in positive y -direction

As seen in Figure 74 the distance x_{WAKE} between the aerofoil trailing edge and the center of the X-probe is adjusted to three millimetres. The probe is controlled with the same traverse system used for the single-wire measurements. The first experiment is designed to acquire data both on the pressure side and suction side in the wake covering two wavelengths in spanwise direction. Figure 78 shows a total of 1378 probe locations ranging in z -direction from 0 to 52 mm. The range in y -direction is extended to $-50 \text{ mm} \leq y \leq 50 \text{ mm}$ expecting to provide some additional information about the shear layer distribution from the nozzle exit. The measurement of this plane is conducted for both the straight leading edge and the serrated LE A45W26 ($A/c = 0.3$, $\lambda/c = 0.173$) according to Table 4. Additionally, acquisition of detailed velocity profiles at the peak, midpeak and trough of the serration as well as for the baseline LE is performed with more points close to the surface of the aerofoil. Here, too, all three velocity components are measured by rotating the X-probe and repeating the acquisition.

Figure 78: Measurement positions X-probe in the wake of the aerofoil at $x/c = 1.02$

10 Data analysis wake measurements

This chapter presents the data analysis for the near wake measurements at three millimeters downstream of the trailing edge which have been realised with a hot-wire X-probe.

10.1 Velocity profiles

This chapter presents the velocity distribution in the near wake by using contour plots and single boundary layer profiles. Figure 79 shows contour plots of the velocity components u , v and w . Each baseline is compared to each serration. The y -axis of the contour plots ranges from -50 to 50 mm, where 0 is the plane of the trailing edge. In z -direction two wavelengths are examined reaching from -26 mm to 26 mm. Colourbars represent the particular velocity. The comparison of all three velocity components shows that vortical structures are only visible at the lower side of the aerofoil. Here, the vortices seem to lift up from the surface. The flow pattern from the boundary layer measurements on the upper side is not visible in the near wake region. It seems as if the vortices were weakened after passing the streamwise position of $x/c = 0.5$ and dissolved completely. This could be related to the adverse pressure gradient in this region. Anyway, the vortices on the pressure side seem to be very dominant over the whole chord of the aerofoil. Single boundary layer profiles are presented in Figure 80 and give a more detailed look on the near wake area. It can be seen that the profile at the tip of the aerofoil is shallower, not only compared to the root but also to the baseline. The profile at the root is showing the highest thickness which is related to the vortices. For the velocity components v and w (Figure 81 & Figure 82) again the root and this time the midpeak are the areas with the most spanwise and vertical flow, respectively. This underlines the assumption that the main flow at the tip position is flowing in u -direction and vortical structures are only present at the root and its surroundings.

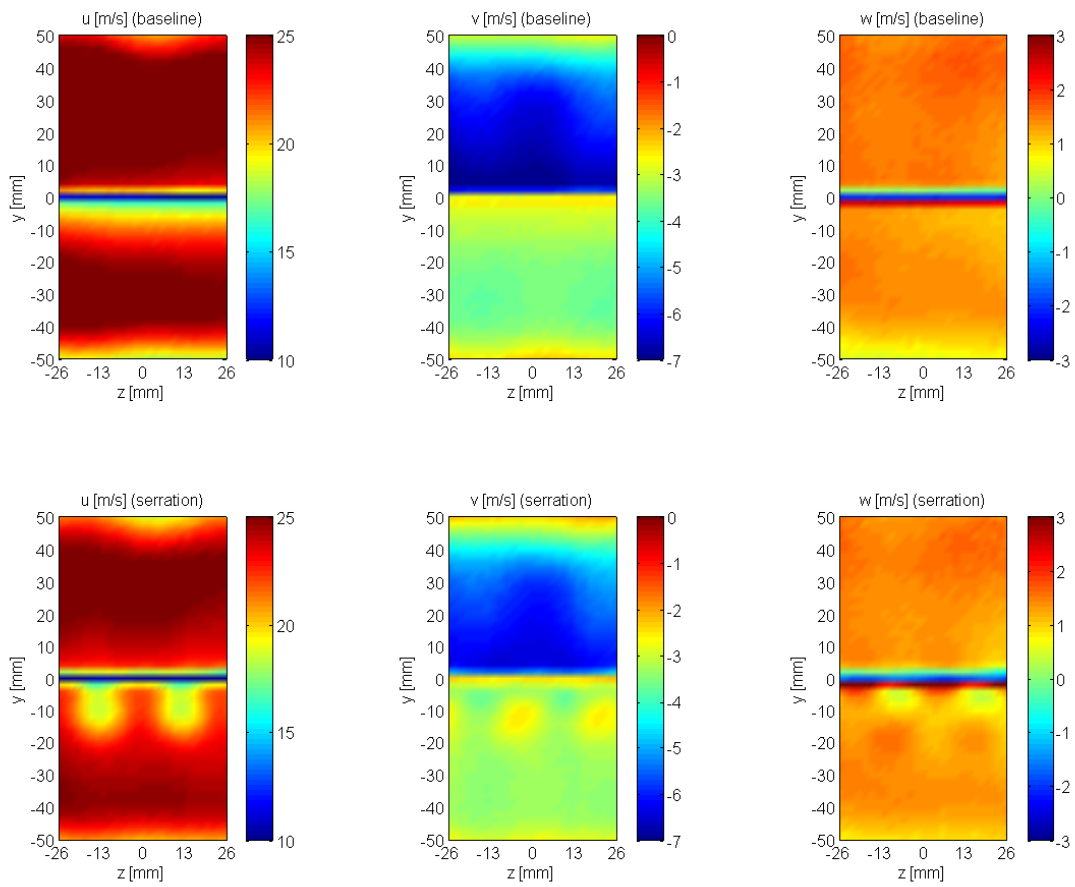


Figure 79: Velocity components u, v, w for the baseline vs. A45W26 at $x/c = 1.02$ in the wake of the aerofoil, $AoA = 0^\circ$, $Tu(u) = 5\%$, $U = 25\text{ms}^{-1}$

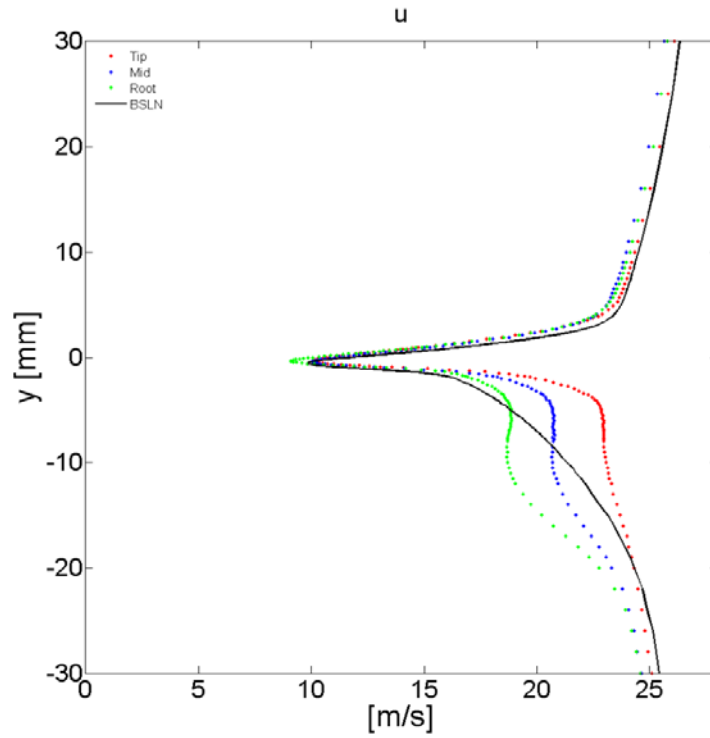


Figure 80: Boundary layer profile (u) for the baseline vs. A45W26. Comparison of the tip (red), mid (blue) and root (green) position at $x/c = 1.02$ in the wake of the aerofoil, $AoA = 0^\circ$, $Tu(u) = 5\%$, $U = 25\text{ms}^{-1}$

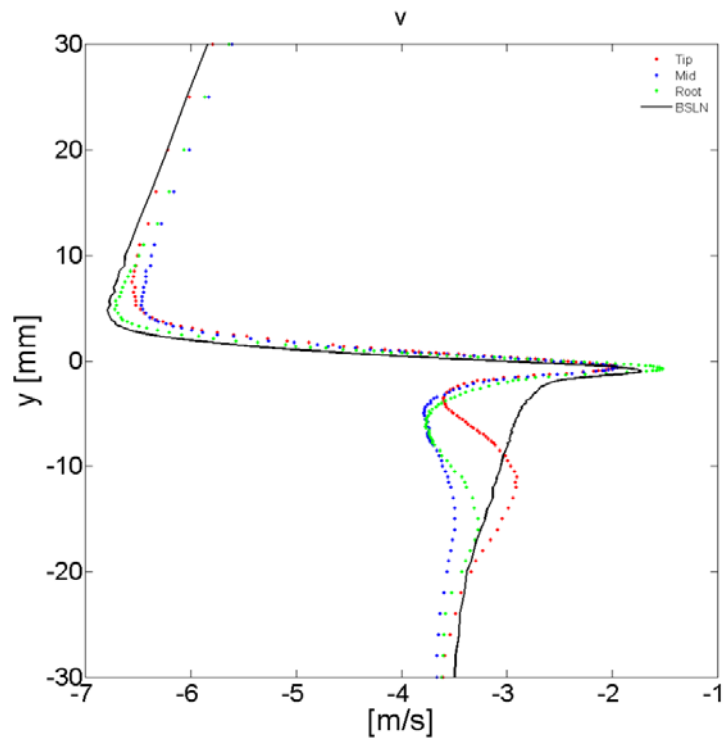


Figure 81: Boundary layer profile (v) for the baseline vs. A45W26. Comparison of the tip (red), mid (blue) and root (green) position at $x/c = 1.02$ in the wake of the aerofoil, $AoA = 0^\circ$, $Tu(u) = 5\%$, $U = 25\text{ms}^{-1}$

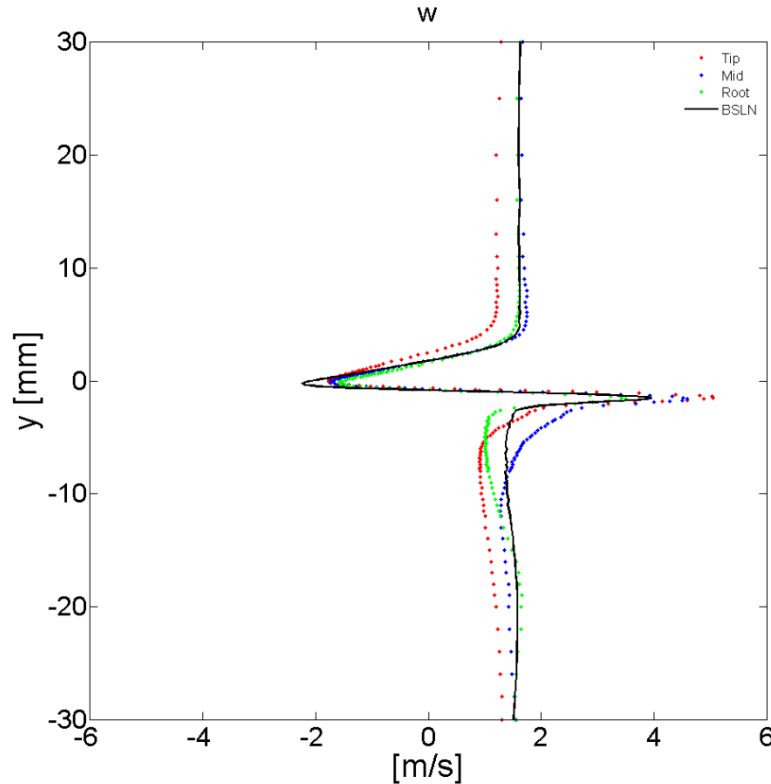


Figure 82: Boundary layer profile (w) for the baseline vs. A45W26. Comparison of the tip (red), mid (blue) and root (green) position at $x/c = 1.02$ in the wake of the aerofoil, $AoA = 0^\circ$, $Tu(u) = 5\%$, $U = 25\text{ms}^{-1}$

10.2 Turbulence intensity

Contour plots of the turbulence intensity for all three velocity components are presented in Figure 83. Similar to the boundary layer measurements on the pressure side of the aerofoil, turbulent structures for the undulated leading edge are only visible at the roots, whereas a high turbulence intensity of 10% (u) can be observed for the baseline over the whole span. It is noticeable that the turbulence is relatively low for the v component but shows a value of 8% for the fluctuating w velocity for the straight LE. Figure 84 presents the combined velocity fluctuations of $u'v'$ and $u'w'$. Especially the contour plot of $u'w'$ is interesting since it represents the mode of operation of the counter rotating vortices. Low speed flow from the near aerofoil surface is dragged to high speed and energised by the vortices. The single turbulence profiles underline this assumption and show that the turbulence increases from low (8%) to high (10 – 11%) in the root and midpeak region relatively far away from the surface, whereas the baseline has its highest value of 11% at $y = -5\text{ mm}$ (Figure 85). The components v and w show a similar behaviour

with the root and midpeak turbulence being the dominant factors (Figure 86 and Figure 87).

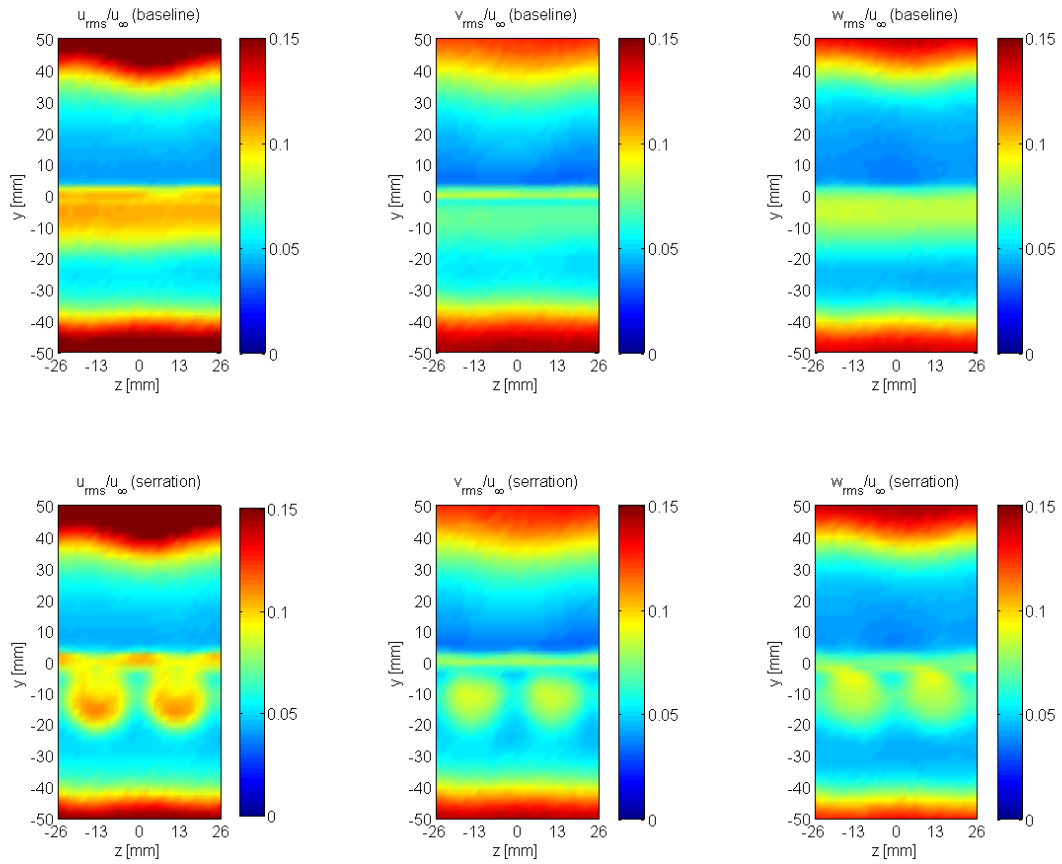


Figure 83: Tu profiles of u, v, w for the baseline vs. A45W26 at $x/c = 1.02$ in the wake of the airfoil, $AoA = 0^\circ$, $Tu(u) = 5\%$, $U = 25\text{ms}^{-1}$

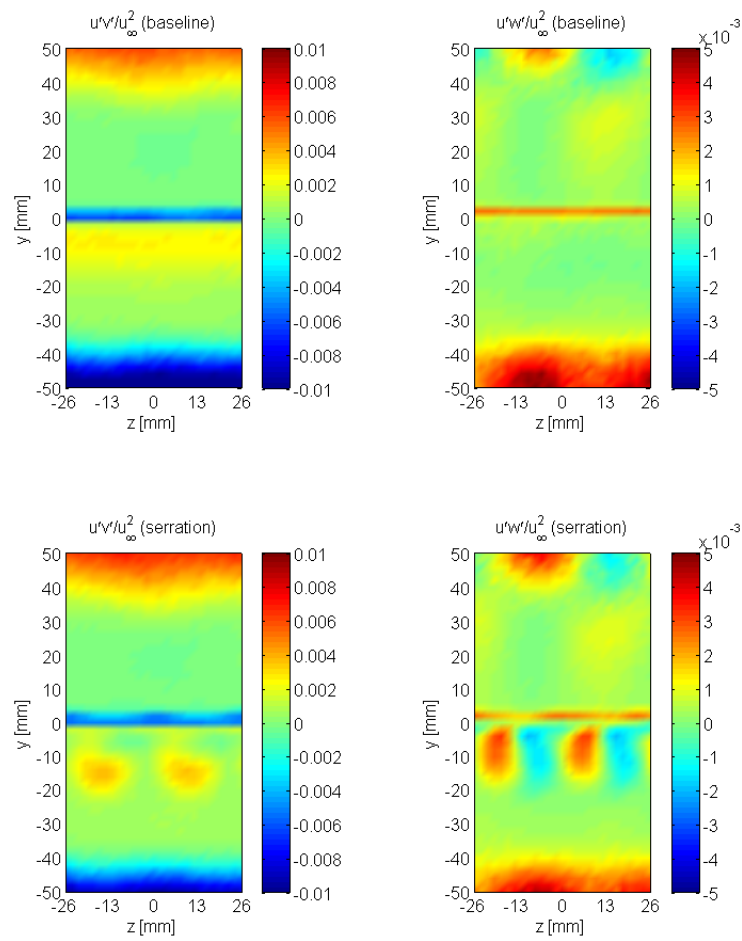


Figure 84: Tu fluctuations of $u'v'$ and $u'w'$ for the baseline vs. A45W26 at $x/c = 1.02$ in the wake of the aerofoil, $AoA = 0^\circ$, $Tu(u) = 5\%$, $U = 25\text{ms}^{-1}$

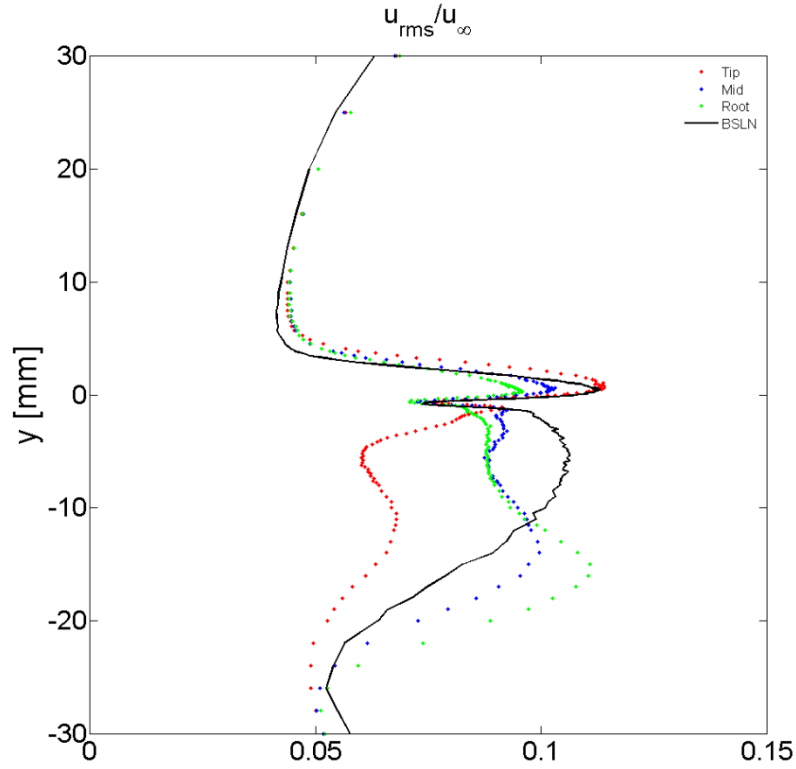


Figure 85: Tu profile (u_{rms}) for the baseline vs. A45W26. Comparison of the tip (red), mid (blue) and root (green) position at $x/c = 1.02$ in the wake of the aerofoil, $AoA = 0^\circ$, $Tu(u) = 5\%$, $U = 25\text{ms}^{-1}$

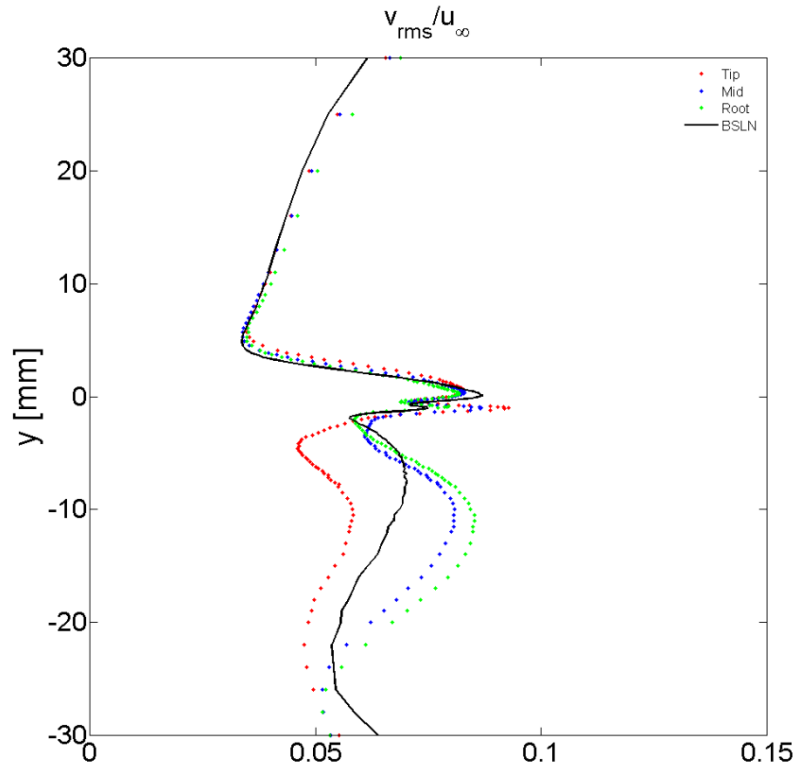


Figure 86: Tu profile (v_{rms}) for the baseline vs. A45W26. Comparison of the tip (red), mid (blue) and root (green) position at $x/c = 1.02$ in the wake of the aerofoil, $AoA = 0^\circ$, $Tu(u) = 5\%$, $U = 25\text{ms}^{-1}$

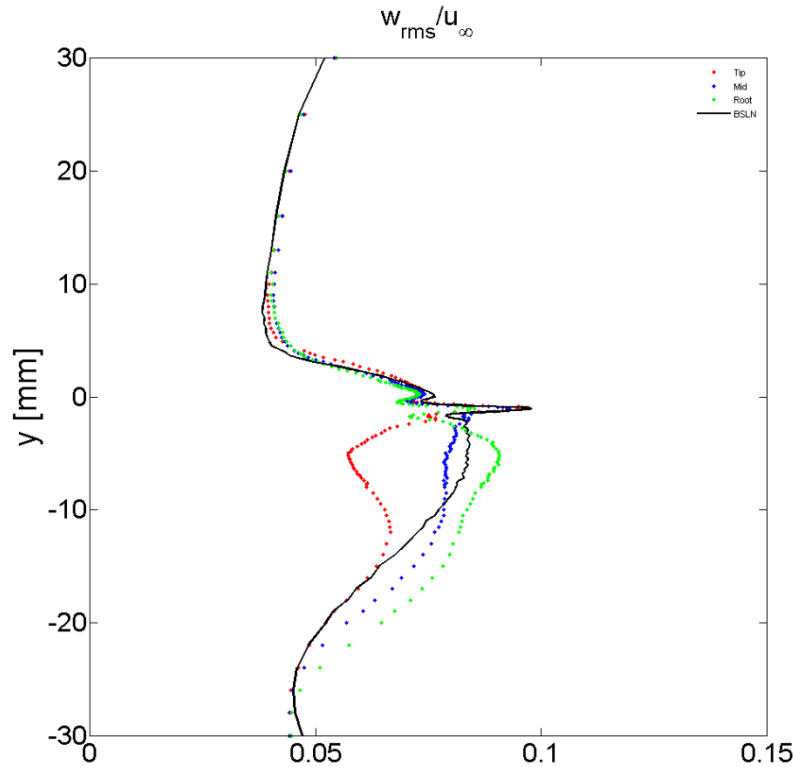


Figure 87: Tu profile (w_{rms}) for the baseline vs. A45W26. Comparison of the tip (red), mid (blue) and root (green) position at $x/c = 1.02$ in the wake of the aerofoil, $AoA = 0^\circ$, $Tu(u) = 5\%$, $U = 25\text{ms}^{-1}$

10.3 Spectral analysis

Three dimensional contour plots have been generated using isosurfaces to illustrate the turbulence fluctuations with respect to the leading edge geometry. Figure 88 shows the turbulence of the baseline leading edge at the streamwise position of $x/c = 1.02$ in the near wake for u' , u_1' , v' , w' , $u'v'$ and $u'w'$. The x-axis describes the spanwise positions ranging from -26 to 26 mm. The z-axis (*log scale*) presents the frequency and the y-axis (*log scale*) the measurement positions starting from the aerofoil surface. A colourbar helps to identify the magnitude of the fluctuations. Figure 89 presents the turbulence of the velocity components for the leading edge A45W26. It can be observed that the low frequency fluctuations can be reduced by the serration compared to the baseline for all velocity components. Solely, the turbulent structures of the counter-rotating vortices are very dominant. Furthermore, it is noticeable that the layer behind the trailing edge takes the form of a wave compared to the straight LE. It is assumed that this pattern results from the vortice structures on the suction side of the aerofoil and can be associated to the findings made by Hansen, et al. (2012) which were describe in Chapter 2.

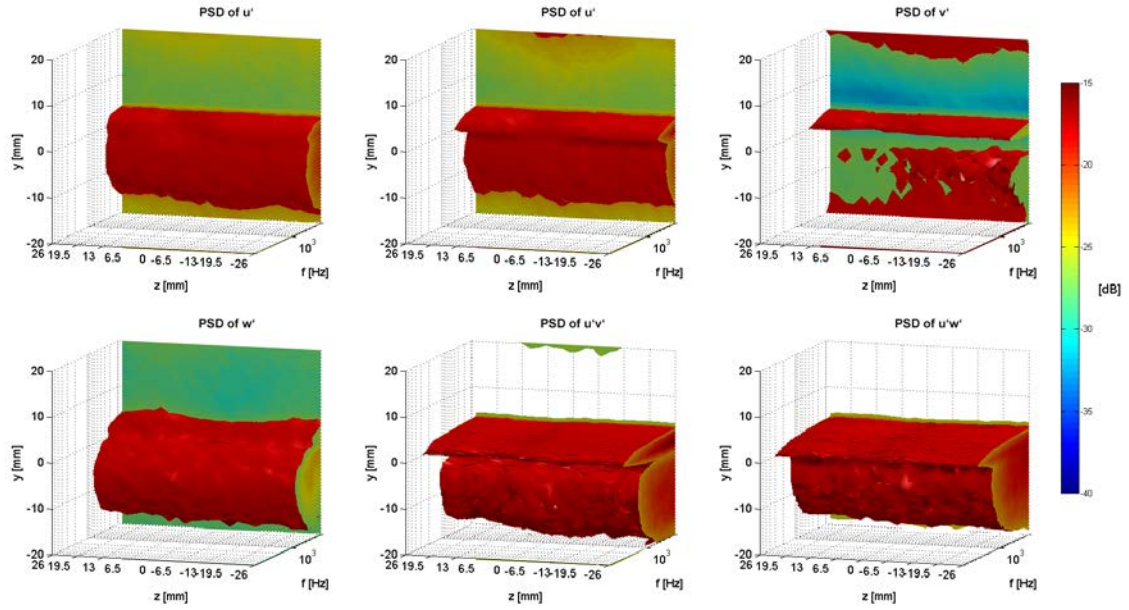


Figure 88: Comparison of PSD for u' , v' , w' , $u'v'$ and $u'w'$ for the baseline at $x/c = 1.02$ in the wake of the aerofoil, $AoA = 0^\circ$, $Tu(u) = 5\%$, $U = 25\text{ms}^{-1}$

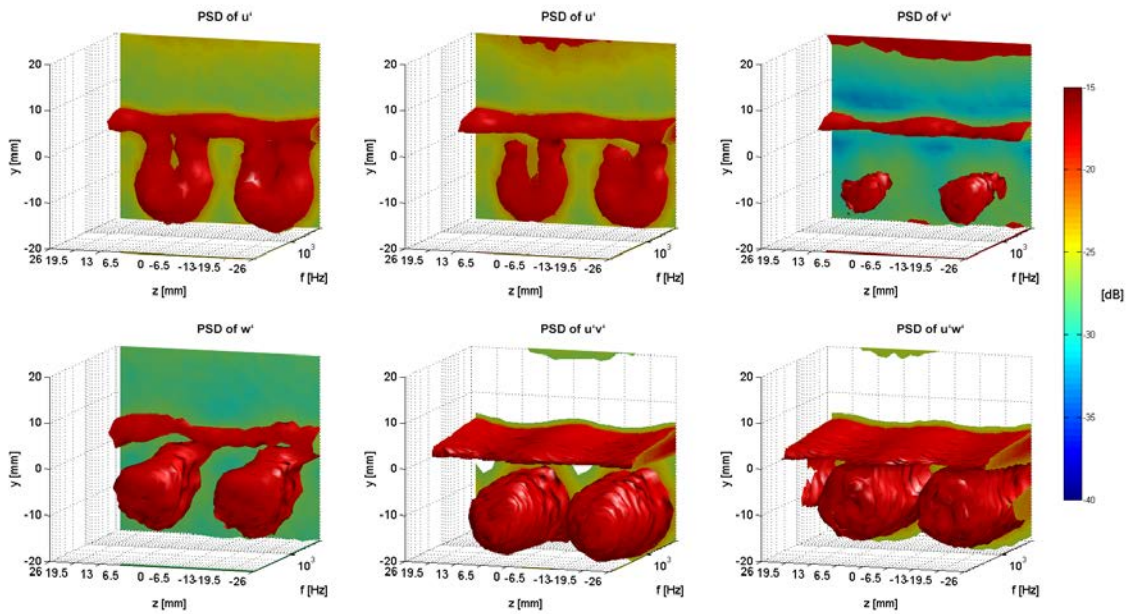


Figure 89: Comparison of PSD for u' , v' , w' , $u'v'$ and $u'w'$ for the A45W26 leading edge at $x/c = 1.02$ in the wake of the aerofoil, $AoA = 0^\circ$, $Tu(u) = 5\%$, $U = 25\text{ms}^{-1}$

11 Conclusion

This thesis presents results of a study on the application of leading edge undulations as a passive flow-control device for enhancing aerofoil performance and reducing AGI noise. The aim of this study was to describe the influence of serrated leading edges on aerofoil performance and on the streamwise flow pattern downstream of the serrated edges. Therefore an aerodynamic study was conducted where ten different leading edges of a NACA65(12)-10 aerofoil were tested in an open-circuit suction type wind tunnel to gain more information about the aerodynamic characteristics. It was found that the aerodynamic performance is mainly a function of amplitude and less sensitive to the serration wavelength. Small amplitudes can effectively delay the stall and thus considerably improve the aerodynamic performance. Boundary layer measurements have been conducted on the pressure side and on the suction side of the aerofoil. Two different serrated leading edges and the baseline were tested. The first leading edge is characterised by superior aerodynamic performance and is defined by an amplitude of 12 mm and a wavelength of 26 mm. The second leading edge stands out when it comes to the reduction of aerofoil-gust-interaction noise (AGI) where the free stream turbulence interacts with the aerofoil leading edge what leads to broadband noise radiation and is defined by an amplitude of 45 mm and a wavelength of 26 mm. The results of the boundary layer measurements show, that solely the serrated leading edge with the large amplitude has a remarkable impact on the flow pattern in the serration and downstream of the leading edge. It can be observed that the turbulence intensity is reduced by 1 - 2% in the interstices of the serration. Contour plots and three dimensional illustrations have shown that streamwise vortices emanate from the roots of the leading edge on the suction side and propagate to the spanwise position of the undulation peaks while approaching the trailing edge. On the pressure side of the aerofoil even more dominant counter-rotating vortices could be visualised. These vortices managed to achieve a massive reduction in low frequency velocity fluctuations. Measurements in the near wake of the aerofoil showed the structure of the counter-rotating vortices. It was possible to illustrate the single velocity components of these vortices and get an understanding of the mode of operation. The ability of these flow structures to reduce tonal noise at the trailing edge is left for future work.

References

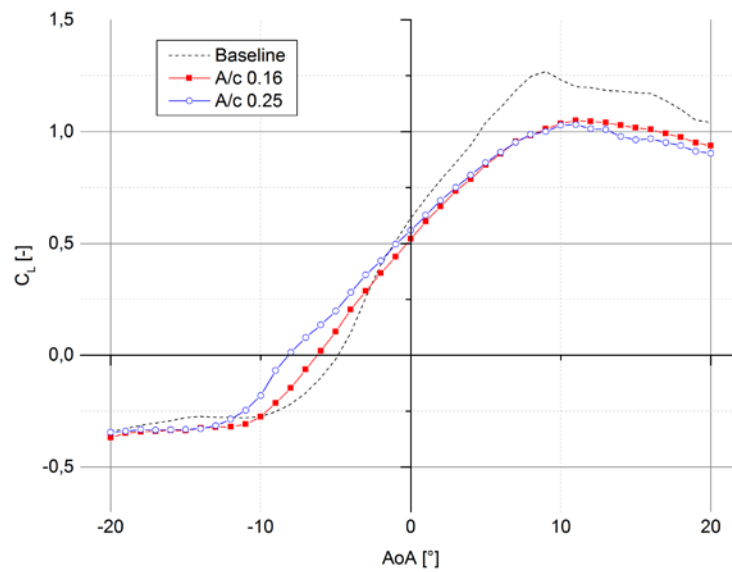
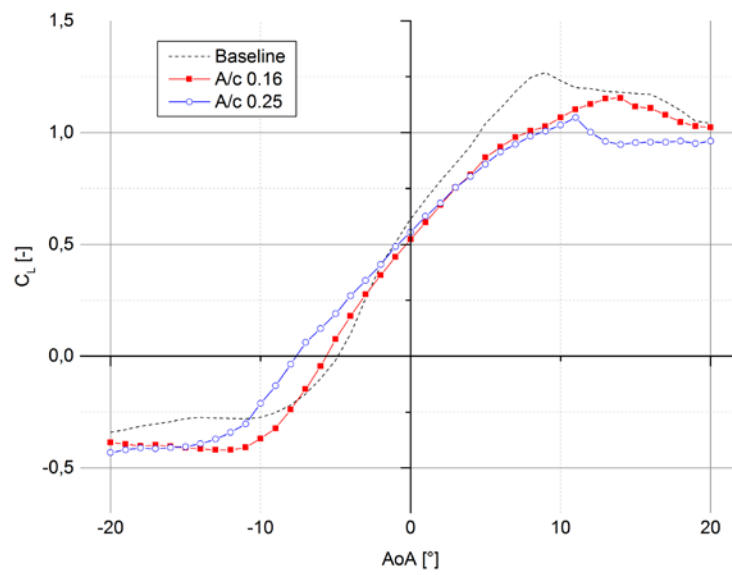
- Abbot, I. H., von Doenhoff, A. E. & Stevers Jr., L. S., 1945. *Summary Of Airfoil Data, Report No. 824*, Langley: NACA.
- Abbott, I. H. & Von Doenhoff, A. E., 1949. *THEORY OF WING SECTIONS*. New York: Dover Publications, Inc..
- ACARE, 2015. *Annual Report, Activity Summary 2014-15*, s.l.: Advisory Council for Aviation Research and Innovation in Europe.
- Amiet, R. K., 1975. *ACOUSTIC RADIATION FROM AN AIRFOIL IN A TURBULENT STREAM*, USA: J. Sound Vib. 41, 407-420.
- Arndt, R. E. A. & Nagel, R. T., 1972. *Effect of leading edge serrations on noise radiation from a model rotor*, s.l.: AIAA J. 72-655.
- Atassi, H. M., Subramaniam, S. & Scott, J. R., 1972. *Acoustic radiation from lifting airfoils in compressible subsonic flow*, s.l.: AIAA J. 72-655.
- Biedermann, T., 2015. *Aerofoil noise subjected to leading edge serration*, Duesseldorf: University of Applied Sciences Duesseldorf / Brunel University London.
- Biedermann, T., Chong, T. P. & Kameier, F., 2016. *Satistical-Empirical Modelling of Aerofoil Noise Subjected to Leading Edge Serrations and Aerodynamic Identification of Noise Reduction Mechanisms*, Lyon, France: 22nd AIAA/CEAS Aeroacoustics Conference .
- Brooks, T., Pope, D. & Marcolini, M., 1989. *Airfoil self-noise and prediction*, Washington, D.C.: National Aeronautics and Space Administration, Office of Management, Scientific and Technical Information Division.
- Bruun, H., 2002. *Hot-wire anemometry : principles and signal analysis*. New York: Oxford University Press, Oxford.
- Camara, J. F., 2013. *Numerical Study on the Use of a Sinusoidal Leading Edge for Passive Stall Control at Low Reynolds Number*, s.l.: s.n.
- Chong, T. P. et al., 2015. *Aeroacoustic and Aerodynamic Performances of an Aerofoil Subjected to Sinusoidal Leading Edges*. Dallas, Texas: 21st AIAA/CEAS Aeroacoustics Conference (22 - 26 June 2015).

-
- Chong, T. P. et al., 2015. *Aeroacoustic and Aerodynamic Performances of an Aerofoil Subjected to Sinusoidal Leading Edges*, Dallas, TX: AIAA Aviation 22-26 June 21st AIAA/CEAS Aeroacoustics Conference.
- Clair, V. et al., 2013. *Experimental and numerical investigation of turbulence-airfoil noise reduction using wavy edges*, s.l.: AIAA J. 51(11), 2695-2713.
- Crites R., S. F. J., 1995. *Wall Interference Reduction Methods for Subsonic Wind Tunnels*, Reno, NV: 33rd Aerospace Sciences Meeting and Exhibit.
- Dantec Dynamics, n.d. *Probes for Hot-wire Anemometry*, DENMARK: Dantec Dynamics A/S Nova Instruments.
- European Commission, 2011. *Flightpath 2050. Europe's Vision for Aviation*, Luxembourg: Report of the High Level Group on Aviation Research, Publications Office of the European Union.
- European Commission, 2012. *Research & Innovation Transport ACARE Goals Progress Evaluation*. [Online]
Available at: http://ec.europa.eu/research/transport/projects/items/agape_en.htm
[Accessed 12 07 2016].
- Fish, F. E. & Battle, J. M., 1995. *Hydrodynamic Design of the Humpback Whale Flipper*, s.l.: Journal of Morphology Vol. 225, No. 1.
- Fish, F. E., Weber, P. W., Murray, M. M. & Howle, L. E., 2011. *The Tubercles on Humpback Whales' Flippers: Application of Bio-Inspired Technology*, Salt Lake City, Utah: Integrative and Comparative Biology, volume 51, number 1, pp. 203-213.
- Geyer, T., Sarradj, E. & Fritzsche, C., 2014. *Measuring owl flight noise*, Melbourne: inter.noise.
- Glauert, H., 1933. *Wind Tunnel Interference on Wings, Bodies and Airscrews*, London: ARC R&M 1566.
- Goldstein, M. E., 1978. *Unsteady vertical and entropic distortions of potential flows around arbitrary obstacles*, s.l.: J. Fluid Mech. 89, 433-468.
- Graham, R., 1934. *The silent flight of owls*, s.l.: J Roy Aero Soc, 38:837-843.
- Gruber, M., 2012. *Airfoil noise reduction by edge treatments*, Ph.D. Dissertation, University of Southampton, Faculty of Engineering and the Environment : Institute of Sound and Vibration Research, Southampton, UK.

-
- Haeri, S., Kim, J. W., Narayanan, S. & Joseph, P., 2014. *3D calculations of aerofoil-turbulence interaction noise and the effect of wavy leading edges*, AIAA, Atlanta, GA: 20th AIAA/CEAS Aeroacoustics Conference, 16-20 June 2014.
- Hansen, K., Kelso, R. & Doolan, C., 2012. *Reduction of flow induced airfoil tonal noise using leading edge sinusoidal modifications*, Australia: Acoust. Australia 40(3), 172-177.
- Hansen, K. L., Kelso, R. M. & Dally, B. D., 2011. *Performance variations of leading-edge tubercles for distinct airfoil profiles*, s.l.: AIAA J. 49, 185-194.
- Hersh, A. S., Soderman, P. T. & Hayden, R. E., 1974. *Investigation of acoustic effects of leading edge serrations on airfoils*, s.l.: J. Aircr. 11(4), 197-202.
- Ito, S., 2009. *Aerodynamic influence of leading-edge serrations on an airfoil in a low Reynolds number - a study of an owl wing with leading edge serrations*, s.l.: J. Biomech. Sci. Eng. vol 4(1), 117-123.
- Johari, H., Henoch, C., Custodio, D. & Levshin, L., 2007. *Effects of leading-edge protuberances on airfoil performance*, s.l.: AIAA J. 45, 2634-2642.
- Jørgensen, F. E., 2002. *How to measure turbulence with hot-wire anemometers - a practical guide*. Publication no.: 9040U6151 ed. Skovlunde, Denmark: Dantec Dynamics.
- Kim, J. W., Haeri, S. & Joseph, P. F., 2016. *On the reduction of aerofoil-turbulence interaction noise associated with wavy leading edges*, s.l.: J. Fluid Mech. 792 (2016) 526-552.
- Lau, A. S., Haeri, S. & Kim, J.-W., 2013. *The effect of wavy leading edges on aerofoil-gust interaction noise*, s.l.: Journal of Sound and Vibration, Vol. 332.
- Laws, E. M. & Livesey, J. L., 1978. *FLOW THROUGH SCREENS*, England: Department of Aeronautical and Mechanical Engineering, University of Salford, In: Annu.Rev.Fluid Mech. 1978.10:247-266.
- Longhouse, R. E., 1977. *Vortex shedding noise of low tip speed, axial flow fans*, s.l.: J. Sound Vib. 53, 25-46.
- McEwen, A., 2015. *Aerofoil Noise Reduction By Leading Edge Tubercles*, London, UK: Department of Mechanical, Aerospace and Civil Engineering, Brunel University.
- Migliore, P. & Oerlemans, S., 2004. *Wind tunnel aeroacoustic tests of six airfoils for use on small wind turbines*, s.l.: J. Sol. Energy Eng. 126, 974-985.

-
- Narayanan, S. et al., 2015. *Airfoil noise reductions through leading edge serrations*, s.l.: Physics of fluids 27, 025109.
- Oerlemans, S., 2011. *Wind turbine noise: primary noise sources*, s.l.: National Aerospace Laboratory NLR.
- Perry, A. E., 1982. *Hot-Wire Anemometry*. Oxford: Oxford University Press.
- Plint & Partners LTD Engineers, 1986. *Operating Instructions TE.81/D*, s.l.: PLINT.
- Schade, H. & Kunz, E., 2007. *Strömungslehre 3., neu bearbeitete Auflage*. Berlin, Germany: Walter de Gruyter.
- Schlichting, H., Gersten, K., Krause, E. & Oertel Jr., H., 2006. *Grenzschicht-Theorie*. 10., überarbeitete Auflage ed. Berlin: Springer.
- Schmitt, O. H., 1969. *Some interesting and useful biomimetic transforms*. Proc. 3rd Int. Biophysics Congress, Boston, MA: p. 297.
- Schreiber, D., 2017. *Aerodynamische Untersuchung eines NACA 65-(12)10 mit Leading Edge Serrations unter Verwendung numerischer Methoden*, Düsseldorf: s.n.
- Skillen, A. & Revell, A., 2015. *Flow over a Wing with Leading-Edge Undulations*, s.l.: AIAA Journal Vol. 53 (2).
- Skillen, A. et al., 2014. *Flow over a wing with leading-edge undulations*, s.l.: AIAA J. 53 (2), 464-472.
- Sonderman, P. T., 1974. *Leading edge serrations which reduce the noise of low-speed rotors, NASA technical note*, s.l.: Report No. NASA TN D-7371.
- Vathylakis, A., Kim, J. H. & Chong, T. P., 2014. *Design of a low-noise aeroacoustic wind tunnel facility at Brunel University*, School of Engineering and Design, Brunel University, London, UK: AIAA Aviation.

Appendix A – Aerodynamic measurements

Figure 90: Lift coefficient vs. AoA for $\lambda/c=0.12$ varying the serration amplitude at $Re = 1.0 \times 10^5$ Figure 91: Lift coefficient vs. AoA for $\lambda/c=0.23$ varying the serration amplitude at $Re = 1.0 \times 10^5$

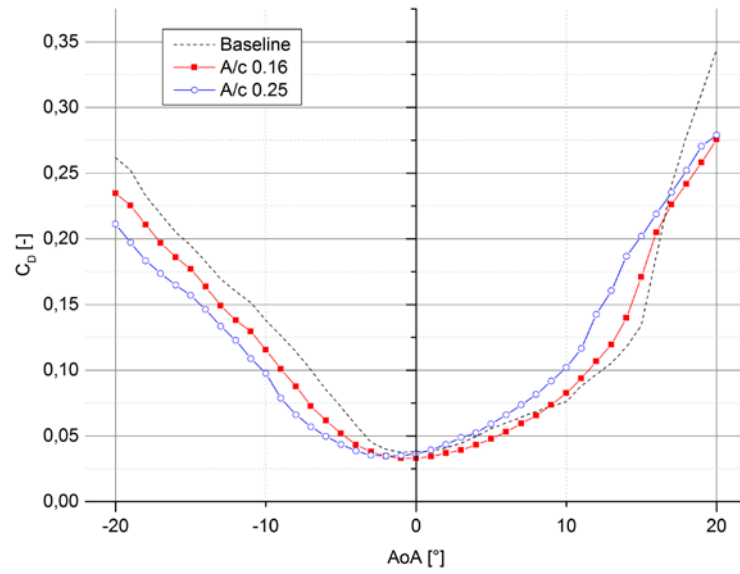


Figure 92: Drag coefficient vs. AoA for $\lambda/c=0.12$ varying the serration amplitude at $Re = 1.0 \times 10^5$

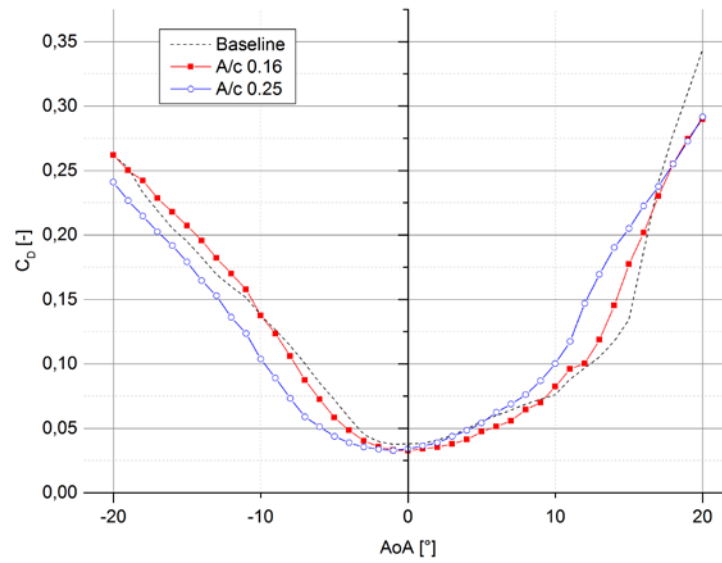


Figure 93: Drag coefficient vs. AoA for $\lambda/c=0.23$ varying the serration amplitude at $Re = 1.0 \times 10^5$

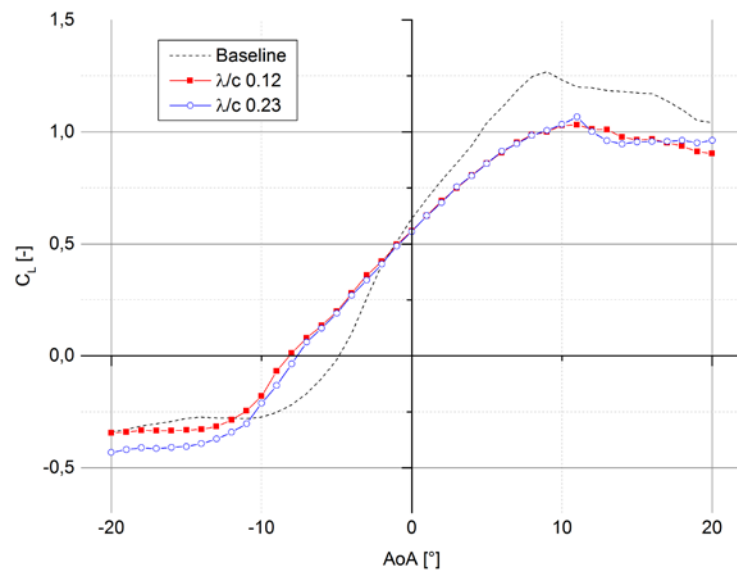


Figure 94: Lift coefficient vs. AoA for $A/c=0.25$ varying the serration wavelength at $Re = 1.0 \times 10^5$

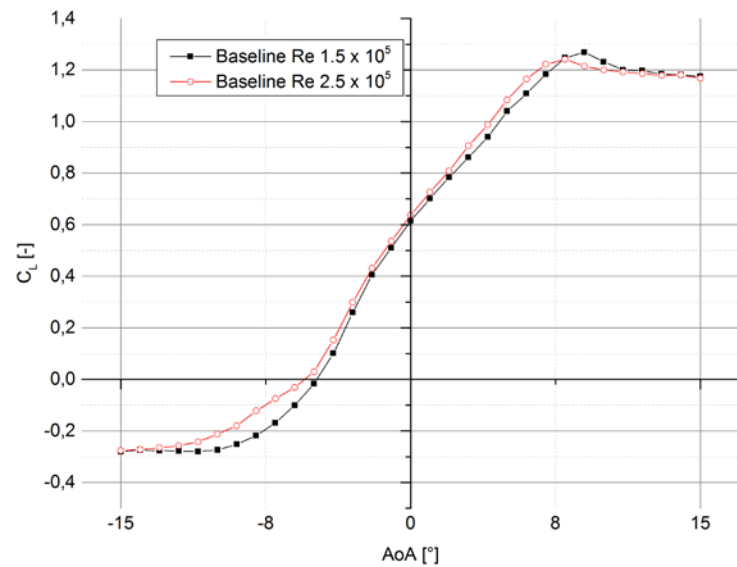


Figure 95: Lift coefficient vs. AoA for the baseline LE varying the Reynolds number

Appendix B – Boundary layer measurements

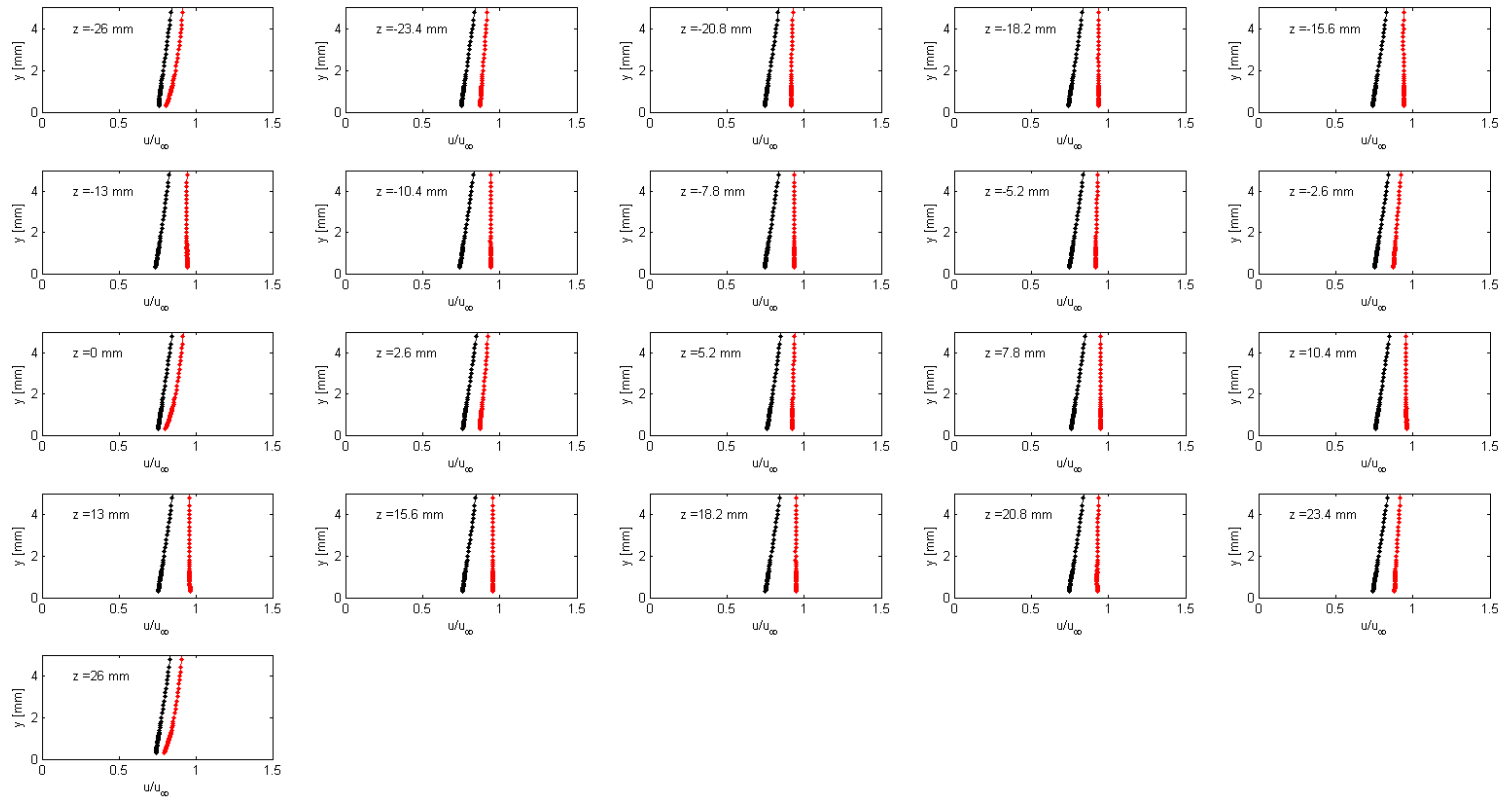


Figure 96: Boundary layer profiles baseline (black) vs. A45W26 (red) in spanwise direction (z) with 2.6 mm intervals at $x/c = 0.04$ for the suction side where the initial reading is performed at the tip of the sinusoidal leading edge, $\text{AoA} = 0^\circ$, $Tu = 5\%$, $U = 25\text{ms}^{-1}$

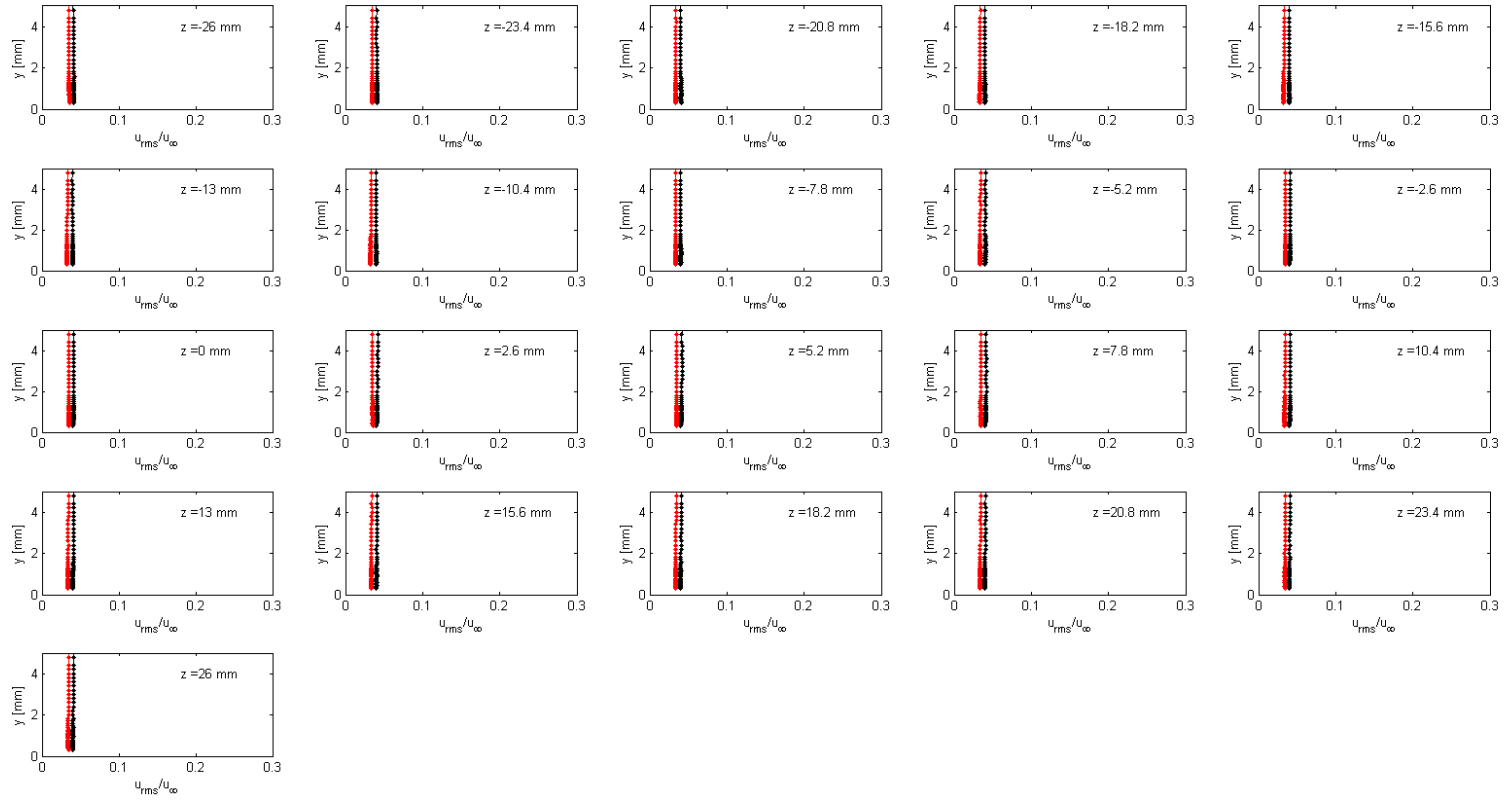


Figure 97: Tu profiles baseline (black) vs. A45W26 (red) in spanwise direction (z) with 2.6 mm intervals at $x/c = 0.04$ for the suction side where the initial reading is performed at the tip of the sinusoidal leading edge, $AoA = 0^\circ$, $Tu = 5\%$, $U = 25\text{ms}^{-1}$

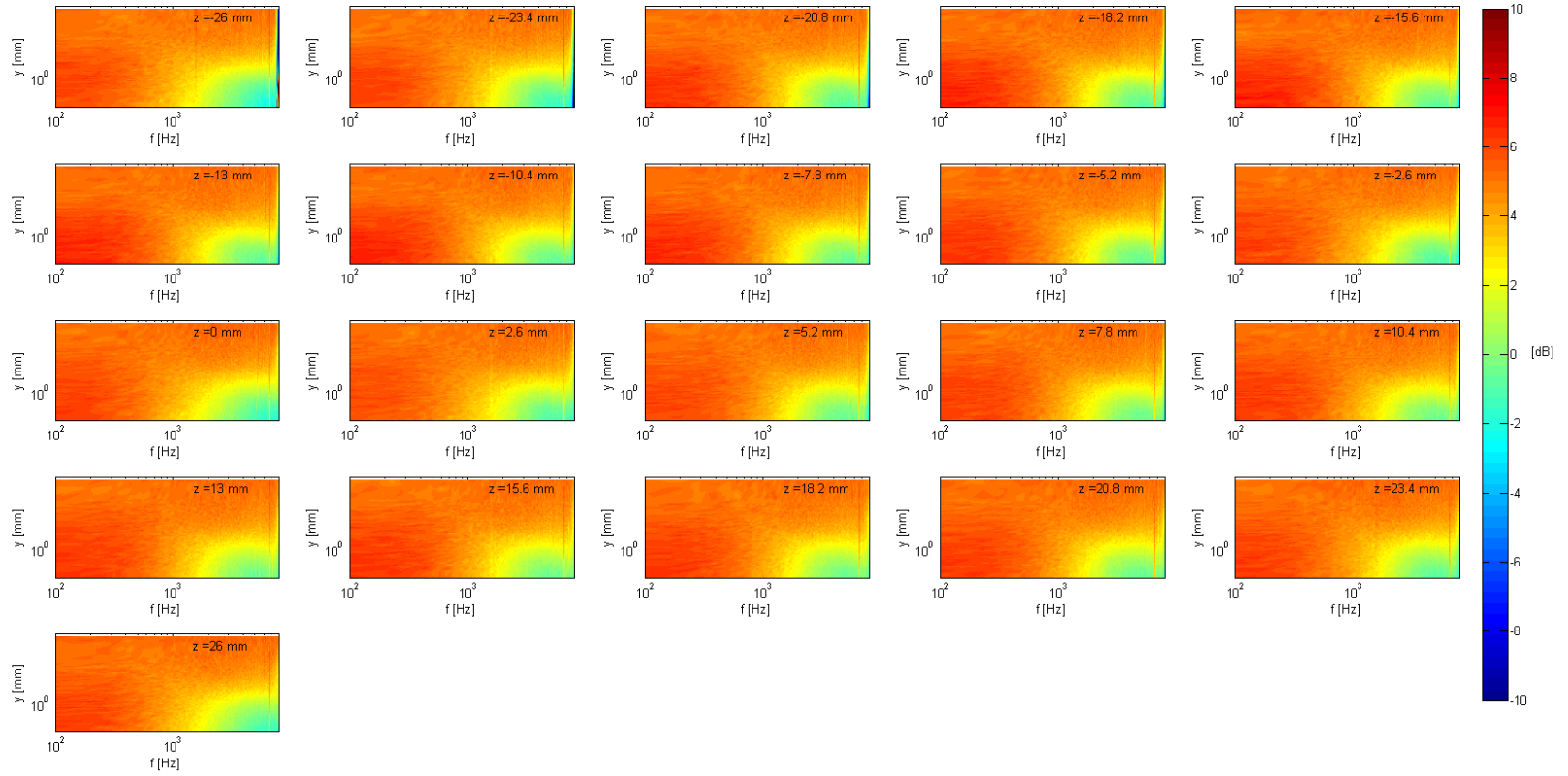


Figure 98: Contour plots of the delta in turbulence fluctuations between the baseline and A45W26 in spanwise direction (z) with 2.6 mm intervals at $x/c = 0.04$ for the suction side where the initial reading is performed at the tip of the sinusoidal leading edge, $AoA = 0^\circ$, $Tu = 5\%$, $U = 25\text{ms}^{-1}$

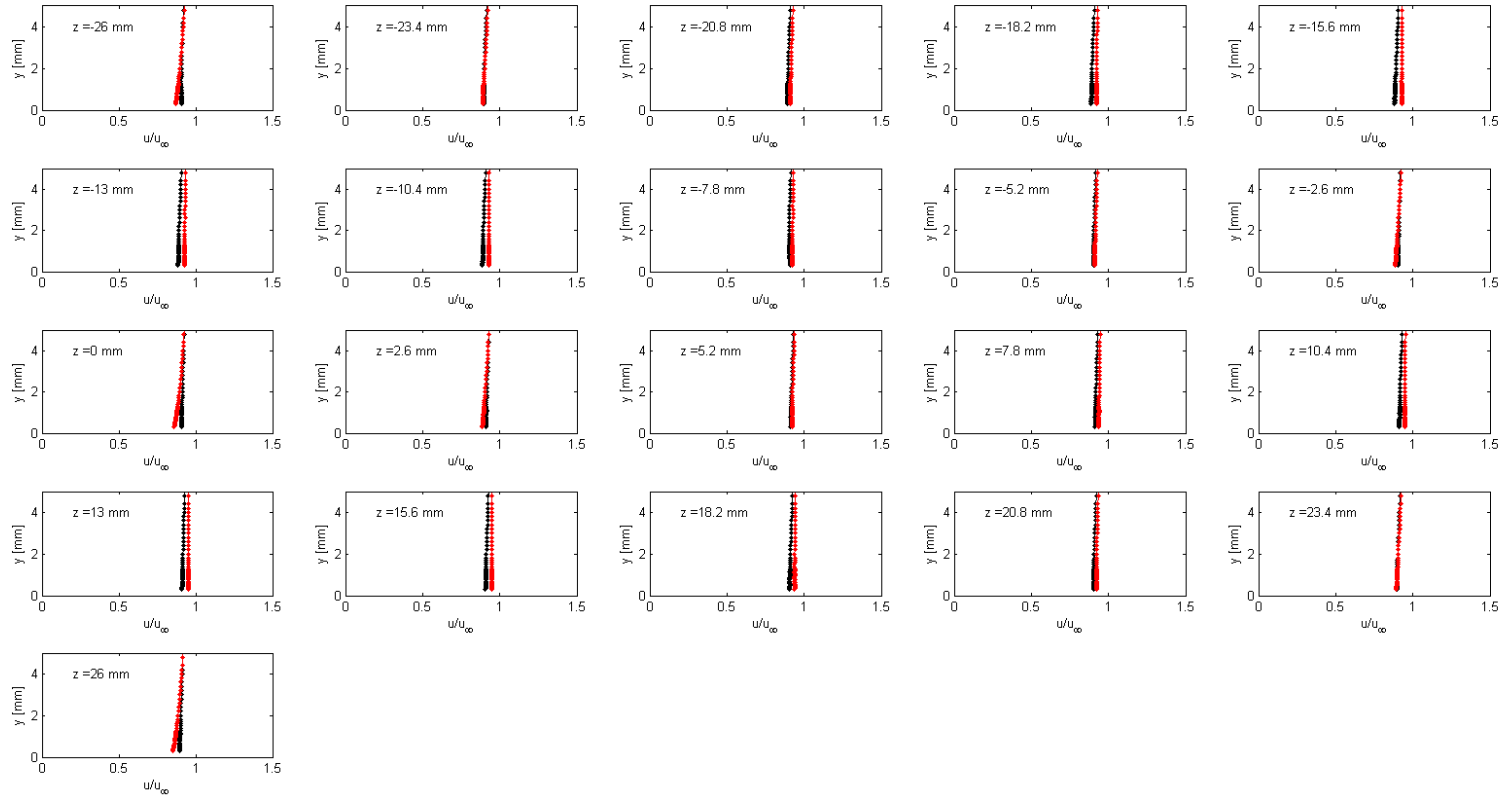


Figure 99: Boundary layer profiles baseline (black) vs. A45W26 (red) in spanwise direction (z) with 2.6 mm intervals at $x/c = 0.08$ for the suction side where the initial reading is performed at the tip of the sinusoidal leading edge, $AoA = 0^\circ$, $Tu = 5\%$, $U = 25\text{ms}^{-1}$

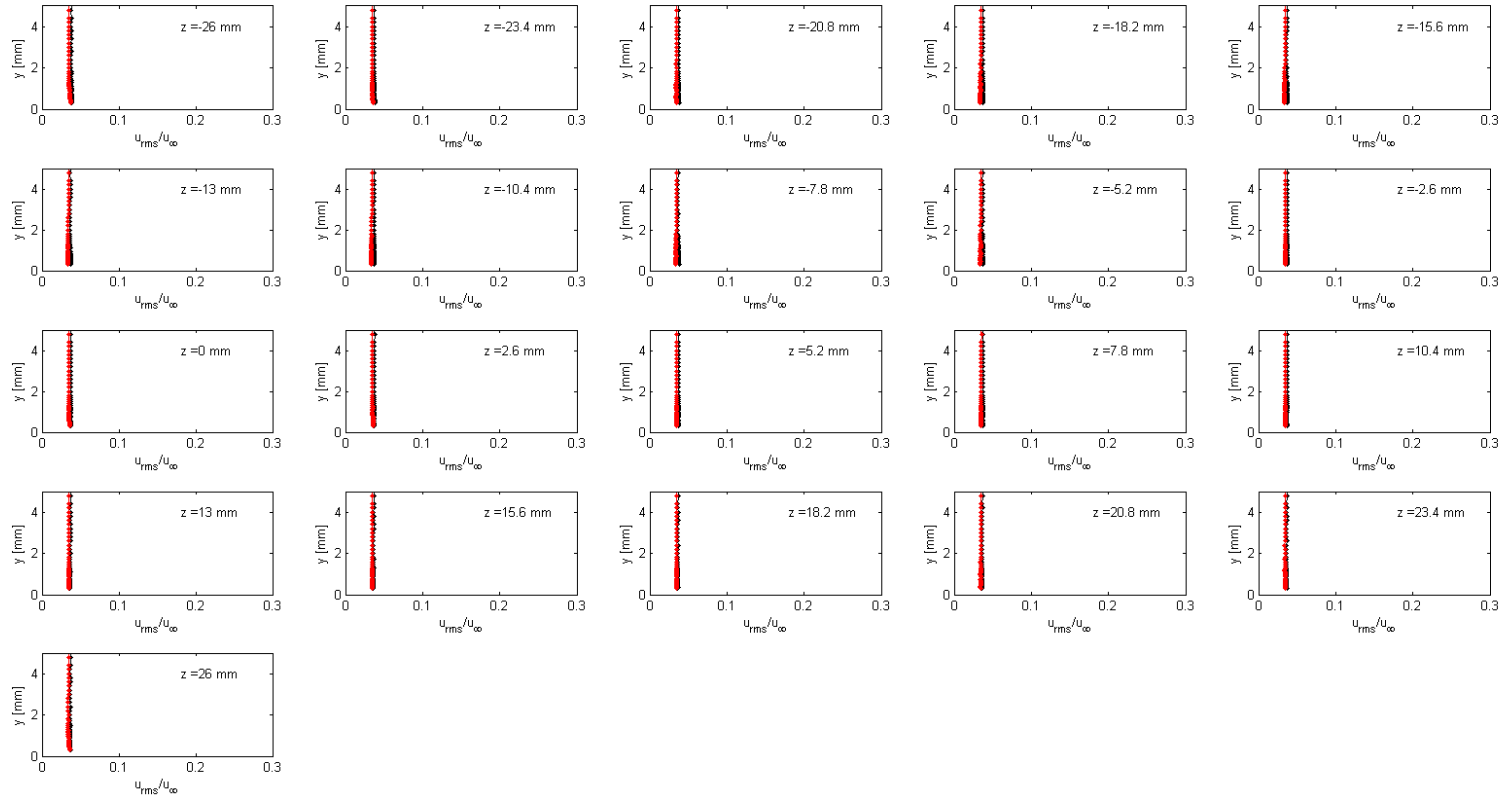


Figure 100: Tu profiles baseline (black) vs. A45W26 (red) in spanwise direction (z) with 2.6 mm intervals at $x/c = 0.08$ for the suction side where the initial reading is performed at the tip of the sinusoidal leading edge, $AoA = 0^\circ$, $Tu = 5\%$, $U = 25\text{ms}^{-1}$

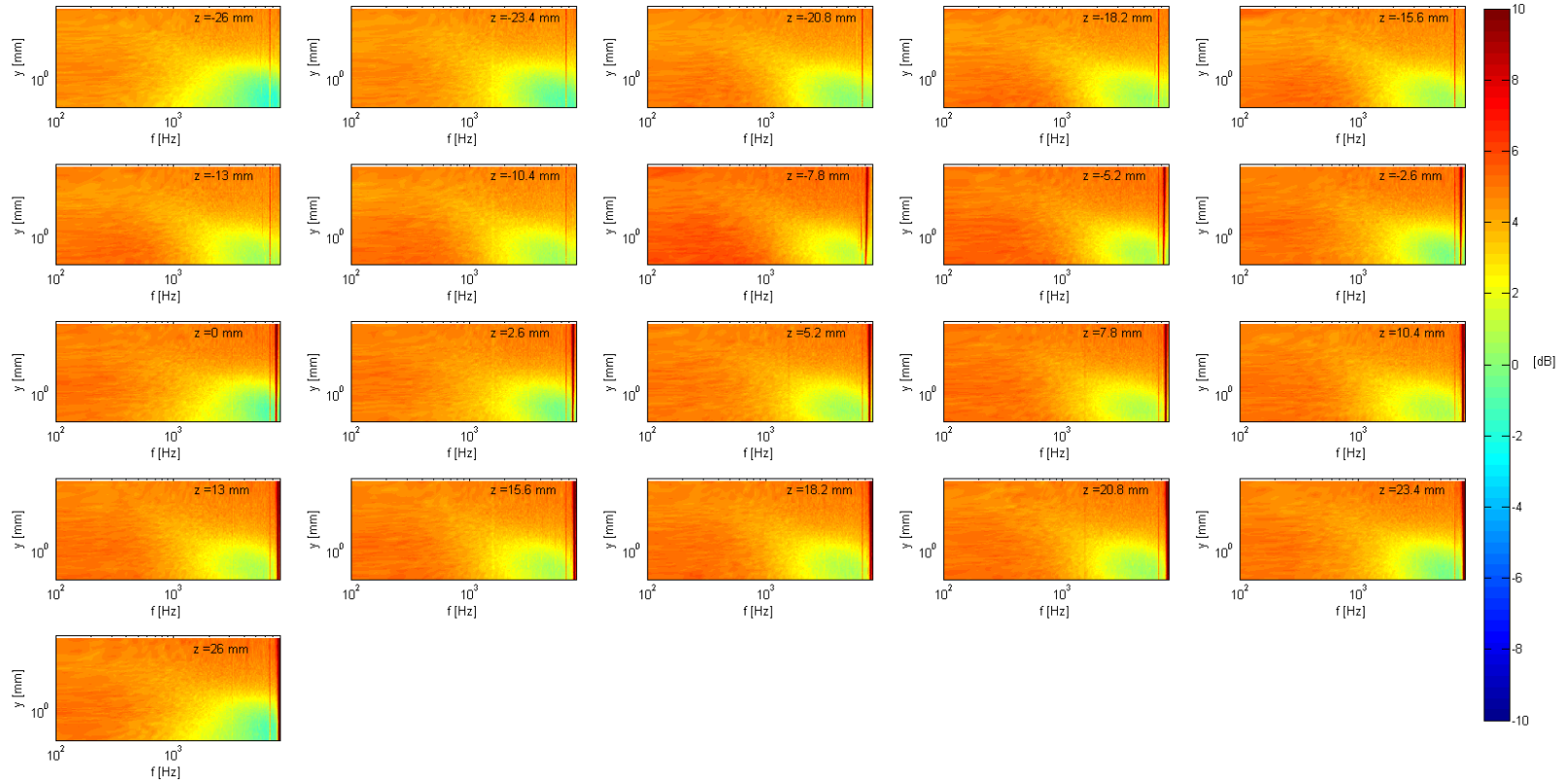


Figure 101: Contour plots of the delta in turbulence fluctuations between the baseline and A45W26 in spanwise direction (z) with 2.6 mm intervals at $x/c = 0.08$ for the suction side where the initial reading is performed at the tip of the sinusoidal leading edge, $AoA = 0^\circ$, $Tu = 5\%$, $U = 25\text{ms}^{-1}$

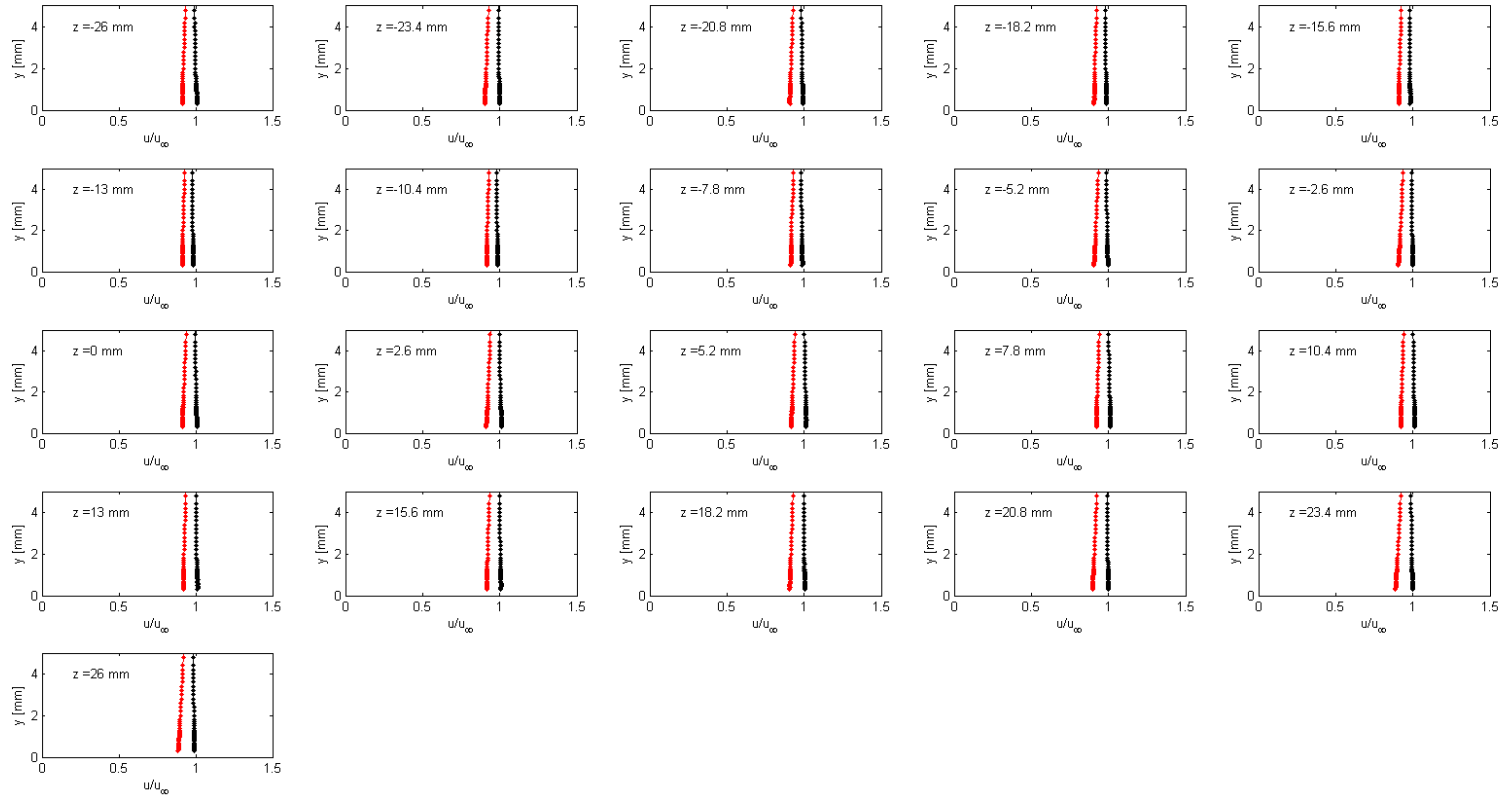


Figure 102: Boundary layer profiles baseline (black) vs. A45W26 (red) in spanwise direction (z) with 2.6 mm intervals at $x/c = 0.15$ for the suction side where the initial reading is performed at the tip of the sinusoidal leading edge, $AoA = 0^\circ$, $Tu = 5\%$, $U = 25\text{ms}^{-1}$

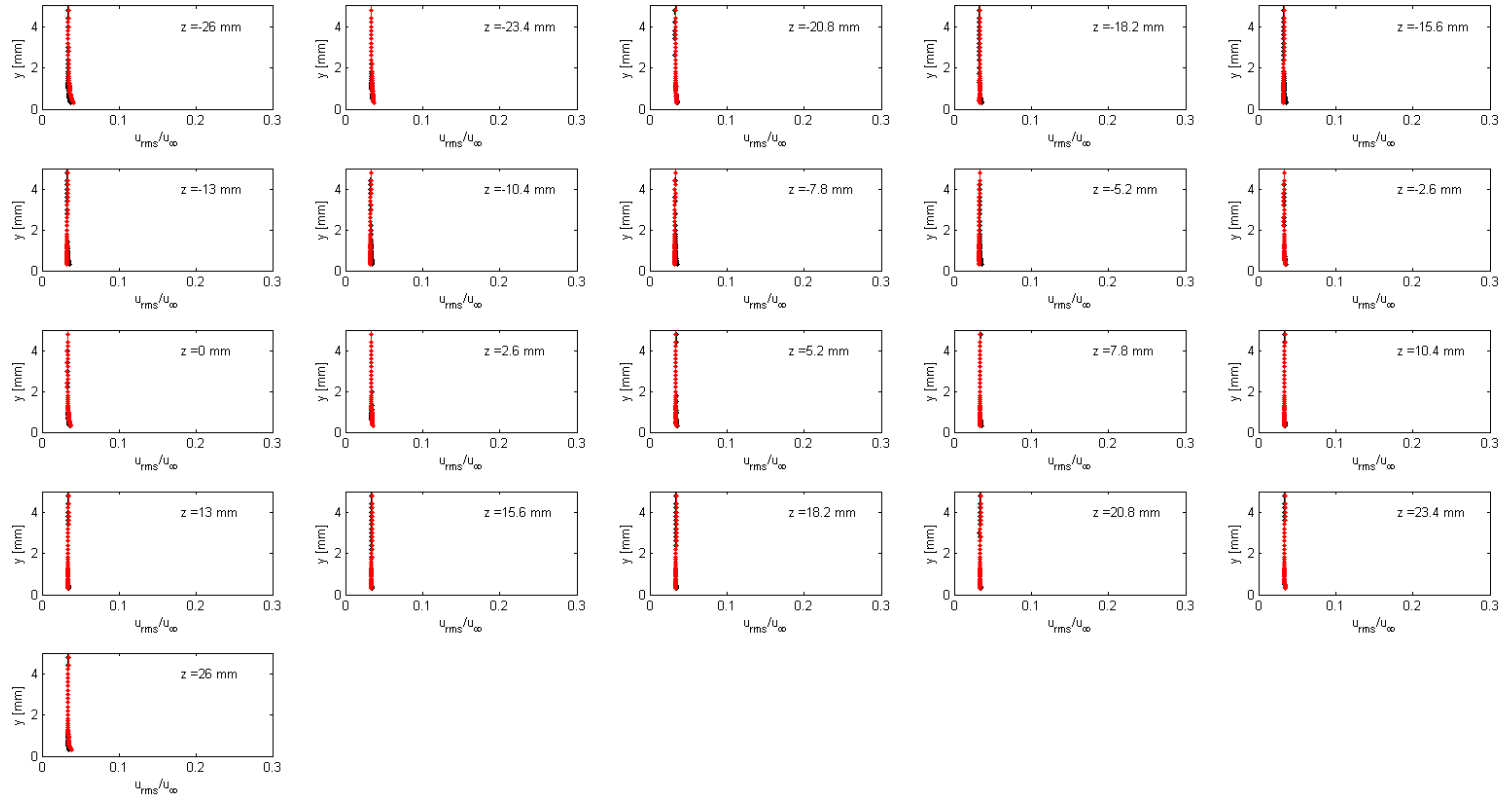


Figure 103: Tu profiles baseline (black) vs. A45W26 (red) in spanwise direction (z) with 2.6 mm intervals at $x/c = 0.15$ for the suction side where the initial reading is performed at the tip of the sinusoidal leading edge, $\text{AoA} = 0^\circ$, $Tu = 5\%$, $U = 25\text{ms}^{-1}$

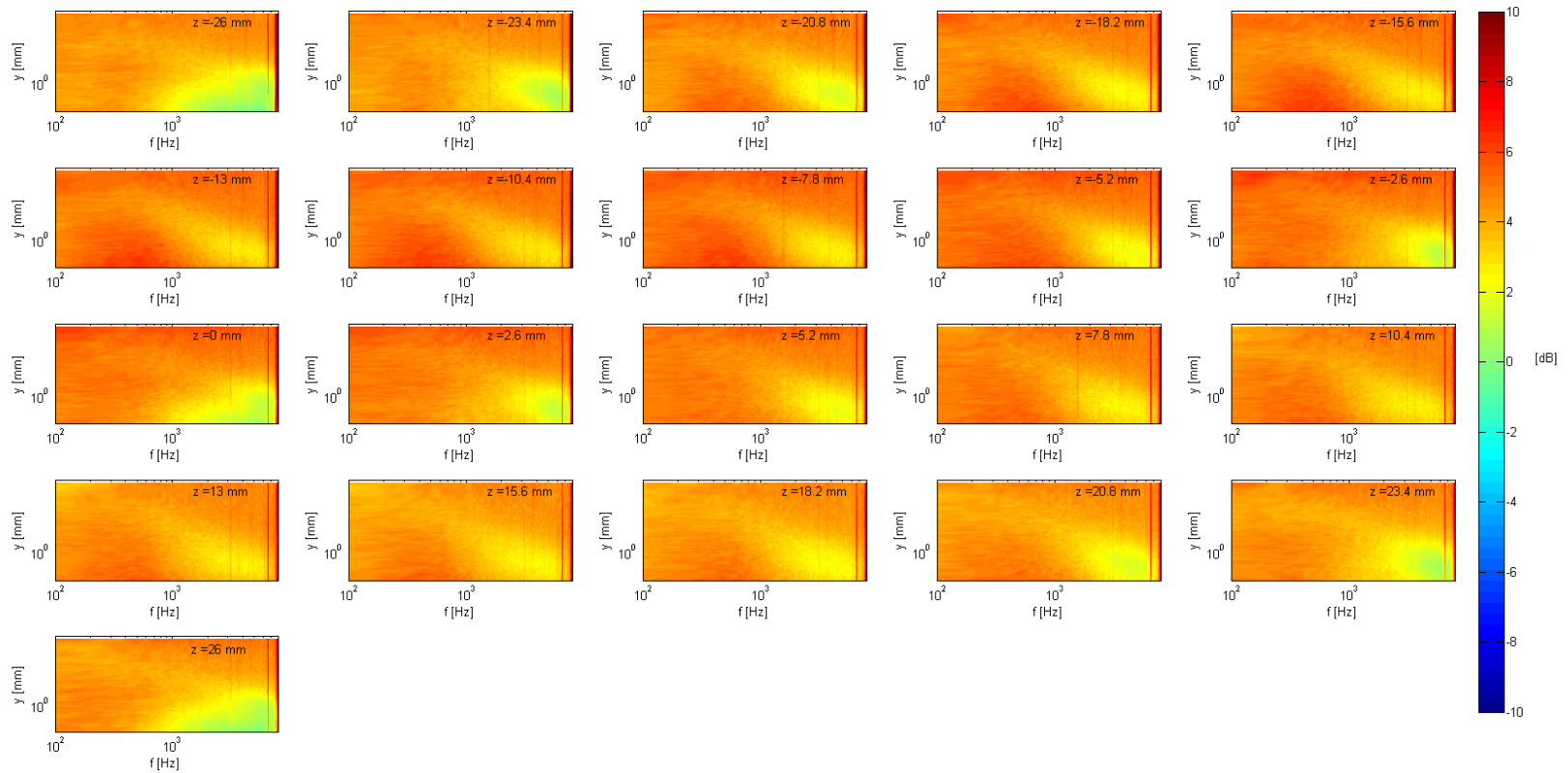


Figure 104: Contour plots of the delta in turbulence fluctuations between the baseline and A45W26 in spanwise direction (z) with 2.6 mm intervals at $x/c = 0.15$ for the suction side where the initial reading is performed at the tip of the sinusoidal leading edge, $AoA = 0^\circ$, $Tu = 5\%$, $U = 25\text{ms}^{-1}$

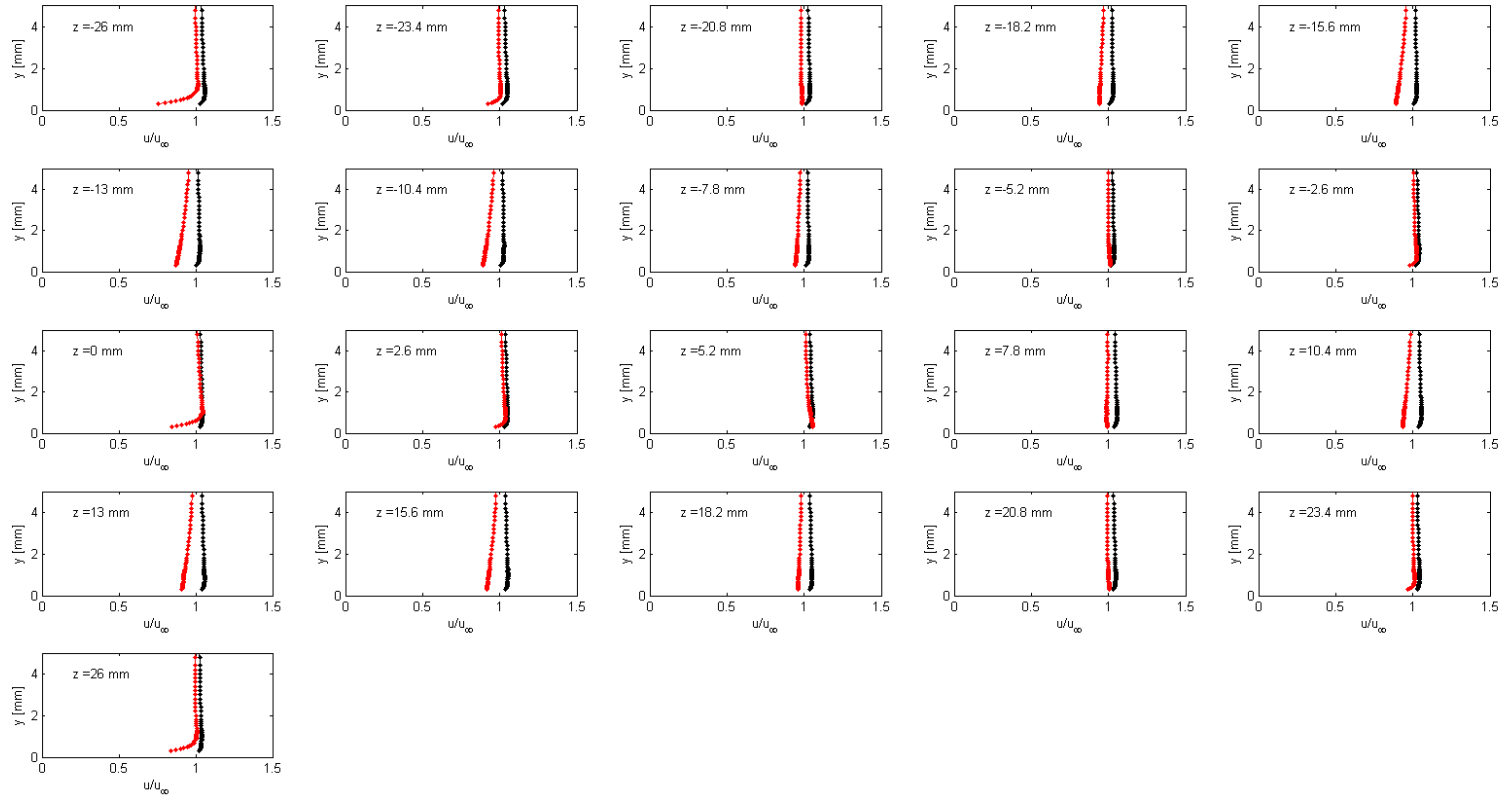


Figure 105: Boundary layer profiles baseline (black) vs. A45W26 (red) in spanwise direction (z) with 2.6 mm intervals at $x/c = 0.3$ for the suction side where the initial reading is performed at the tip of the sinusoidal leading edge, $AoA = 0^\circ$, $Tu = 5\%$, $U = 25\text{ms}^{-1}$

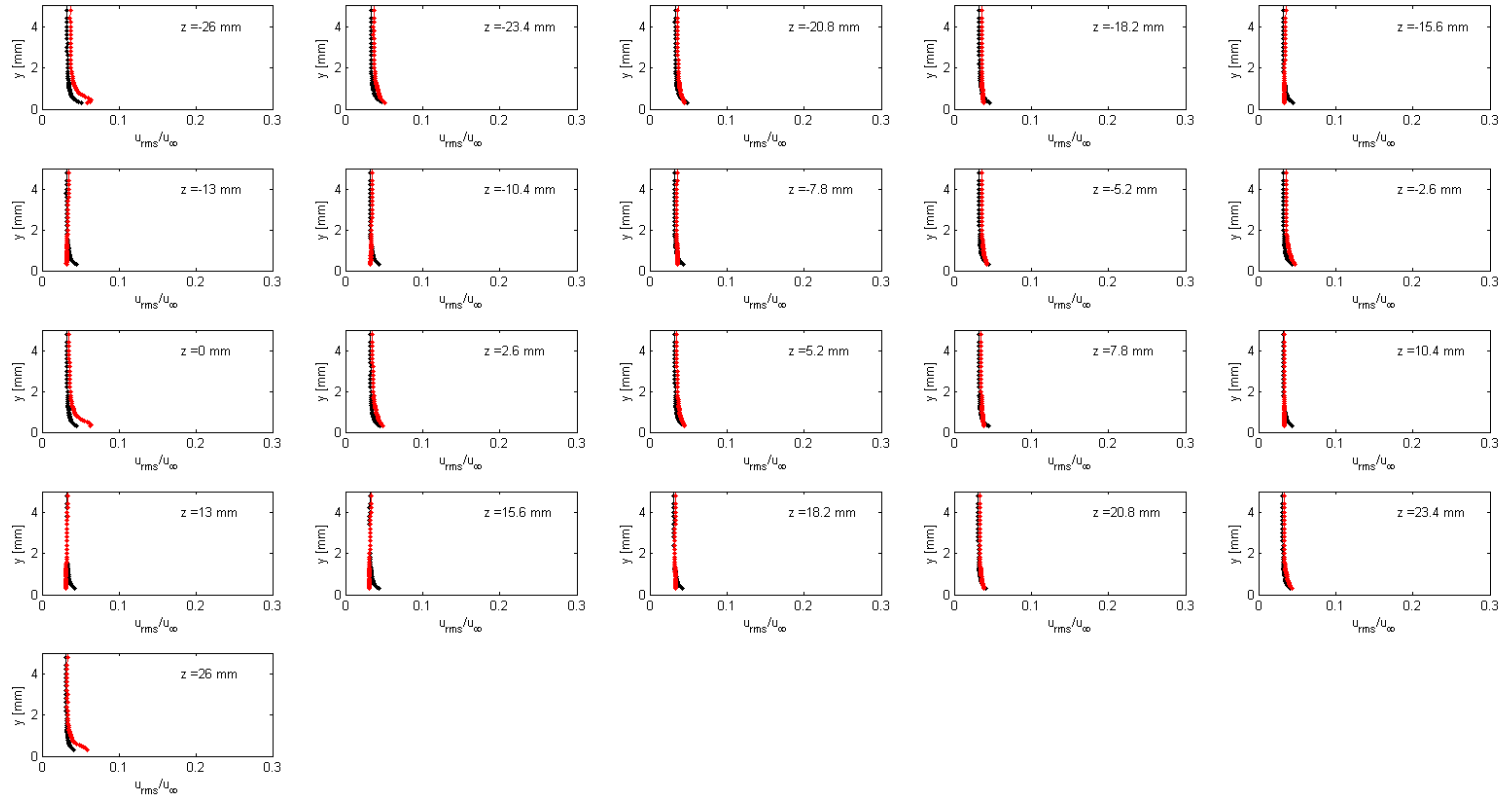


Figure 106: Tu profiles baseline (black) vs. A45W26 (red) in spanwise direction (z) with 2.6 mm intervals at $x/c = 0.3$ for the suction side where the initial reading is performed at the tip of the sinusoidal leading edge, $AoA = 0^\circ$, $Tu = 5\%$, $U = 25\text{ms}^{-1}$

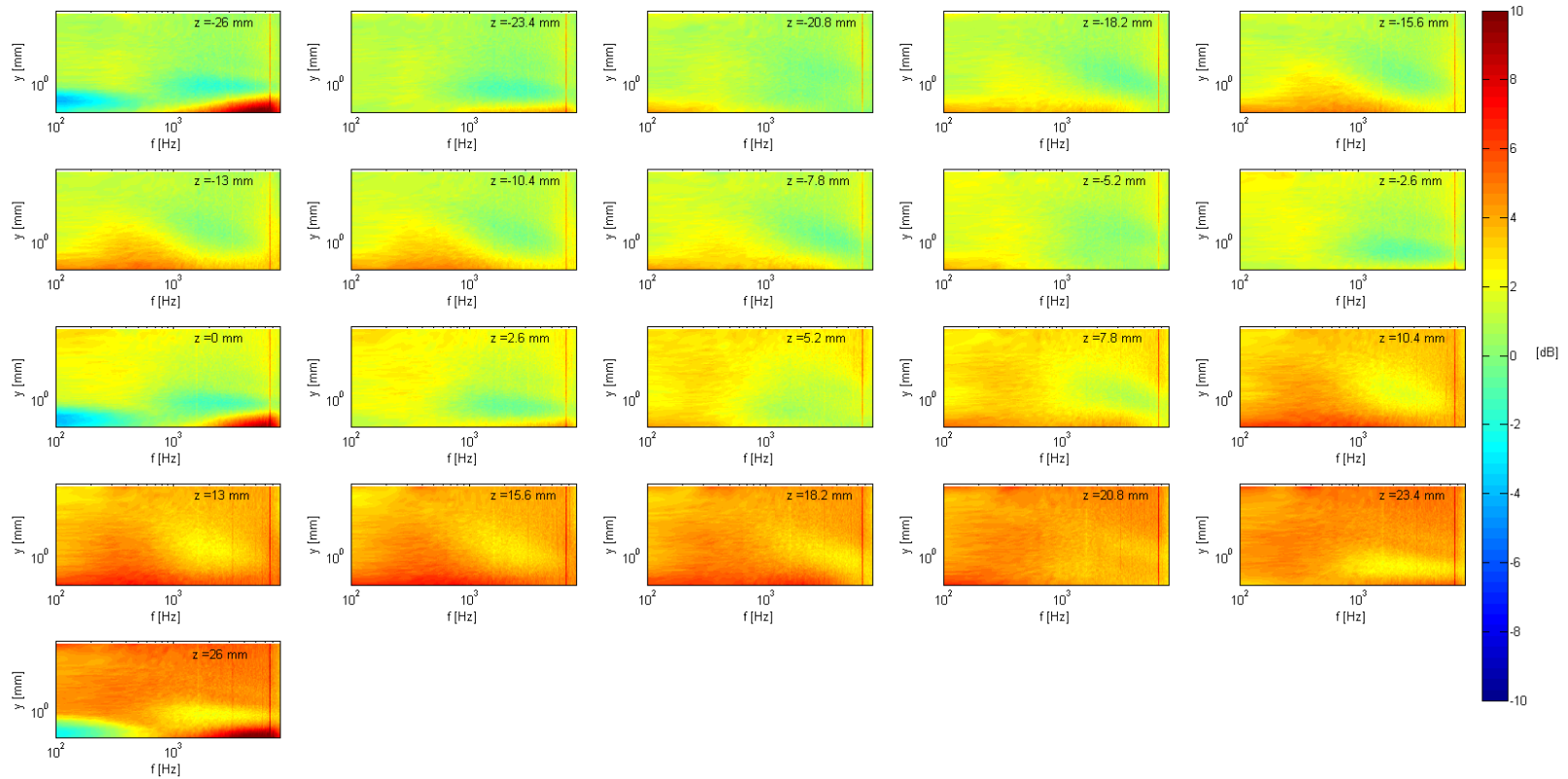


Figure 107: Contour plots of the delta in turbulence fluctuations between the baseline and A45W26 in spanwise direction (z) with 2.6 mm intervals at $x/c = 0.3$ for the suction side where the initial reading is performed at the tip of the sinusoidal leading edge, $AoA = 0^\circ$, $Tu = 5\%$, $U = 25\text{ms}^{-1}$

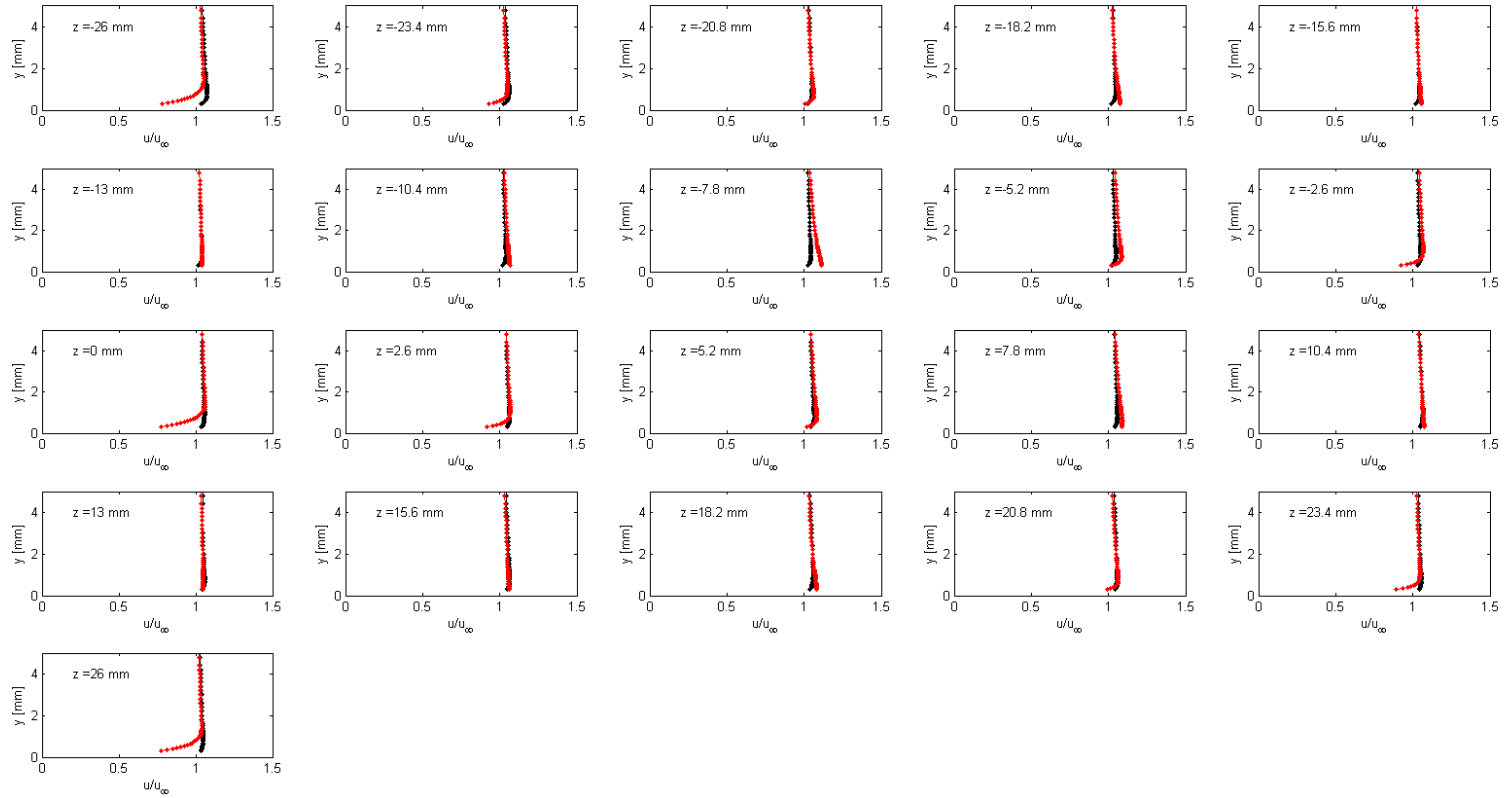


Figure 108: Boundary layer profiles baseline (black) vs. A45W26 (red) in spanwise direction (z) with 2.6 mm intervals at $x/c = 0.33$ for the suction side where the initial reading is performed at the tip of the sinusoidal leading edge, $\text{AoA} = 0^\circ$, $Tu = 5\%$, $U = 25\text{ms}^{-1}$

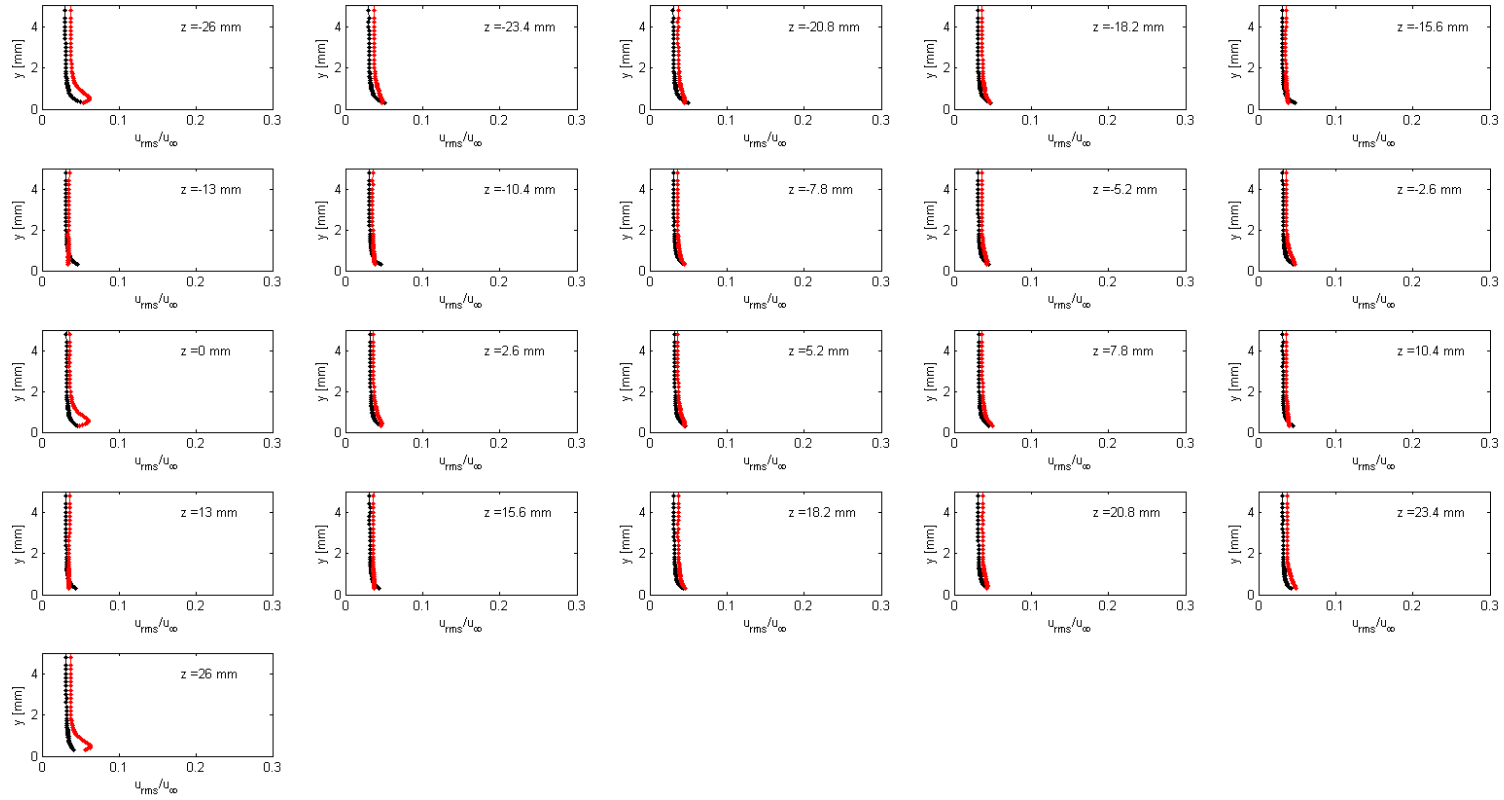


Figure 109: Tu profiles baseline (black) vs. A45W26 (red) in spanwise direction (z) with 2.6 mm intervals at $x/c = 0.33$ for the suction side where the initial reading is performed at the tip of the sinusoidal leading edge, $AoA = 0^\circ$, $Tu = 5\%$, $U = 25\text{ms}^{-1}$

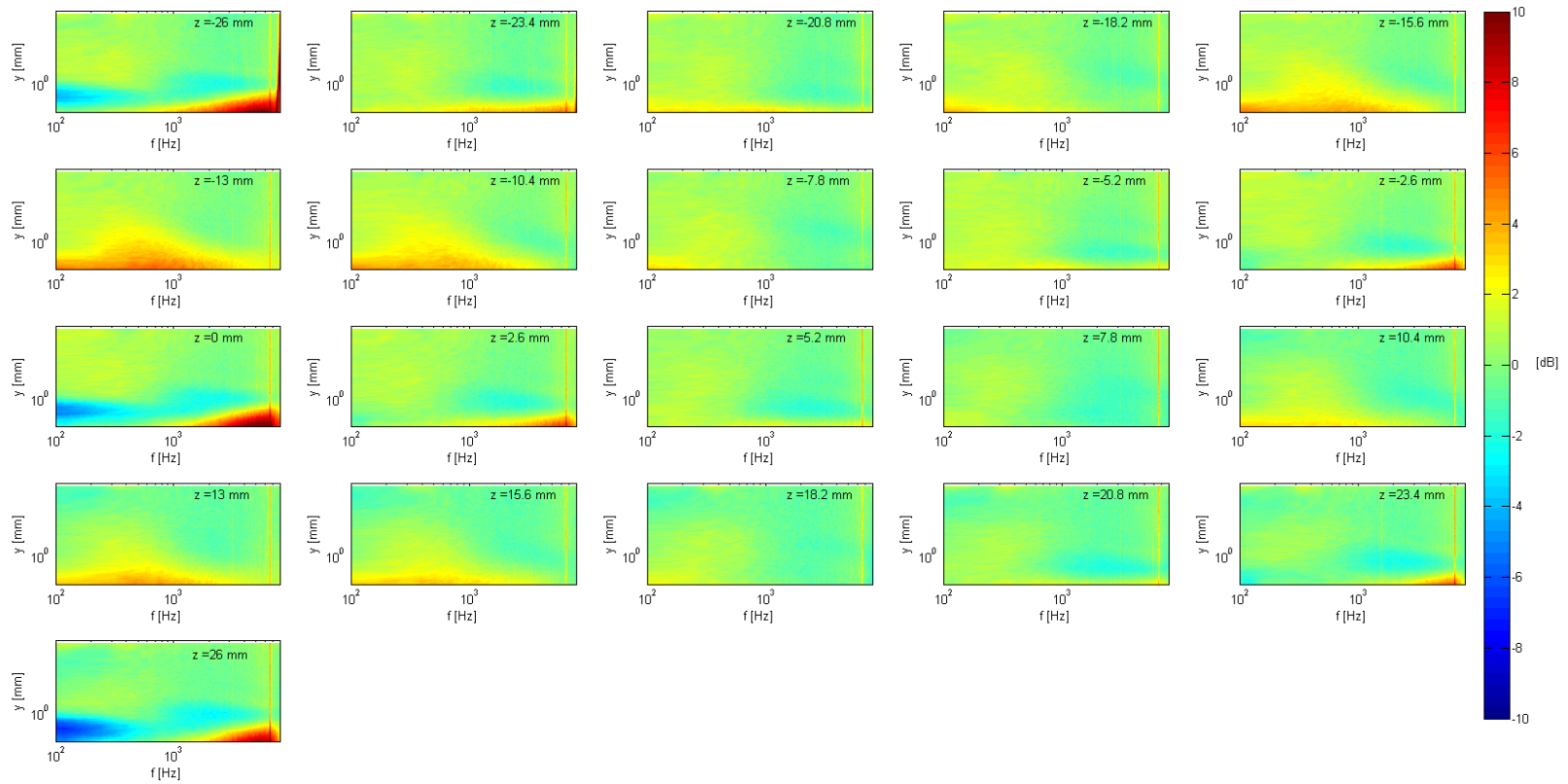


Figure 110: Contour plots of the delta in turbulence fluctuations between the baseline and A45W26 in spanwise direction (z) with 2.6 mm intervals at $x/c = 0.33$ for the suction side where the initial reading is performed at the tip of the sinusoidal leading edge, $AoA = 0^\circ$, $Tu = 5\%$, $U = 25\text{ms}^{-1}$

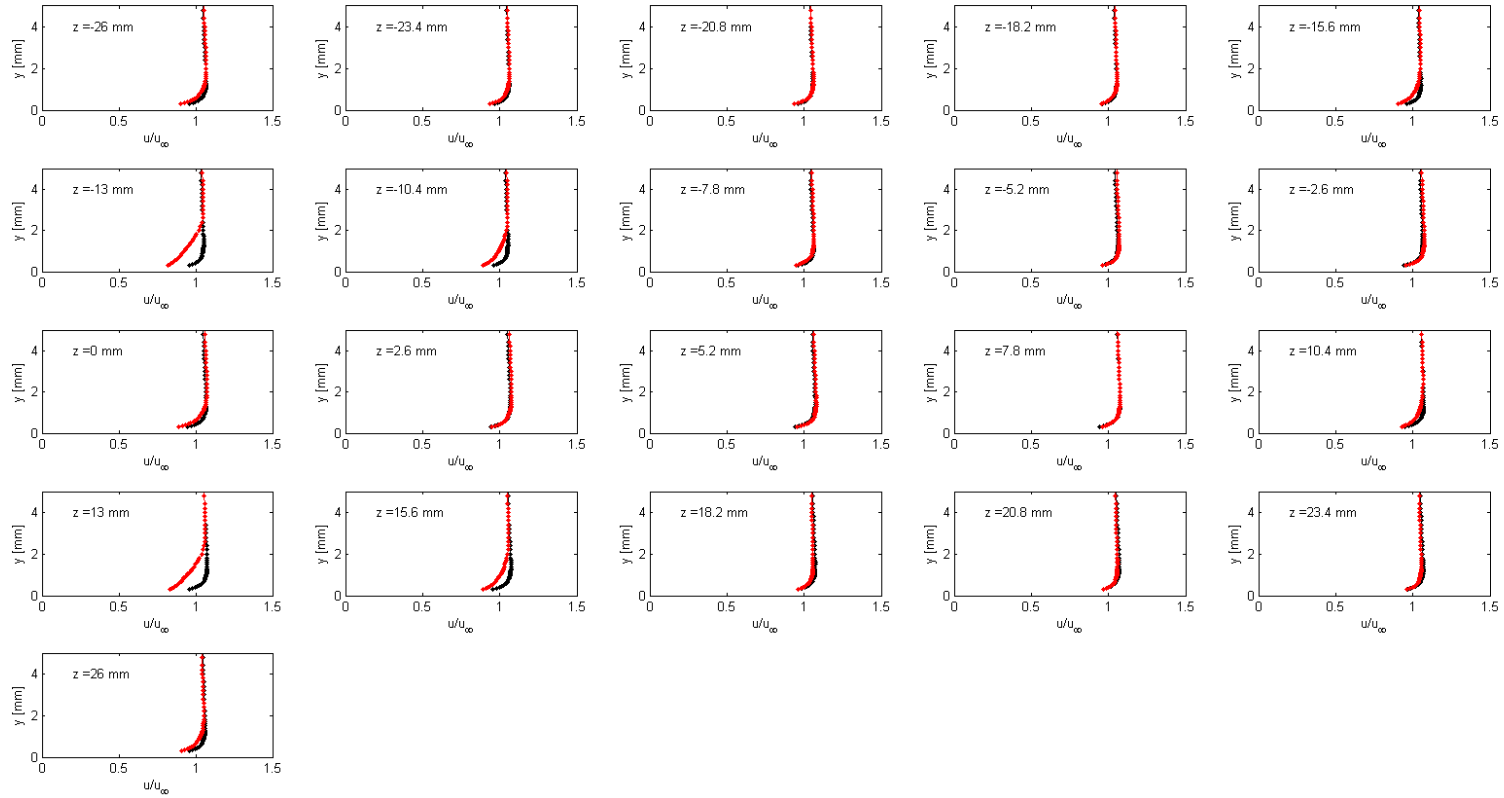


Figure 111: Boundary layer profiles baseline (black) vs. A45W26 (red) in spanwise direction (z) with 2.6 mm intervals at $x/c = 0.5$ for the suction side where the initial reading is performed at the tip of the sinusoidal leading edge, $AoA = 0^\circ$, $Tu = 5\%$, $U = 25\text{ms}^{-1}$

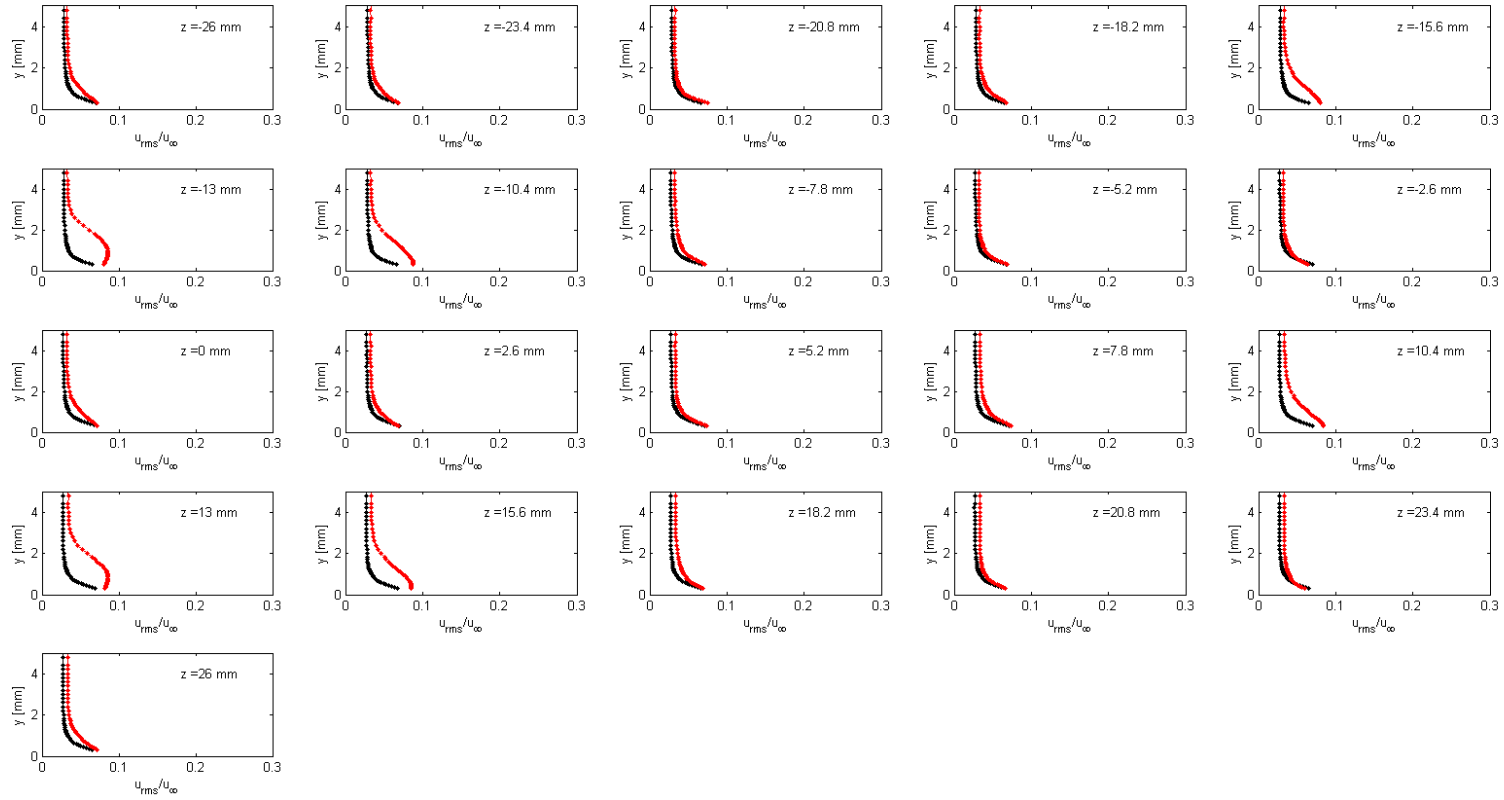


Figure 112: Tu profiles baseline (black) vs. A45W26 (red) in spanwise direction (z) with 2.6 mm intervals at $x/c = 0.5$ for the suction side where the initial reading is performed at the tip of the sinusoidal leading edge, $AoA = 0^\circ$, $Tu = 5\%$, $U = 25\text{ms}^{-1}$

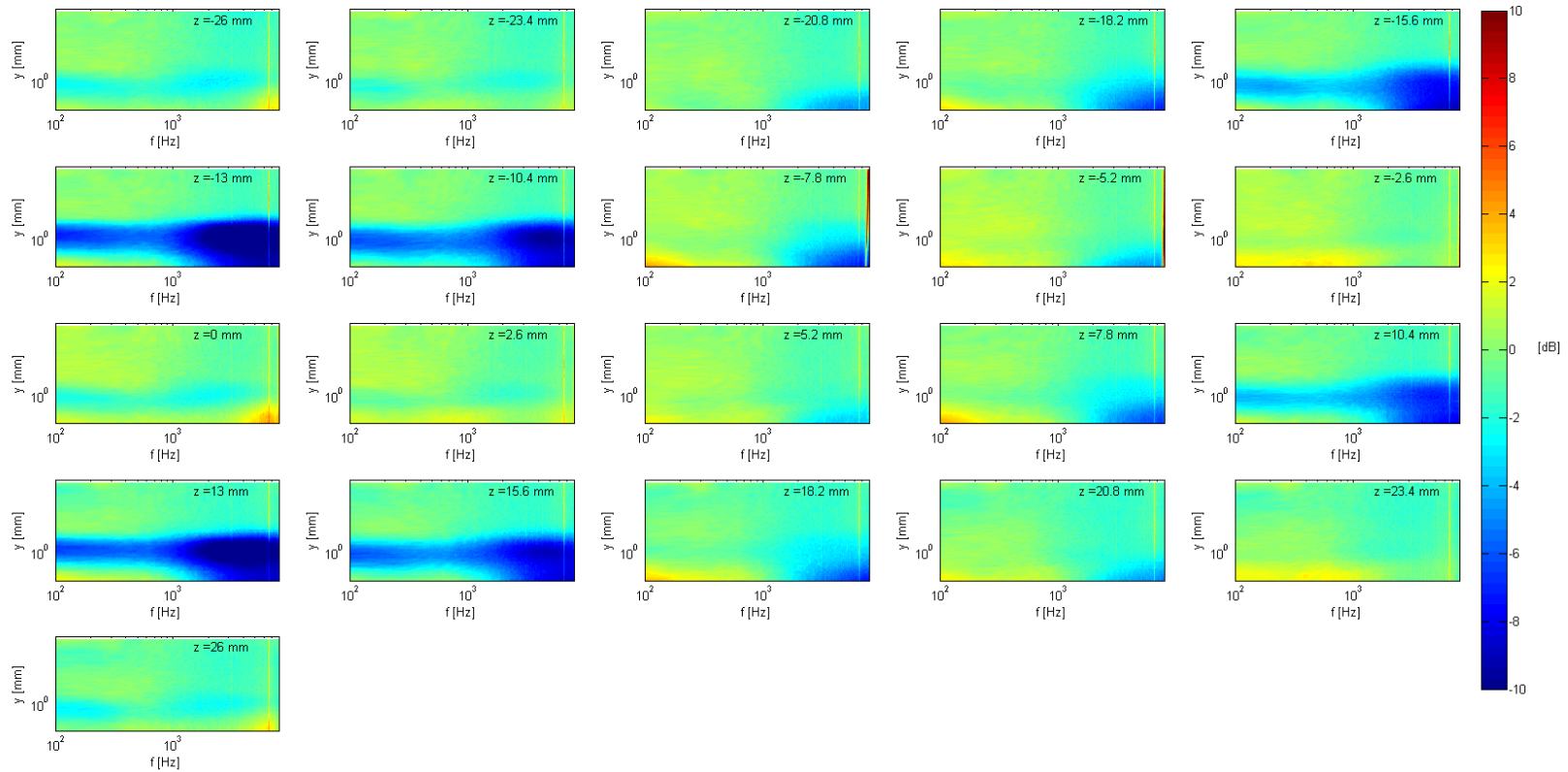


Figure 113: Contour plots of the delta in turbulence fluctuations between the baseline and A45W26 in spanwise direction (z) with 2.6 mm intervals at $x/c = 0.5$ for the suction side where the initial reading is performed at the tip of the sinusoidal leading edge, $AoA = 0^\circ$, $Tu = 5\%$, $U = 25\text{ms}^{-1}$

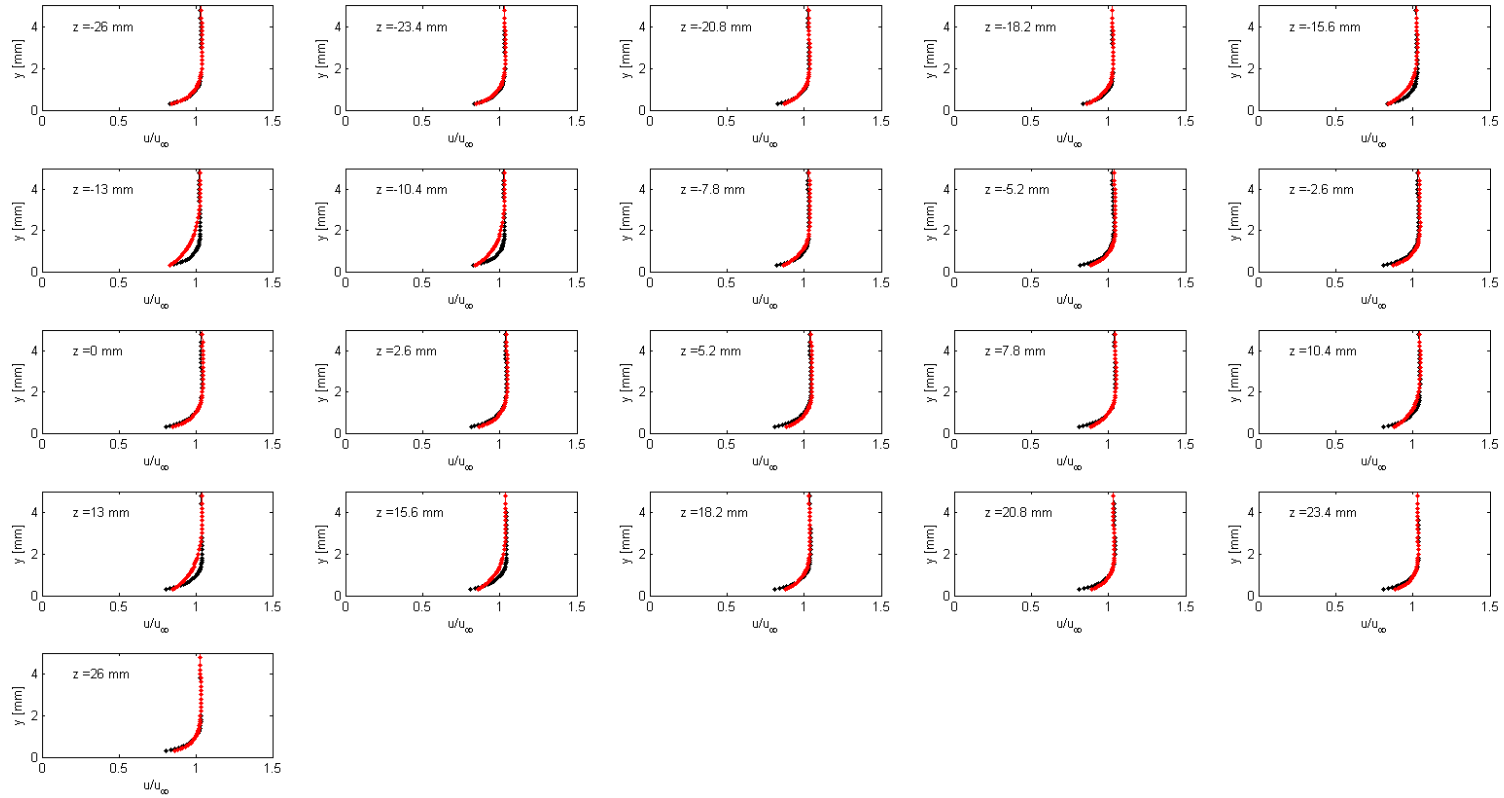


Figure 114: Boundary layer profiles baseline (black) vs. A45W26 (red) in spanwise direction (z) with 2.6 mm intervals at $x/c = 0.67$ for the suction side where the initial reading is performed at the tip of the sinusoidal leading edge, $AoA = 0^\circ$, $Tu = 5\%$, $U = 25\text{ms}^{-1}$

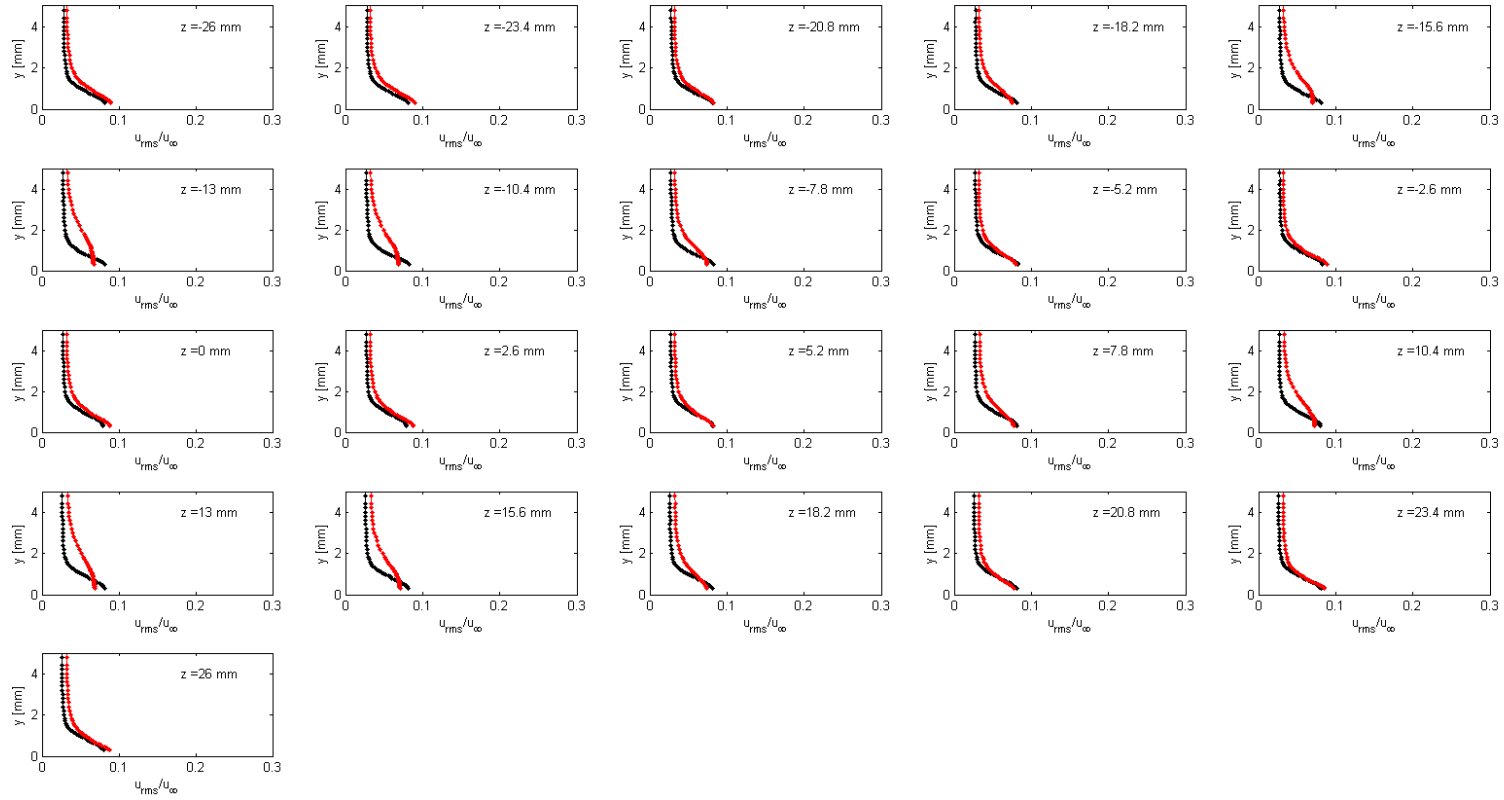


Figure 115: Tu profiles baseline (black) vs. A45W26 (red) in spanwise direction (z) with 2.6 mm intervals at $x/c = 0.67$ for the suction side where the initial reading is performed at the tip of the sinusoidal leading edge, $AoA = 0^\circ$, $Tu = 5\%$, $U = 25\text{ms}^{-1}$

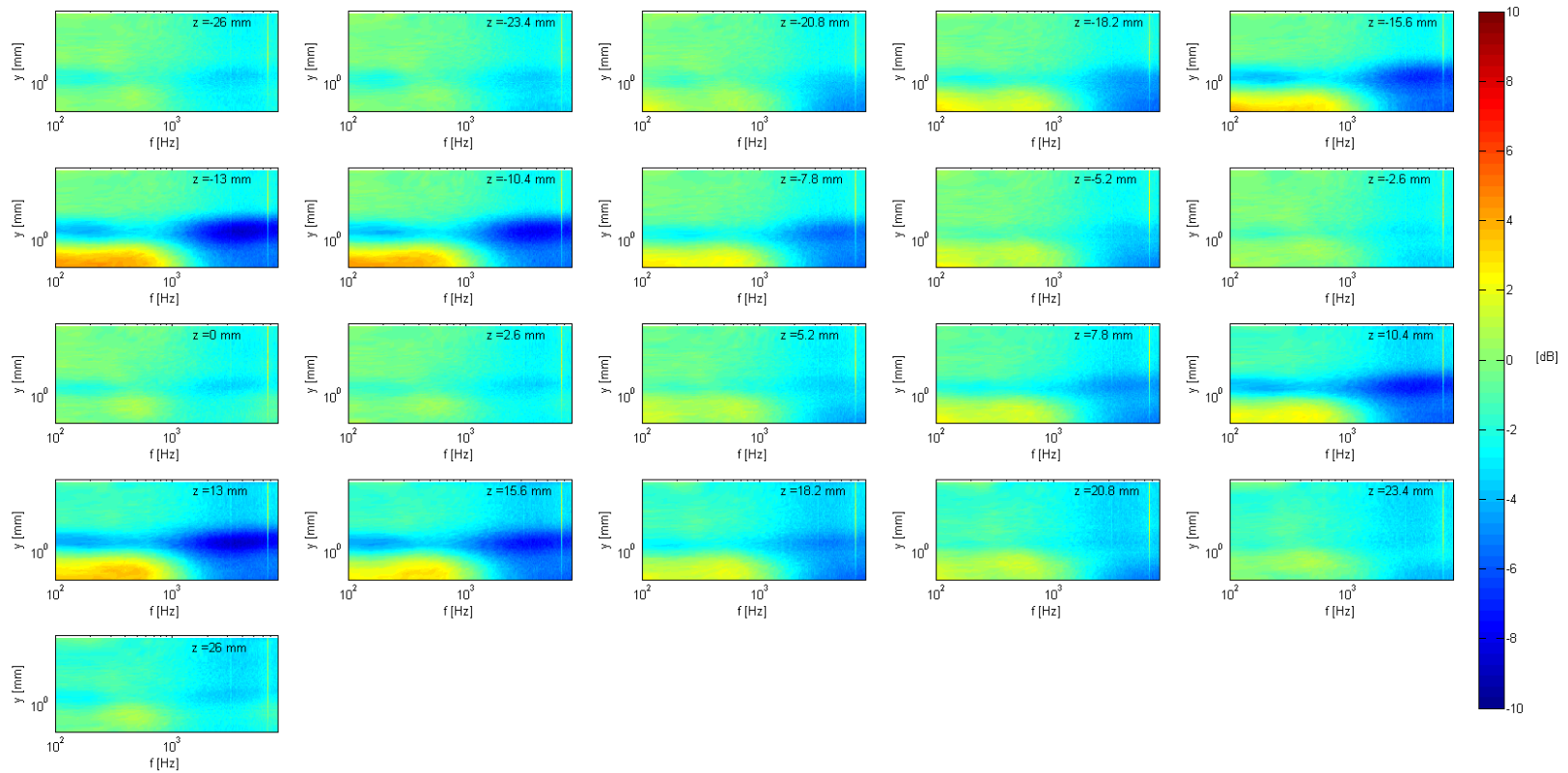


Figure 116: Contour plots of the delta in turbulence fluctuations between the baseline and A45W26 in spanwise direction (z) with 2.6 mm intervals at $x/c = 0.67$ for the suction side where the initial reading is performed at the tip of the sinusoidal leading edge, $AoA = 0^\circ$, $Tu = 5\%$, $U = 25\text{ms}^{-1}$

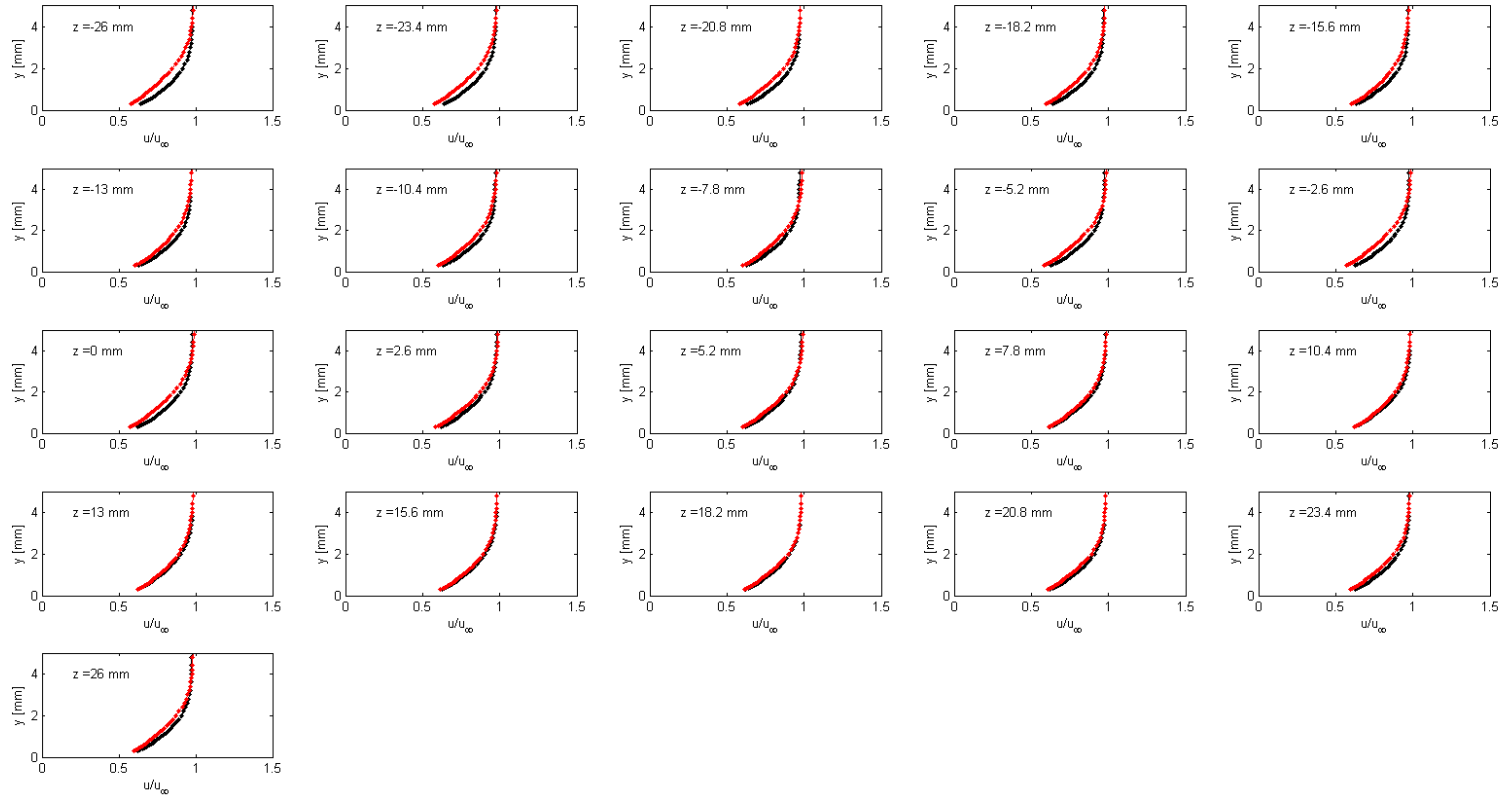


Figure 117: Boundary layer profiles baseline (black) vs. A45W26 (red) in spanwise direction (z) with 2.6 mm intervals at $x/c = 0.93$ for the suction side where the initial reading is performed at the tip of the sinusoidal leading edge, $AoA = 0^\circ$, $Tu = 5\%$, $U = 25\text{ms}^{-1}$

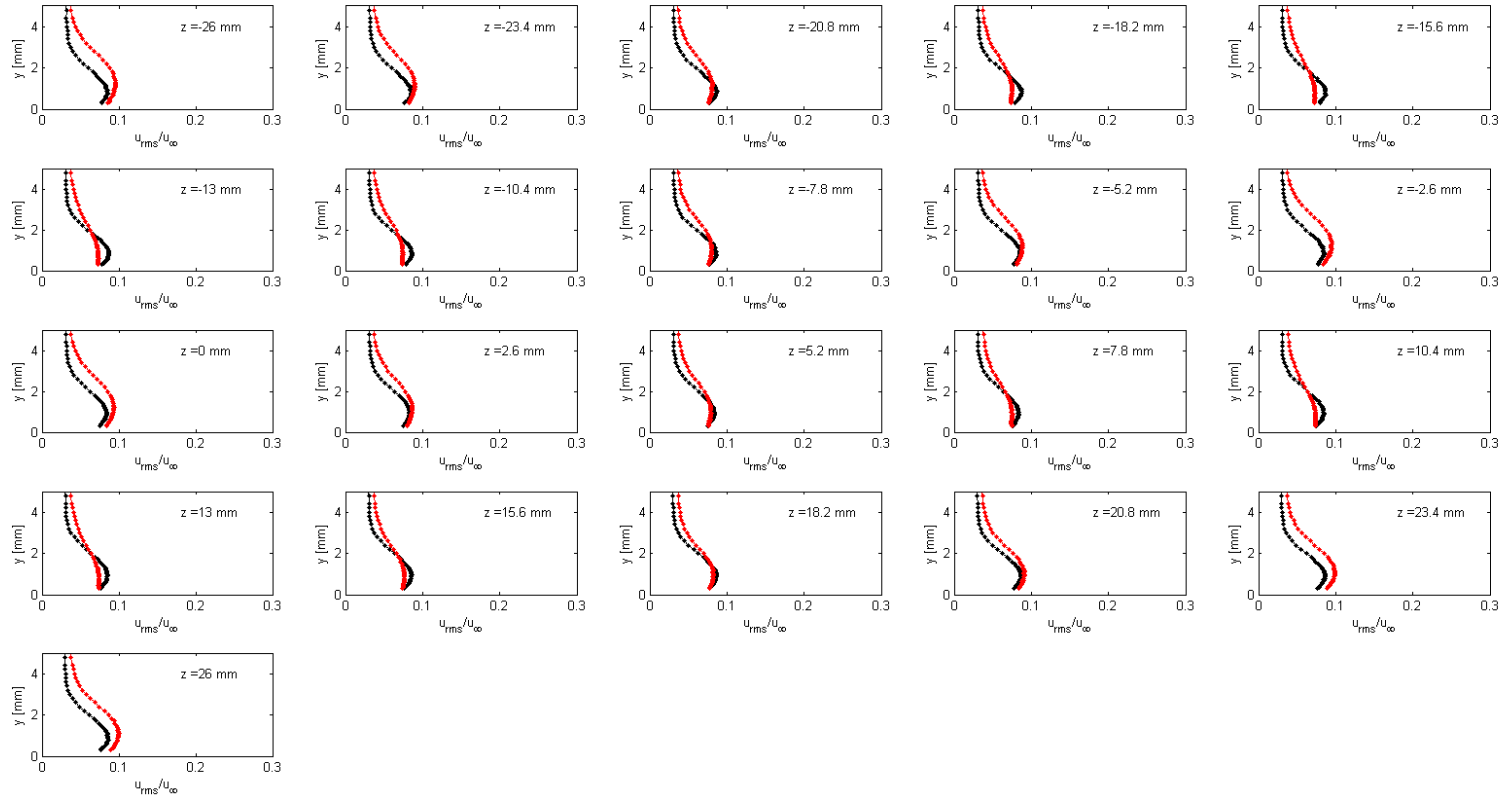


Figure 118: Tu profiles baseline (black) vs. A45W26 (red) in spanwise direction (z) with 2.6 mm intervals at $x/c = 0.93$ for the suction side where the initial reading is performed at the tip of the sinusoidal leading edge, $AoA = 0^\circ$, $Tu = 5\%$, $U = 25\text{ms}^{-1}$

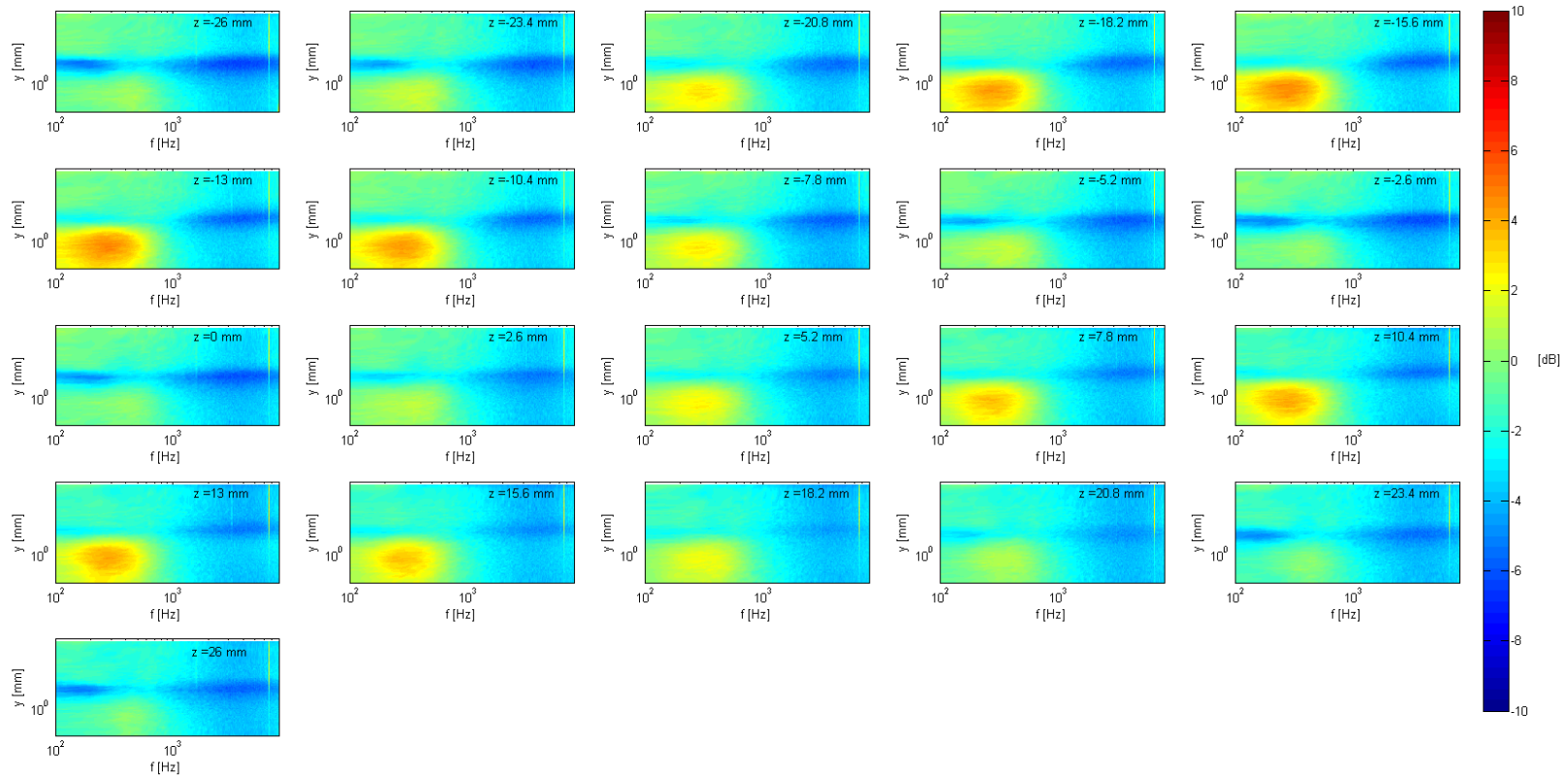


Figure 119: Contour plots of the delta in turbulence fluctuations between the baseline and A45W26 in spanwise direction (z) with 2.6 mm intervals at $x/c = 0.93$ for the suction side where the initial reading is performed at the tip of the sinusoidal leading edge, $AoA = 0^\circ$, $Tu = 5\%$, $U = 25\text{ms}^{-1}$

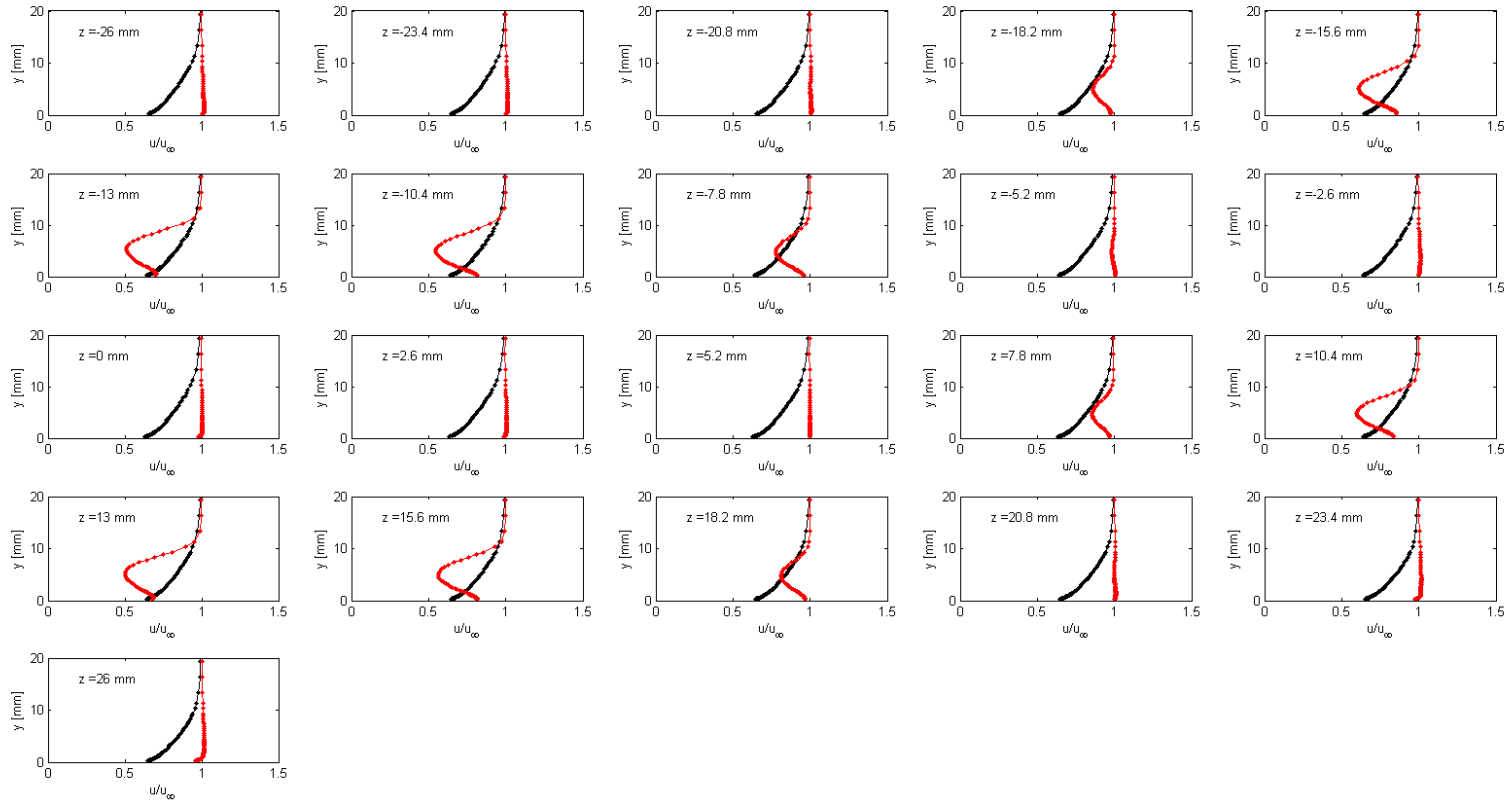


Figure 120: Boundary layer profiles baseline (black) vs. A45W26 (red) in spanwise direction (z) with 2.6 mm intervals at $x/c = 0.5$ for the pressure side where the initial reading is performed at the tip of the sinusoidal leading edge, $AoA = 0^\circ$, $Tu = 5\%$, $U = 25\text{ms}^{-1}$

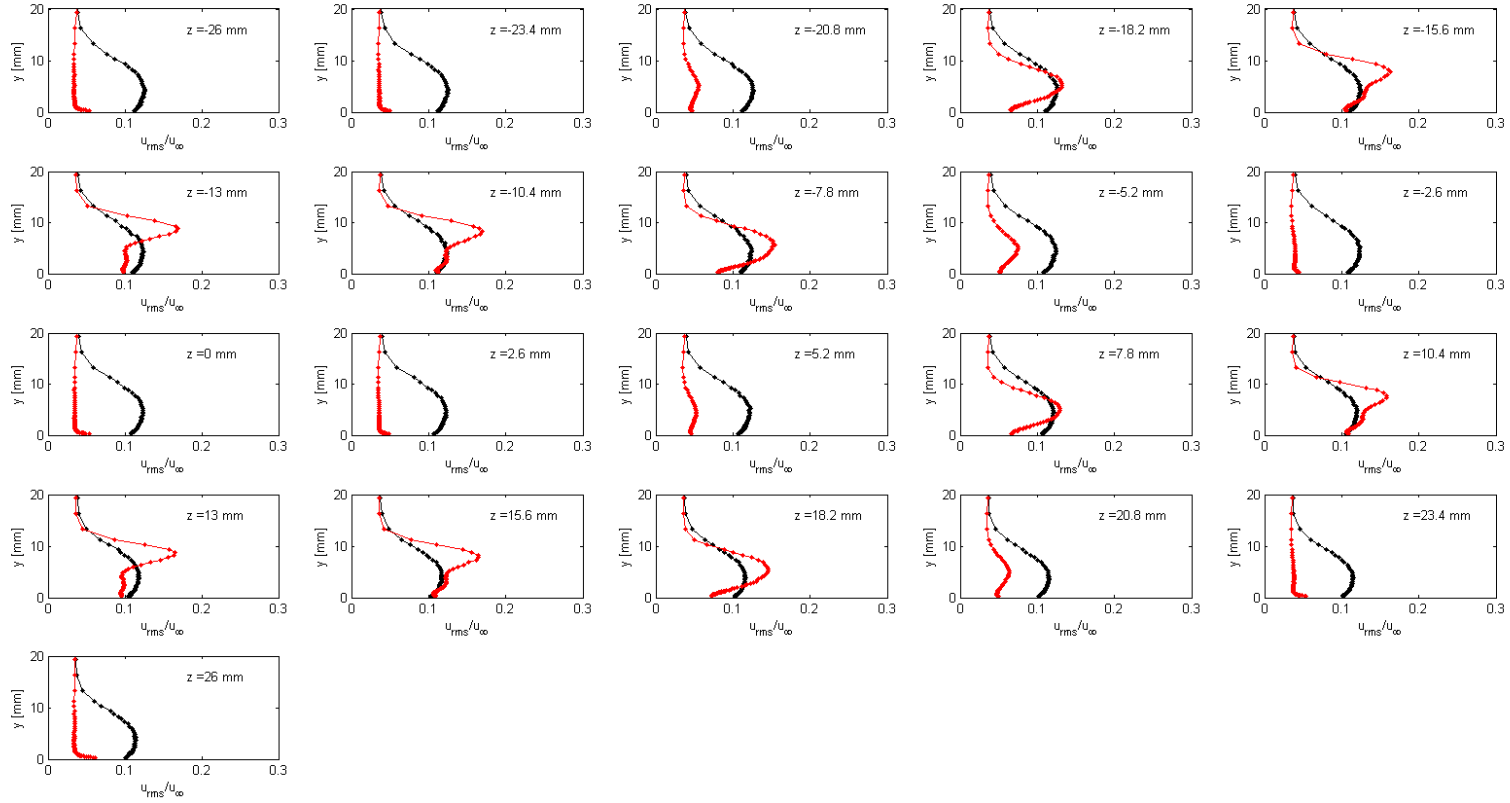


Figure 121: Tu profiles baseline (black) vs. A45W26 (red) in spanwise direction (z) with 2.6 mm intervals at $x/c = 0.5$ for the pressure side where the initial reading is performed at the tip of the sinusoidal leading edge, $AoA = 0^\circ$, $Tu = 5\%$, $U = 25\text{ms}^{-1}$

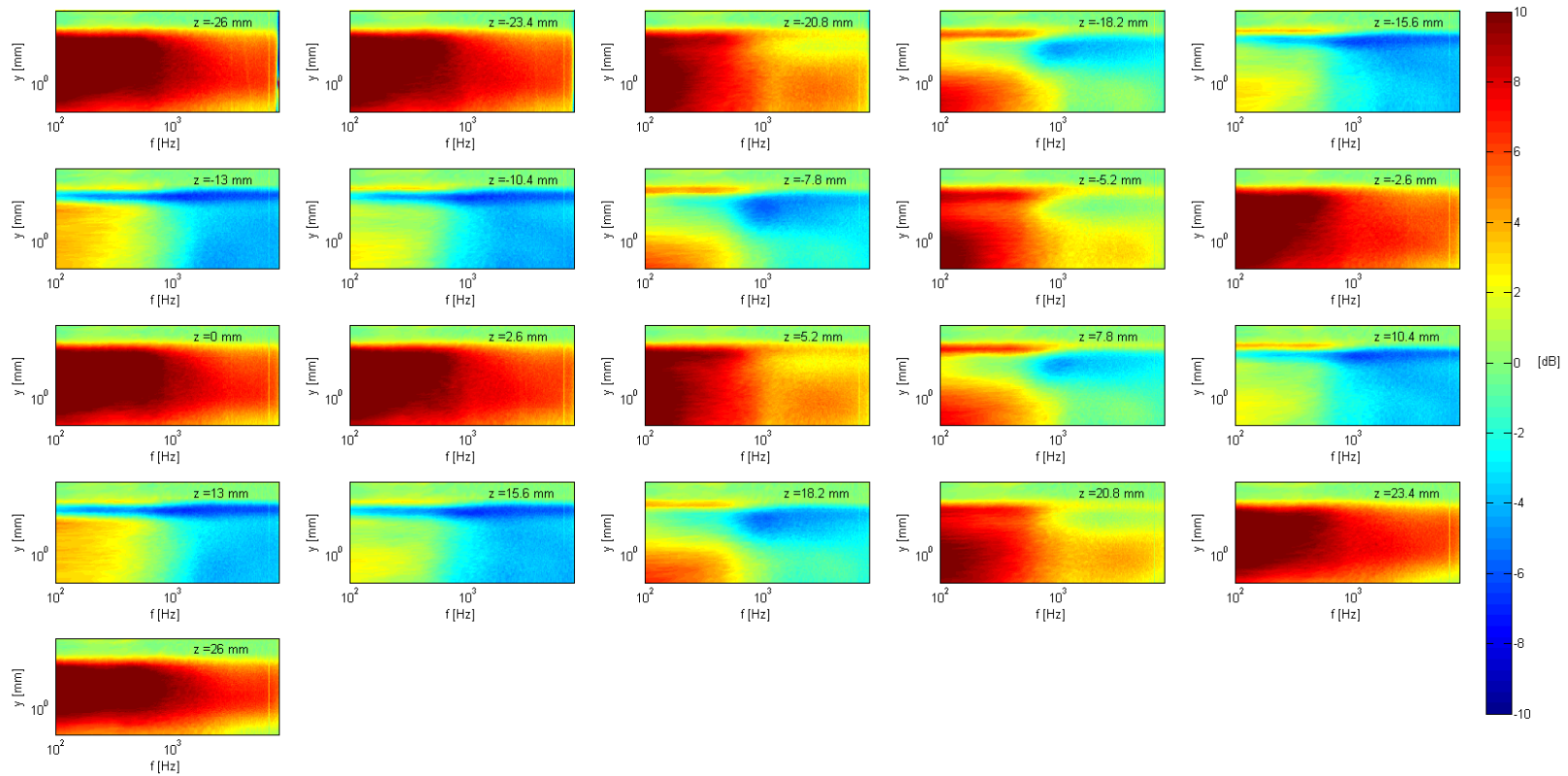


Figure 122: Contour plots of the delta in turbulence fluctuations between the baseline and A45W26 in spanwise direction (z) with 2.6 mm intervals at $x/c = 0.5$ for the pressure side where the initial reading is performed at the tip of the sinusoidal leading edge, $AoA = 0^\circ$, $Tu = 5\%$, $U = 25\text{ms}^{-1}$

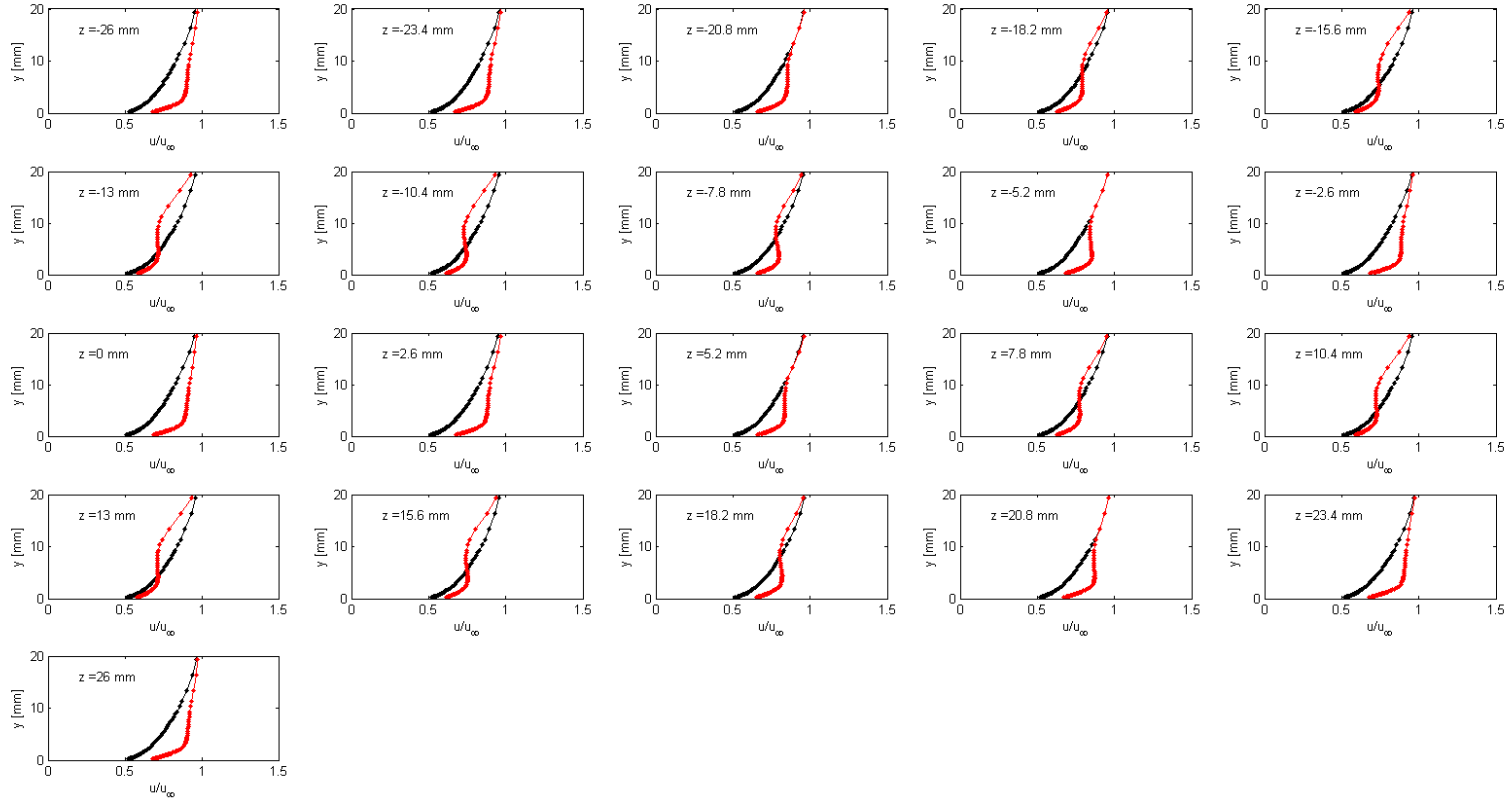


Figure 123: Boundary layer profiles baseline (black) vs. A45W26 (red) in spanwise direction (z) with 2.6 mm intervals at $x/c = 0.93$ for the pressure side where the initial reading is performed at the tip of the sinusoidal leading edge, $AoA = 0^\circ$, $Tu = 5\%$, $U = 25\text{ms}^{-1}$

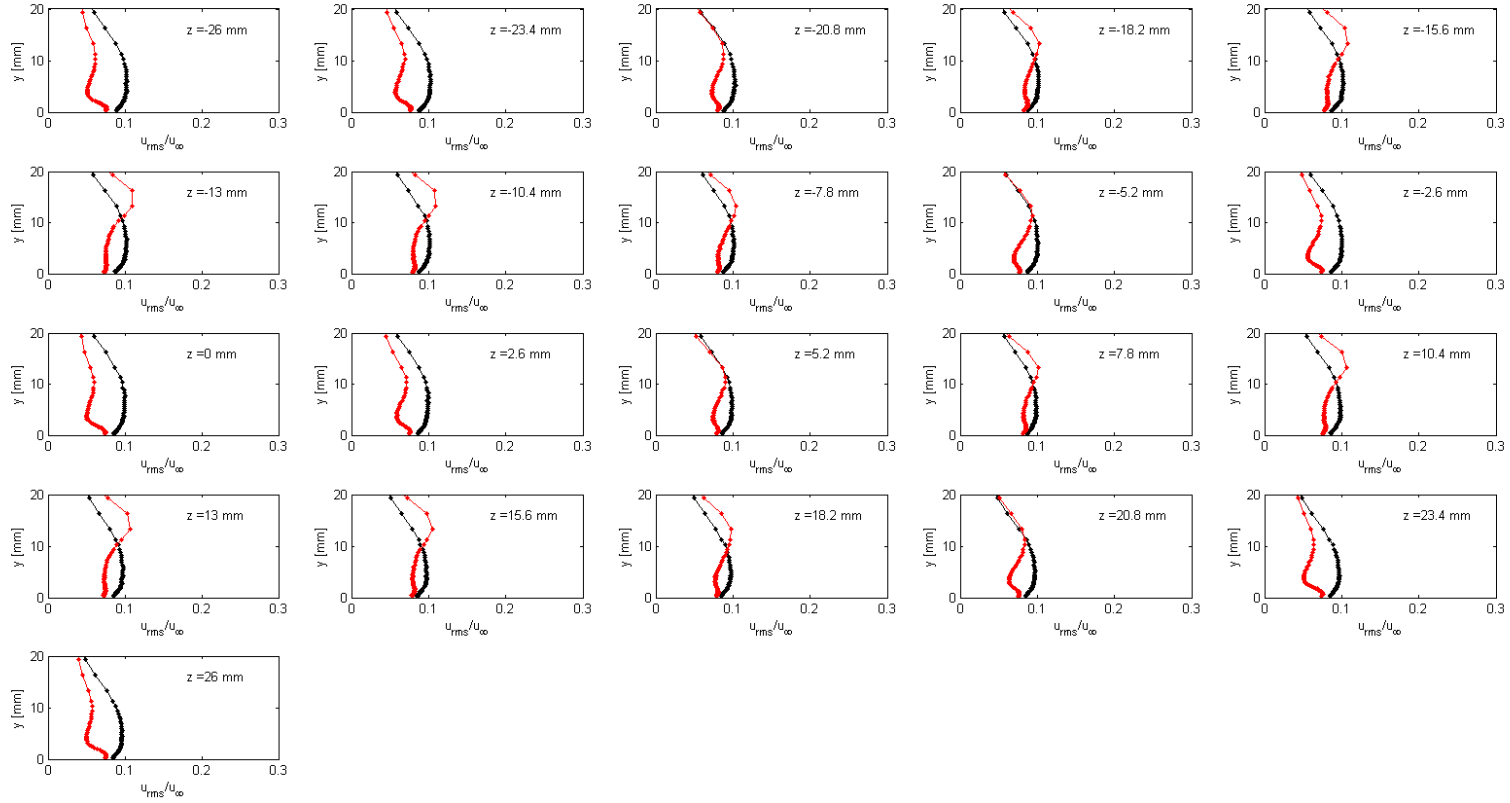


Figure 124: Tu profiles baseline (black) vs. A45W26 (red) in spanwise direction (z) with 2.6 mm intervals at $x/c = 0.93$ for the pressure side where the initial reading is performed at the tip of the sinusoidal leading edge, $AoA = 0^\circ$, $Tu = 5\%$, $U = 25\text{ms}^{-1}$

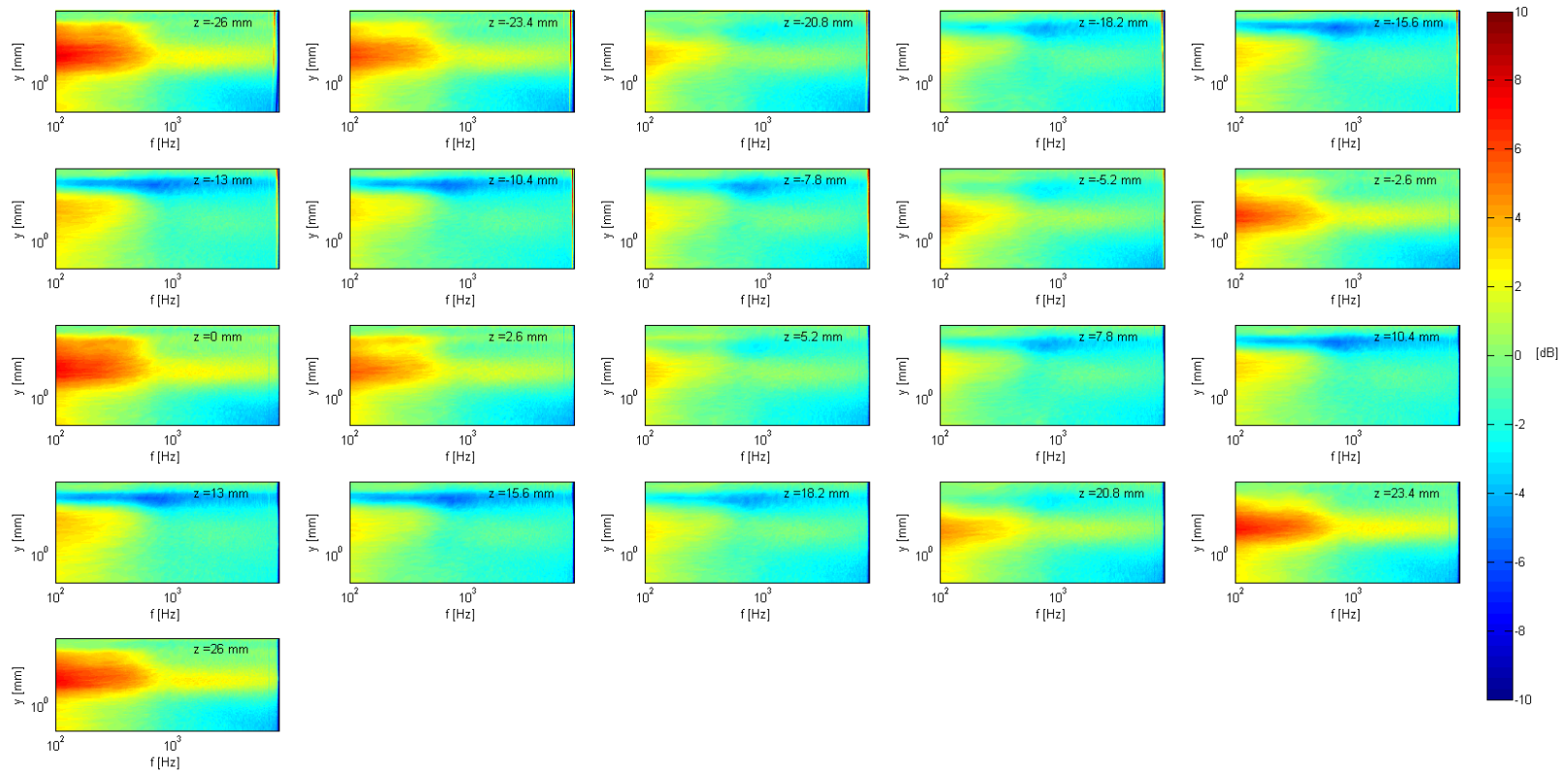


Figure 125: Contour plots of the delta in turbulence fluctuations between the baseline and A45W26 in spanwise direction (z) with 2.6 mm intervals at $x/c = 0.93$ for the pressure side where the initial reading is performed at the tip of the sinusoidal leading edge, $AoA = 0^\circ$, $Tu = 5\%$, $U = 25\text{ms}^{-1}$

Appendix C – Wake measurements

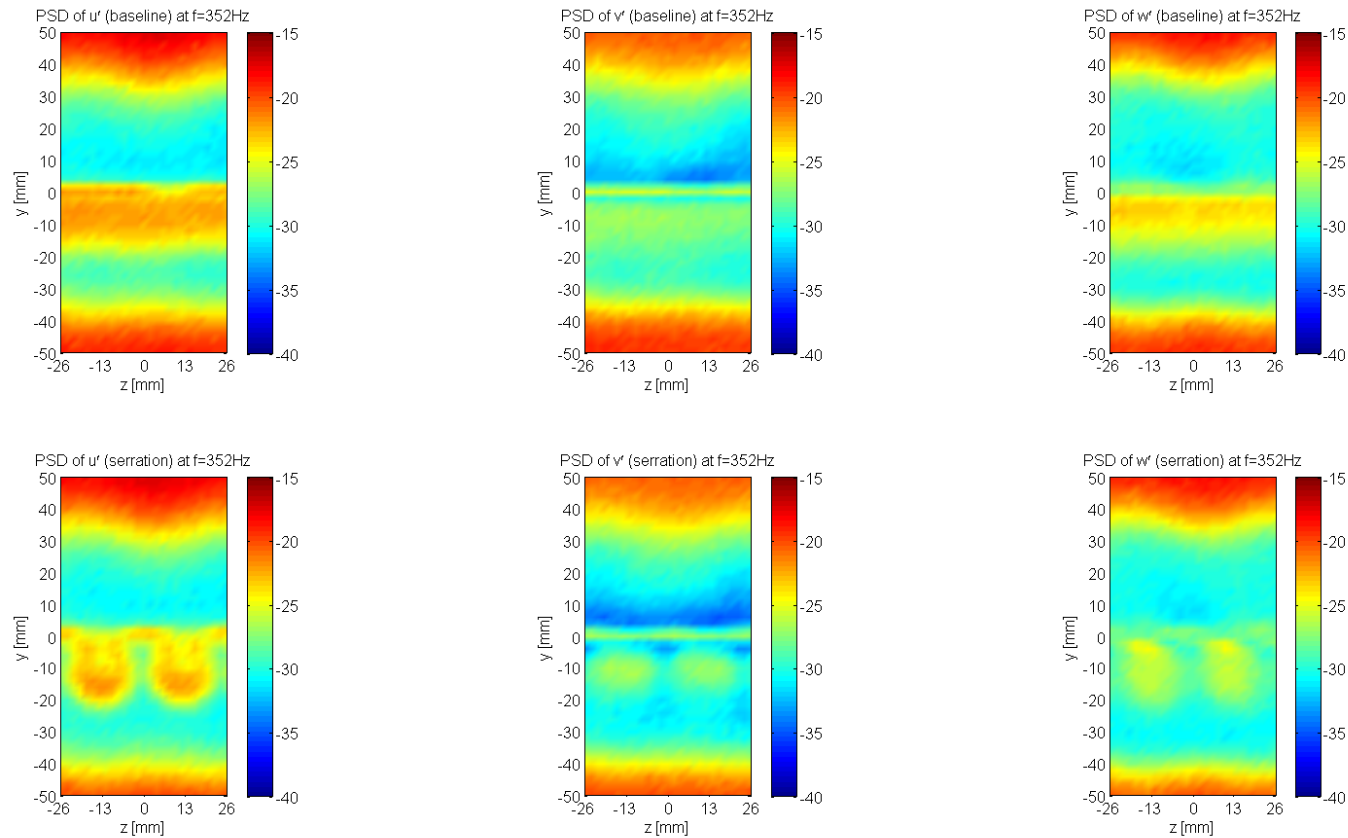


Figure 126: PSD [dB] at $f = 352\text{ Hz}$ of u' , v' and w' for the baseline vs. A45W26 at $x/c = 1.02$ in the wake of the aerofoil, $\text{AoA} = 0^\circ$, $\text{Tu}(u) = 5\%$, $U = 25\text{ms}^{-1}$

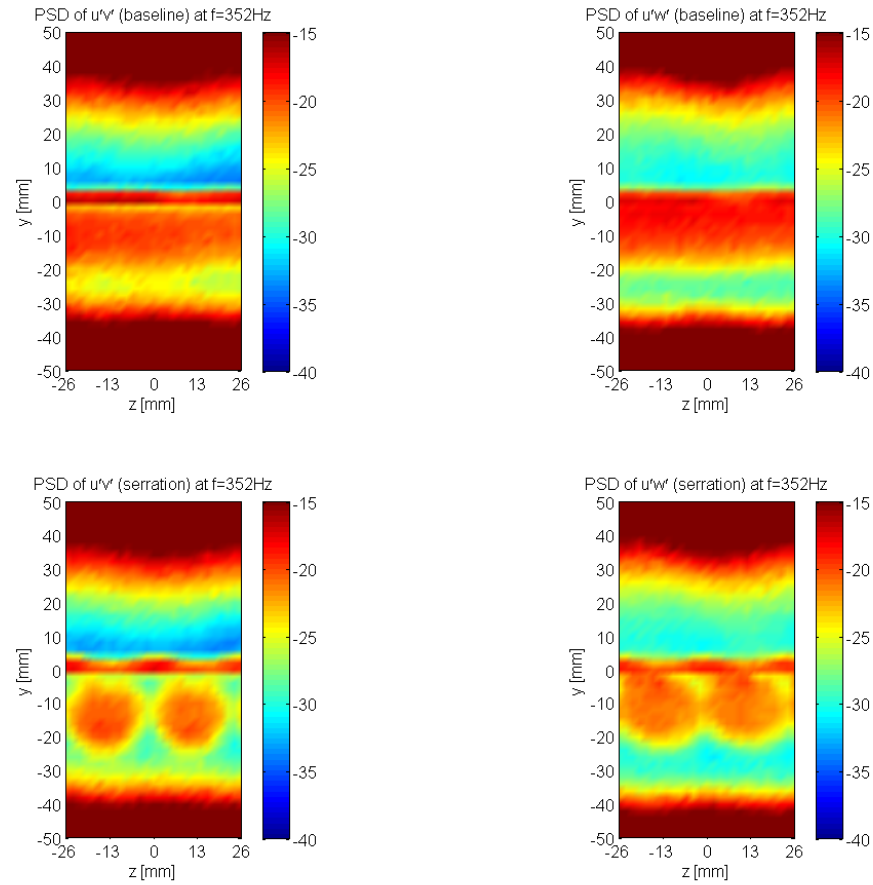


Figure 127: PSD [dB] at $f = 352 \text{ Hz}$ of $u'v'$ and $u'w'$ for the baseline vs. A45W26 at $x/c = 1.02$ in the wake of the aerofoil, $\text{AoA} = 0^\circ$, $Tu(u) = 5\%$, $U = 25 \text{ ms}^{-1}$

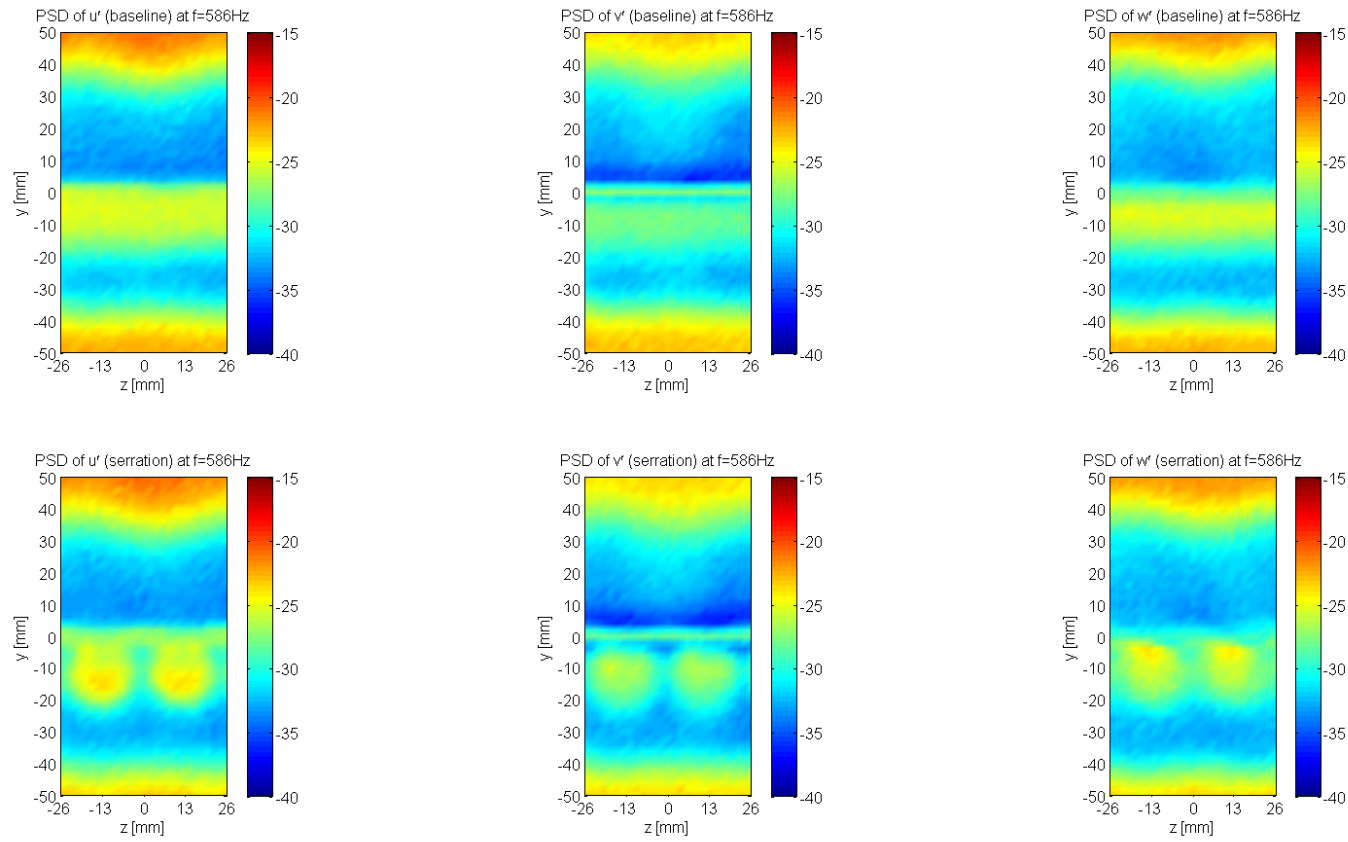


Figure 128: PSD [dB] at $f = 586$ Hz of u' , v' and w' for the baseline vs. A45W26 at $x/c = 1.02$ in the wake of the aerofoil, $AoA = 0^\circ$, $Tu(u) = 5\%$, $U = 25\text{ms}^{-1}$

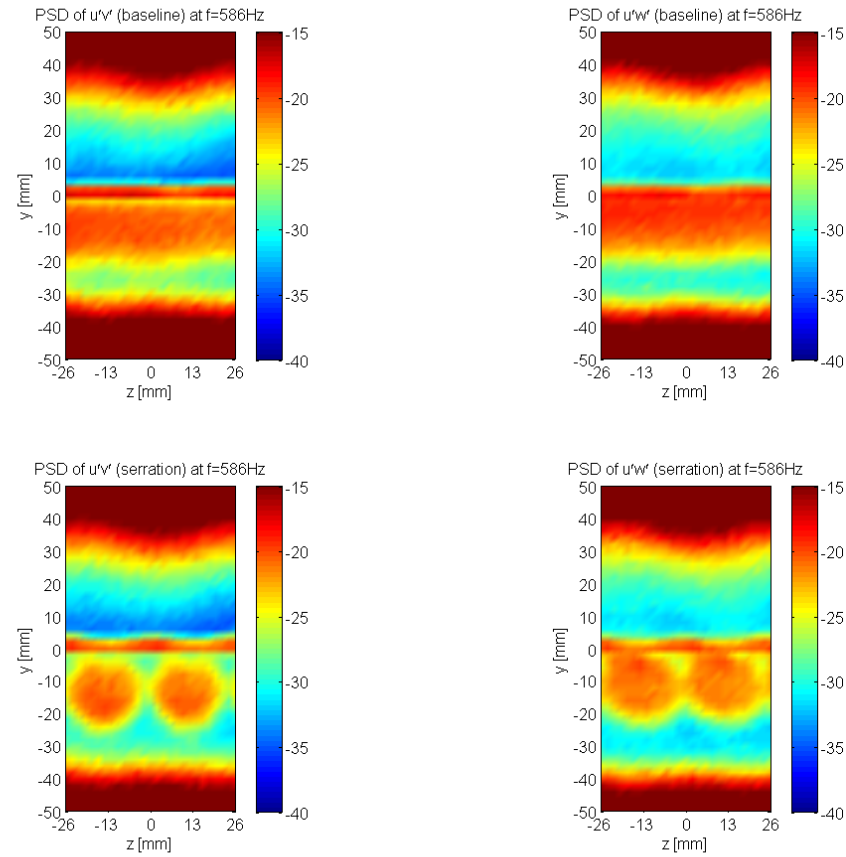


Figure 129: PSD [dB] at $f = 586 \text{ Hz}$ of $u'v'$ and $u'w'$ for the baseline vs. A45W26 at $x/c = 1.02$ in the wake of the aerofoil, $\text{AoA} = 0^\circ$, $Tu(u) = 5\%$, $U = 25 \text{ ms}^{-1}$

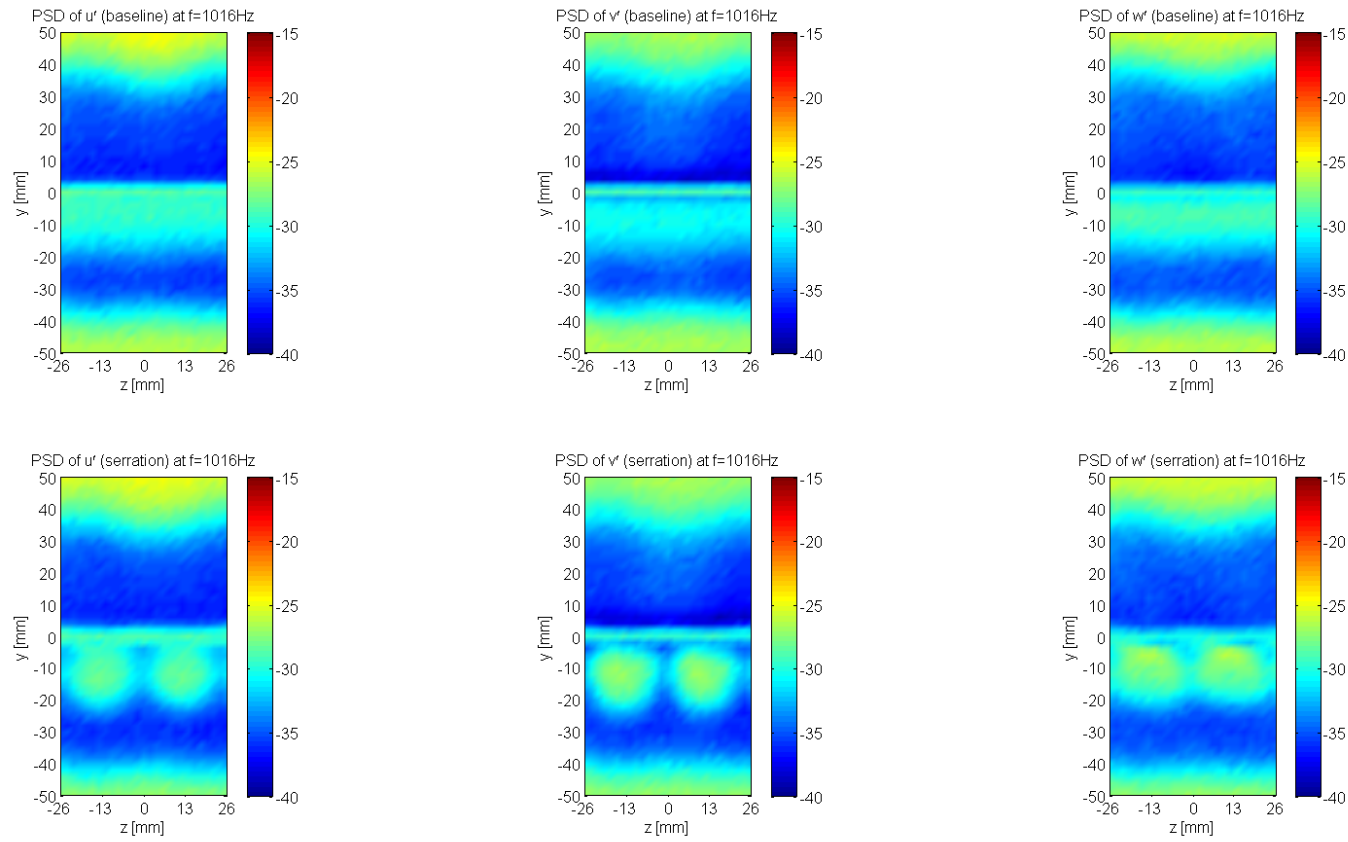


Figure 130: PSD [dB] at $f = 1016\text{ Hz}$ of u' , v' and w' for the baseline vs. A45W26 at $x/c = 1.02$ in the wake of the aerofoil, $\text{AoA} = 0^\circ$, $Tu(u) = 5\%$, $U = 25\text{ms}^{-1}$

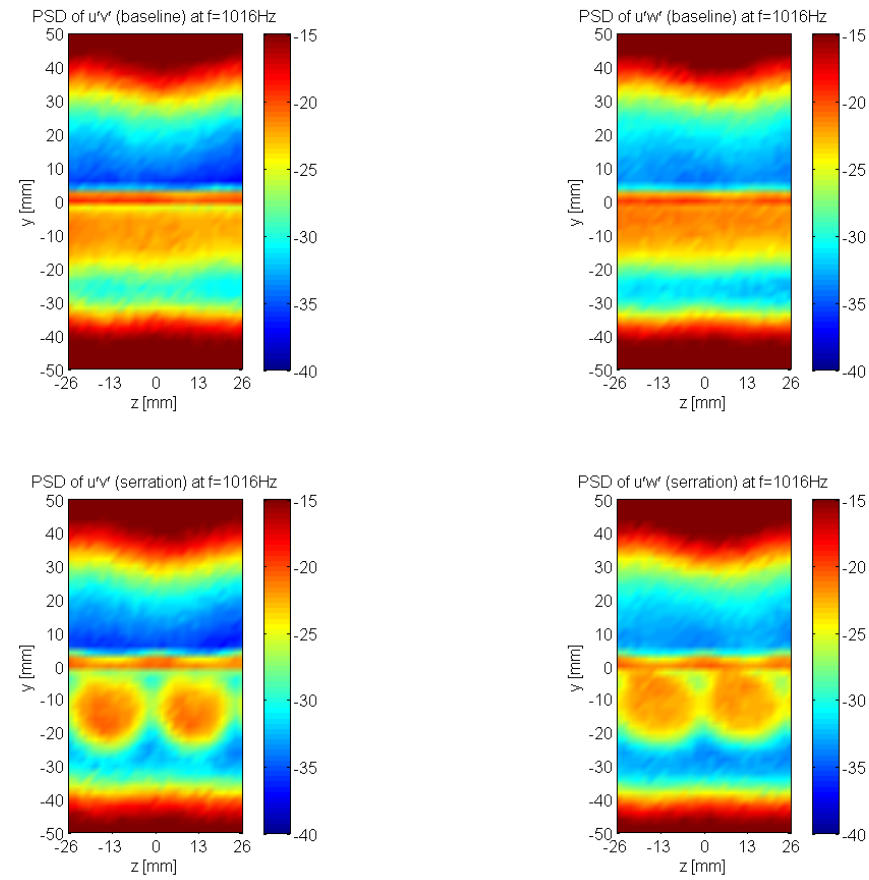


Figure 131: PSD [dB] at $f = 1016$ Hz of $u'v'$ and $u'w'$ for the baseline vs. A45W26 at $x/c = 1.02$ in the wake of the aerofoil, $AoA = 0^\circ$, $Tu(u) = 5\%$, $U = 25 \text{ ms}^{-1}$

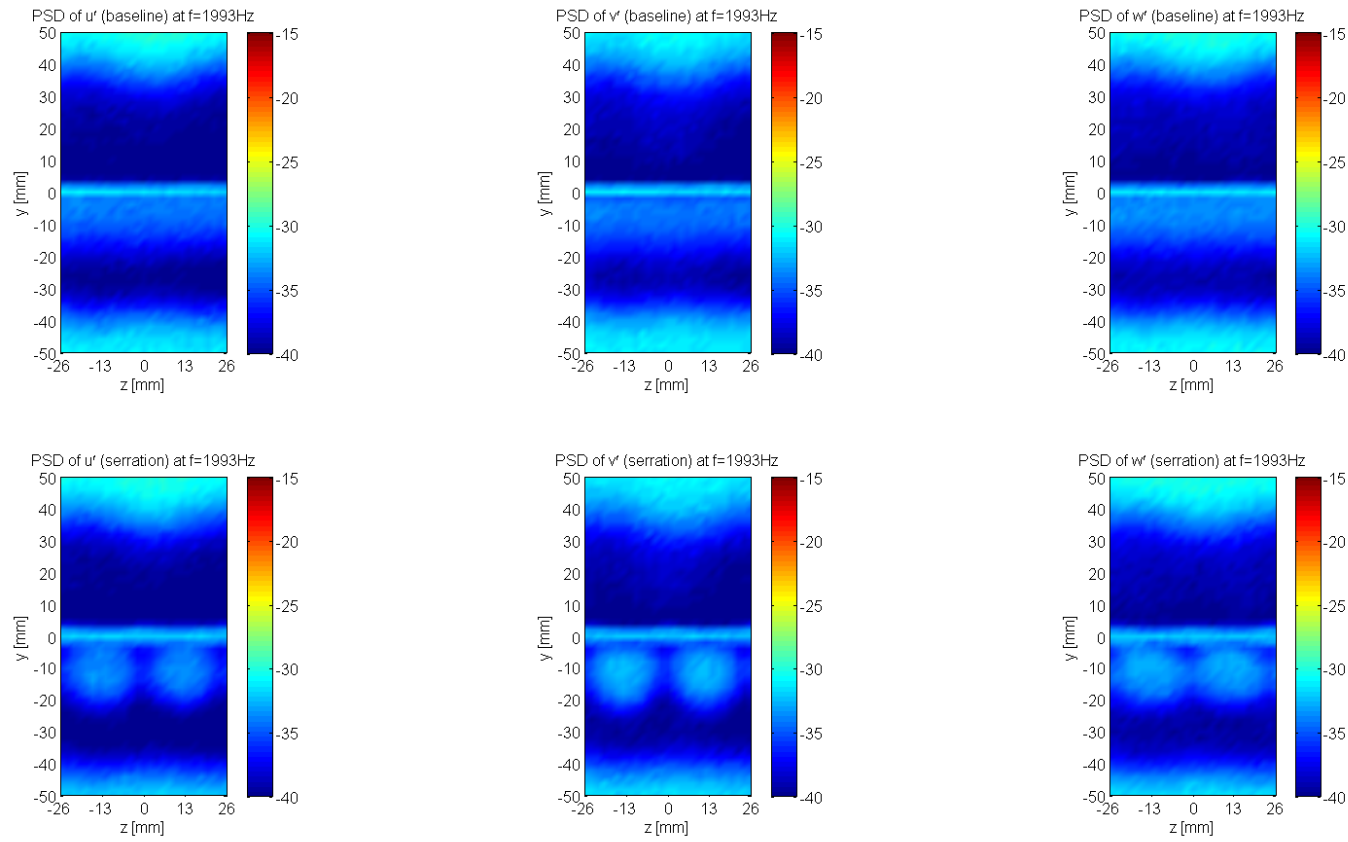


Figure 132: PSD [dB] at $f = 1993$ Hz of u' , v' and w' for the baseline vs. A45W26 at $x/c = 1.02$ in the wake of the aerofoil, $\text{AoA} = 0^\circ$, $Tu(u) = 5\%$, $U = 25\text{ms}^{-1}$

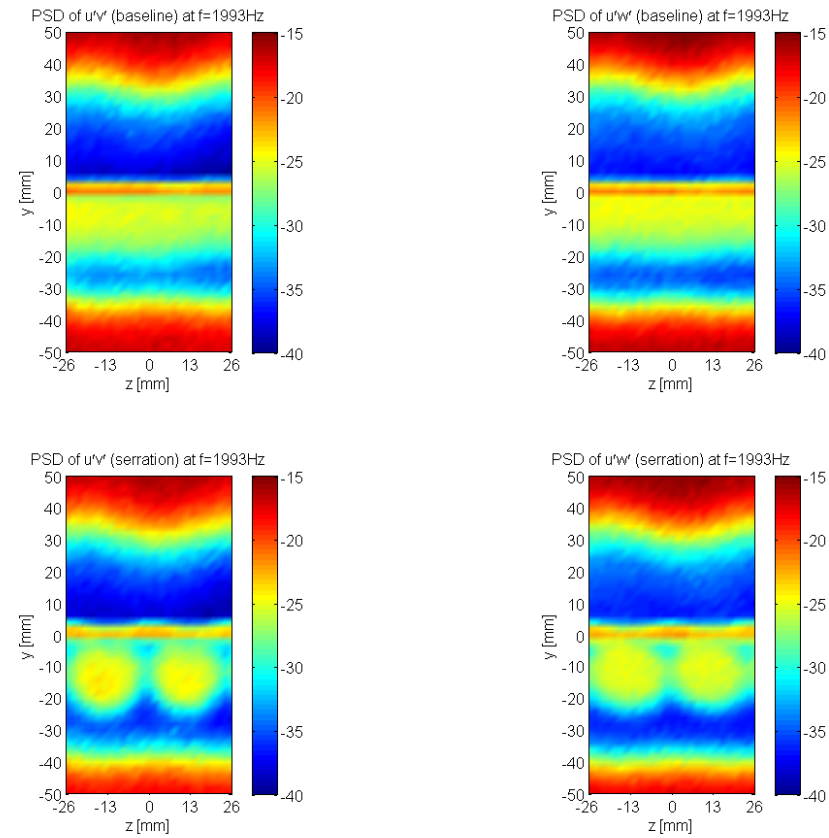


Figure 133: PSD [dB] at $f = 1993 \text{ Hz}$ of $u'v'$ and $u'w'$ for the baseline vs. A45W26 at $x/c = 1.02$ in the wake of the aerofoil, $\text{AoA} = 0^\circ$, $Tu(u) = 5\%$, $U = 25 \text{ ms}^{-1}$

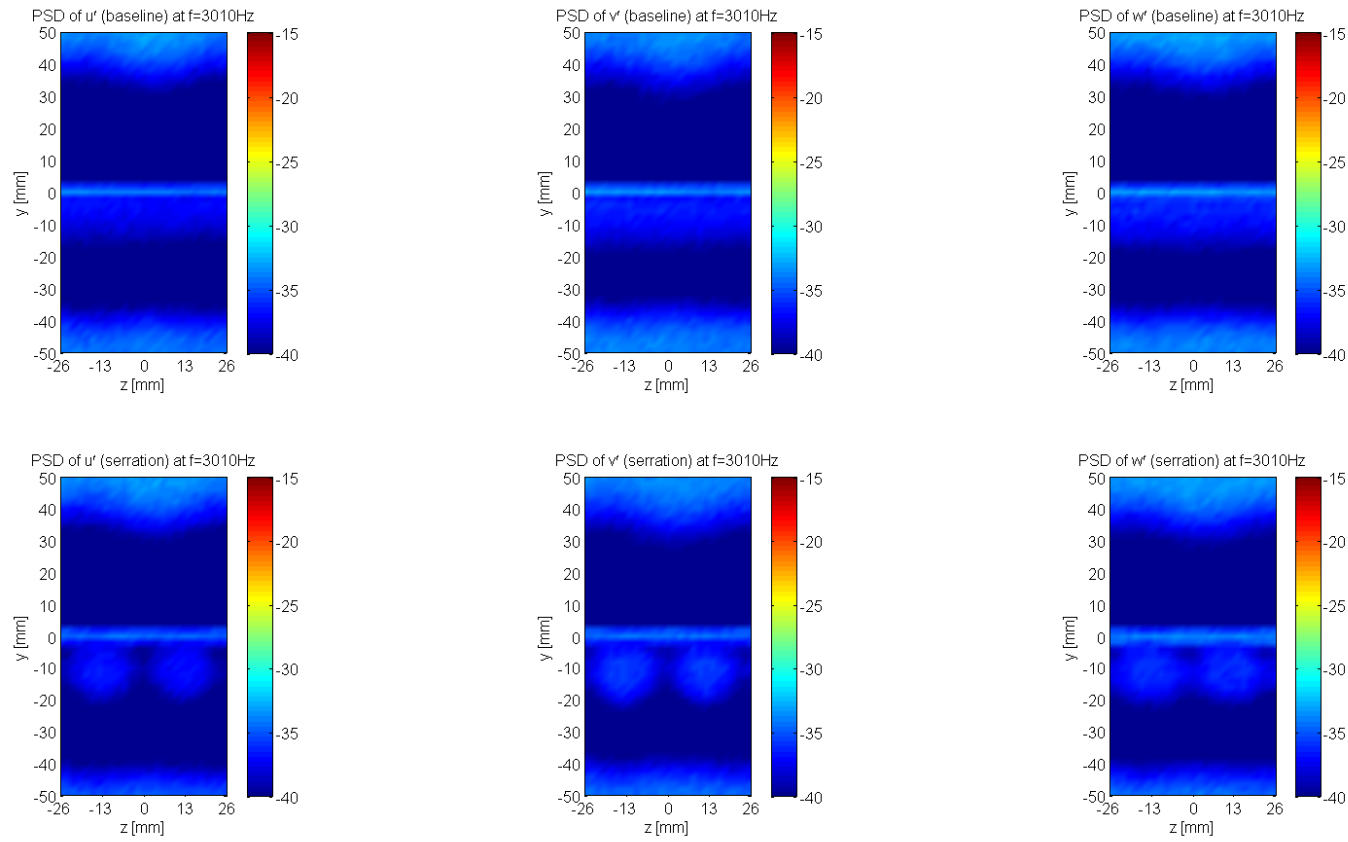


Figure 134: PSD [dB] at $f = 3010$ Hz of u' , v' and w' for the baseline vs. A45W26 at $x/c = 1.02$ in the wake of the aerofoil, $AoA = 0^\circ$, $Tu(u) = 5\%$, $U = 25\text{ms}^{-1}$

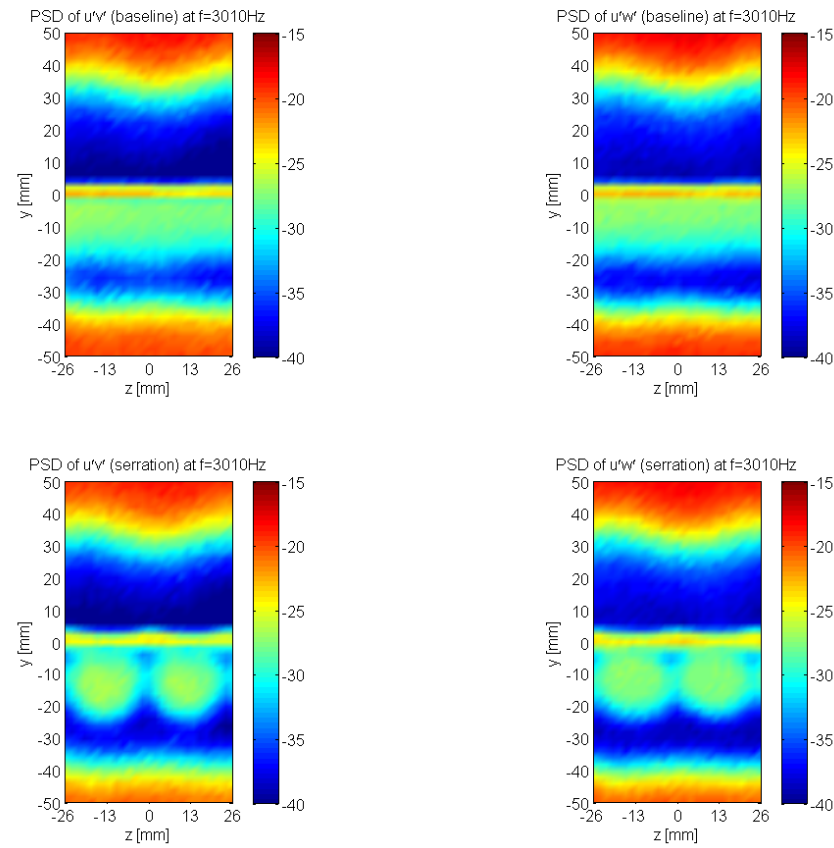


Figure 135: PSD [dB] at $f = 3010$ Hz of $u'v'$ and $u'w'$ for the baseline vs. A45W26 at $x/c = 1.02$ in the wake of the aerofoil, $\text{AoA} = 0^\circ$, $Tu(u) = 5\%$, $U = 25 \text{ ms}^{-1}$

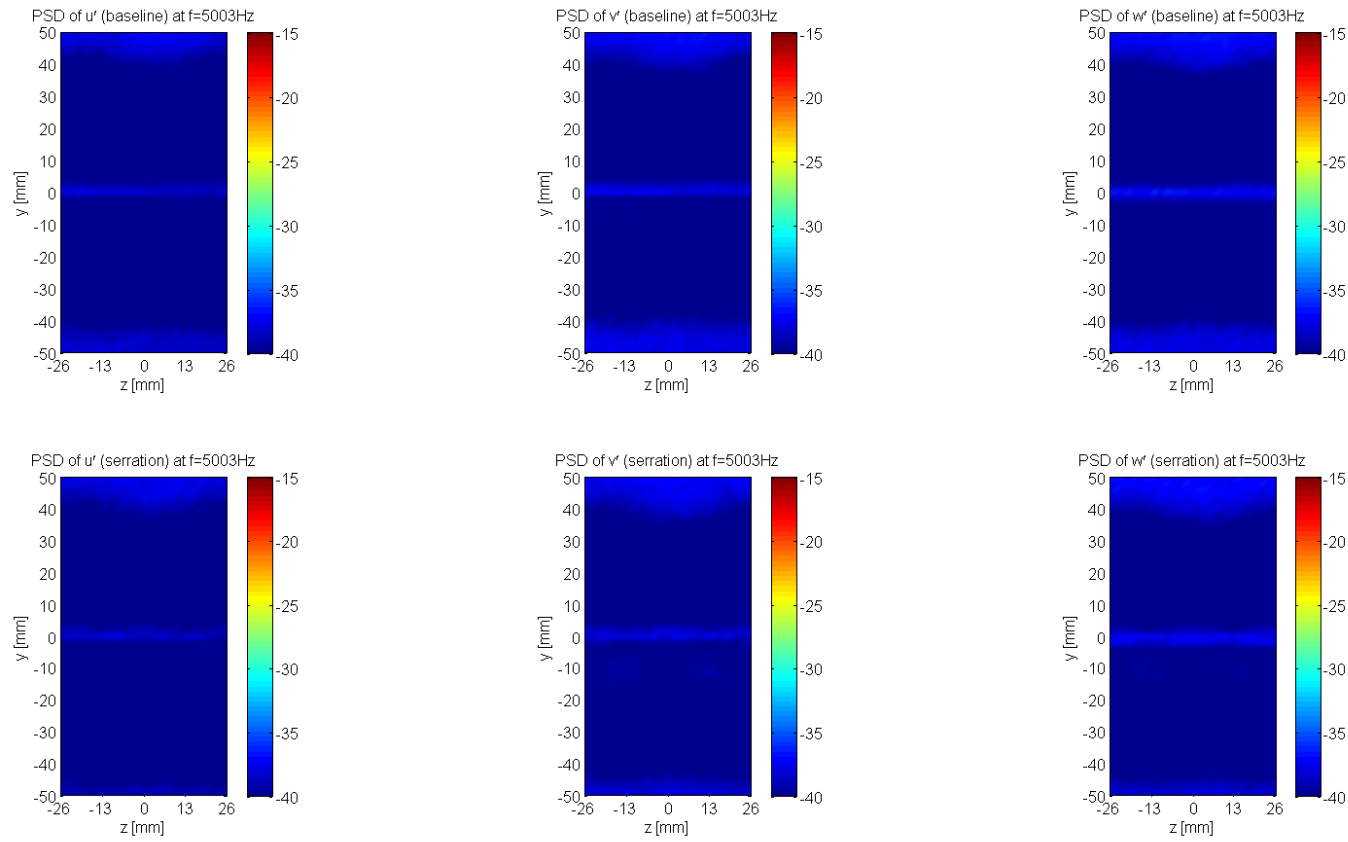


Figure 136: PSD [dB] at $f = 5003$ Hz of u' , v' and w' for the baseline vs. A45W26 at $x/c = 1.02$ in the wake of the aerofoil, $\text{AoA} = 0^\circ$, $Tu(u) = 5\%$, $U = 25\text{ms}^{-1}$

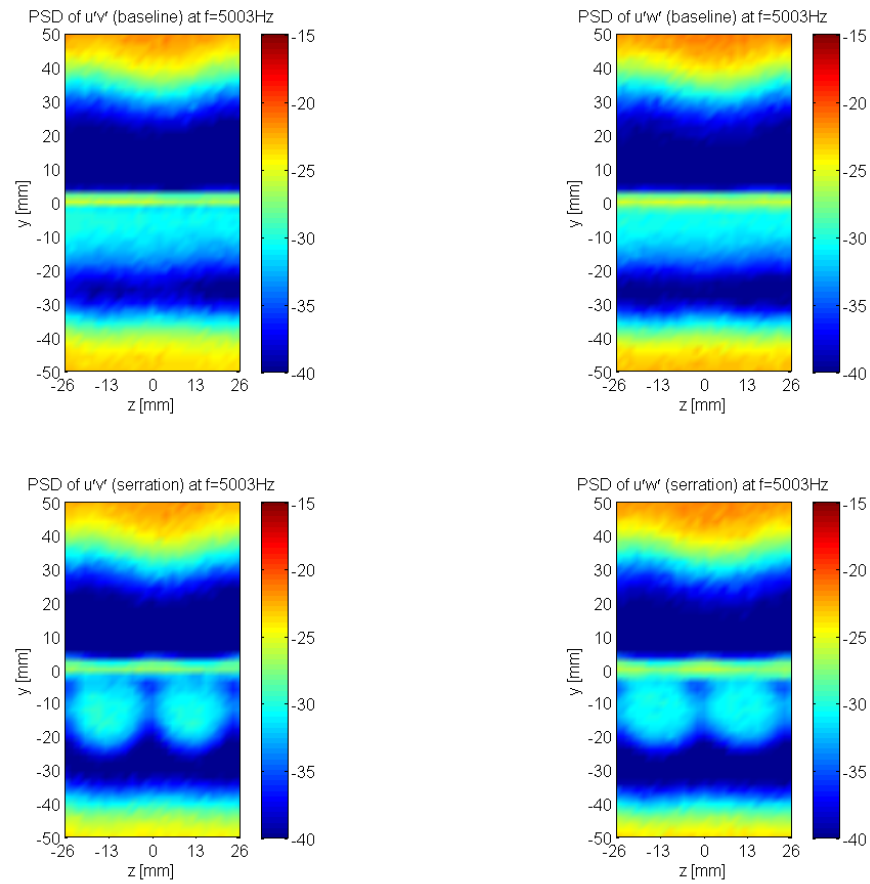


Figure 137: PSD [dB] at $f = 5003 \text{ Hz}$ of $u'v'$ and $u'w'$ for the baseline vs. A45W26 at $x/c = 1.02$ in the wake of the aerofoil, $\text{AoA} = 0^\circ$, $Tu(u) = 5\%$, $U = 25 \text{ ms}^{-1}$

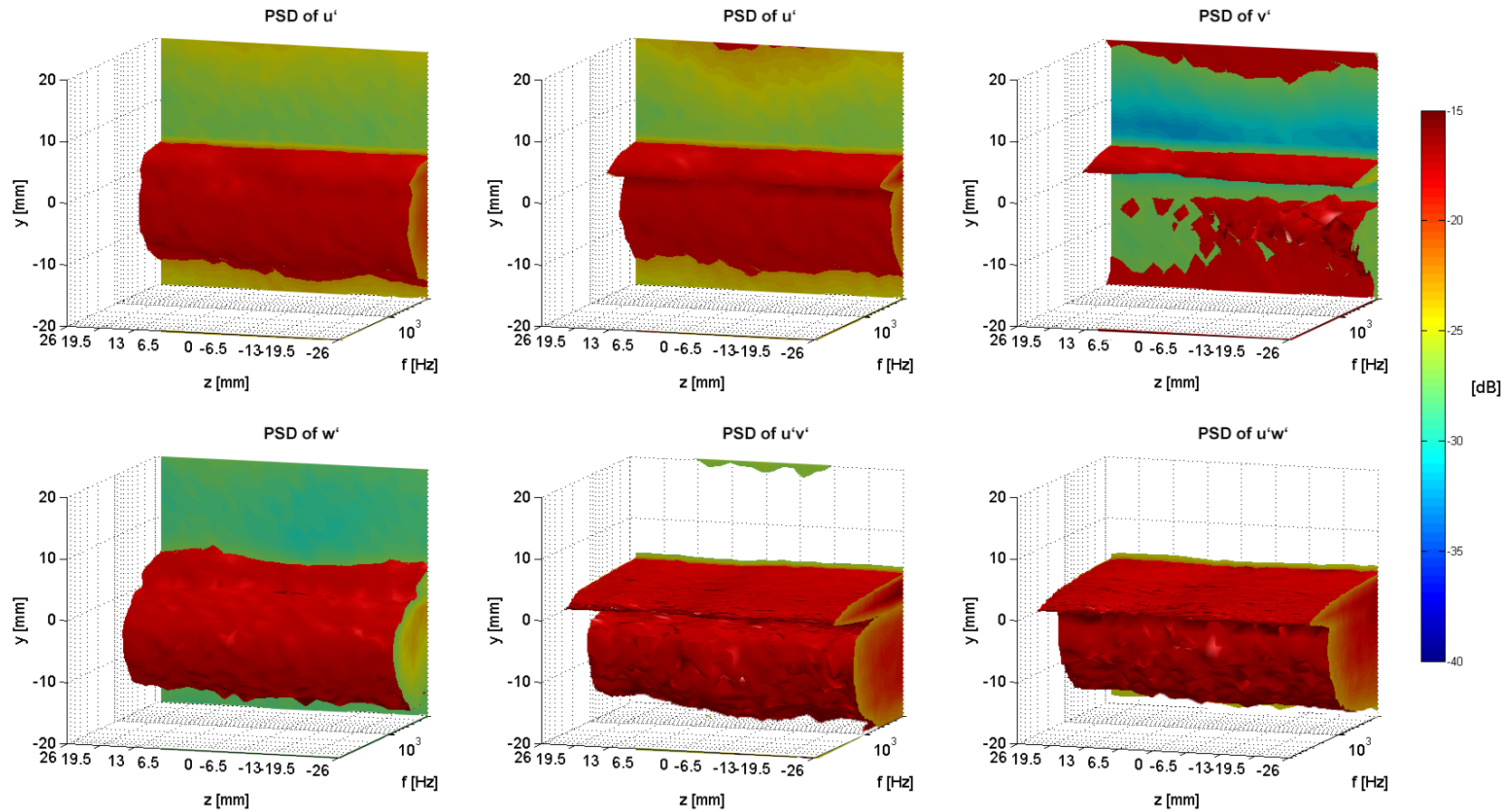


Figure 138: Comparison of PSD for u' , v' , w' , $u'v'$ and $u'w'$ for the baseline at $x/c = 1.02$ in the wake of the aerofoil, $AoA = 0^\circ$, $Tu(u) = 5\%$, $U = 25\text{ms}^{-1}$

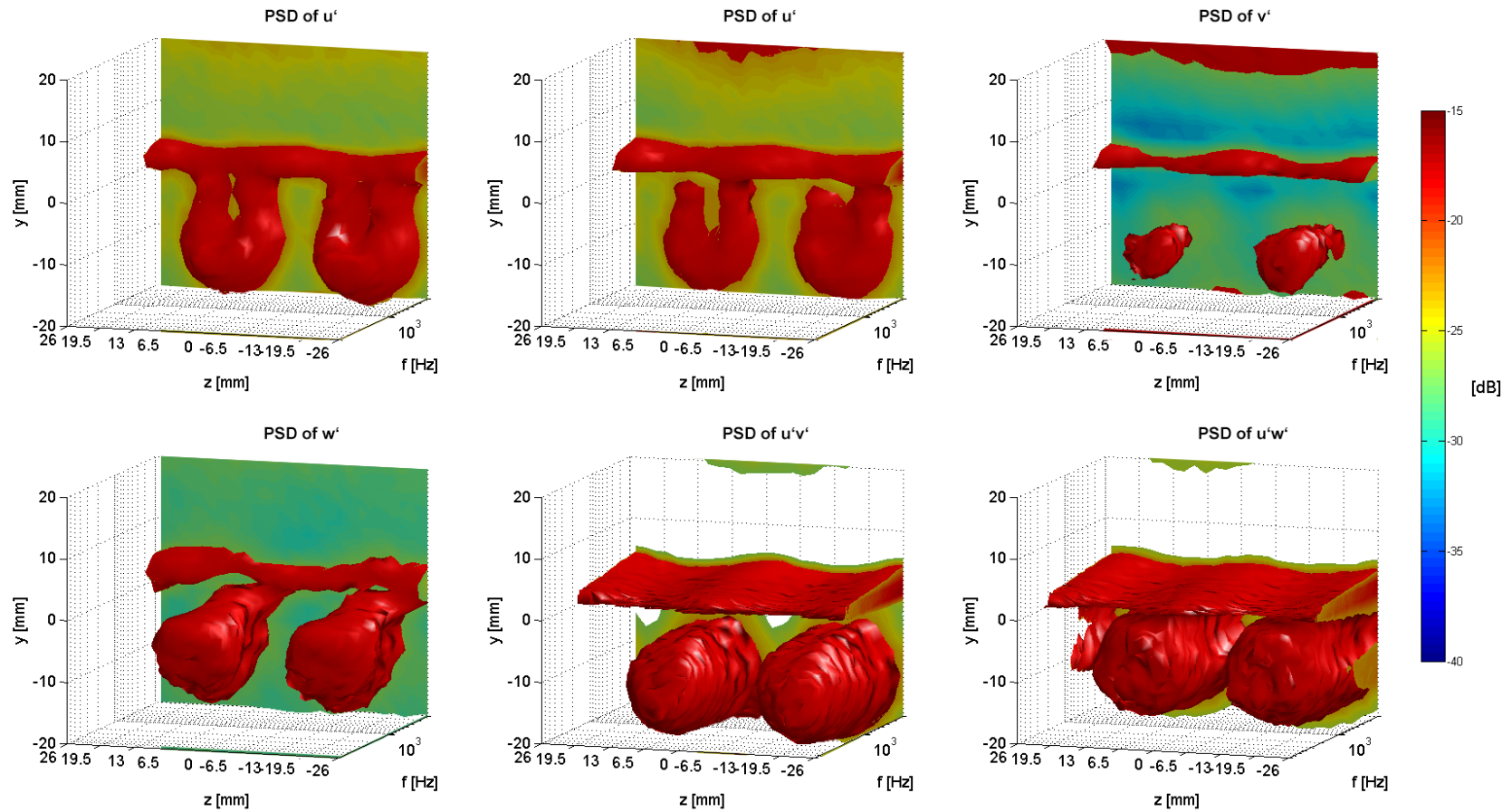


Figure 139: Comparison of PSD for u' , v' , w' , $u'v'$ and $u'w'$ for the A45W26 leading edge at $x/c = 1.02$ in the wake of the aerofoil, $AoA = 0^\circ$, $Tu(u) = 5\%$, $U = 25\text{ms}^{-1}$

Appendix D – A12W26 LE

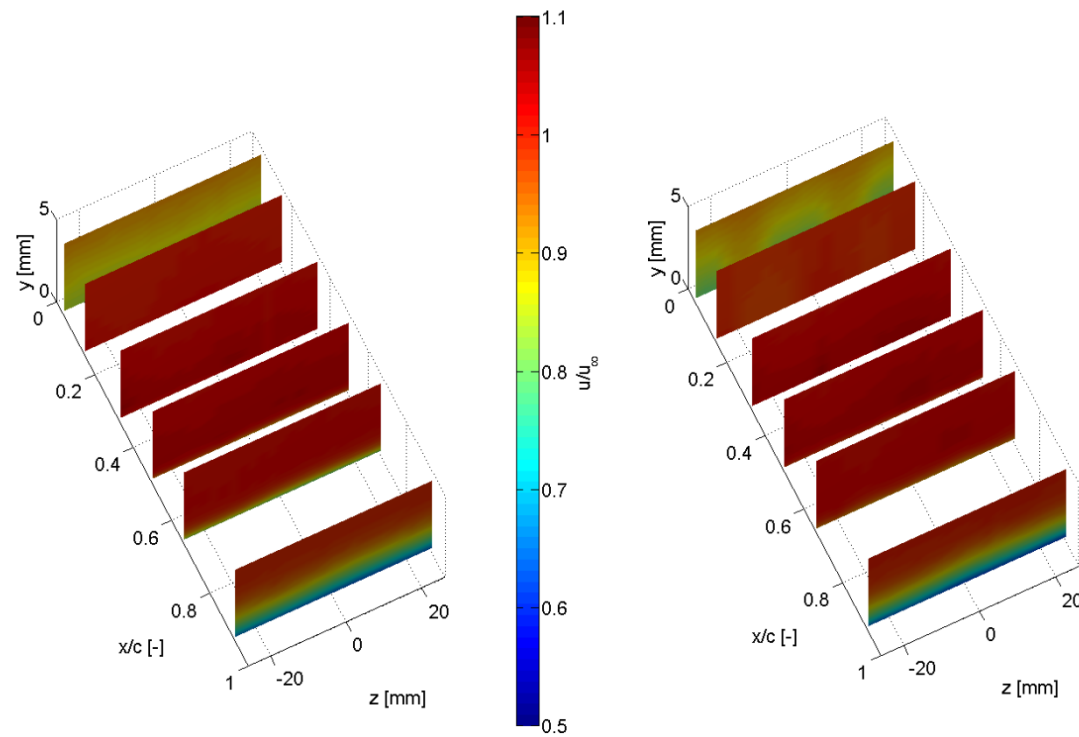


Figure 140: Overview boundary layer profiles normalised by the free-stream, baseline (left) vs. A12W26 (right) suction side, $\text{AoA} = 0^\circ$, $Tu = 5\%$, $U = 25\text{ms}^{-1}$

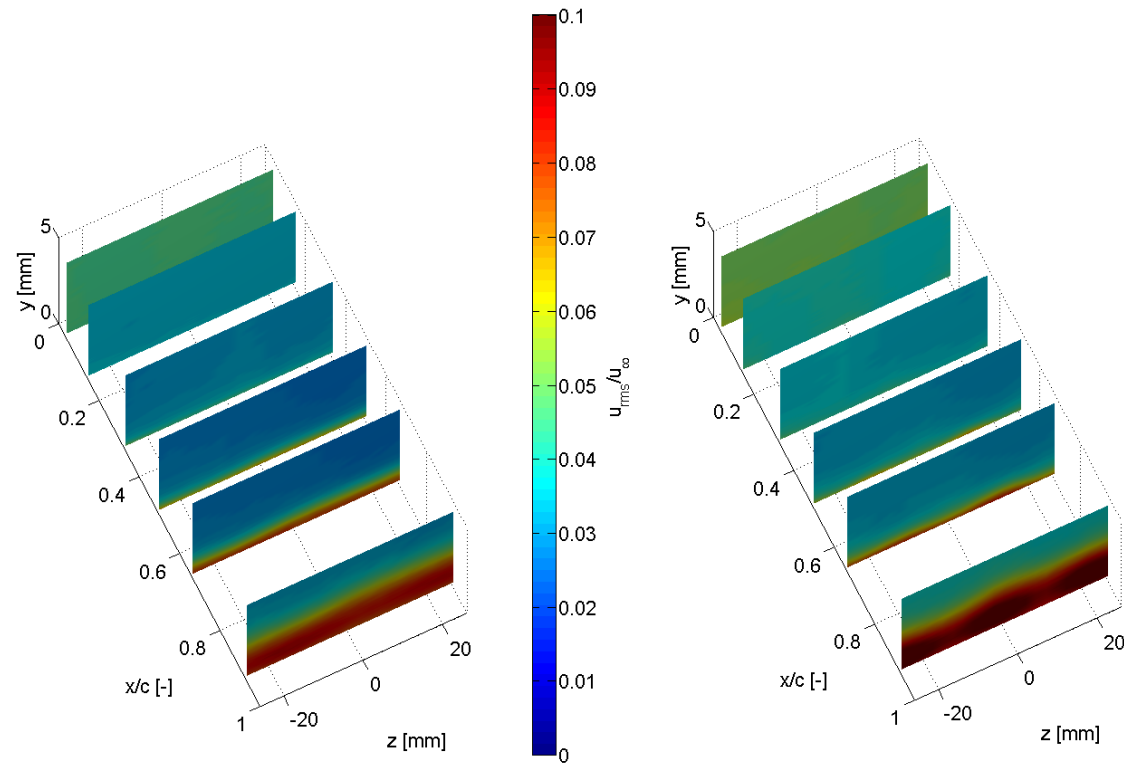


Figure 141: Turbulence profiles, baseline (left) vs. A45W26 (right) suction side, $\text{AoA} = 0^\circ$, $Tu = 5\%$, $U = 25\text{ms}^{-1}$

Eidesstattliche Erklärung

Hiermit versichere ich, Oliver Koster, an Eides statt, die vorliegende Master-Thesis selbständig verfasst und keine weiteren als die angegebenen Hilfsmittel und Quellen benutzt zu haben.

Dies ist die von der Hochschule Düsseldorf zu bewertende Version.

Ort, Datum _____ Unterschrift _____